

# Post Ligation Modification of Metallotetrazines as Prospective Surface Molecular Probes

Von der Fakultät Chemie der Universität Stuttgart  
zur Erlangung der Würde eines  
Doktors der Naturwissenschaften (Dr. rer. nat.)  
genehmigte Abhandlung

vorgelegt von  
**Marc Schnierle**  
aus Nagold

Hauptberichter: PD Dr. Mark R. Ringenberg  
Mitberichter: Jun.-Prof. Dr. Deven P. Estes  
Prüfungsvorsitz: Prof. Dr. René Peters

Tag der mündlichen Prüfung: 30. Mai 2023

*Institut für Anorganische Chemie der Universität Stuttgart*  
**2023**





*This work was carried out from July 2018 to December 2022 at the Institute of Inorganic Chemistry (University of Stuttgart, Germany) under the supervision of PD Dr. M. R. Ringenberg.*

### **Selbstständigkeitserklärung**

Hiermit versichere ich, die vorliegende Arbeit mit dem Titel *Post Ligation Modification of Metallotetrazines as Perspective Surface Molecular Probes* selbständig verfasst, keine anderen als die angegebenen Quellen benutzt und alle wörtlich oder sinngemäß aus anderen Werken übernommenen Aussagen als solche gekennzeichnet zu haben. Das elektronische Exemplar stimmt mit den anderen Exemplaren überein.

---

Stuttgart, .....

### **Declaration of Authorship**

I hereby assure that I have independently written the present work with the title *Post Ligation Modification of Metallotetrazines as Perspective Surface Molecular Probes*, that I have not used any other sources than those indicated, and that I have marked as such all statements taken literally or analogously from other works. The electronic copy agrees with the other copies.

---

Stuttgart, .....



## Acknowledgement

My first and most important thanks goes to Dr. Mark Ringenberg with whom I had the honor of founding his work group at the University of Stuttgart. There is no better group-leader. Also thanks for all the tips and support.

I want to thank Willi for the inspiration, Wolfgang for the crystals and Mario and Ziggi for the entertainment.

Another big thanks goes to all the Lemminge, thank god all of them got their own brains, which were smarter than mine ;). One lemming stood out, thank you Laura for the best time in the lab and the best time during COVID I could imagine. Thanks for all.

Because I can never list all of you a general thanks to all of you who have supported me in any way.



Exposé zur Dissertation

## “Post Ligation Modification of Metallotetrazines as Perspective Surface Molecular Probes”

Marc Schnierle, Institut für Anorganische Chemie der Universität Stuttgart

The chemical industry is constantly growing to meet the future needs of society. Energy efficiency, recycling, better resource management are major places where research chemists can make contributions. Catalysis is one place that efforts have been focused, where catalysts often fall into two categories: heterogeneous catalysts and homogeneous catalysts. There are however, often a trade off between robustness and separation, versus faster and milder conditions and higher selectivity between the two types of catalysts. An ideal catalyst would take the advantages of both systems, and one way this is achieved is by amending homogeneous catalysts to heterogeneous support to create a hybrid catalyst. The way in which the catalyst is fixed to a surface is generally the most important step, because it can either detrimental or synergistic effects on its reactivity.

Several methods for binding catalyst to surfaces are known from the literature, including: methoxysilanes functionalized linker which interact with surface-OH<sup>[1]</sup>, thiol-alkyl chains forming SAMs on Au surfaces<sup>[2]</sup>, functionalized COFs<sup>[3]</sup> and charged SBA-15 materials<sup>[4]</sup>.

In the following work, the focus is on the synthesis of metal complexes containing a tetrazine moiety. The 4+2 cycloaddition between a tetrazine and an olefin allows for kinetically controlled click reaction. Norbornene is a particularly interesting olefin because it can be easily derivatized.<sup>[5]</sup> In addition, the electrochemical properties of the synthesized compound were analyzed to better understand how the changing tetrazine affects after olefin addition its electronic properties<sup>[6-8]</sup>.

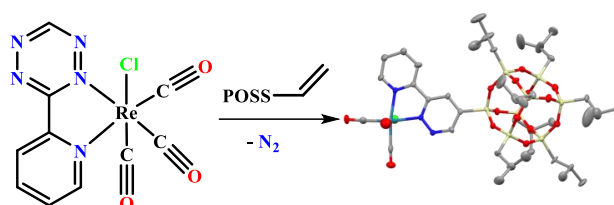


**Figure 1:** The reaction of a tetrazine ligand based Re-complex with a vinyl POSS serving as a surface analog.

## References

- [1] F. Ziegler, J. Teske, I. Elser, M. Dyballa, W. Frey, H. Kraus, N. Hansen, J. Rybka, U. Tallarek and M. R. Buchmeiser, *J. Am. Chem. Soc.* **2019**, *141*, 19014-19022.
- [2] J. P. Collmann, N. K. Devaraj, T. P. A. Eberspacher, Ch. E. D. Chidsey, *Langmuir* **2006**, *22*, 2457-2464.
- [3] S. T. Emmerling, F. Ziegler, F. R. Fischer, R. Schoch, M. Bauer, B. Plietker, M. R. Buchmeiser and B. V. Lotsch, *Chem. Eur. J.* **2021**, *10*.
- [4] Z. Li, C. Rieg, A. K. Beurer, M. Benz, J. Bender, Ch. Schneck, Y. Traa, M. Dyballa and M. Hunger, *Adsorption* **2021**, *27*, 49-68.
- [5] A. D. Hennis, J. D. Polley, G. S. Long, A. Sen, D. Yandulov, J. Lipian, G. M. Benedikt, L. F. Rhodes, and J. Huffman *Organometallics* **2001**, *20*, 13, 2802-2812.
- [6] M. Schnierle, S. Blicke, V. Filippou and M. R. Ringenberg, *Chem. Commun.* **2020**, *56*, 12033-12036.
- [7] M. Schnierle, M. Leimkühler and M. R. Ringenberg, *Inorg. Chem.* **2021**, *60*, 6367-6374.
- [8] Marc Schnierle, Mario Winkler, Vasileios Filippou, Joris van Slageren,\* and Mark R. Ringenberg\* DOI: 10.1002/ejic.202100998R1 / *Eur. J. Inorg. Chem.* (accepted).

## List of Papers imbedded in this Thesis

### **Paper 1. Tetrazine metallation boosts rate and regioselectivity of inverse electron demand Diels–Alder (iEDDA) addition of dienophiles**

Marc Schnierle, Svenja Blickle, Vasileios Filippou and Mark R. Ringenberg

*Chem. Commun.*, **2020**, *56*, 12033-12036. (DOI: 10.1039/d0cc03805a) - Open Access

### **Paper 2. $[(\eta^6\text{-p-Cymene})[3\text{-(pyrid-2-yl)-1,2,4,5-tetrazine}]\text{chlororuthenium(II)}]^+$ , Redox Noninnocence and Dienophile Addition to Coordinated Tetrazine**

Marc Schnierle, Marie Leimkühler, and Mark R. Ringenberg

*Inorg. Chem.* **2021**, *60*, (9), 6367–6374. (<https://doi.org/10.1021/acs.inorgchem.1c00094>)

Appropriate credit for the requested material should be given as follows:

"Reprinted (adapted) with permission from  $[(\eta^6\text{-p-Cymene})[3\text{-(pyrid-2-yl)-1,2,4,5-tetrazine}]\text{chlororuthenium(II)}]^+$ , Redox Noninnocence and Dienophile Addition to Coordinated Tetrazine. Marc Schnierle, Marie Leimkühler, and Mark R. Ringenberg. *Inorg. Chem.* 2021, *60*, (9), 6367–6374. Copyright 2021 American Chemical Society."

### **Paper 3. (Spectro)Electrochemistry of 3-Pyrid-2-yl- Tetra- or Diazine Tricarbonylrhenium-(I)-chloride**

Marc Schnierle, Mario Winkler, Vasileios Filippou, Joris van Slageren, and Mark R. Ringenberg

*Eur. J. Inorg. Chem.* **2022**, e202100 (DOI: 10.1002/ejic.202100998R1) Open Access

### **Paper 4. Immobilization by iEDDA [4+2] cycloaddition of a 3-(pyrid-2-yl)-methyl-tetrazine-tricarbonylrhenium(I)-chloride derivative onto a norbonen-trimethoxysilane functionalized SBA-15.**

Marc Schnierle, Laura Neumüller, Felix Ziegler, Mario Winkler, Osman Bunjaku, Johanna Bruckner, Michael R. Buchmeiser, Joris van Slageren, Deven P. Estes, Mark R. Ringenberg

Manuscript

## Contribution Report

**Paper 1.** Responsible for the idea of the reaction of metallotetrazines with the dienogames presented in the publication, as well as the recording and evaluation of experimental data. In particular, the determination of many different products. Another part of the publication is the construction of a measuring apparatus and its use for the kinetic data of the different reactions. The writing of the manuscript was also in the hands of the first author. The co-authors have revised the first version of the manuscript and added input concerning the DFT calculations.

**Paper 2.** Responsible for synthesis, purification, electrochemical as well as spectroscopic studies and interpretation of data. The writing of the manuscript was also in the hands of the first author. The co-authors have revised the first version of the manuscript and added input concerning the DFT calculations.

**Paper 3.** The preliminary publication includes a shared first authorship. Parts of the bachelor thesis of Marie Leimkühler were used. The topic and the supervision (supervision of the preparative work - evaluation of the data - interpretation of the data - planning of the further procedure) was given and carried out by Marc Schnierle. Furthermore, the part of the work is the following of the reaction kinetics, the electrochemical investigations as well as the oxidative investigations of the product at the reaction with vinylferrocene. The writing of the manuscript was also in the hands of the first author (Marc Schnierle). The co-authors have revised the first version of the manuscript and added input concerning the DFT calculations.

**Paper 4.** The pre-release includes a joint first authorship. The idea and planning, as well as the synthesis, analysis, evaluation and interpretation of three of the four ligands and complexes and their turnover with TCO is the share of Marc Schnierle. Furthermore, also the fixation in the porous system. The writing of the manuscript was also in the hands of the first author (Marc Schnierle). The co-authors have revised the first version of the manuscript and added input concerning the solid state analytics and the DFT calculations.

---

## List of other Publications

### Experimental and Theoretical Study on the Role of Monomeric vs. Dimeric Rhodium Oxazolidinone Norbornadiene Complexes in Catalytic Asymmetric 1,2- and 1,4-Additions

Manuel Kirchhof, Katrin Gugeler, Felix Richard Fischer, Michal Nowakowski, Alina Bauer, Sonia Alvarez-Barcia, Karina Abitaev, Marc Schnierle, Yaseen Qawasmi, Wolfgang Frey, Angelika Baro, Deven P. Estes, Thomas Sottmann, Mark R. Ringenberg, Bernd Plietker, Matthias Bauer, Johannes Kästner, and Sabine Laschat

*Organometallics* **2020**, *39*, (17), 3131–3145. (<https://doi.org/10.1021/acs.organomet.0c00310>)

### Electronic Structure of a Diiron Complex: A Multitechnique Experimental Study of [(dppf)Fe(CO)<sub>3</sub>]<sup>+0</sup>

Mario Winkler, Marc Schnierle, Felix Ehrlich, Kim-Isabelle Mehnert, David Hunger, Alena M. Sheveleva, Lukas Burkhardt, Matthias Bauer, Floriana Tuna, Mark R. Ringenberg, and Joris van Slageren

*Inorg. Chem.* **2021**, *60*, (5), 2856–2865. (<https://doi.org/10.1021/acs.inorgchem.0c03259>)

### Electrochemical Reduction Mechanism of [( $\eta^5$ -C<sub>5</sub>H<sub>5</sub>)Fe(dppf)(CO)]<sup>+</sup> (dppf = 1,1'-Bis(diphenylphosphino)ferrocene)

Yixian Pan, Marc Schnierle, Daniel Auweiler, and Mark R. Ringenberg

*Organometallics* **2021**, *40*, (6), 760–765. (<https://doi.org/10.1021/acs.organomet.1c00010>)

### Organobimetallic Nickel-Iron Complexes, Valence Tautomer or Charge Localized Ferrocene Ligands Upon Oxidation

Mark R. Ringenberg, Marc Schnierle, and Christina Sondermann

*Eur. J. Inorg. Chem.* **2022**, e202100940. ([doi.org/10.1002/ejic.202100940](https://doi.org/10.1002/ejic.202100940))

### Metal–metal communication between 1, 1'-bis (diphenylphosphino) cobaltoce-nium and an organonickel moiety

Daniel Auweiler, Marc Schnierle, Valentin Rapp and Mark R. Ringenberg

*Dalton Transactions* **2022**, *51* (16), 6293-6298. (DOI:10.1039/D2DT00650B)

### An orthogonal labeling strategy to accelerate bioconjugation of [<sup>99m</sup>Tc] Tc-building blocks

Henrik Braband, Marc Schnierle, Mark R. Ringenberg and Roger Alberto

*Nuclear Medicine and Biology*, **2022**, *114*. Jg., S. S32-S33.





---

## List of Abbreviations

<b>Ar</b>	aryl group
<b>bpy</b>	2,2'-bipyridine
<b>BIAN</b>	bis-(imino)-acenaphten
<b>CO</b>	carbonyl
<b>CV</b>	cyclic voltammetry
<b>COF</b>	covalent organic frameworks
<b>CN</b>	coordination number
<b>CE</b>	counter electrode
<b>CF<sub>3</sub></b>	trifluoromethyl
<b>DPV</b>	differential pulse voltammetry
<b>DFT</b>	density functional theory
<b>E</b>	electrochemical potential
<b>EDG</b>	electron-donating group
<b>EA</b>	elemental analysis
<b>EDTA</b>	ethylenediaminetetraacetic acid
<b>EPR</b>	electron paramagnetic resonance spectroscopy
<b>EWG</b>	electron-withdrawing group
<b>FcH</b>	ferrocene
<b>FcH<sup>+</sup></b>	ferrocenium
<b><math>\Delta G^\ddagger</math></b>	Gibbs free energy
<b>HOMO</b>	highest occupied molecular orbital
<b>H</b>	proton
<b><math>\Delta H^\ddagger</math></b>	free enthalpy
<b>iEDDA</b>	inverse electron-demand Diels-Alder reaction
<b>iclick</b>	inorganic click
<b>IR</b>	infrared
<b>I</b>	nuclear spin
<b>k<sub>2</sub></b>	reaction kinetic
<b>LUMO</b>	lowest unoccupied molecular orbital
<b>L</b>	ligand
<b>m</b>	meter
<b>M</b>	metal
<b>M</b>	molar
<b>Me</b>	methyl

---

<b>MLCT</b>	metal to ligand charge transfer
<b>MO</b>	molecular orbital
<b>NBE</b>	norbonene
<b>n</b>	number of wquivalent coupling partners
<b>NMR</b>	nuclear magnetic resonance
<b>OMe</b>	methoxy
<b><i>Ox</i></b>	oxidation
<b>Py</b>	pyridine
<b>PMO</b>	periodic mesoporous organosilica
<b>RT</b>	room temperature
<b>R</b>	alkyl group
<b>RDE</b>	rotation disk electrode
<b>RE</b>	reference electrode
<b>Red</b>	reduction
<b>SiO<sub>n/x</sub></b>	silica surface
<b>s</b>	second
<b>SEC</b>	spectroelectrochemistry
<b>SBA-15</b>	Santa Barbara Amorphous-15 - highly stable mesoporous silica
<b><math>\Delta S^\ddagger</math></b>	free entropy
<b>TCO</b>	transcyclooctene
<b>TEOA</b>	triethanolamine
<b>Tz</b>	tetrazine
<b>TLC</b>	thin layer chromatography
<b>UV</b>	ultraviolet radiation
<b>UV/Vis</b>	ultraviolet visible
<b>V</b>	voltge
<b>WE</b>	working electrode
<b>XPS</b>	x-Ray photoelectron spectroscopy
<b>x-Ray</b>	roentgen radiation

## Abstract

In this work, a novel immobilization method is discussed, the [4+2] cycloaddition between tetrazines and dienophiles. The scientific novelty is the synthesis of tetrazine compounds and metallotetrazine complex with rhenium and ruthenium as metal centers. Furthermore, the reaction of these tetrazine compounds with various dienophiles such as styrene, vinyl ferrocene, ethynyl ferrocene, norbornene and transcyclooctenes is presented. Other aspects studied include the kinetics of this [4+2] cycloaddition, the oxidation of the dihydropyridazine formed, and the immobilization of a complex in an SBA-15 pore. The [4+2] cycloaddition is an inverse electron-demand Diels-Alder (IEDDA) reaction. In this reaction, the diene (here the tetrazine) contains an electron-withdrawing group (EWG) and the dienophile has an electron-donating group. Thus, the LUMO of the diene and the HOMO of the dienophile overlap and react.

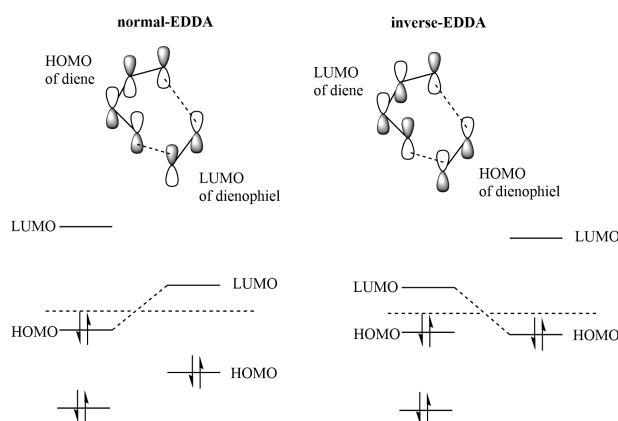


**Figure 0.1:** Frontier orbital theory for the normal (*left*) and inverse electron demand (*right*) Diels Alder.

In the [4+2] cycloaddition reaction, the dienophile approaches the tetrazine from below or above. The elimination of an  $N_2$  molecule forms a dihydropyridazine, which now combines the two starting molecules. In a final step of the [4+2]-cycloaddition, the resulting product can still be oxidized.

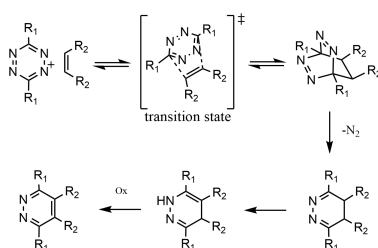


**Figure 0.2:** Reaction mechanism of tetrazine with dienophile.

In the course of the dissertation the first crystal structure of a metallotetrazine accessible for the [4+2] cycloaddition with H-tetrazine was published. Furthermore, one of the fastest reactions with TCO, with a reaction rate constant  $k_2$  of  $4.06 \cdot 10^5 \text{ M}^{-1}\text{s}^{-1}$ , could be presented. Another aspect investigated is the influence of the pyrid-2-yl residual on the tetrazine on the kinetics. Here it could be shown that the reaction kinetics can be influenced by manipulating the electron density, by electron donating or withdrawing groups. The decrease of the electron density is also responsible for the fact that the complexed tetrazine reacts faster on rhenium or ruthenium compared to the free ligand itself. In the [4+2] cycloaddition of  $\eta^6$ -p-cymene)[3-(pyrid-2-yl)-1,2,4,5-tetrazine]-chlororuthenium(II)]PF<sub>6</sub>, oxidation of the dihydropyridazine species was also successfully demonstrated.

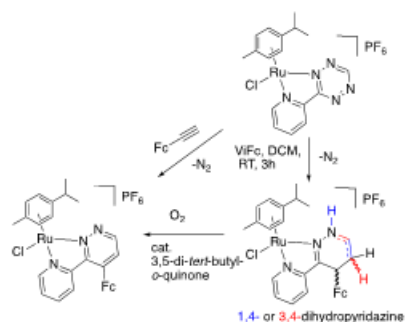


**Figure 0.3:** [4+2] cycloaddition with vinylferrocene and subsequent oxidation to the conjugated product, which is also formed in a reaction with ethynylferrocene.

Finally, it was shown that the [4+2] cycloaddition is a suitable method to immobilize a metal complex onto a surface or into a pore. For this purpose, SBA-15 was functionalized with a norbornenetrिमथoxysilane and reacted with a 3-(pyrid-2-yl)-s-tetrazine tricarbonylrhenium(I) chloride derivative.

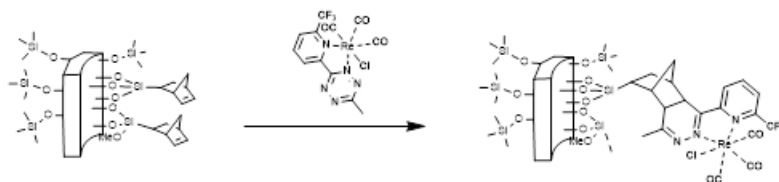


**Figure 0.4:** Immobilization of a metallotetrazine in a norbornenetrिमथoxysilane functionalized SBA-15 pore.

## Kurzzusammenfassung

In dieser Arbeit wird auf eine neuartige Fixierungsmethode eingegangen, auf die [4+2] Cycloaddition zwischen Tetrazinen und Dienophilen. Der wissenschaftliche neue Anteil ist die Synthese von neuen Tetrazin- und von Metallotetrazin-komplex-derivaten mit Rhenium und Ruthenium als Metallzentrum, sowie wie die erfolgreiche Reaktion dieser mit verschiedenen Dienophilen wie Styrol, Vinylferrocen, Ethynylferrocen, Norbonen und Transcyclooctenen. Weitere untersuchte Aspekte sind die Kinetik dieser [4+2] Cycloaddition, die Oxidation des entstandenen Dihydropyridazin und die Immobilisierung eines Komplexes auf in einer SBA-15 Pore.

Bei der [4+2] Cycloaddition handelt es sich um eine inverse Elektronenbedarfs Diels-Alder (iEDDA) Reaktion. Bei diesem besitzt das Diene (hier das Tetrazin) eine Elektronen ziehende Gruppe (EWG) und das Dienophil eine Elektronen schiebende Gruppe. Somit überlappen und reagieren das LUMO des Dienes und das HOMO des Dienophils.

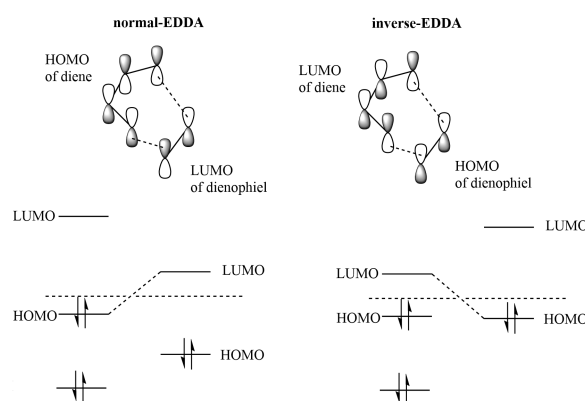


**Figure 0.1:** Grenzorbitaltheorie für den normalen (*links*) und den inversen Elektronenbedarf (*rechts*) Diels Alder.

Bei der Reaktion nähert sich das Dienophil von unten oder oben dem Tetrazin an, bricht das konjugierte  $\pi$ -System auf und durch die das Eliminieren eines  $N_2$  Moleküls wird ein Dihydropyridazin gebildet. Das entstandene Molekül verbindet nun beide Ausgangsmoleküle miteinander. In einem letzten Schritt der [4+2] Cycloaddition kann das entstandene Produkt noch oxidiert werden.

Im Zuge der Dissertation konnte die erste Kristallstruktur eines für die [4+2] Cycloaddition zugänglichen Metallotetrazin mit H-Tetrazin publiziert werden. Des Weiteren konnte eine der schnellsten Reaktionen mit TCO, mit einer Reaktionsgeschwindigkeit  $k_2$  von  $4.06 \cdot 10^5 / M^{-1}s^{-1}$ , vorgestellt werden.

Ein weiterer untersuchter Aspekt ist der Einfluss des Pyrid-2-yl Restes am Tetrazin auf die Kinetik. Hier konnte gezeigt werden, dass mit Änderung der Elektronendichte, durch

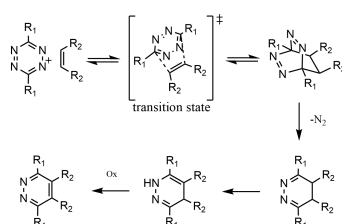


**Figure 0.2:** Reaktionsmechanismus von einem Tetrazin mit einem Dienophil.

Elektronen ziehende oder schiebende Gruppen die Reaktionskinetik beeinflusst werden kann. Selbiger Grund ist auch dafür verantwortlich, dass das Komplexierte Tetrazin am Rhenium oder Ruthenium schnellere Reaktionskinetiken aufweist wie als der freier Liagnd. Bei der [4+2] cycloaddition von  $\eta^6$ -p-Cymene)[3-(pyrid-2-yl)-1,2,4,5-tetrazine]-chlororuthenium(II)]PF<sub>6</sub> konnte auch erfolgreich eine Oxidation der dihydropyridazine Species gezeigt werden.

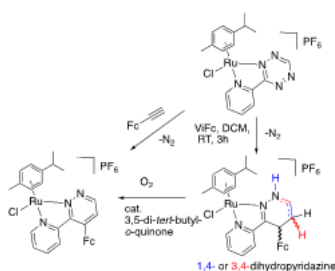


**Figure 0.3:** [4+2]-Cycloaddition mit Vinylferrocen und anschließender Oxidation zum konjugierten Produkt, welches auch direkt aus der Reaktion mit Ethynylferrocen gebildet werden kann.

Schlussendlich konnte auch gezeigt werden, dass die [4+2] Cycloaddition eine geeignete Methode ist um einen Metallkomplex auf eine Oberfläche, bzw. in eine Pore zu immobilisieren. Hierzu wurde ein SBA-15 mit einem Norbonentrimethoxysilan funktionalisiert und mit einem 3-(Pyrid-2-yl)-s-Tetrazine Tricarbonylrhenium(I)chloride derivative reagiert.

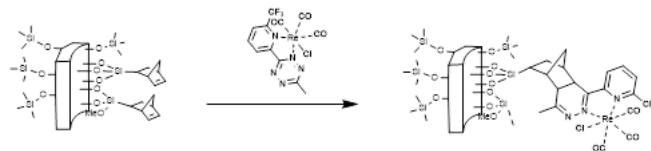


**Figure 0.4:** Immobilisierung eines Metalltetrazins in einer mit Norbeontrimethoxysilan funktionalisierten SBA-15-Pore.

# Contents

<b>Acknowledgement</b>	<b>I</b>
<b>Exposé zur Dissertation</b>	<b>II</b>
<b>List of Papers imbedded in this Thesis</b>	<b>IV</b>
<b>Contribution Report</b>	<b>V</b>
<b>List of other Publications</b>	<b>VI</b>
<b>List of Abbreviations</b>	<b>VIII</b>
<b>Abstract</b>	<b>X</b>
<b>Kurzzusammenfassung</b>	<b>XII</b>
<b>1 Motivation and Task Description</b>	<b>1</b>
<b>2 Introduction</b>	<b>3</b>
2.1 Catalysis . . . . .	3
2.2 Organometallic Complexes . . . . .	6
2.2.1 [(bpy)ReCl(CO) <sub>3</sub> ] . . . . .	8
2.3 Immobilization techniques and materials . . . . .	10
2.4 Click chemistry . . . . .	13
2.5 iEDDA . . . . .	15
2.6 Tetrazine: iEDDA - Synthesis - Properties - Application: . . . . .	17
2.6.1 Synthesis . . . . .	18
2.6.2 Properties . . . . .	19
2.6.3 Application . . . . .	21
2.7 Metallotetrazine . . . . .	21
<b>3 Preliminary work from the literature</b>	<b>24</b>
<b>4 Methods</b>	<b>26</b>
4.1 Volammetry . . . . .	26
4.1.1 Cyclic voltammetry . . . . .	27
4.1.2 Rotating disk electrode voltammetry . . . . .	30
4.2 Spectroelectrochemistry (SEC) . . . . .	31



4.3	Kinetics . . . . .	33
4.3.1	Measurement setup . . . . .	33
4.3.2	Kinetics: 0th order, 1st order, 2nd order and pseudo 1st order . . . . .	35
<b>5</b>	<b>Summary of Research</b>	<b>38</b>
5.1	Metallotetrazines increase regioselectivity and reactivity in the [4 + 2] cycloaddition reaction . . . . .	39
5.2	3-(Pyrid-2-yl)-s-Tetrazine Tricarbonylrhenium(I)chloride - Dienophile Addition - (Spectro)Electrochemistry . . . . .	42
5.3	[( $\eta^6$ -p-Cymene)[3-(pyrid-2-yl)-1,2,4,5-tetrazine]chlororuthenium(II)] <sup>+</sup> - Dienophile Addition - (Spectro)Electrochemistry . . . . .	46
5.4	Various 3-(Pyrid-2-yl)-s-Tetrazine Tricarbonylrhenium(I)chloride derivatives and their influence on reactivity . . . . .	49
<b>6</b>	<b>Conclusion &amp; Outlook</b>	<b>52</b>
<b>7</b>	<b>Publications</b>	<b>55</b>
7.1	Publication Paper 1. . . . .	55
7.2	Publication Paper 2. . . . .	60
7.3	Publication Paper 3. . . . .	67
7.4	Manuscript Paper 4. . . . .	76
	<b>References</b>	<b>83</b>
<b>8</b>	<b>Appendices</b>	<b>ii</b>
	Supporting Infos of Paper 1. . . . .	ii
	Supporting Infos of Paper 2. . . . .	xlix
	Supporting Infos of Paper 3. . . . .	lxxiv
	Supporting Infos of Paper 4. . . . .	cxxx
	Curriculum vitae . . . . .	clxx

## 1 Motivation and Task Description

Catalytic processes are standard in the industrial chemistry, but the synthesis, recovery or separation of homogeneous catalysts is often complicated. One approach is to minimize this effort, such as immobilization of a molecular catalyst to a solid support material. These asymmetric catalysts promise several benefits such as higher yields and selectivity as well as easy recovery and recyclability of the catalyst itself.[1][2][3][4][5][6][7][8]

The aim of this work is to demonstrate one potentially useful anchoring method to incorporate catalytically active transition metal centers on a carrier surface. This work focuses on covalent bonding through [4+2] cycloaddition between a metallotetrazine with a dienophile functionalized surface.

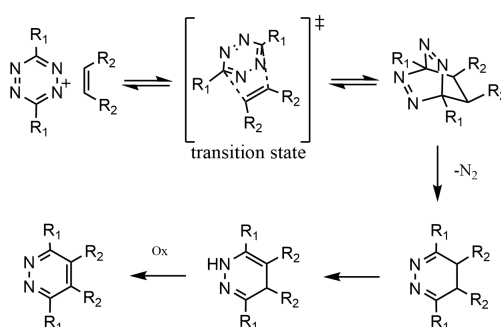


**Figure 1.1:** [4+2] cycloaddition of a tetrazine and a dienophile.

Organorhenium and -ruthenium compounds were made for the purpose of demonstrating the feasibility of modification of coordinated tetrazine ligands. The synthesis and characterization of these metallotetrazine complexes, as well as their reaction with dienophiles, e.g., norbornene, transcyclooctene, vinylferrocene and ethynylferrocene were studied in detail. Finally, it will be shown that immobilization on an SBA-functionalized surface is possible using this method.

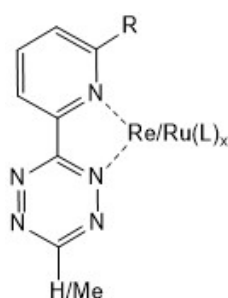


**Figure 1.2:** Illustration of possible metallotetrazine complexes.

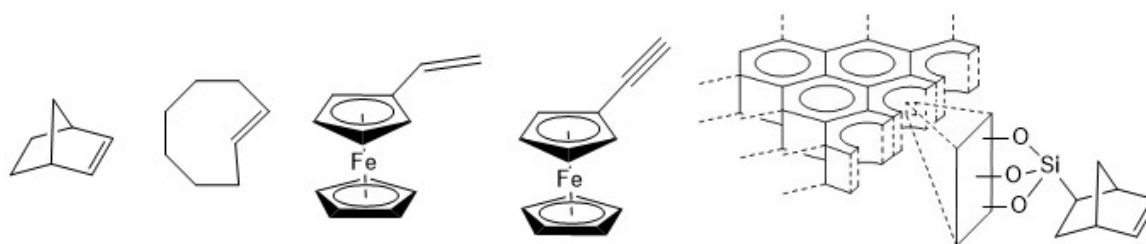


**Figure 1.3:** Illumination of the used dienophiles (norbornene, trans-cyclooctene, vinyl-ferrocene and ethynyl-ferrocene) and the functionalized SBA-15.

The research was divided into two parts: metallotetrazine reactivity and electrochemical investigations. **(Paper 1-4)** A closer look into the [4+2] cycloaddition  $\text{Ru}([\text{CyRu}(\text{TzPy})])$  with a vinyl- and ethynyl-ferrocene and the closing oxidation of the dihydropyridazine. **(Paper 3)** In addition to the synthesis of various metallotetrazines and their reaction with NBE and TCO, the final focus was the immobilization of metallotetrazines in an SBA-15 pore. **(Paper 4)**

## 2 Introduction

### 2.1 Catalysis

Catalysts influence the transition energy of the respective reaction in such a way that the energy of the transition state is lowered and thus speed up the process (Figure 2.1).[9][10][11] Catalysts provide an alternative reaction coordination path, which can be used to lower the activation energy. This enables higher productivity in the synthesis of many products, which is essential for today's industry. A distinction can be made between homogeneous and heterogeneous catalysts. Heterogeneous catalysts occur in 2 or more phase reaction mixtures and thus, have the advantage that they are easier to separate from the reaction solution. The most common are solid catalyst on solution starting material/products.[12][13] Homogeneous and heterogeneous catalysts each offer advantages and disadvantages in many applications.[14][15][16][17][18]

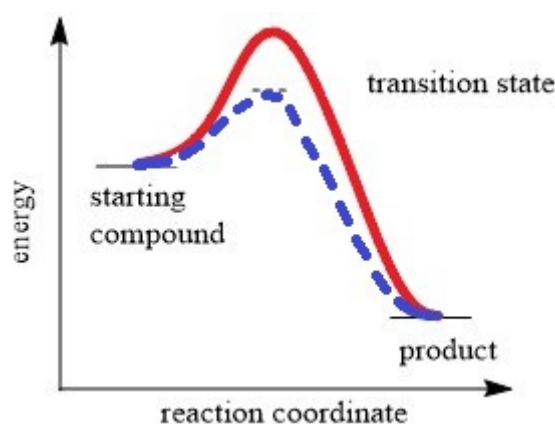


**Figure 2.1:** Energy diagram of a catalytically assisted and an uncatalyzed reaction. The required activation energy is lower in the catalytically assisted reaction due to the stabilized transition state.

One of the earliest documented cases of a heterogeneously catalyzed reaction was in 1783 by Joseph Priestley, who observed the decomposition of ethanol to ethylene on alumina; further decomposition reactions were also observed, such as ammonia to nitrogen and hydrogen and hydrogen peroxide to  $O_2$  and  $H_2O$ . Jöns Jakob Berzelius discovered the connection between all these reactions in 1835, that the substance (often a metal) was involved in the reaction but remained unchanged by the reaction. It was not until another half century later, in 1894, that Wilhelm Ostwald defined this process as catalysis.[19][20][19]

This type of catalyst is often used in the chemical industry, that have contact points to

everyday life. One example is the catalyst in the exhaust of cars with combustion engines. This catalyst often consists of a ceramic monolith mixed with precious metals such as palladium, rhodium and platinum, and catalyzes the conversion of  $O_2$ ,  $CO$ ,  $NO_2$  to  $CO_2$ ,  $N_2$  and  $H_2O$ . [21]

Recently, the focus has been on the synthesis of homogeneous catalysts, which are most often based on (transition) metal complexes. The reason is that it enables (enantio)selective formation of  $C-H$ ,  $C-C$ ,  $C-O$  and  $C-N$  bonds. However, this requires a very complicated asymmetric catalyst system. [6] Especially the construction of different sterically demanding organometallic complexes offers an almost endless possibility of new catalyst systems and possible applications. [22][23]

Homogeneous catalyst systems have, however, been limited in industrial applications. Often cited reasons are that expensive, sensitive ligands are required to develop homogeneous asymmetric catalysts, and their reuse, recovery and most of all the recycling is costly and inefficient. Additionally the acceptance of heavy metals in the final products, especially pharmaceutical products, is extremely low. [15]

Combining heterogeneous and homogeneous catalysts in a chemical reaction presents a range of potential advantages and disadvantages. One key benefit lies in the potential for synergistic effects. [24] [25] When these two catalyst types are employed together, they can collaborate in a manner that enhances overall efficiency beyond what each could achieve independently. This synergy often translates into higher yields and improved selectivity toward desired products. Moreover, the combination allows for an accelerated reaction pace. Homogeneous catalysts are adept at initiating swift initial reactions, while heterogeneous catalysts provide an extended surface area conducive to the ongoing progression of the reaction. This dual-action acceleration can significantly expedite the overall reaction kinetics. However, this approach is not without its challenges. One notable drawback is the separation of the catalysts after the reaction. Extracting homogeneous catalysts from the reaction mixture can be labor-intensive and may require additional separation steps, potentially impeding the reaction's efficiency. Additionally, heterogeneous catalysts might be susceptible to poisoning by residues or byproducts generated during the reaction, causing a decline in their activity and selectivity over time. [26] The management of such a system can be complex, demanding precise control of various reaction conditions to ensure the optimal interaction between the catalysts and minimize unintended consequences. Financial considerations also come into play, as utilizing two distinct catalyst types could escalate the overall costs of the reaction process due to the expense of both

heterogeneous and homogeneous catalysts.[27]

One other possible solution to this problem is to immobilize catalytic centers on a heterogeneous support, as mentioned in the motivation and create a heterogeneous asymmetric catalyst. The different substrates and the fixation method will be discussed in more detail in the following section 2.3.

There is an example from 2022 that fits very well with the work which I would like to highlight. The group Esquivel et al. published a  $\text{CuCl}_2$  complex fixed on vinyl-functionalized ethylene-bridged-periodic mesoporous organosilica (see figure 2.2).[28] For immobilization, a mixture of 1,2-bis(trimethoxysilyl)ethanes and vinyltriethoxysilanes was first added to a periodic mesoporous organosilica (PMO) and adsorbed onto the surface for 24 h at 45 °C. The mixture was then mixed with a PMO. In a second step, the symmetric 3,6-di-2-pyridyl-1,2,4,5-tetrazine vis iEDDA was fixed to the vinylsilane. For this purpose, the reaction solution was stirred at 150 °C for 13 days. In a final step  $\text{CuCl}_2$  was added to the fictionalized PMO. Clear evidence of successful immobilization was provided by XPS. They were able to detect two characteristic Cu peaks at 934.8 ( $\text{Cu}_{2p3/2}$ ) and 954.6 eV ( $\text{Cu}_{2p1/2}$ ).

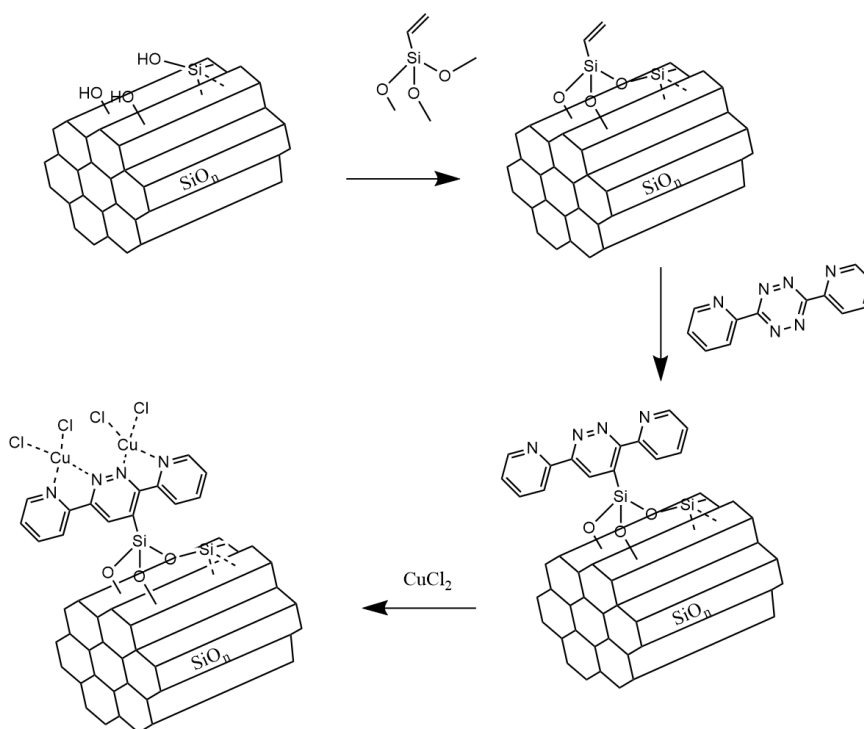


**Figure 2.2:** Schematic synthesis of  $\text{CuCl}_2$  attached to the silica surface via a symmetric TzPy<sub>2</sub> and a trimethoxysilane group.[28]

## 2.2 Organometallic Complexes

Organometallic complexes are classified as containing bonds between (transition) metals and carbon. These M–C bonds are called ligand bonds and they have become increasingly more sophisticated and in particular, the construction of complexes has been strongly promoted by organometallic chemistry in an effort to create molecular catalysts.[29][30] Complexes are composed of a metal center (M) and organic ligands (L). The binding of these dative ligands to a metal center can be described by the Lewis acid Lewis base concept. A free electron pair of the ligand (the Lewis base) coordinates to a typically cationic metal center (Lewis acid)[31]. The free electron pair interacts with an empty orbital of the metal and a  $\sigma$ -bond is formed between the ligand and the metal. If the ligand has a low energy empty  $\pi$ -orbital, a back-bonding from the metal to the ligand can occur and a  $\pi$ -bond is formed. In this process, the metal donates electron density to the ligand. CO ligands form such a  $\pi$ -back-bond, which makes them very strongly coordinating ligands. This is however not always the case, there are also examples where electron density is given to the metal via a  $\pi$ -bond. In the case of CO ligand, this is referred to as a  $\pi$  acceptor, and in the case of an imide ligand that donates electron density, this is referred to as a  $\pi$  donor. Figure 2.3 shows schematically the different types of bonds, such as covalent and dative bonds, as well as the outward and the back bonding and the electron flow[32].

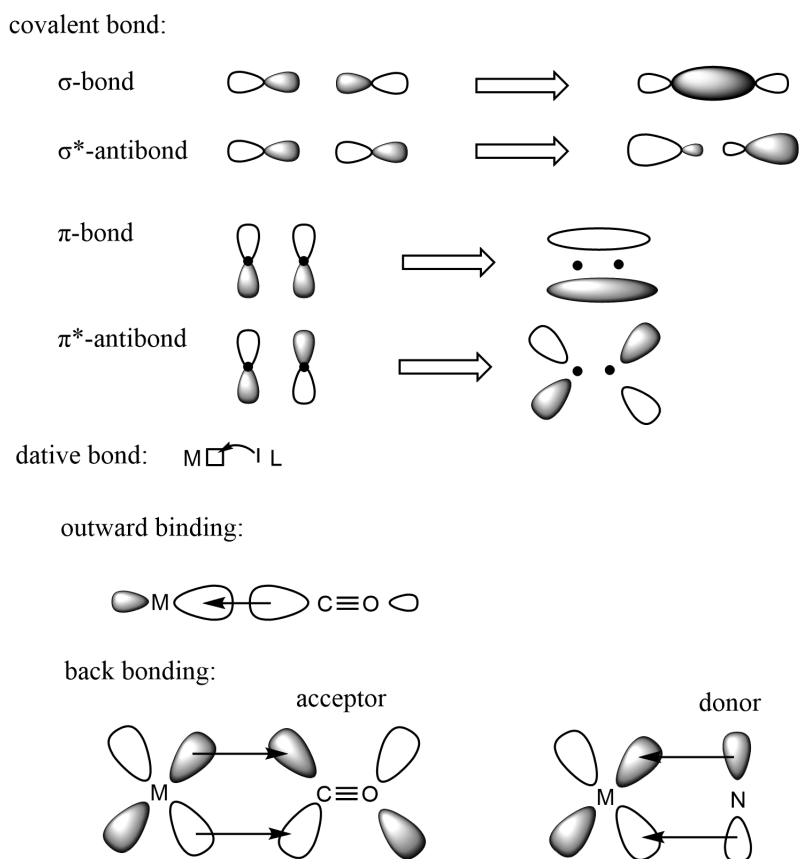


**Figure 2.3:** Schematic structure of a metal complexes with a metal as central atom (M) and ligands (L), which coordinate to the metal. The single bond ( $\sigma$ -bond) and a double bond ( $\sigma$ - and an  $\pi$ -back bond) is illustrated by the example of CO as ligand.

Important factors to consider in using organometallic complexes in catalysis are the metal centers (M) and the ligands (L). The central atom is the transition metal atom, which acts as the reactive center for ligand coordination. There are, however, examples of main group compounds and rare earths elements in catalysis. They are not as frequently used. Ligand designed around organic synthesis can be versatile, because the geometry, scalability and properties can be controlled. Generally, ligands are neutral (L-type) or (negatively) charged (X-type), and there are a broad range of ligands based on from mono atomic, single coordinating (H- or O<sup>2-</sup>) to large, multi-chelate chiral ligands. These chelating ligands are constructed in such a way that they provide multiple coordination sites to the same metal center allowing for a pocket to be generated around it. Popular examples for macro ligand in literature are EDTA or biology proteins. More generally transition metals have coordination numbers (CN) between 2-8, where the so-called 18 e<sup>-</sup> rule or closed-shell configuration is often correlated with stability. Based on the coordination number and energetic stabilizations of the shell, conclusions can be drawn about the coordination geometry.[33][32][31]



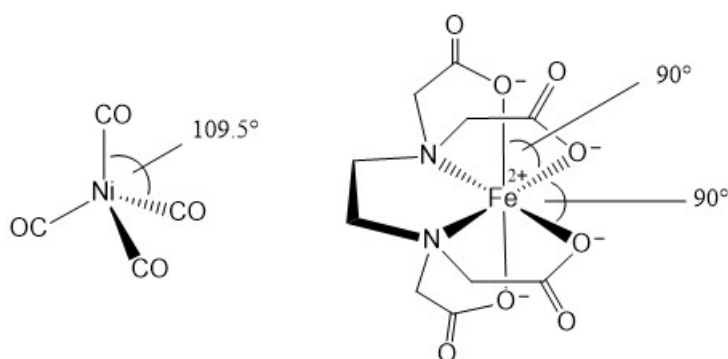


**Figure 2.4:** Schematic structure of a tetrahedral metal surrounded by a single ligand (e.g.  $\text{Ni}(\text{CO})_4$ ) and an octahedral metal surrounded by a chelate ligand (e.g.  $\text{Fe}(\text{EDTA})$ ).

In the present work, the focus is on various organorhenium and organoruthenium compounds, some of which contain ferrocene. Fe has also been explored. The used ligand systems are TzPy derivatives which act like a  $\text{N}^{\wedge}\text{N}$  ligand.

Well-known representatives for  $\alpha$ -diimine ligand systems include 2,2'-bpy, 1,10-phen and BIAN ligands (figure 2.5). The property of tetrazines is discussed further in the chapter 2.6.[34][35]

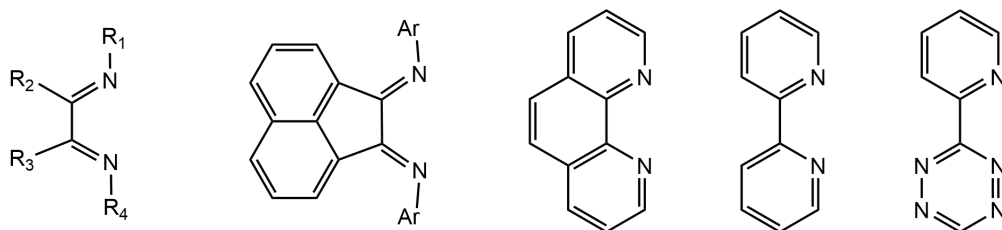


**Figure 2.5:** Representation of  $\alpha$ -diimine ligand systems. *from left to right* :  $\alpha$ -diimine; BIAN; 1,10-phen; 2,2'-bpy and TzPy.

### 2.2.1 $[(\text{bpy})\text{ReCl}(\text{CO})_3]$

$[(\alpha\text{-diimine})\text{ReCl}(\text{CO})_3]$  is a well established complex in the literature in which the aromatic  $\alpha$ -diimine ligand systems, such as 1,10-phenanthroline and 2,2'-bipyridine, are well represented. This system is widely applicable, as a molecular switch and is used as a photosensitizer.[36][37] These applications are of interest in electrochemical, photophysical, and photocatalytic systems. The reason is that these complexes have an energetically easily accessible excited state to which electron density can be transferred after optical excitation from electron rich metals to the extended  $\pi^*$  on the ligand.[38][35]

The most well-known catalytic reaction of this complex is the electrochemical or photochemical reduction of  $\text{CO}_2$  to  $\text{CO}$ . The compounds with 2,2'-bipyridine derivatives are mainly known for this purpose. During photochemical reduction, the  $[(\text{bpy})\text{ReCl}(\text{CO})_3]$  is in solution and mixed with a sacrificial reducing agent (triethanolamine (TEOA) is often used). The exact photochemical conditions are however not yet fully explained.[39] Roughly, the mechanism can be described as follows:

In a first step, the complex is placed in an optically excited state. Oxidation of a sacrificial electron donor, which occurs in parallel, causes an electron to be taken up into the HOMO that has been freed by the optical excitation. This results in cleavage of the  $\text{Cl}^-$ , whereupon  $\text{CO}_2$  can coordinate to the freed coordination site. By taking up a second electron from another singly reduced complex, the reduction of  $\text{CO}_2$  to  $\text{CO}$  then takes place. Subsequent release of carbon monoxide and recoordination of the labile coligand lead back to the initial complex.[37]

Three properties of  $[(\alpha\text{-diimine})\text{ReCl}(\text{CO})_3]$  contribute significantly to this photochemical application: an energetically low-lying  $\pi^*$ -orbital (LUMO), which is indicative of a low reduction potential and ease of reduction. A long wavelength MLCT absorption, enabling photosensitivity.[40][41] The third point is the labile bound coligand  $\text{Cl}^-$ , this allows the release of the coordination cell for the  $\text{CO}_2$ . [42]

The second possible reduction of  $\text{CO}_2$  to  $\text{CO}$  by an  $[(\alpha\text{-diimine})\text{ReCl}(\text{CO})_3]$  is electrochemical. The corresponding catalytic cycle is shown in Fig.2.6 and can be described as follows: In the first step, the compound accepts an electron and a singly reduced species is formed. The weakly bound coligand (the  $\text{Cl}^-$ ) is split off. First, a solvent molecule coordinates to the free coordination site. In a further step, a  $\text{CO}_2$  molecule attaches and converts to a  $\text{COOH}$  fragment by accepting an electron and a proton. In a final step,  $\text{CO}$  and  $\text{H}_2\text{O}$  are split off with the help of  $\text{H}^+$  and  $\text{Cl}^-$ , thus returning to the initial complex. As with photochemical reduction, electrochemical reduction is based on the properties of the energetically low-lying  $\pi^*$ -orbital (LUMO) and the weakly bound coligand (the  $\text{Cl}^-$ ). [43]

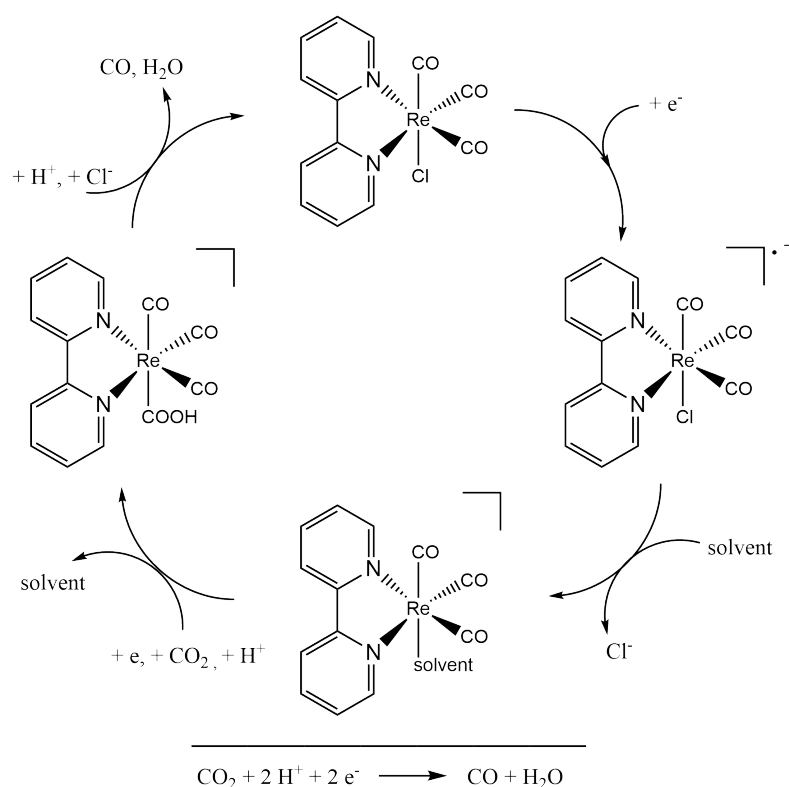


**Figure 2.6:** Catalytic cycle for the electrochemical reduction of CO<sub>2</sub> by [(bpy)ReCl(CO)<sub>3</sub>].

### 2.3 Immobilization techniques and materials

There are essentially four methods for immobilizing transition metal complexes onto a surface. These range from simple adsorption, to electrostatic interaction of charged complexes and ligands with the contrary charged surface, to the formation of covalent bonds, to encapsulation in the porous structure.[6][4] Using the example of covalent immobilization, the synthesis of well-defined model catalysts on metal oxide surfaces using the techniques of metal-organic surface chemistry (SOMC) and molecular heterogeneous catalysis (MHC) should be emphasized.[44] [45] [46]

Only two of the four immobilization techniques are in use frequently for built heterogeneous asymmetric catalysts, namely covalent bond formation and electrostatic interaction. An early reported example of a catalyst immobilized on silica via a covalent linker was described in 1990 by Soai et al.. This group established the binding of trimethoxy- and triethoxysilanes on Si-OH surfaces. MeOH elimination from trimethoxysilanes is the most widespread used method. The silanes provide a broad range of linkers based on organosilane chemistry.[47]

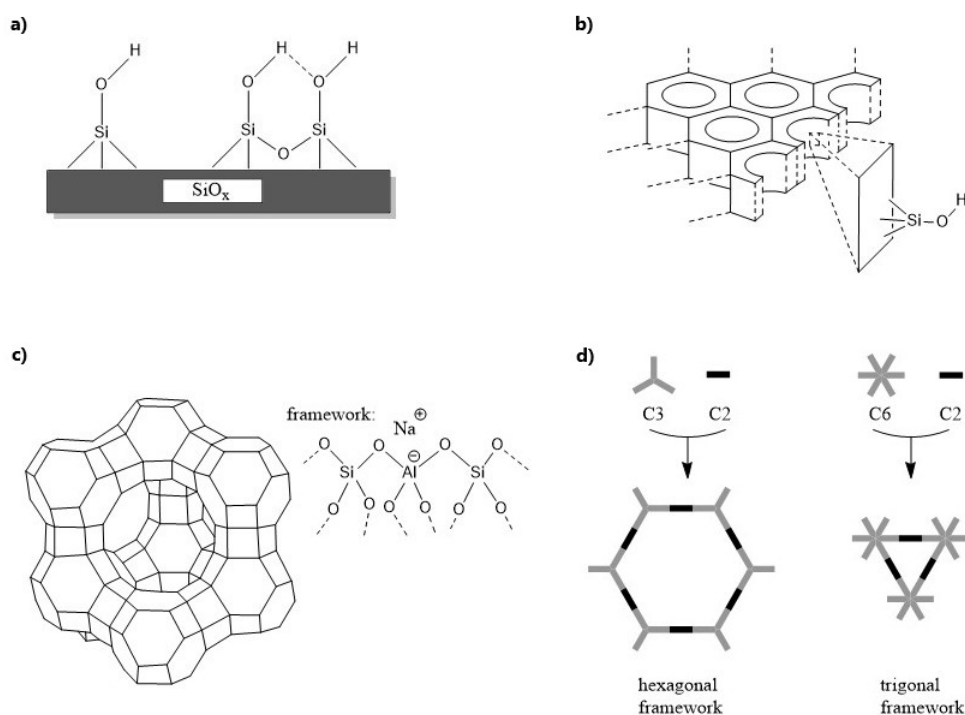


**Figure 2.7:** Schematic representation of various surfaces for different immobilization techniques. Illustration a and b are materials for covalent bonding to surfaces. Illustration c is a zeolite and an example of encapsulation. Illustration d is another example of covalent binding, but here in a covalent organic framework.

The immobilization techniques mentioned all have advantages and disadvantages. The advantages include the reusability of the catalyst, improved stability, higher selectivity and easier product separation. The disadvantages, however, include potential mass transport limitations, risk of reduced catalytic activity, higher production costs, limited applicability to all types of catalysts or reactants and the complexity of the immobilization process. Other major disadvantages are the release of catalysts that are not firmly anchored. Therefore, the immobilization method is very important. structure.[6][4] Another sticking point is the immobilization in pores. This promises a higher selectivity by imitating enzymatic processes. However, it is also difficult to prove that the catalysts are actually immobilized in the pores.

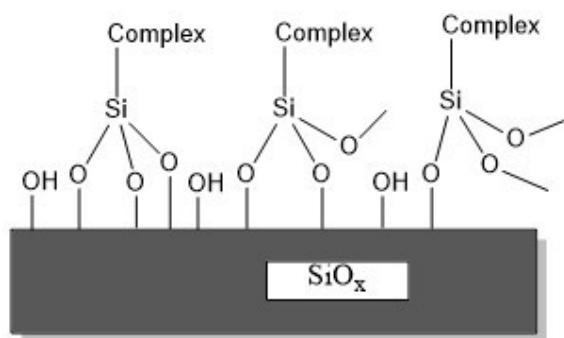


**Figure 2.8:** Schematic illustration of an immobilization of a trimethoxy silane derivative on a silica -OH surface.

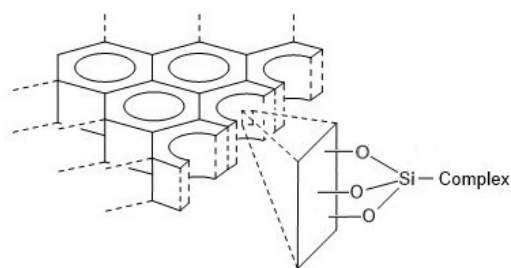


**Figure 2.9:** Schematic representation of immobilization within a pore of an SBA-15.

To ensure that the anchor for the catalyst in porous materials is really inside the pore and not outside of it, a lot of effort has been put into developing several methods for interporous fixation in recent years. Crudden et al. have developed a method that allows selective immobilization within porous silica. This selective incorporation is shown schematically in figure 2.10. It is divided into 4 steps: filling the pore with pluronic P-123, which protects the OH groups in the pore. The esterification of the OH groups on the outside with hexamethyldisilazane. In a third step the Pluronic P-123 is solubilized via soxhlet extraction and in a last step any organo- trimethoxy or ethoxysilane can be incorporated.[48]

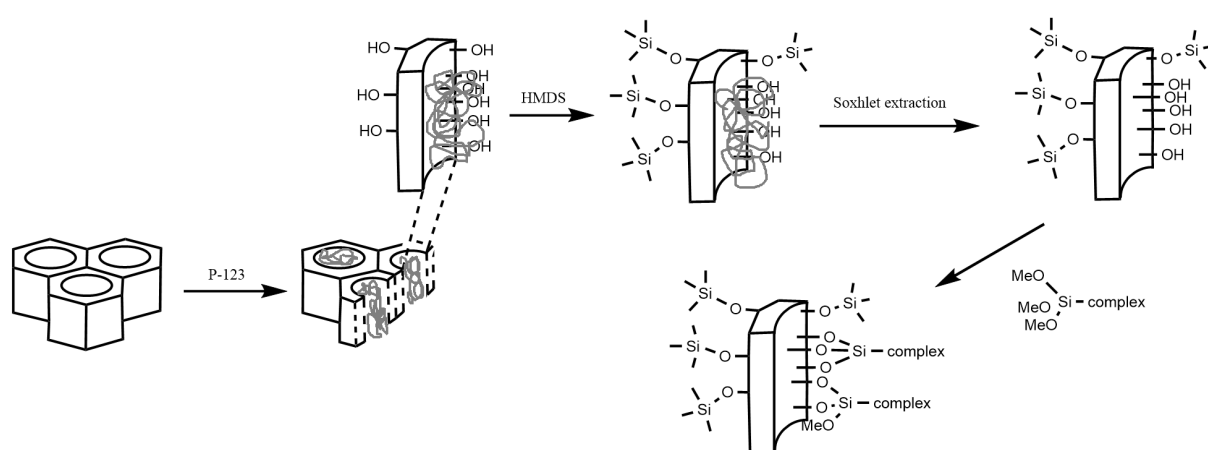


**Figure 2.10:** Illustration of a multi step modification of a pore-selective immobilization of SBA-15 pores by the method of Crudden.

## 2.4 Click chemistry

Click chemistry is a concept in chemical synthesis that emphasizes the use of modular, efficient, and highly selective reactions to quickly assemble complex molecular structures. It was introduced by K. Barry Sharpless in 2001. The term "click" in click chemistry refers to the idea that the reactions should be as simple and reliable as clicking together two pieces of a puzzle.[49]

The main purpose of click chemistry is to streamline the synthesis of various compounds, like Drug Development. Here click chemistry plays a significant role in medicinal chemistry by enabling the rapid and efficient assembly of diverse libraries of compounds for drug discovery. This approach allows researchers to efficiently modify and optimize molecular structures to improve their pharmacological properties. Also in material science click chemistry is used in the synthesis of polymers, dendrimers, and other advanced materials. The modular nature of click reactions allows for precise control over the size, shape, and functionality of these materials, which is important for various applications such as coatings, adhesives, and nanotechnology.[50] [51]

Two last areas of application are in click chemistry are bioconjugation and surface modification. In bioconjugation it has been widely adopted for the conjugation of biomolecules, such as proteins, peptides, and nucleic acids, with other molecules like fluorophores, drugs, or nanoparticles. This is crucial in fields like biochemistry, molecular biology, and diagnostics. Click chemistry in surface modification can be employed to modify surfaces of materials like nanoparticles, polymers, or even biological structures. This is useful for tailoring the properties of these materials, improving compatibility, and creating functional interfaces.[52] [53]

Some reactions that meet these conditions are: nucleophilic substitution on small strained rings such as epoxides or aziridines, cycloadditions, such as the catalyzed Huisgen-1,3-dipolar cycloaddition and the thiol-ene reaction.[54][55][56] These types of reactions have found uses in bioorthogonal and pharmacological applications. The two reactions that were first branded as "click" were the Cu-catalyzed [2+3] cycloaddition between azides and alkynes and the UV-light induced thiol-ene reaction between thiols and olefines. The thiol-ene reaction has been known since 1905 and is stereo selective. The addition products always form the anti-Markovnikov product (figure 2.11).[56][57]

A closer look at the uncatalyzed [2+3] cycloaddition of azide and alkyne shows the most criteria for "click" reaction. The problem is that the products are a mixture of two regioisomers (figure 2.12), and therefore, the thermal [2+3] cycloaddition is not click chemistry.[58]

Only by using catalysts can a single product can be formed and the conditions fulfilled.

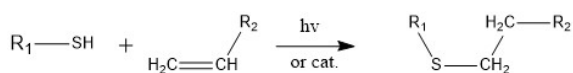


**Figure 2.11:** Reaction equation of the thiol-ene reaction.

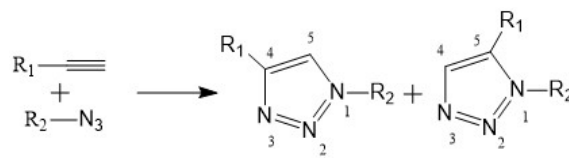


**Figure 2.12:** Reaction equation of the thermic induced Huisgen-Cycloaddition with the two regioisomeric products, the 1,4 and the 1,5 product.

By using a copper catalyst the 1,4-disubstituted 1,2,3-triazoles are selectively formed and a ruthenium catalyst provides that the corresponding 1,5 product is formed (figure 2.13).

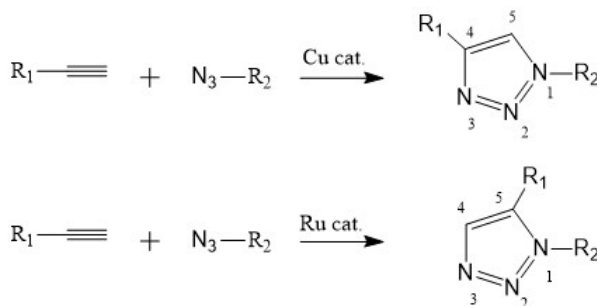


**Figure 2.13:** *top:* The copper-catalyzed-, *bottom:* the base or ruthenium-catalyzed Huisgen cycloaddition of azide and alkyne.

Another extension of the azide alkyne reaction is the iclick (inorganic click) introduced by Veige et al. Here, the azide coordinates to a metal (e.g. Mn) and reacts with an alkyne. The reaction products are different triazine derivatives than classical Cu(I)-catalyzed azide–alkyne cycloaddition, which still remain coordinated to the metal (see figure 2.14). [59][60]

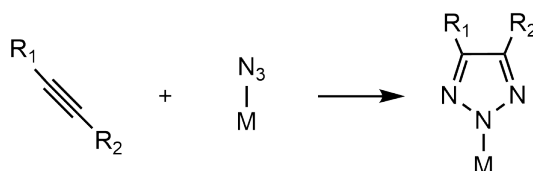


**Figure 2.14:** Reaction equation of an alkyne with an azide bond to a metal. The resulting triazole is still bound to the metal.

## 2.5 iEDDA

In the present work, the focus will be on the inverse electron demand [4+2]-Diels-Alder (iEDDA) between an 1,2,4,5-tetrazines (s-tetrazine) and electron-rich dienophiles. iEDDA cycloaddition was reported by Bachmann and Deno in 1949. In general, the reaction is a [4+2] pericyclic reaction in which two new bonds are formed between diene and dienophile.[61][62] The factor that controls this reaction is in contrast to a "normal" electron demand [4+2] cycloaddition, in which an electron-rich diene reacts with an electron-poor dienophile, iEDDA is the reaction of an electron-poor diene with an electron-rich dienophile.[63] A Example for a normal Diels-Alder are 1,3-butadiene (Diene) and Maleic anhydride (Dienophile).[64] An well known example for an iEDDA is diazines with electron-rich furans. However, the most popular example in recent years has been tetrazines with TCO, which are also used in this work.[65] Analysis of the frontier orbitals provide insight into what factors can be used to drive the reaction. The Diels-Alder reaction can be divided into three types of reactions with "normal", "neutral" or "inverse" electron demand (see figure 2.15). In a "normal" electron demand the diene can add electron-donating groups (EDG) that raise the highest occupied molecular orbital (HOMO) and the lowest unoccupied molecular orbital (LUMO), while electron-withdrawing groups (EWG) on the dienophile have the opposite effect.[62] As shown in figure 2.15, in the Diels-Alder reaction with "normal" electron demand, the HOMO of the diene reacts with the LUMO of the dienophile, whereas if the LUMO of the diene reacts with the HOMO of the dienophile, the reaction would be a Diels-Alder reaction with reverse electron demand.[62][66][67]

The EDG and EWG groups, which influence the HOMO and LUMO of the dienes and dienophiles, do not only exist as substituents that are directly bound to them via a covalent bond. Other types of bonds can also have this influence. Especially in organometallic complexes, where the ligands bind coordinatively to a metal and act as Lewis acid, they give off electron density and thus their HOMO and LUMO are also considerably influenced.[58]



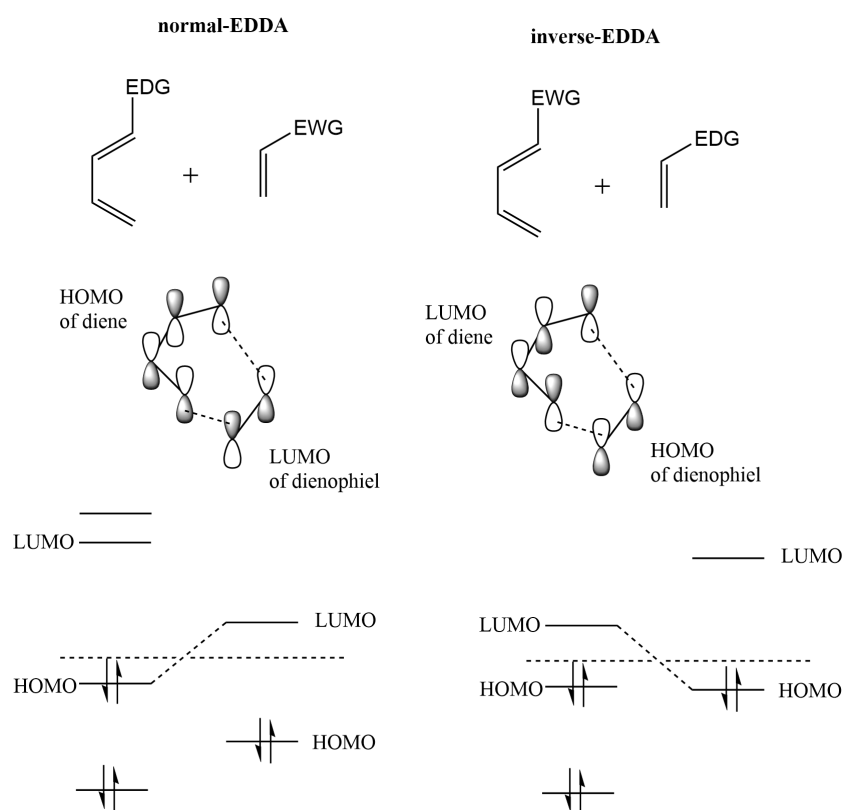


**Figure 2.15:** Frontier orbital theory for the normal (*left*) and inverse electron demand (*right*) Diels Alder.

## 2.6 Tetrazine: iEDDA - Synthesis - Properties - Application:

This iEDDA reaction of tetrazine with dienophiles also generally satisfies the conditions of a "click" reaction. Tetrazines consist of a six-membered aromatic ring containing four nitrogen atoms and are isoelectronic to benzene. There are three different heterocycle isomers, the 1,2,3,4-tetrazines, the 1,2,3,5-tetrazines, and the 1,2,4,5-tetrazines (s-tetrazine), as shown in figure 2.16.[68] However, compared to benzene, the aromatic system of the tetrazines is electron poor due to the electronegativity of the N, which makes them useful in iEDDA.[66]

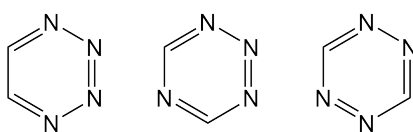


**Figure 2.16:** The three different heterocycles, *left* the 1,2,3,4-tetrazines, *middle* the 1,2,3,5-tetrazines, and *right* the 1,2,4,5-tetrazines (s-tetrazine).

The iEDDA reaction between s-tetrazine and dienophiles generates new C–C bonds and heterocycles. N<sub>2</sub> elimination is the driving force for the reaction. This reaction is applicable in biological labeling due to the high reaction rate. The reaction mechanism is shown in figure 2.17.[66]

In detail the iEDDA of 1,2,4,5-tetrazines as dienes with alkenes or alkynes as dienophiles, a highly strained bicyclic intermediate is first formed, which cleaves off an equivalent of nitrogen by running off a retro-Diels-Alder reaction. While in the case of an alkyne the pyridazine is formed directly as the dienophile, in the case of an alkene a 4,5-dihydropyridazine is formed first. This can isomerize to the 1,4-dihydropyridazine or react by oxidation to the pyridazine.[69][70]

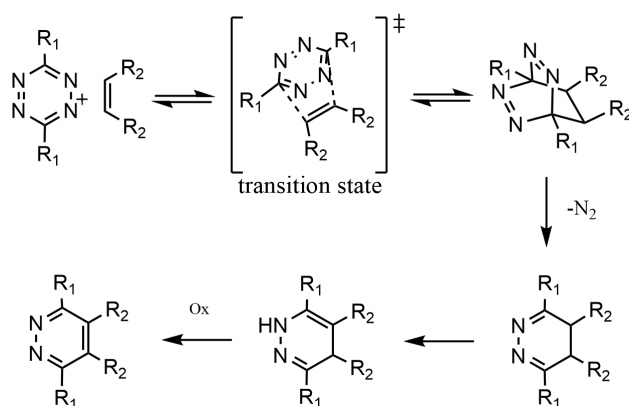


**Figure 2.17:** Reaction mechanism of tetrazine with dienophile.

### 2.6.1 Synthesis

The synthesis of tetrazines has been known for over 100 years. Pinner published in 1893 the synthesis of a 1,2,4,5-tetrazine. This two-step synthesis used hydrazine with aromatic nitriles followed by subsequent oxidation of the dihydrotetrazine. This synthesis provides only aromatically substituted tetrazines.[71] This synthesis has been the standard method, however, renewed interest in tetrazine has boosted the investigation in new synthetic paths in the last several years. Devaraj's group published in 2012 a Lewis acid catalyzed (Zn(II) or Ni(II) salts) reaction of nitriles with anhydrous hydrazine. The advantage is a wide application of aromatic and aliphatic nitriles, but the use of anhydrous hydrazine poses a clear hazard.[72] In 2014, Caulton reported a catalyst-free reaction that uses mono-hydro-hydrazine. This use of mono-hydro-hydrazine is significantly less risky in terms of explosion. In this reaction, a nitrile is reacted with mono-hydro-hydrazine and sulfur. In a subsequent step, another nitrile is added in excess, such as MeCN. This reaction is particularly important for the preparation of asymmetric tetrazines.[73] Another innovation in the synthesis of asymmetric tetrazine described in 2018 by Audebert. The group published a reaction in which a H-capped-tetrazine could be synthesized through a one-pot reaction in which a nitrile, mono-hydro hydrazine, sulfur, ethanol and one equivalent CH<sub>2</sub>Cl<sub>2</sub> were combined and exposed to microwave condition for 24 hours, but the yield was very low (1-16%).[74] The various synthesis schemes mentioned are shown in figure 2.18.

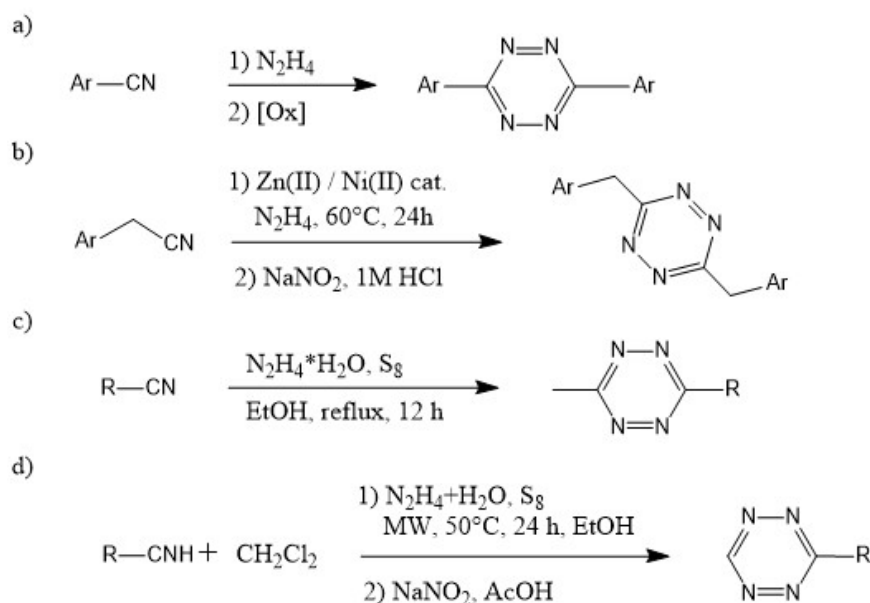


**Figure 2.18:** Different syntheses of tetrazine derivatives: (a) by Pinner, (b) lewis acid catalyzed by Devaraj, (c), by Caulton und (d) by Audebert.

## 2.6.2 Properties

The colors of the different tetrazines are very unique and intense. The energetically low-lying  $\pi^*$  MO is a well-suited target for transitions that extend into the visible range. For most tetrazines, these are in the 520-550 nm range and are thus responsible for the mostly red to pink color of the tetrazines ( $n \rightarrow \pi^*$ ). A further absorption is shown in the range of approximately 220-380 nm ( $\pi \rightarrow \pi^*$ ).<sup>[75]</sup>

Another interesting property of tetrazines is their electrochemistry. Also due to their low-lying  $\pi^*$ -MO, tetrazines can be reversibly reduced at a potential between -0.3 V and -1.3 V vs. Fc/Fc<sup>+</sup>. The radical anion formed during the one-electron reduction is quite stable. The radical anion formed in the one-electron reduction exhibits high stability, which is why a second possible tetrazine reduction usually occurs only at lower cathodic potentials. This, however, is usually irreversible.<sup>[75]</sup>

The neutral tetrazines are all diamagnetic and not EPR active, however in connection with the electrochemical reduction, the rather stable singly-reduced species shows a prominent EPR signal. In the case of a symmetrical, 3,5-substituted tetrazine, for example, it exhibits a cleavage into nine signals after 1-fold reduction. The hyperfine splitting is the result of the coupling of the delocalized electron in the six-membered ring with the four N of the tetrazine ring. The nine detected signals thus fit with the  $2nI+1$  rule, where  $n$  describes the number of equivalent coupling partners with the radical and  $I$  is their nuclear spin.<sup>[75]</sup>

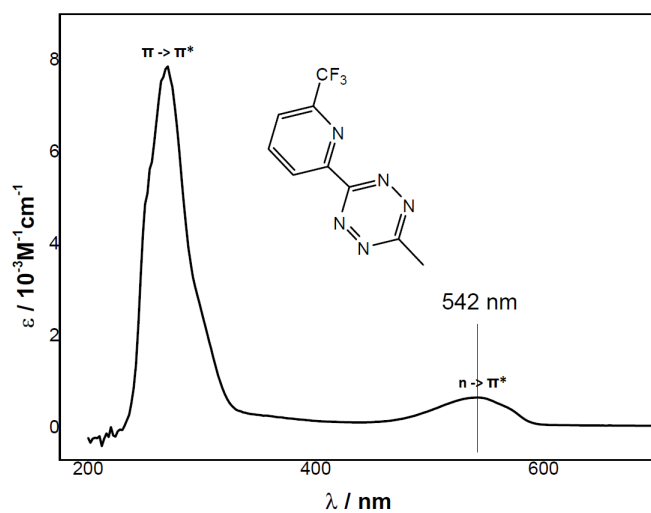


Figure 2.19: UV/Vis spectrum of a tetrazine with an absorption at 542 nm.[76]

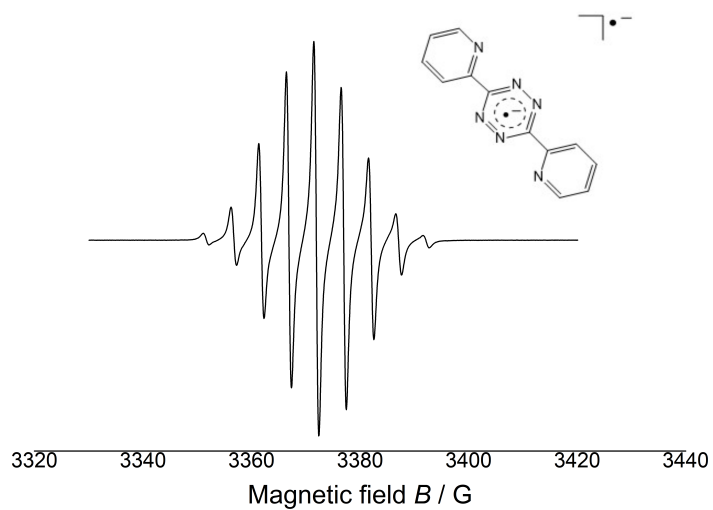
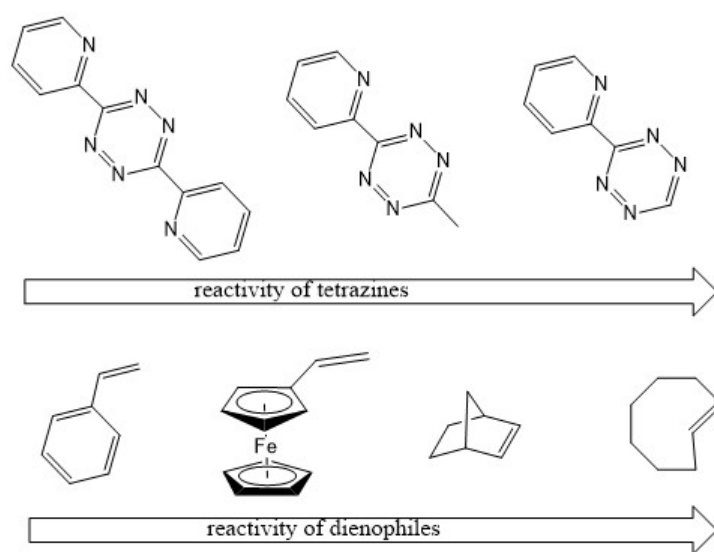


Figure 2.20: EPR spectrum of a reduced tetrazine.[77]

### 2.6.3 Application

Tetrazine derivatives have found uses in pyrotechnics and polymer chemistry. In recent decades, however, they have been used mainly in organometallic complex chemistry. With the tetrazine derivatives as ligands, many metal complexes have been synthesized and investigated for their spectro-electrochemical properties.[78][79][80][81] In the last few years, tetrazines have been increasingly used in biology, medicine and related fields. Tetrazines function as linkers in biolabeling. They are used for this purpose due to their high reactivity or faster kinetics respectively. Recently, the nobel prize in chemistry in 2022 was awarded for research on bioorthogonal click chemistry, where the [4+2] cycloaddition is included.[82] This includes the recently started clinical studies with tetrazines in the human body. Depending on the chemical structure of the chosen dienophile as partner, the kinetic of the [4+2] cycloaddition is variably fast and can thus be adapted to the corresponding application. Figure 2.21 shows different tetrazines and dienophiles (used in this thesis) sorted by their reactivity with each other.[66]



**Figure 2.21:** Different tetrazines (*top*) and dienophiles (*bottom*) sorted according to their estimated relative reactivity in iEEDA reactions.

## 2.7 Metallotetrazine

An early report on the coordination chemistry of metallotetrazines (Fe, Co and Ni) was published in the 1970s.[83][84] It took several years until the first tetrazine ligands and their complexes were fully characterized. Kaim et al. in particular has reported on this topic.[75]

The synthesis of metallotetrazines is similar to the synthesis of complexes containing

2,2'-bipy and other azo- $\alpha$ -diimine ligands. Other commonly used precursors are metal carbonyls, a popular example and important for this work is pentacarbonyl chlororhenium. In the literature there are several examples of metallotetrazines. This is due to the variety of tetrazines that can act as ligands. For example, these different tetrazines have different numbers of  $\alpha$ -diimine groups or other Lewis base groups to coordinate to metal centers. Figure 2.22 shows an illustration of various complexed metallotetrazine derivatives.[85]

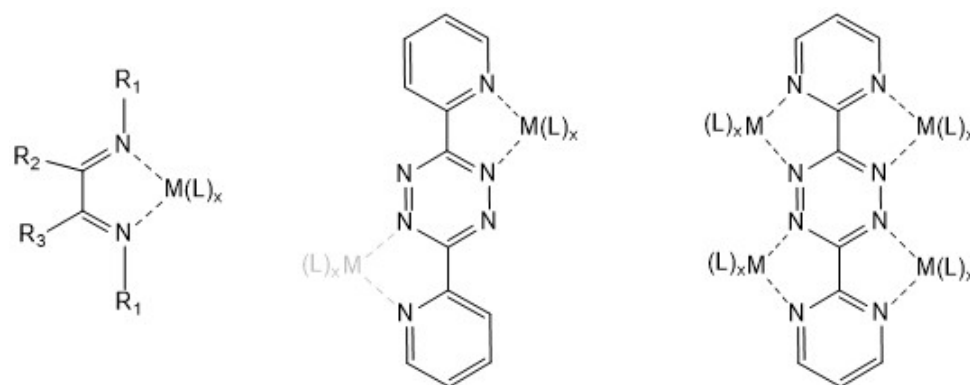


**Figure 2.22:** Schematic illustration of a  $\alpha$ -diimine ligand coordinated to a metal (*left*), single and double complexed metallotetrazine (*middle*) and four times complexes metallotetrazine (*right*).

The application and use of metallotetrazine to date has been very much focused on electrochemical investigation coupled with IR, UV/Vis and EPR.

Tetrazines are having a renaissance, especially due to metallotetrazines having found new applications. Currently, the main application is bio-imaging and bioorthogonal peptide labeling.[86] One of the first examples was published by Lo et al. in 2017, who presented an Ir complex whose photoluminescence is quenched by the tetrazine ligand. Reaction with a bicyclo[6.1.0]non-4-yne produces a diazine ligand that no longer quenches emission, and thus the resulting complex emits light (Figure 2.23).[87][86]

This application takes advantage of the different properties between the tetrazine and the addition products. Both the starting compound and the products are externally irradiated with light, which excites an outer electron to a higher orbital. When the electron falls back to its ground state, the excess energy is emitted as light. In contrast to tetrazine, the addition products emit light in the visible range. This feature is interesting for many applications, because an emission is switched on by the click reaction.

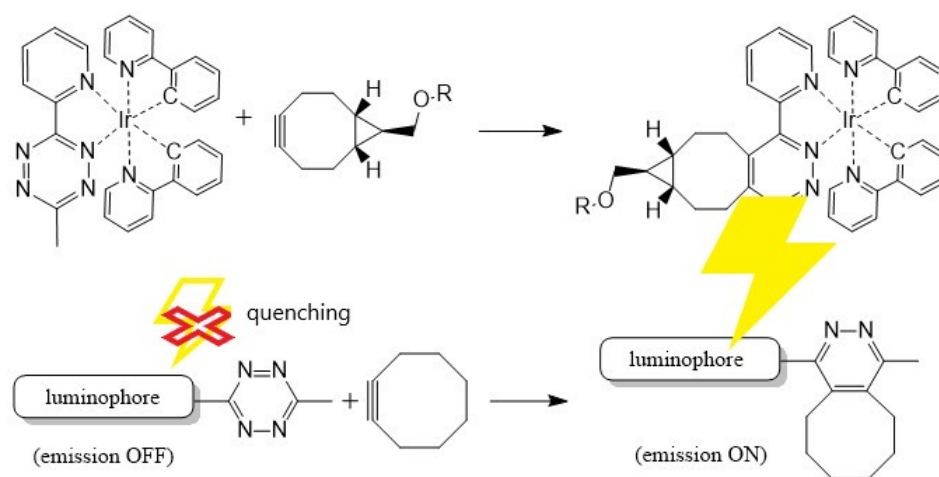


**Figure 2.23:** Schematic representation of click activation for luminescence.



### 3 Preliminary work from the literature

The present work is embedded in a collaborative research project of the University of Stuttgart within the CRC1333. The focus of this subproject is on the synthesis of novel organometallic complexes, with particular attention being paid to the design of the ligand system. The aim is to develop ligands that allow subsequent modification. In this context, various functional groups were considered and after careful consideration, the tetrazine moiety was selected as a promising ligand system. The tetrazine unit enables the synthesis of novel ligand systems through its reaction with dienophiles. Tetrazine functionalization can also be used to immobilize the complex on a surface.

Tetrazines have gained a significant role in science, especially through their application in bioorthogonal chemistry. The iEDDA reaction with tetrazines and alkenes, also known as tetrazine-based click chemistry, has proven to be an extremely useful tool. This method enables the selective labeling of biomolecules in complex biological environments, including living cells. The ability of tetrazines to react with high selectivity under mild conditions has led to advances in chemical biology, medicine and materials science. This class of compounds not only serves as a building block for the production of new materials, but also has applications in catalysis, sensing and drug development. Scientific research into tetrazines and their diverse applications reflects the continuous search for innovative chemical methods that enable precise and selective reactions in complex systems. In the iEDDA reaction, which is important for this work, the group led by Bertozzi et al. made a great contribution in 2008 with their pioneering publication of the use of tetrazines.[88] [89]

Research into the properties of metallotetrazines and their ability to react with dienophiles is a relatively new field of research that has only been known since the late 2010s. Within this short period of time, the work of Lo et al. has proven to be groundbreaking. It is important to emphasize that the synthesis of metallotetrazines per se has been known since the mid to late 20th century and that researchers such as Kaim et al. have been instrumental in the development and exploration of this class of chemicals.[90] [91]

The click chemistry reactions of tetrazines, especially their use in the synthesis of metallotetrazines, are particularly intriguing. The speed of these reactions gives tetrazines a unique role as building blocks in chemistry, with applications in living biological systems where rapid and specific labeling of biomolecules is required. For this reason, the kinetic studies are discussed in detail in this thesis, as they have considerable scientific value. Especially in comparison to other click reactions, the reaction of tetrazines stands out and is superior to the classical and well-known copper catalyzed reaction of azides

and alkynes. Azide-alkyne reactions are reported in the literature with a first-order rate constant of up to  $10 - 100 \text{ M}^{-1} \text{ s}^{-1}$ , whereas tetrazines exhibit a first-order rate constant of up to  $10^5 \text{ M}^{-1} \text{ s}^{-1}$ . The first measurements by Bertozzi et al. in 2008 already showed a  $k_2$  of  $2000 \text{ M}^{-1} \text{ s}^{-1}$ . [92] [93] [94] [95] [89] [96]

Electrochemical and spectroscopic studies of similar compounds, including metallotetracene, have been established for some time. Researchers such as Kaim, Lahiri and Audebert have excelled in contributing to the understanding of these compounds and their properties. [97] [98] [91]

The direct immobilization of metallotetrazines is an innovation that has not yet been documented in the scientific literature. In recent years, however, the immobilization of complexes on surfaces has gained considerable importance, especially in the development of asymmetric heterogeneous catalysts. The immobilization method used in this research has been known since 2000 and 2015, respectively, and was introduced by Soai et al. and modified by Crudden et al. The authors have made considerable efforts to ensure that the functionalization occurs at the desired location, especially in porous materials, be it specifically in the pores or outside. [99] [100]

Within the CRC1333 research network, Ziegler et al. made a significant contribution through their preliminary work, which made the immobilization presented in this paper possible in the first place. A further look at the literature shows that other researchers have also pursued similar approaches. [101]

Another example from the literature of immobilization via tetrazines is by Esquivel et al. from 2022, for example, they worked by using an uncoordinated tetrazine on a functionalized surface and later coordinated the metal complex to the immobilized ligands. This underlines the diversity of research in the field of immobilized metallotetracelles and the potential applications in different chemical contexts. [102]

## 4 Methods

Different methods were used in the work for analysis and evaluation. TLC, NMR, EA and x-ray were used to check the synthesized compounds. EPR, UV/Vis, IR, CV, DFT, SEC, and kinetics analyses were also performed to check the (electrochemical) behavior of this compounds.

In the following, voltammetry, SEC and kinetics will be discussed in more detail.

### 4.1 Voltammetry

Voltammetry is an electrochemical analysis technique used to obtain information about the electrochemical properties of substances. In voltammetry, an electrical voltage is applied to an electrode and the resulting current is measured as it flows through an electrochemical cell. The measured current depends on the redox reaction taking place at the electrode and on the current which is applied. In industry, voltammetry is often used for the trace analysis of metals or organic impurities. A redox process can be reversible, i.e. the electron transfer can be reversed so that the original oxidation state is restored. In other cases, subsequent chemical reactions can also take place after the electron transfer, and electrochemistry provides a powerful method for studying these phenomena. This is the case with an irreversible reaction, as the initial state cannot be restored by electron retransfer, resulting in a change in the form of the voltammogram.[103][104][105]

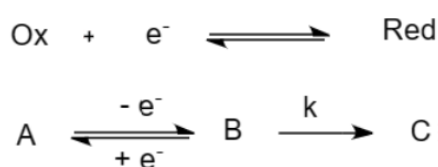


**Figure 4.1:** Schematic representation of an electrochemical process (*top*) and an electrochemical process followed by a chemical reaction (*bottom*).

Potentiostatic measurements are usually performed in a three-electrode arrangement (Figure 4.2). It consists of a working electrode (WE), a counter electrode (CE) and a reference electrode (RE). The three electrodes are immersed in an electrolyte solution and controlled by a potentiostat. With the aid of a function generator, the potentiostat has the task of controlling a precisely known potential curve at the working electrode against the reference electrode. The electrochemical reaction takes place at the working electrode. The WE and CE usually consist of inert material, such as platinum, gold or glassy carbon. The RE

is often made of silver. Typically in non aqueous electrochemical measurements the system is referenced against ferrocene/ferrocenium redox couple as a standard reference.[105]

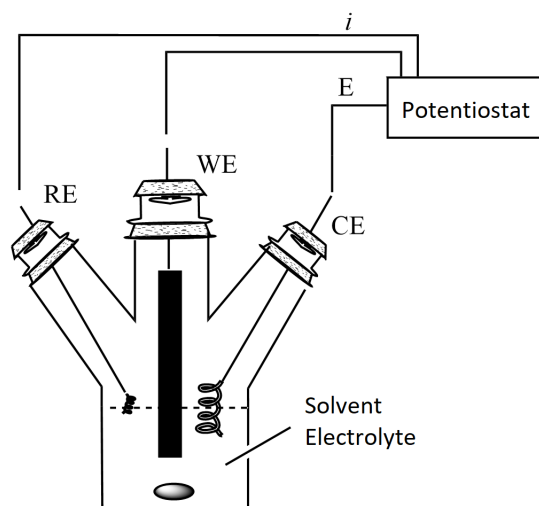


**Figure 4.2:** Schematic structure of a three-electrode arrangement.

There are many different types of voltammetry, but for this work only cyclic voltammetry (CV), differential pulsed voltammetry (DPV) and rotating electrode voltammetry (RDE) are important. In the following section CV and RDE will be described in detail.

#### 4.1.1 Cyclic voltammetry

One particular feature of the CV is, as the name suggests, that the voltammogram is cycled. This means that the voltage is varied over a maximum and a minimum back to the output potential. Figure 4.3 illustrates this clearly.[106]

This method is used to investigate reversibility and stability of electrochemically oxidized or reduced species. In the simplest cases, a distinction is made between reversible and an irreversible processes.

The CV of a reversible electrochemical process is shown in Figure 4.4. Furthermore, there are several features that can be read out of a CV. For example,  $i_{p,a}$  and  $i_{p,c}$  are the currents flowing in the redox process between the anode and cathode, respectively. In a reversible process, these values are identical, since the initial state is reached again, which means  $i_{p,a} = i_{p,c}$ .  $E_{p,a}$  and  $E_{p,c}$  are the potentials at which the reduction or oxidation takes place. For a one-electron process, the theoretical difference is 57 mV, this difference results from the Nernst equation and the ion concentration ratio. The redox potential of an electrochemical process is given as  $E_{1/2}$ , which corresponds to the mean value of  $E_{p,a}$

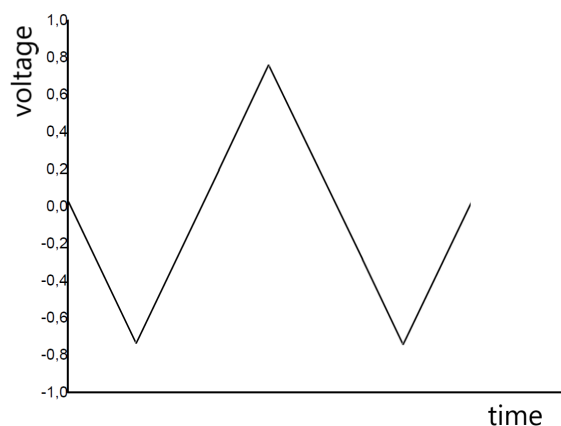


**Figure 4.3:** CV waveform - time vs. voltage.

and  $E_{p,c}$ . The data is always specified against a reference process. Often the hydrogen half-cell is used or, as here in Figure 4.4, the process from ferrocene to ferrocenium. [107][106]

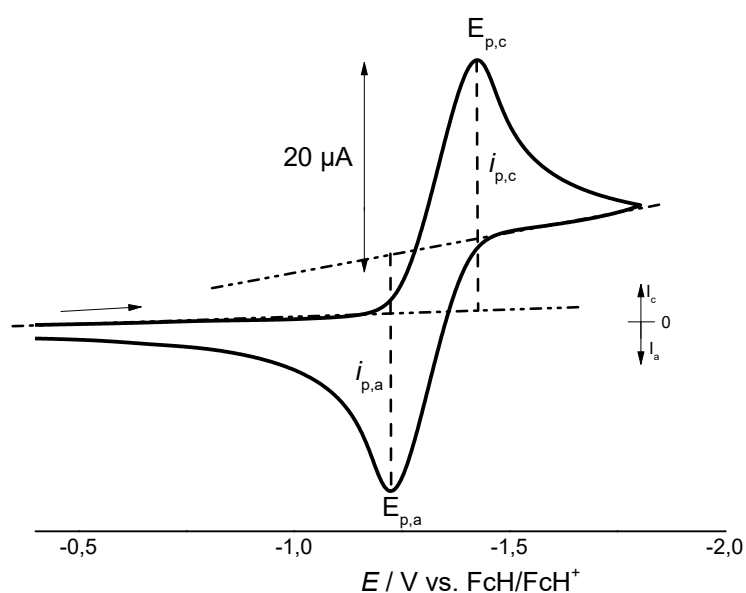


**Figure 4.4:** Figure a CV with the technically important parameters  $E_{p,a}$ ,  $E_{p,c}$ ,  $i_{p,a}$  and  $i_{p,c}$  drawn.

An irreversible electrochemical process is expressed in the CV as follows: the outward process is like a reversible process, an increase in current flow. The backward process however, is shifted or non-existent due to a chemical reaction in the redox state (sometimes

decay of the substance due to lack of stability of the redox state) and thus a change in the chemical structure of the substrate (see Figure 4.5).[106]

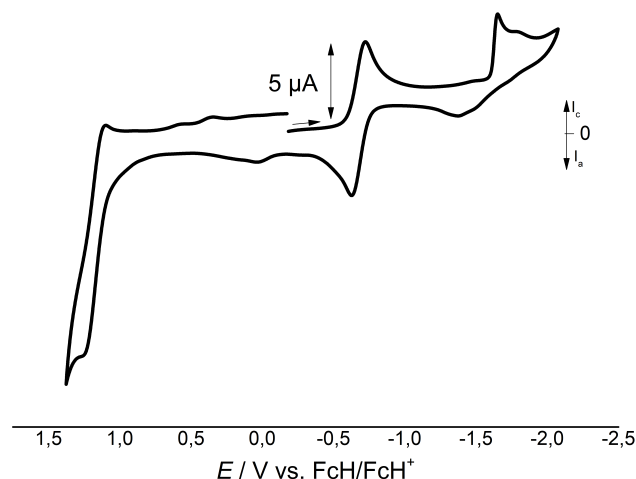


**Figure 4.5:** Figure of a CV with a reversible reduction at -0.7 V as well as an irreversible reduction at -1.7 V and an irreversible oxidation at 1.0 V.[76]

A CV can have multiple reversible and irreversible processes. This depends on the substance. In some cases, irreversible processes can also take on a reversible character at high scan rates, which is equivalent to the speed at which the potential cycle is run. This is the case when the electrochemical redox process is faster than the subsequent chemical reaction. Another possibility is the addition of a ligand source. In this way, the frequently observed irreversible reductive cleavage of a  $\text{Cl}^-$ -M bond in organometallic chloro compounds can be suppressed due to the high concentration of  $\text{Cl}^-$  in the conducting salt. For example when  $n\text{-Bu}_4\text{NCl}$  is added.[108] Figure 4.6 shows, the electrochemical reduction of  $[(\eta^6\text{-p-Cymene})[\alpha\text{-diimine}]\text{chlororuthenium(II)}]^+$ . In the first step, a purely electrochemical one, two electrons flow and the compound is reduced twice. This reaction directly follows a chemical process, the abstraction of the  $\text{Cl}^-$ . However, if the conducting salt is exchanged in this CV experiment, the compound remains in the doubly negatively charged state and is stable with the chloride.

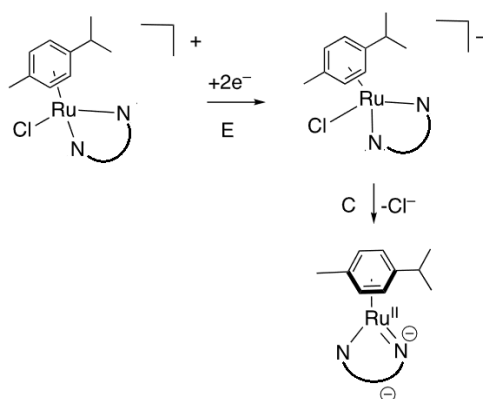


**Figure 4.6:** Electrochemical (E) and chemical (C) reduction of  $[(\eta^6\text{-p-Cymene})[\alpha\text{-diimine}]\text{chlororuthenium(II)}]^+$ . [109]

#### 4.1.2 Rotating disk electrode voltammetry

The RDE differs from the classical three-electrode setup of voltammetry only in that the WE can be rotated at a certain angular velocity, which creates a defined inflow of the substrate solution to the WE. The RDE is also a linear sweep voltammetry. Figure 4.7 shows a plot of an RDE measurement with different rotation speeds.

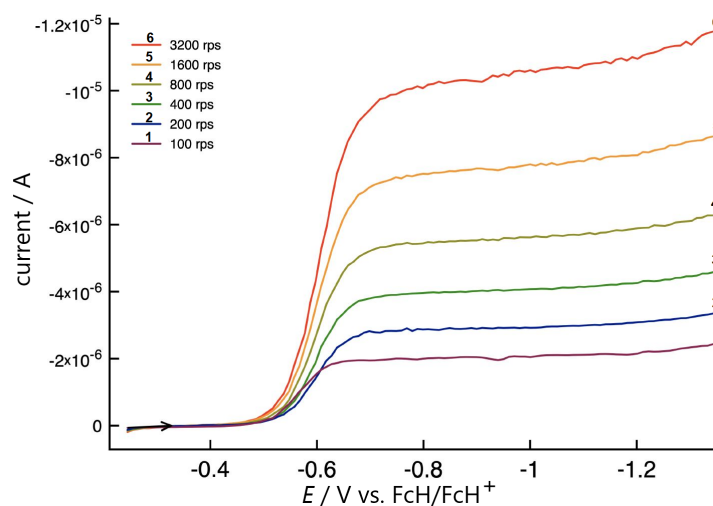


**Figure 4.7:** RDE measurement with different rotation speeds.[109]

By using the Levich ( $I_{lim,c} = 0.620 nF\pi r^2 D^{\frac{2}{3}} \nu^{-\frac{1}{6}} C \omega^{\frac{1}{2}} B$ ) and the Koutecky-Levich equation ( $\frac{1}{i_m} = \frac{1}{i_K} + \frac{1}{B_L \omega^{\frac{1}{2}}}$ ), which contains the measured current ( $I$ ), the Faraday constant ( $F$ ), the number of electrons ( $n$ ), the radius of the electrode, the diffusion coefficient ( $D$ ), the cinematic viscosity ( $\nu$ ), the known rotation speed ( $\omega$ ), the known concentration ( $c$ ) of the substrate solution and the Levich constant ( $B$ ), this method allows the determination

of the number of electrons flowing in the redox process. This makes RDE an important tool for characterizing chemical processes. This is important, for example, to support a predicted electrochemical mechanism. Important in the case of **Paper 3**, where the redox process was followed by a  $\text{Cl}^-$  abstraction. Using the rotating disk, it is possible to determine how many electrons flow with and how many electrons flow without the  $\text{Cl}^-$  abstraction, thus supporting the predicted mechanism.[110]

## 4.2 Spectroelectrochemistry (SEC)

Spectroelectrochemistry is the combination of spectroscopy methods such as UV/Vis, IR and EPR with electrochemistry. The method has been known since 1964 and is an important tool especially in the field of analysis of electrochemical reaction mechanisms. Spectroelectrochemical measurements aim to gain detailed insights into the electrochemical properties of molecules, ions or solids. This technique combines electrochemical methods with spectroscopic techniques to investigate redox reactions, characterize electrode materials and analyze structural changes during electrochemical processes in real time. The correlation of spectroscopic information with electrochemical data enables the exploration of structure-activity relationships and plays a crucial role in the development of new materials for applications in batteries, fuel cells and catalysts. Overall, spectroelectrochemistry is used for the comprehensive characterization and better understanding of electrochemical systems.

In this work, spectroelectrochemistry measurements are performed to gain a comprehensive understanding of the electrochemical and structural properties of organometallic compounds. This method enables the investigation of redox properties, the determination of structural changes during redox reactions in real time and the identification of intermediates. The correlation of electrochemical data with spectroscopic information allows a precise analysis of the structure-activity relationship, which is crucial to characterize the properties and behavior of newly synthesized organometallic compounds.

In general, the method can be described in such a way that, as in voltammetry, the substance to be examined is present in a conductive solution. In this setup, however it is in a very thin layer. There is also a three electrode setup. For example, the UV/Vis and IR measurements, which are taken in parallel with voltammetry, have only a small measuring area, directly at the WE. This ensures that only the newly generated species is spectroscopically investigated.

There are several specially designed three electrode setups for these measurements. Figure 4.8 shows a thin film measurement cell, which is accordingly prepared with a three electrode setup. For EPR measurements, a two or three electrode setup is used in an



EPR tube and care is taken to arrange the WE and the CE in such a way as to provide the greatest possible spacing. This allows selective electromagnetic investigation of the species generated at the WE.[111]

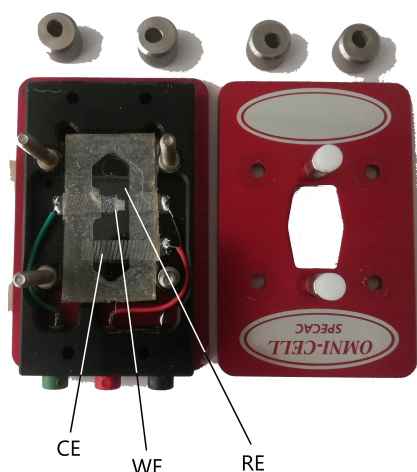


**Figure 4.8:** Illustration of an OTTLE cell made by Hartl.

A good example is the reduction of  $[\text{Re}(\text{bpy})(\text{CO})_3\text{Cl}]$  published by Hartl in 1996. Figure 4.9 shows IR spectroscopy parallel to the reduction. Here it can be seen that the intensity of the characteristic vibrational bands of the starting substance decreases and three new bands are formed, which are assigned to the radical anion  $[\text{Re}(\text{bpy})(\text{CO})_3\text{Cl}]^{\cdot-}$ . [35]

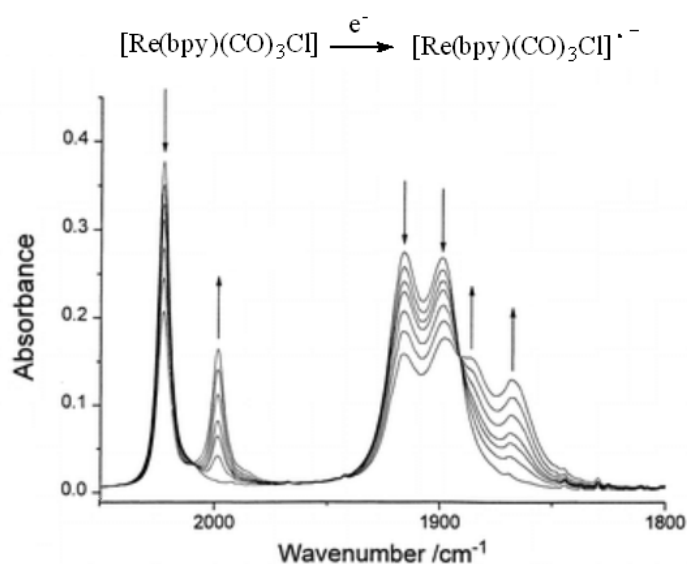


**Figure 4.9:** IR-SEC measurement of the reduction of  $[\text{Re}(\text{bpy})(\text{CO})_3\text{Cl}]$  performed by Hartl.[35]

## 4.3 Kinetics

The measurement of kinetics, especially reaction rates, is of central importance in chemistry as it provides insights into the dynamics of chemical reactions. Kinetics refers to the study of the rates at which chemical species transform during a reaction and thus enables the detailed analysis of the time course of reactions. Knowledge of kinetics is crucial for several reasons. Firstly, kinetics enables the deduction of the reaction mechanism, i.e. how molecules interact with each other and transform during a reaction. This is fundamental to the basic understanding of chemical processes. Secondly, knowledge of kinetics contributes to the identification of optimal reaction conditions. By studying the rate dependence of parameters such as temperature, pressure and concentration, researchers can optimize conditions to maximize the yield of desired products and minimize by-products. Third, kinetics plays a key role in the development and optimization of catalysts. By identifying the rate-determining steps, catalysts can be specifically designed to make reactions more efficient and selective. Overall, the measurement of kinetics enables a precise understanding of the temporal sequence of events during a chemical reaction. This knowledge is not only fundamental for basic research in chemistry, but also has far-reaching applications in industrial production, medicine, environmental science and many other areas.

### 4.3.1 Measurement setup

Two different measurement methods were used to determine the kinetics. For slower reaction kinetics, the conversion of the reaction was followed by NMR and for the faster reactions UV/Vis. For this purpose, not only time-resolved measurements were performed, they were also repeated at different temperatures. Figure 4.10 shows one of these setups for tempered measurements of kinetics via UV/Vis.

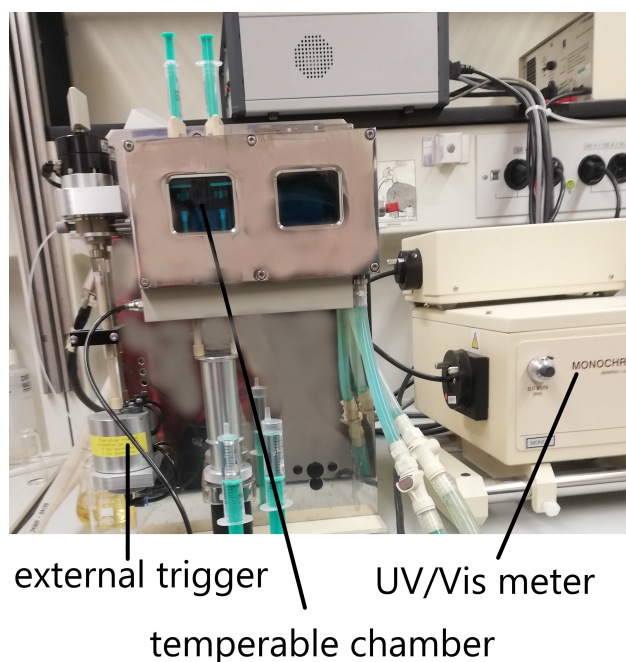


**Figure 4.10:** Illustration and setup of the temperature controlled UV/Vis set up for kinetics measurements.

For the evaluation, the decrease in intensity of characteristic signals was plotted against time and a function of the integrated rate law is fitted to the curve. The measurement is repeated at different temperatures and the results of the constant  $K$  from the rate law are plotted reciprocally to the temperature. By applying the corresponding kinetics equation and the equation for the Eyring plot, the kinetics  $k_2$ , the free enthalpy  $\Delta H^\ddagger$ , the free entropy  $\Delta S^\ddagger$  and the Gibbs free energy  $\Delta G^\ddagger$  can be calculated. Examples of such plots is shown in Figure 4.11.[112]

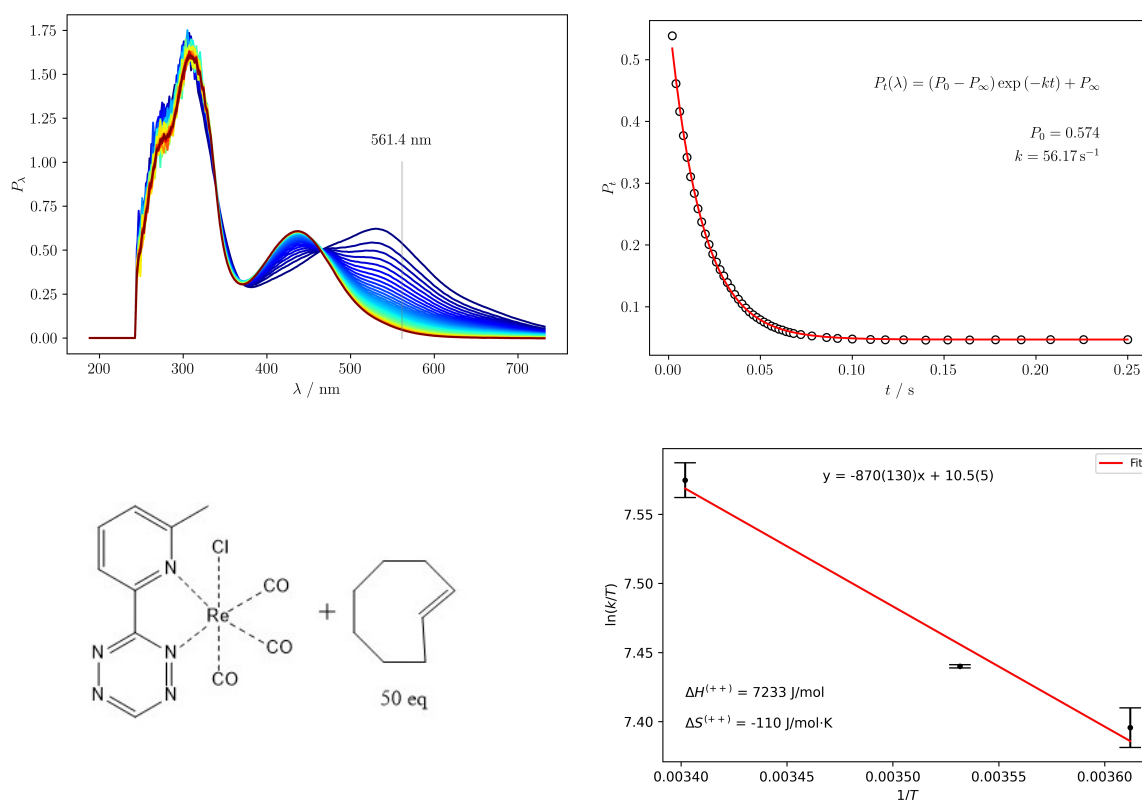


**Figure 4.11:** *top left:* Time-dependent UV/Vis during reaction; *top right:* section along one wavelength; *bottom left:* Reaction of metallotetrazine with 50eq TCO; *bottom right:* Eyring plot of different temperature dependent measurements.[76]

For the determination of the kinetics, the pursued mechanism is decisive. More precisely, how many particles are involved in the reaction. The main distinction is between 1st order kinetics, 2nd order kinetics and pseudo 1st order kinetics.[113]

### 4.3.2 Kinetics: 0th order, 1st order, 2nd order and pseudo 1st order

For the determination of the reaction rate constant  $k$ , the order of the kinetics must first be determined. Basically, the order of the reaction is differentiated by how many particles are involved in the reaction and how the concentration of the reactants decreases over time.

A 0th order reaction describes a reaction, whose chemical turnover always proceeds at the same rate. The reaction rate is therefore independent of the concentration of the reactants. It can be described mathematically as follows:  $-d[A]/dt = k$ . A well-known example is the radioactive decay of certain nuclides. Take, for example, the radioactive decay of radium-226.

In the 1st order a particle A is present which reacts to one or more products, this is a uni-

molecular reaction:  $A \rightarrow P_{1-n}$ . An example is the decomposition of dinitrogen pentoxide ( $N_2O_5$ ) to  $NO_2$  and  $O_2$ . Such a decomposition initially has a rapid decrease in concentration and towards the end of the reaction at lower concentrations. Logarithmizing this concentration results in a constant decrease of the  $\ln[A]$  against time  $t$ . In figure 4.12 such a behavior which speaks for a 1st order kinetics is shown graphically and expressed mathematically:  $k[A] = -d[A]/dt$  and integrated for a better representation and determination of the reaction rate constant  $k$ :  $\ln([A]/[A]_0) = -kt$ . With a 1. order kinetic we get a unit of  $s^{-1}$  for  $k$ . Thus we get a reaction rate which is proportional to the concentration of A.[112]

In the 2nd order two particles react together to one or more products. There are two different possibilities to represent this as a reaction equation. Either two equal parts react together to one or more products:  $2A \rightarrow P_{1-n}$  or two different particles react stoichiometrically to one or more products:  $A+B \rightarrow P_{1-n}$ .

For the 2nd order the reaction rate constant  $k$  is determined as follows:  $k[A]^2 = -d[A]/dt$  and integrated:  $1/[A] = 1/[A]_0 + kt$ . The units for  $k$  in this case are:  $M^{-1} \cdot s^{-1}$ . Using the example of a mixed-second order kinetic of  $A+B \rightarrow P_{1-n}$ , the rate law is described as follows:  $k[A][B] = -d[A]/dt$ . Assuming a stoichiometric reaction and an identical start co-centering, the rate law can be described identically to the non-mixed-second order. For the reaction rate, this means that it is linear to the concentrations of the two reactants or quadratic to that of one reactant.[112]

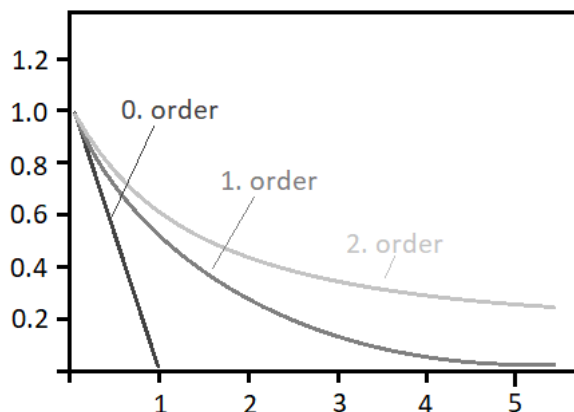


**Figure 4.12:** The degrees of 0th, 1st and 2nd order kinetics over time.

The more reactants are involved in a reaction, the calculation of the reaction rate constant  $k$  can become complicated. However, by using single reactants in significant excess, there is also the possibility of removing a single concentration parameter and thus to simplify the equation. An example is the kinetics of the pseudo 1st order. In the kinetics of the pseudo 1st order one of the two reactants is present in excess (20-50 eq). Thus, this factor

is shortened and the kinetics of the 2nd order is calculated identically to the kinetics of the 1st order.[112]

## 5 Summary of Research

The work can generally be divided into 4 publications: (5.1) Metallotetrazines increase regioselectivity and reactivity in the [4 + 2] cycloaddition reaction; (5.2) 3-(Pyrid-2-yl)-s-Tetrazine Tricarbonylrhenium(I)chloride - Dienophile Addition - (Spectro)Electrochemistry; (5.3)  $[(\eta^6\text{-p-Cymene})[3\text{-(pyrid-2-yl)-1,2,4,5-tetrazine}]chlororuthenium(II)]^+$  - Dienophile Addition - (Spectro)Electrochemistry; (5.4) Various 3-(Pyrid-2-yl)-s-Tetrazine Tricarbonylrhenium(I)chloride derivatives and their influence on reactivity.

The results haven been published largely (5.1-5.3). The Part (5.4) is embedded as a manuscript. In the following subsection the most important results of the publications will be summarized shortly.

## 5.1 Metallotetrazines increase regioselectivity and reactivity in the [4 + 2] cycloaddition reaction

Complexation of tetrazines provides a new tool for the [4+2] inverse electron demand Diels-Alder reaction. The complexed tetrazines can further be used as reaction partners with dienophiles. For this purpose, a number of different reactants were tested. These are shown in figure 5.1. Via this reaction it could be shown that novel ligand systems can be constructed, which otherwise could only be prepared with difficulty or not at all via previously known synthesis methods.

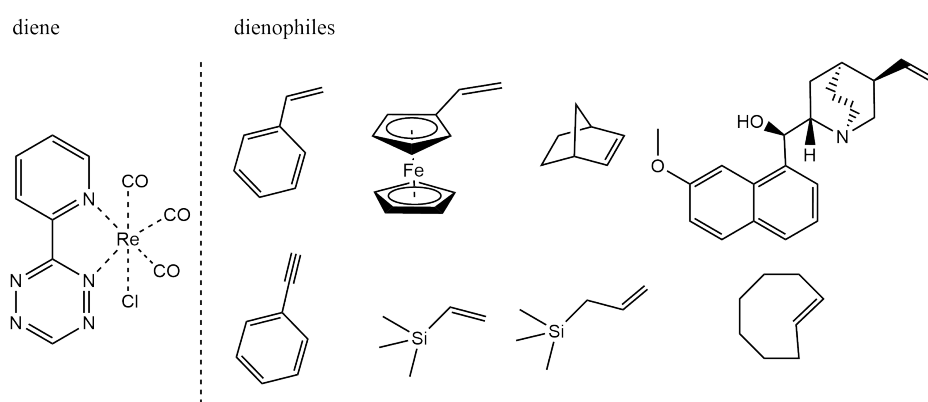


**Figure 5.1:** Representation of the reaction partners. *left:* The diene 3-(Pyrid-2-yl)-s-tetrazine tricarbonylrhenium(I)chloride and *right:* the dienophiles like vinylferrocen, etynylferrocen, norbonen, quinine .

Theoretically, up to eight products would be conceivable. Four each in the case of a 1,4-addition and the 1,5-addition. In the reaction of metallotetrazines there was no 1,5-addition observed. The 1,4-addition is strongly favored by the electronic charge distribution of the vinyl unit, so that only this can be observed. The four remaining isomers result from two 4,5-dihydropyridazines and two 1,4-dihydropyridazines each. Two each are formed, since the dienophile can attack from either the CO- or Cl-face.



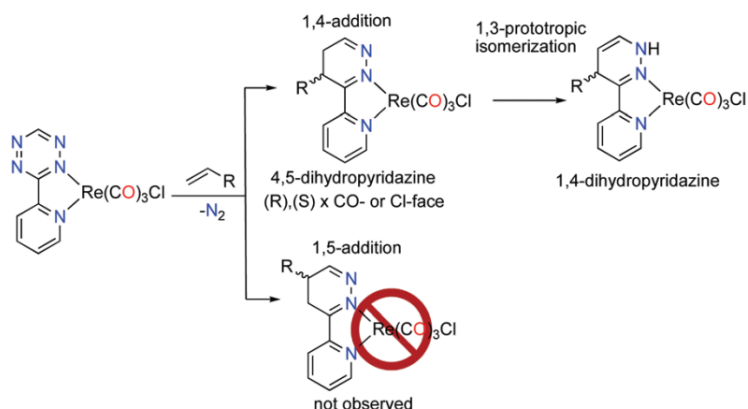


**Figure 5.2:** Addition of dienophile to 3-(pyrid-2-yl)-s-tetrazine tricarboxylrhodium(I)-chloride and the different products.

The reactivity of the metallotetrazines with some selected dienophiles was also investigated kinetically and the rate constant  $k$  as well as  $\Delta G^\ddagger$ ,  $\Delta H^\ddagger$  and  $\Delta S^\ddagger$  were determined. For the determination of the kinetics, the reaction was monitored by UV/Vis at different temperatures and with different equivalents. Figure 5.3 shows these kinetic measurements of the reaction of 3-(pyrid-2-yl)-s-tetrazine tricarboxylrhodium(I)-chloride with styrene. Furthermore, Figure 5.4 shows the molecular structures of the three main products studied, the addition with TCO, vinyl ferrocene and styrene. The determined values for  $k$  as well as  $\Delta G^\ddagger$ ,  $\Delta H^\ddagger$  and  $\Delta S^\ddagger$  are shown in table 5.1. It was found that the complexed tetrazines react much faster than the free ligand. As a comparison, one of the fastest known tetrazine kinetics is also listed in the table (Py<sub>2</sub>Tz + TCO).

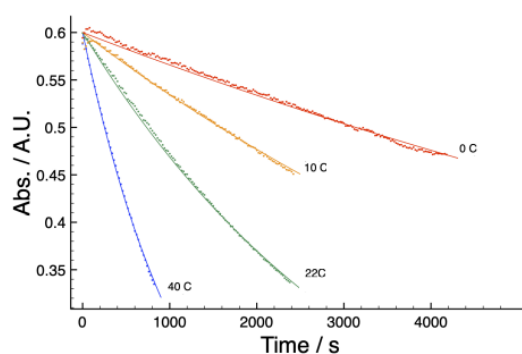


**Figure 5.3:** Pseudo 1. order kinetic measurements of styrene + 3-(pyrid-2-yl)-1,2,4,5-tetrazine-tricarboxylrhodium(I)chloride, at different temperatures. Concentration of 3-(pyrid-2-yl)-1,2,4,5-tetrazine-tricarboxylrhodium(I)chloride = 0.000190 M, styrene = 0.00949 M.

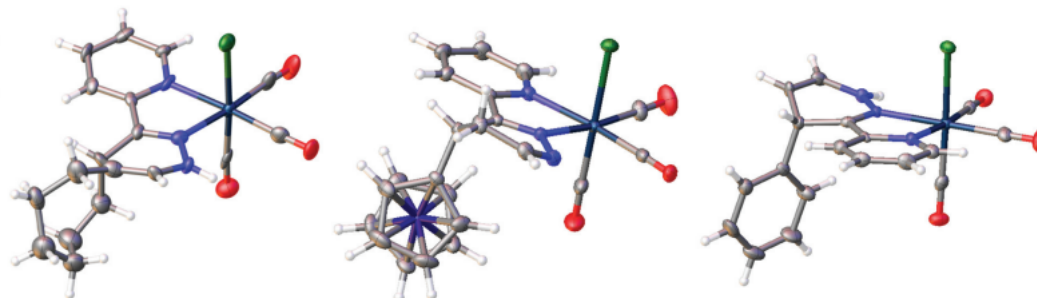


**Figure 5.4:** Molecular structure of the addition products with TCO left, vinylferrocene middle and styrene right.

**Table 5.1:** 2. order rate constants  $k_2$  and thermodynamic values  $\Delta H^\ddagger$ ,  $\Delta S^\ddagger$  and  $\Delta G^\ddagger$  for selected click reactions.

	$k_2 /$ $\text{M}^{-1} \text{s}^{-1}$	$\Delta H^\ddagger /$ $\text{kJ mol}^{-1}$	$\Delta S^\ddagger /$ $\text{J mol}^{-1} \text{K}^{-1}$	$\Delta G^\ddagger /$ $\text{kJ mol}^{-1}$
TzPy + vinylferrocene	$1.8 \cdot 10^{-2}$	27	-192	84 (54)
complex + vinylferrocene	2.80(10)	23	-150	68 (40)
complex + styrene	$6.03(2) \cdot 10^{-2}$	55	-125	92 (62)
complex + TCO	$4.06(52) \cdot 10^5$	26	-50	41 28
Py <sub>2</sub> Tz + TCO	$2.0 \cdot 10^3$			

## 5.2 3-(Pyrid-2-yl)-s-Tetrazine Tricarbonylrhenium(I)chloride - Dienophile Addition - (Spectro)Electrochemistry

Starting from **paper 1**, the compounds 3-(pyrid-2-yl)-1,2,4,5-tetrazine-tricarbonylrhenium(I)chloride, 3-(pyrid-2-yl)-4-ferrocenyl-4,5-dihydropyridazine-tricarbonylrhenium(I)-chloride and additionally 3-(pyrid-2-yl)-4-ferrocenyl-pyridazine-tricarbonylrhenium(I)chloride, were investigated by spectroelectrochemistry and by Mössbauerspectroscopy. In contrast to the addition of vinyl ferrocene, only one product was detected and isolated in the addition of ethynyl ferrocene. The molecular structures of the three compounds investigated are shown in figure 5.5.

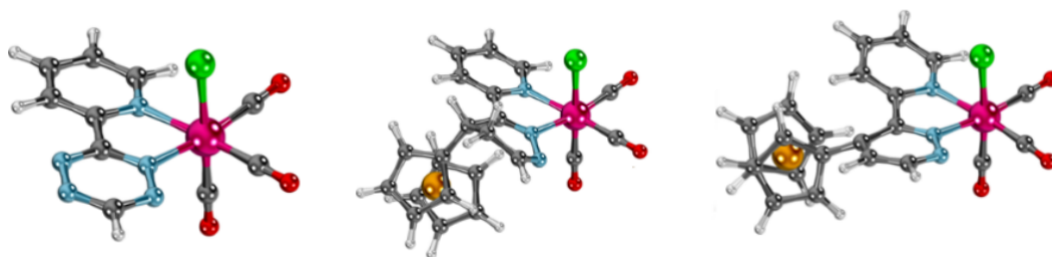


**Figure 5.5:** Molecular structure of 3-(pyrid-2-yl)-1,2,4,5-tetrazine-tricarbonylrhenium(I)chloride left, 3-(pyrid-2-yl)-4-ferrocenyl-4,5-dihydropyridazine-tricarbonylrhenium(I)chloride middle and 3-(pyrid-2-yl)-4-ferrocenyl-pyridazine-tricarbonylrhenium(I)chlorid right.

The coloration of the compounds goes from violet (3-(pyrid-2-yl)-1,2,4,5-tetrazine-tricarbonylrhenium(I)chloride) to orange (3-(pyrid-2-yl)-4-ferrocenyl-4,5-dihydropyridazine-tricarbonylrhenium(I)chloride) to red (3-(pyrid-2-yl)-4-ferrocenyl-pyridazine-tricarbonylrhenium(I)chloride).

The two different addition products of adding vinylferrocene and ethynylferrocene are structurally similar. However, the dihydropyridazine and the conjugated product are electrochemically quite different. In the CV measurements it can be clearly seen that, starting from the initial compound (3-(pyrid-2-yl)-1,2,4,5-tetrazine-tricarbonylrhenium(I)chloride), the potential of the reduction centered at the ligand shifts cathodically by approximately 1 V due to the [4+2] cycloaddition. The reduction potential of (3-(pyrid-2-yl)-4-ferrocenyl-4,5-dihydropyridazine-tricarbonylrhenium(I)chloride) is at -1,7 V, whereas that of 3-(pyrid-2-yl)-4-ferrocenyl-pyridazine-tricarbonylrhenium(I)chloride with its conjugated ligand system is shifted cathodically deeper to -1.9 V. In addition, greater reversibility of the reduction was shown. The CV spectra also still show a shifting irreversible ox-

idations. Finally, two addition products naturally exhibit a reversible oxidation of the ferrocene units. The dihydro product is a mixture with overlapping processes and the conjugated product is a pure substance with only one reversible process.

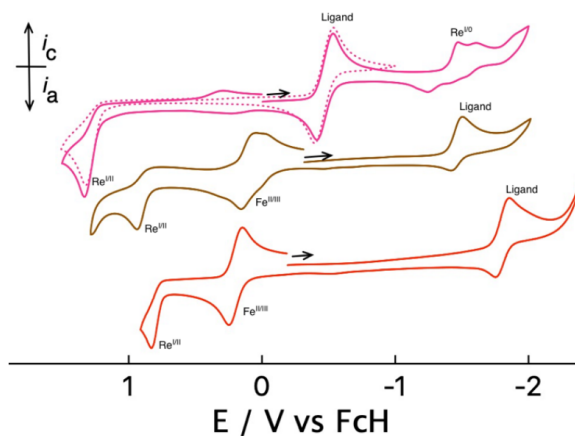


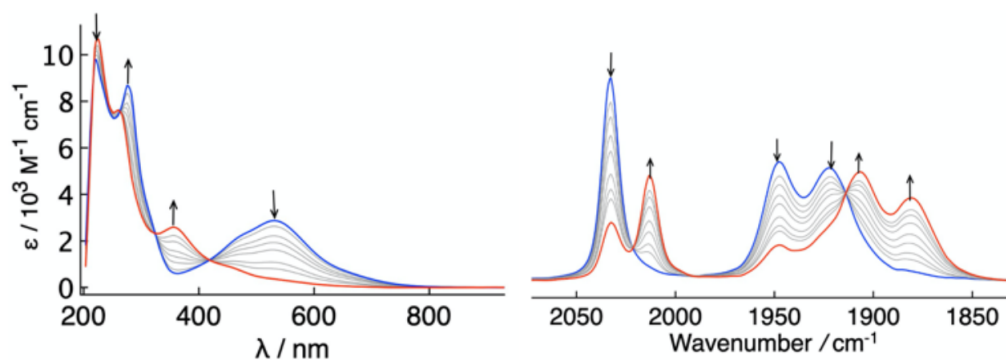
**Figure 5.6:** CV spectra of 3-(pyrid-2-yl)-1,2,4,5-tetrazine-tricarbonylrhenium(I)chloride top, 3-(pyrid-2-yl)-4-ferrocenyl-4,5-dihydropyridazine-tricarbonylrhenium(I)chloride center and 3-(pyrid-2-yl)-4-ferrocenyl-pyridazine-tricarbonylrhenium(I)chloride bottom.

The CV measurements were additionally supported by spectroelectric measurements in order to make more substantiated statements about the localization of the oxide ions and reductions. Table 5.2 lists the measured IR shifts of the CO vibrations of the individual compounds. Additionally the  $\Delta$  of the shift after oxidation and reduction are listed. Thus, it can be concluded that the reduction with a CO shift of 20-30  $\text{cm}^{-1}$  is metal based and the oxidation with a shift of 2-4  $\text{cm}^{-1}$  is ligand based because the oxidation can be attributed to the ferrocene substituent.

**Table 5.2:** Summary of IR-SEC measurements of the starting compound [E], the dihydropyridazine product [PH<sub>2</sub>Fc] and the conjugated product [PFc]. Listed are the wavenumbers of CO bands, neutral species, reduced and oxidized, respectively. In addition, the average and delta of the shift due to oxidation and reduction are given.

	$\nu / \text{cm}^{-1}$	$\nu / \text{cm}^{-1}$	$\nu / \text{cm}^{-1}$	$\nu$ average	$\Delta$
[E]	2032	1948	1921	1967	
[E] <sup>-</sup>	2021	1906	1880	1937	30
[PH <sub>2</sub> Fc]	2023	1924	1900	1949	
[PH <sub>2</sub> Fc] <sup>+</sup>	2025	1927	1902	1951	2
[PH <sub>2</sub> Fc] <sup>-</sup>	2007	1897	1869	1924	23
[PFc]	2023	1923	1898	1948	
[PFc] <sup>+</sup>	2026	1927	1903	1952	4
[PFc] <sup>-</sup>	1999	1893	1862	1918	30

The additional SEC UV/Vis measurements performed, as well as supporting DFT calculations, indicate a metal to ligand charge transition MLCT.

**Figure 5.7:** UV/Vis and IR-SEC measurement of the reduction of 3-(Pyrid-2-yl)-s-tetrazine tricarbonylrhenium(I)chloride in 0.1 M n-Bu<sub>4</sub>NPF<sub>6</sub>/CH<sub>2</sub>Cl<sub>2</sub>.

In addition, Mößbauer measurements were performed on the vinyl ferrocene, the ethynyl ferrocene and the addition products with 3-(pyrid-2-yl)-s-tetrazine-tricarbonylrhenium(I)-chloride. Small shifts could be detected.

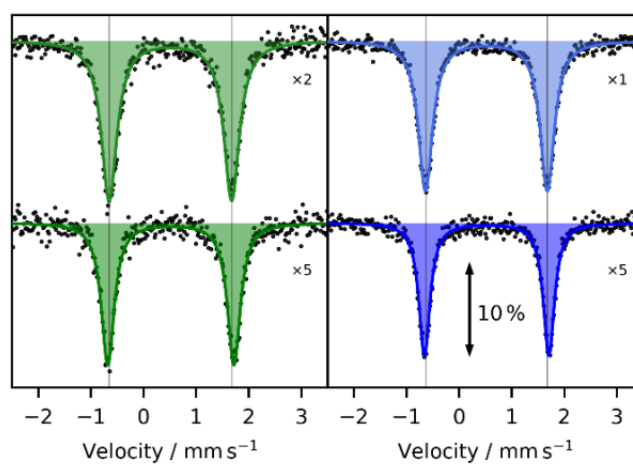


**Figure 5.8:** Mössbauer measurements of vinylferrocen top-left, etynylferrocen top-right and their corresponding product with the 3-(pyrid-2-yl)-s-tetrazine-tricarbonylrhenium(I)-chloride.

### 5.3 $[(\eta^6\text{-p-Cymene})[3\text{-(pyrid-2-yl)-1,2,4,5-tetrazine}]chlororutheni-um(II)]^+$ - Dienophile Addition - (Spectro)Electrochemistry

In this publication, the synthesis of the  $(\eta^6\text{-p-cymene})[3\text{-(pyrid-2-yl)-1,2,4,5-tetrazine}]chlororuthenium(II)]^+$  starting from the bidentate TzPy ligand was presented. The source of the metal is the dimer of the corresponding ruthenium cymene chloride compound.

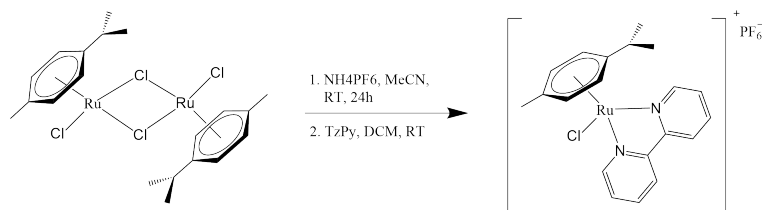


**Figure 5.9:** Synthèse des  $(\eta^6\text{-p-Cymene})[3\text{-(pyrid-2-yl)-1,2,4,5-tetrazine}]chlororuthenium(II)]^+$ .

The addition of vinyl ferrocene as a dienophile showed not only the mixture of products already presented in Paper 1. In addition, an oxidation of a part of the product was observed here, which results in the conjugated sideproduct. By adding 3,5-di-*tert*-butyl-*o*-quinone and oxygen, a complete conversion was observed. This product was compared with the addition product of ethynylferrocene and both products are identical.

This autooxidation with 3,5-di-*tert*-butyl-*o*-quinone and oxygen is an important step on the way to the synthesis of isomeric pure compound by the [4+2] cycloaddition and is shown in figure 5.10.

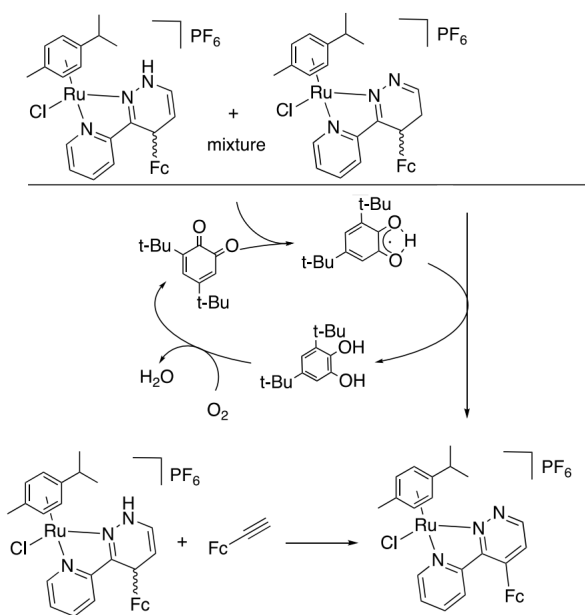


**Figure 5.10:** Synthesis of  $(\eta^6\text{-p-Cymene})$ [Proposed *o*-quinone-catalyzed Oxidation of dihydropyridazine with O<sub>2</sub>].

The compound  $(\eta^6\text{-p-cymene})[3\text{-(pyrid-2-yl)-1,2,4,5-tetrazine}]chlororuthenium(II)]^+$  exhibits a noninnocent behavior and was therefore investigated in more detail by voltammetry. The 1,2,4,5-tetrazine compound as well as the two addition products show an irreversible reduction. This reduction is cathodically shifted by the addition of vinylferrocene and ethynylferrocene. In addition, the two addition products show a reversible oxidation of the added ferrocene unit. The oxidation of the dihydropyridazine product shows an oxidation with at least two processes due to the different isomers.

A closer look was taken at the reduction and the electrochemical mechanism of this reduction of  $(\eta^6\text{-p-cymene})[3\text{-(pyrid-2-yl)-1,2,4,5-tetrazine}]chlororuthenium(II)]^+$  was investigated. In this regard, by using the rotating disk electrode, the number of electrons involved in the electrochemical process was investigated. By using two different conducting salts, one with Cl<sup>-</sup>, the chemical abstraction from the chloride ligand could be suppressed. The postulated electrochemical mechanism is shown in figure 5.11. This predicts a 2 electron reduction, which, after dissociation of the chloride ligand, is followed by a 1 electron reduction.



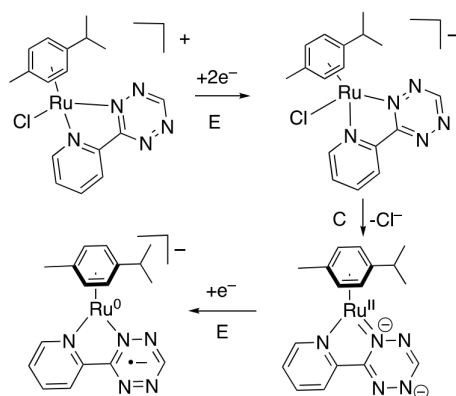


**Figure 5.11:** Proposed electrochemical mechanism of ( $\eta^6$ -p-Cymene)[3-(pyrid-2-yl)-1,2,4,5-tetrazine]chlororuthenium(II)<sup>+</sup>.

## 5.4 Various 3-(Pyrid-2-yl)-s-Tetrazine Tricarbonylrhenium(I)chloride derivatives and their influence on reactivity

The focus in this work is on the synthesis and application of various 3-(pyrid-2-yl)-s-tetrazine tricarbonylrhenium(I) chloride derivatives (see figure 5.12). Included in the application is also the immobilization in a porous material.

The ligands were synthesized via the Caultn method and could all be isolated in yields of 20-40 %. Complexation was carried out with complete conversion.

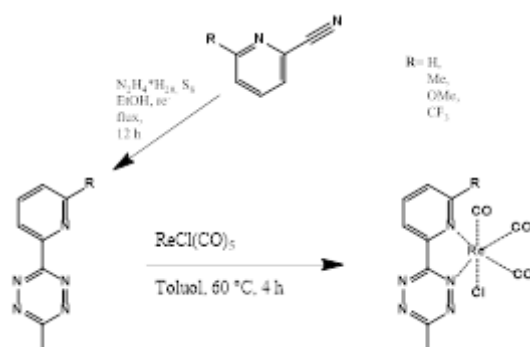


**Figure 5.12:** Synthesis of different 3-(pyrid-2-yl)-s-tetrazine tricarbonylrhenium(I)chloride derivatives, starting from the corresponding nitrile.

The different derivatives were investigated cyclovoltammetrically and in principle show an identical CV spectrum. However, depending on the electron-withdrawing or electron-pushing residue, they show a different shift of the reduction potentials and thus a shift with 0.1 V from 0.8 V for the OMe group to 0.9 V for the  $CF_3$  group for the reversible oxidation of the complexes.

The different derivatives were investigated for their reactivity in the [4+2] addition with TCO and NBE. The kinetics measurements were performed in pseudo 1st order using 50 eq of TCO or NBE for the measurements. The calculated values for the reaction constant  $k$  as well as  $\Delta G^\ddagger$ ,  $\Delta H^\ddagger$  and  $\Delta S^\ddagger$  are shown in table 5.3.

The measured kinetics and the results of the potential of reduction from the CV measurements show a dependence of the reactivity on the reduction potential. The measured values are plotted against each other in figure 5.13.

**Table 5.3:** 2. order rate constants  $k_2$  and thermodynamic values  $\Delta H^\ddagger$ ,  $\Delta S^\ddagger$  and  $\Delta G^\ddagger$  for selected click reactions.

	$k_2$ (+NBE) $M^{-1} s^{-1}$	$k_2$ (+TCO) $M^{-1} s^{-1}$	$\Delta H^\ddagger$ (+TCO) $kJ mol^{-1}$	$\Delta S^\ddagger$ (+TCO) $J mol^{-1} K^{-1}$	$\Delta G^\ddagger$ (+TCO) $kJ mol^{-1}$
[L]-H	0.012	21	13.35	- 136	53.88
[L]-Me	0.008	17	17.96	- 122	54.32
[L]-OMe	0.010	19	18.71	-119	54.17
[L]-CF <sub>3</sub>	0.027	41	19.50	- 114	53.47
[C]-H	0.032	90	13.00	- 125	50.25
[C]-Me	0.022	63	13.79	- 125	51.04
[C]-OMe	0.021	59	13.76	-126	51.31
[C]-CF <sub>3</sub>	0.480	119	7.97	- 140	49.69

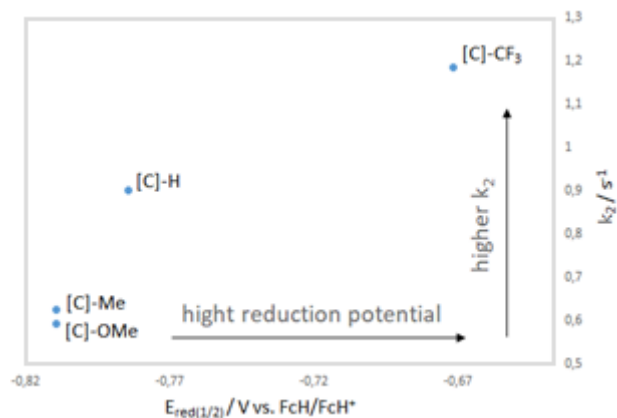


**Figure 5.13:** Reduction potential E vs. kinetics  $k_2$  of the four examined compounds.

For the immobilization a trimethoxysilanenorbonene functionalized SBA-15 silica was chosen, which was prepared via the Crudden method. The Complex with the CF<sub>3</sub> was immobilized on the SBA-15 and analyzed by solid-state UV/Vis, solid-state IR and XPS. The results were compared with the Complex with the CF<sub>3</sub> group itself and the complex reacted with the pure linker. The results indicate successful immobilization. The solid-state UV/Vis spectra are shown in Figure 5.14.

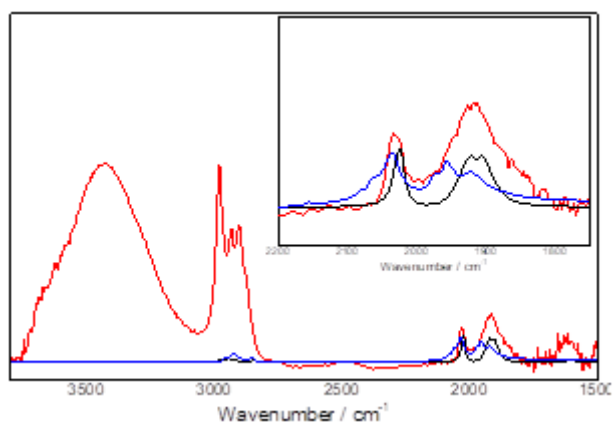


**Figure 5.14:** Solid state IR spectra of complex itself (blue), the complex reacted with the norbonenetrिमethoxysilane linker (black) and the immobilized complex on the SBA-15 (red).

## 6 Conclusion & Outlook

In conclusion, a new tool for the toolbox of click chemistry has been presented and investigated. The work includes the synthesis and characterization of several metallotetrazine complexes, and especially their possibility of ligand modification by the [4+2] cycloaddition.

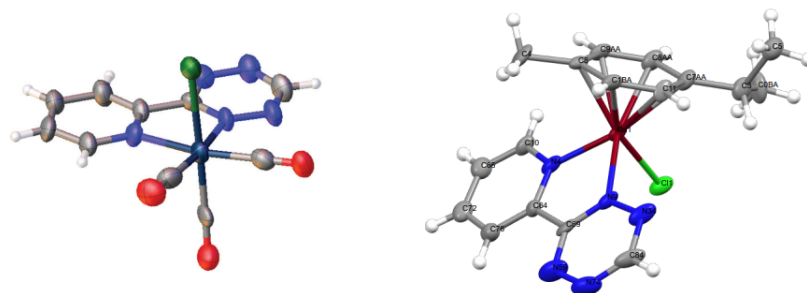


**Figure 6.1:** Molecular structure of 3-(pyrid-2-yl)-1,2,4,5-tetrazine-tricarbonylrhenium(I)chloride left and  $[(\eta^6\text{-p-Cymene})(3\text{-(pyrid-2-yl)-1,2,4,5-tetrazine})\text{chlororuthenium(II)}]^+\text{PF}_6^-$ . Counter anion and hydrogen atoms removed for clarity.

It was shown that the tetrazine moiety in the compounds is active for the [4+2] cycloaddition. For this purpose, various dienes were used to test the iEDDA reaction. In the work vinylferrocene etnylferrocene norbonene and transcyclooctene proved to be important reaction partners. The possibility of [4+2] cycloaddition of complexes provides a unique synthetic pathway for the creation of new ligand synthetics.

Metallotetrazines, compared to free tetrazines, were shown to have a higher reaction rate. This could be attributed to a decrease in the electron density in the tetrazine unit by complexation.

Another important aspect of this click reaction is the large number of different products that can be formed. It was shown here that the spatial requirement of the complex alone influences the variety of reaction products and their ratio.

Another point that could be shown in connection with the reaction products is the possible oxidation of the dihydropyridazine to a conjugate product. For the compound starting from the CymRu complex, this behavior was addressed in more detail and a complete oxidation was specifically sought. In this regard, oxidation with oxygen and quinone was successful. A suitable oxidation cycle could also be postulated.

Finally, it was shown that the [4+2] cycloaddition of metallotetrazines can be used to fix

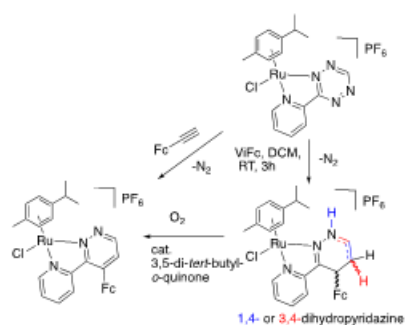


**Figure 6.2:** [4+2] cycloaddition with vinylferrocene and subsequent oxidation to the conjugated product, which is also formed in a reaction with ethynylferrocene.

these metal complexes, or presumably catalysts with a tetrazine unit, into a pore or onto a surface. This allows the synthesis of heterogeneous asymmetric catalysts.

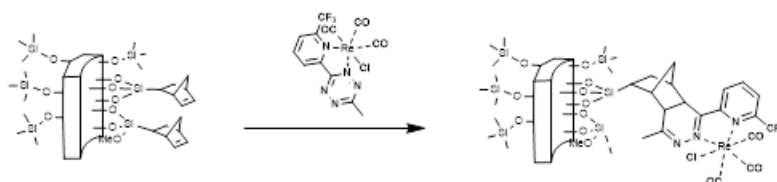


**Figure 6.3:** Immobilization of a metallotetrazine in a norbornene trimethoxysilane functionalized SBA-15 pore.

Regarding further possibilities and the next steps, the field is open in many directions. However, the synthesis of catalysts, their efficacy and comparison in the pore would be a good next target.



## 7 Publications

## 7.1 Publication Paper 1.



ChemComm

COMMUNICATION

View Article Online  
View Journal | View IssueCite this: *Chem. Commun.*, 2020, 56, 12033Received 29th May 2020,  
Accepted 5th August 2020

DOI: 10.1039/d0cc03805a

rsc.li/chemcomm

## Tetrazine metallation boosts rate and regioselectivity of inverse electron demand Diels–Alder (iEDDA) addition of dienophiles†

Marc Schnierle,<sup>a</sup> Svenja Blickle,<sup>a</sup> Vasileios Filippou<sup>ib</sup>\*<sup>ab</sup> and Mark R. Ringenberg<sup>ib</sup>\*<sup>a</sup>

Reported herein is the coordination of rhenium complexes to tetrazine ligand in [ReCl(CO)<sub>3</sub>(TzPy)] [1] (TzPy = 3-(2-pyridyl)-1,2,4,5-tetrazine) and the rates of addition of different dienophiles to the tetrazine. Tetrazine coordination lowers the ΔS<sup>‡</sup> contribution to ΔG<sup>‡</sup> for iEDDA addition.

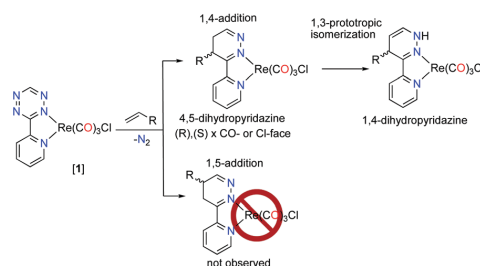
The inverse electron demand Diels–Alder (iEDDA) reaction between 1,2,4,5-tetrazines and olefins is a substrate controlled click-reaction<sup>1,2</sup> and does not require the addition of a catalyst (CuAAC)<sup>3</sup> or light (thiol–ene).<sup>4,5</sup> The modification of the 1,(4)-positions on the tetrazine can be synthetically arduous but rational design of the tetrazine diene and dienophile has resulted in very fast iEDDA reaction rates, where rates >10<sup>6</sup> M s<sup>-1</sup> have been reported.<sup>6,7</sup> These factors have made the iEDDA addition a useful reaction in several applications, chiefly among them in biological labelling experiments.<sup>1,5,8</sup> The iEDDA addition is, however, not regioselective<sup>9</sup> and it produces a mixture of regioisomers, e.g., 1,4- and 1,5-isomers (Scheme 1).

Transition metal(s) are known to coordinate tetrazines and these complexes can exhibit ligand non-innocence.<sup>10,11</sup> Coordinated tetrazines show anodically shifted reduction potentials due to metal back-bonding, i.e., the tetrazine moiety is more electrophilic.<sup>10,12</sup> The metal back-bonding would also lower the activation energy of the addition of a dienophile to the tetrazine diene, however, the often transoid bridging geometry prevents the approach of a dienophile to the tetrazine.<sup>10,11</sup> Unlike the majority of the reported symmetric tetrazines,<sup>10</sup> 2-pyridyltetrazine (TzPy), isoelectronic and isostructural to 2,2'-bipyridine, can be

used as bidentate ligand, and the tetrazine diene is free to add dienophiles. For example, addition of cyclooctyne to the fluorescent iridium complex [Ir(PhPy)<sub>2</sub>(TzPy)]<sup>†</sup> (PhPy = 2-phenylpyridine) have been described and the rate of the iEDDA addition was between 2.5 and 60 times faster than with the free TzPy ligand.<sup>13</sup> The addition of cyclooctyne to [Ir(PhPy)<sub>2</sub>(TzPy)]<sup>†</sup> generates the aromatic 1,2-diazine and thus no stereochemical information was generated from this reaction.

Herein we report the synthesis and rate of addition of three dienophiles to the metallotetrazine [ReCl(CO)<sub>3</sub>(TzPy)] [1], see ESI,† for synthetic and kinetic details. The ReCl(CO)<sub>3</sub> moiety was chosen to coordinate TzPy because tricarbonylrhenium(i) complexes with pyridine donor ligands have found uses as imaging reagents in cells and they have also shown cytotoxic activity for cancer treatment.<sup>14</sup> The water soluble variants [Re(OH<sub>2</sub>)(CO)<sub>3</sub>(L^L)]<sup>†</sup> (L^L = bidentate amine donor ligands) have also been described by replacing the Cl-ligand for the aquo ligand.<sup>15</sup> Additionally, tricarbonylrhenium(i) coordinated to a bidentate ligand, e.g., 2,2'-bipyridine, are electrocatalysts for CO<sub>2</sub> reduction.<sup>16</sup>

The tetrazine moiety in [1] can add dienophiles and the rate of addition of vinylferrocene (ViFc), styrene (Ci), and *trans*-cyclooctene (TCO) to [1] were measured and are reported in Table 1. Different dienophiles were also tested for their ability



Scheme 1 Addition of dienophile to [1].

<sup>a</sup> Universität Stuttgart, Institut für Anorganische Chemie, Pfaffenwaldring 55, 70569 Stuttgart, Germany. E-mail: mark.ringenberg@iac.uni-stuttgart.de

<sup>b</sup> Varimol TGU, Pfaffenwaldring 55, 70569 Stuttgart, Germany.

E-mail: filippou@varimol.de

† Electronic supplementary information (ESI) available: Containing experimental section, DFT calculations, crystallographic tables, and molecule coordinates determined by DFT description. CCDC 1991846–1991849 and 2008845. For ESI and crystallographic data in CIF or other electronic format see DOI: 10.1039/d0cc03805a





View Article Online

ChemComm

## Communication

Table 1 2nd order rate constants of iEDDA and thermodynamic values

Reaction	$k_2^a/M^{-1} s^{-1}$	$\Delta H^\ddagger/kJ mol^{-1}$	$\Delta S^\ddagger/J mol^{-1} K^{-1}$	$\Delta G^\ddagger(DFT)/kJ mol^{-1}$
[1] + ViFc	$2.80 \pm 0.1$	23	-150	68 (40)
TzPy + ViFc	$1.80 \times 10^{-2}$	27	-192	84 (54)
[1] + Ci	$6.03 \pm 0.02 \times 10^{-2}$	55	-125	92 (62)
Py <sub>2</sub> Tz + Ci	$3.0 \pm 0.3 \times 10^{-3d}$	—	—	—
[1] + TCO	$4.06 \pm 0.52 \times 10^5$	26	-50	41 (28)
Py <sub>2</sub> Tz + TCO	$2.0 \times 10^{3e}$	—	—	(37 <sup>f</sup> )

<sup>a</sup> Rate at 25 °C in C<sub>2</sub>H<sub>4</sub>Cl<sub>2</sub>. <sup>b</sup> At 25 °C. <sup>c</sup> Gas phase reaction TPSS/def2-TZVP/J level, see ESI of details. <sup>d</sup> MeOH ref. 18. <sup>e</sup> 9:1 MeOH/H<sub>2</sub>O ref. 7 and CH<sub>2</sub>Cl<sub>2</sub> see ESI figure S. <sup>f</sup> DFT M06L/6(311)+G(d,p) level ref. 7.

to add to [1], such as vinyl and allyl functionality (e.g. vinyltrimethoxysilane and allyltrimethylsilane), a bulky olefin (e.g. quinine) and phenylacetylene to [1] was also demonstrated (see ESI<sup>†</sup>) indicating coordination of TzPy does not inhibit addition of electron rich olefins. The addition of Ci and TCO to [1], respectively, showed enhanced rates compared to the reported rates between the symmetric 3,6-di(pyridin-2-yl)-1,2,4,5-tetrazine (Py<sub>2</sub>Tz) and the self-similar dienophiles.<sup>7,17,18</sup> The work herein was performed in 1,2-dichloroethane (DCE) due to the poor solubility of [1] in H<sub>2</sub>O, although [1] does show moderate solubility in MeOH, the comparison is used to demonstrate the enhanced rate compared to the reported  $k_2$  values.

The rate of the addition of ViFc, Ci, or TCO to [1] was measured using time-resolved variable-temperature UV vis spectroscopy in C<sub>2</sub>H<sub>4</sub>Cl<sub>2</sub>, respectively and the rates and thermodynamic values are reported in Table 1. The rate for [1] + ViFc  $k_2 = 2.80 \pm 0.1 M^{-1} s^{-1}$  at 22 °C was 160 times faster than the control reaction TzPy + ViFc  $k_2 = 0.0180 M^{-1} s^{-1}$  at 22 °C. The Eyring analysis<sup>19</sup> of [1] + ViFc found  $\Delta H^\ddagger = 22.6 kJ mol^{-1}$  and  $\Delta S^\ddagger = -150 J mol^{-1} K^{-1}$ , with  $\Delta G^\ddagger(25 °C) = 68 kJ mol^{-1}$ . The Eyring analysis of TzPy + ViFc showed a small increase in the  $\Delta H^\ddagger = 27 kJ mol^{-1}$ , however the  $\Delta S^\ddagger = -192 J mol^{-1} K^{-1}$  contributed more to the  $\Delta G^\ddagger(25 °C) = 84 kJ mol^{-1}$ . Coordination of TzPy lowers the  $\Delta\Delta G^\ddagger = 16 kJ$ , and the  $\Delta\Delta G^\ddagger(calc.) = 14 kJ$  was in good agreement with experimental value (see ESI<sup>†</sup>). The discrepancy between DFT and experimental values can be attributed to solvent effects.

TzPy shows resonance stabilization of  $\delta^+$  at the C4 of the tetrazine, and coordination of TzPy enhances this resonance structure due to back-bonding of the  $\delta^-$  on the ReCl(CO)<sub>3</sub> moiety (Fig. 2). The addition of ViFc to TzPy shows a larger contribution of  $\Delta S^\ddagger$  to the transition state  $\Delta G^\ddagger$ . One rationale is that the molecular structure of TzPy (see Fig. S27, ESI<sup>†</sup>) is planar while the TzPy in [1] (Fig. 1) tilts towards the Cl-ligand. This distortion may approximate the dien-dienophile transition state (Scheme 2), another contribution could be that back-bonding affords a weakening of the double bonds in the tetrazine. Additionally, coordination of TzPy restricts its motion, which may also contribute to a lower transition state energy. The effect as to why coordination of the tetrazine lowers the  $\Delta G^\ddagger$  is currently under investigation.

ViFc is an electron rich dienophile ( $\delta^-$  on  $\alpha$ -carbon, fulvene resonance with  $\delta^+$  on Fe atom),<sup>20</sup> therefore the addition of the

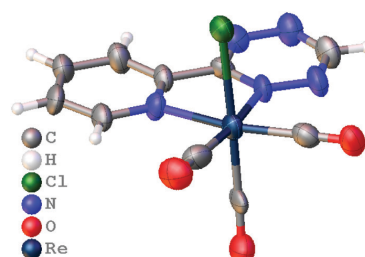
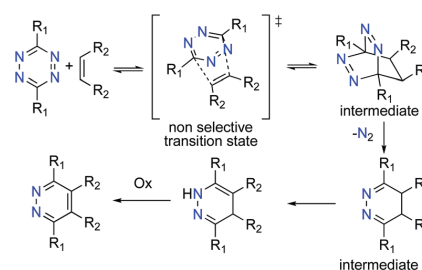


Fig. 1 Molecular structure of [1] determined crystallographically, co-crystallized CH<sub>2</sub>Cl<sub>2</sub> was omitted for clarity.



Scheme 2 Reaction mechanism of olefin with tetrazine.

unactivated styrene (Ci) to [1] was also studied. The rate of addition of Ci to [1],  $k_2 = 6.03 \pm 0.02 \times 10^{-2} M^{-1} s^{-1}$  was nearly 20 times faster than the addition of Ci to Py<sub>2</sub>Tz ( $k_2 = 3.0 \times 10^{-3} M^{-1} s^{-1}$ ).<sup>18</sup> The Eyring analysis of the addition of Ci to [1] found a larger  $\Delta H^\ddagger = 55 kJ mol^{-1}$  was more than double the  $\Delta H^\ddagger$  for the addition of ViFc to [1]. The lower contribution of  $\Delta S^\ddagger = -125 J mol^{-1} K^{-1}$  to the transition state (Table 1) can be attributed to the size of the Ph *verse* Fc. The rate of the addition of TCO to [1] was  $k_2 = 4.06 \pm 0.52 \times 10^5 M^{-1} s^{-1}$  which is 200 time faster than the addition of TCO to Py<sub>2</sub>Tz.<sup>7</sup> The  $\Delta H^\ddagger = 26 kJ mol^{-1}$  is on the order of the addition of ViFc to [1], however there is a significantly lower contribution of the  $\Delta S^\ddagger = -50 J mol^{-1} K^{-1}$  to  $\Delta G^\ddagger = 41 kJ mol^{-1}$ , as should be expected with the strained TCO dienophile. The difference in rates between the addition of ViFc and TCO respectively to [1], shows

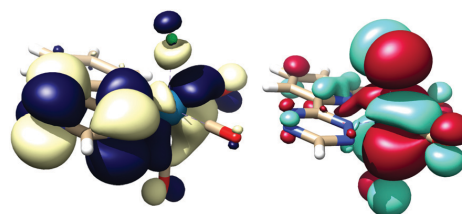


Fig. 2 Lowest unoccupied molecular orbital (LUMO, yellow/blue) and highest occupied MO (HOMO, red/green) of [1], isosurface at 0.02, TPSS basis set at def2-TZVP/J level of theory (see ESI<sup>†</sup> for full details).



## ChemComm

that coordination lowers the entropic barrier ( $\Delta S^\ddagger$ ) as the enthalpic barriers ( $\Delta H^\ddagger$ ) are nearly isoenergetic (Table 1).

The addition of dienophiles to the tetrazine diene is generally unselective (Scheme 2), and the 1,3-prototropic isomerization is rapid which prevents the 4,5-dihydropyridazine (Scheme 2, intermediate 2) from being isolated.<sup>11</sup> The Alder–Stein principle (the relative stereochemistry of dienes and dienophiles is conserved), and Alder's *endo*-rule (the *endo*-adduct is the kinetically preferred product), apply in the iEDDA addition, but stereochemical information is often lost due to rapid isomerization and rearomatization of the 1,4-dhp to the 1,2-pyrazine, especially under aerobic conditions (Scheme 2).

The addition of ViFc, TCO, or Ci to **[1]** at room temperature generated the species **[1Fc]**, **[1TCO]**, and **[1Ci]** and crystals were obtained directly from the reaction mixtures where the molecular structures were determined crystallographically. The molecular structure of **[1Fc]** showed the 4,5-dhp isomer, while **[1TCO]** and **[1Ci]** were found as the 1,4-dhp isomer (Fig. 3). DFT analysis for the 1,3-prototropic isomerization for all three complexes showed the 1,4-dhp was energetically favorable, however, the 1,4-dhp isomer of **[1Fc]** was only observed as a minor product in the <sup>1</sup>H-NMR (see ESI<sup>†</sup>). DFT analysis found rearomatization for both **[1Fc]** and **[1Ci]** were both endergonic (see ESI<sup>†</sup>).

The 4,5-dhp isomer of **[1Fc]** is, to the best of our knowledge, the first molecular structure of this intermediate. Based on the structure of **[1Fc]** the *endo* approach of the dienophile to **[1]** at CO-face of the molecule (Chart 1, Fig. 1) is favorable. The <sup>1</sup>H NMR<sup>21</sup> of the reaction product **[1Fc]** showed a mixture of two major 4,5-dhp products in a ratio of 80:12, and a minor product (~8%) that appears to be the 1,4-dhp isomer due to slow 1,3-prototropic isomerization. The major 4,5-dhp product is the same found in the crystal state, however, based purely on these data the dienophile's *exo* approach at the Cl-face cannot be differentiated from the *endo* approach. However, DFT calculations found that *exo* approach of any dienophile to **[1]** at either Cl- or CO-face produced unrealistic activation energy (>50 kcal mol<sup>-1</sup>) and was therefore not considered. The *endo* approach of ViFc to **[1]** was found to be favorable at the CO-face *versus* the Cl-face of **[1]** based on DFT calculations (Fig. S5, ESI<sup>†</sup>).

View Article Online

## Communication

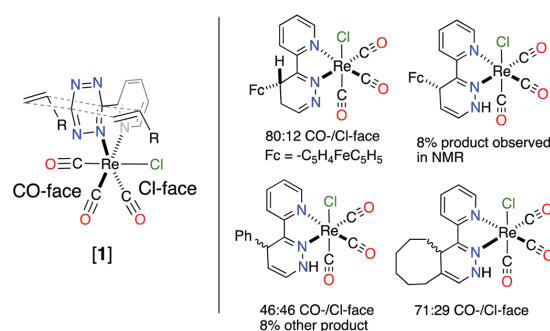


Chart 1 Different facial approach of dienophile (left) and products from the reaction between **[1]** and olefin with observed product ratio from <sup>1</sup>H NMR of reaction mixture (right).

The crystal structure of **[1TCO]** and **[1Ci]** revealed that the 1,3-prototropic isomerization had occurred. The <sup>1</sup>H NMR of the reaction mixture for **[1Ci]** confirmed the 1,4-dhp isomer in a ratio of 46:46 with 8% other products (Fig. S22, ESI<sup>†</sup>). According to DFT analysis the *endo* approach of Ci to **[1]** is nearly isoenergetic at both the faces, however, only the product of the *endo* CO-face addition was found in the crystal state (Fig. 3). Analysis of the reaction mixture from **[1]** + TCO also showed two similar products in a ratio of 71:29, and the 1,4-dhp isomer was assigned based on <sup>1</sup>H NMR analysis, the molecular structure, and DFT calculations (Fig. S25, ESI<sup>†</sup>). These data show that the *endo* approach of dienophiles is favored to occur and only the 1,4-addition and not the 1,5-addition are observed.

We report the increased rate of the iEDDA addition of three dienophiles to the metallotetrazine **[1]**. The combination of the strong *endo* effect and the back-bonding from the tetrazine to the metal is thought to increase the rate of this reaction. Coordination of the rhenium(i) moiety to the tetrazine lowers the  $\Delta S^\ddagger$ , while the nature of the dienophile shows the larger influence on the contribution of  $\Delta H^\ddagger$  to the transition state  $\Delta G^\ddagger$ . The metallotetrazine **[1]** also allows for the facial approach of the dienophile to be prejudiced, albeit the Cl- and CO-face of **[1]** only imparts a small influence. Currently we are exploring this

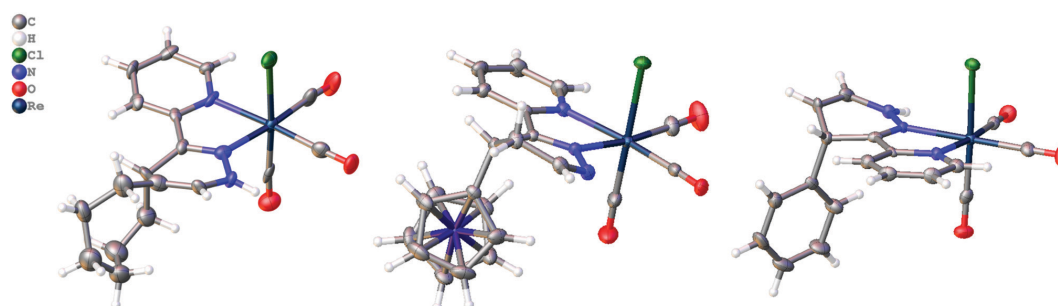


Fig. 3 Molecular structure of **[1TCO]**, **[1Fc]** and **[1Ci]** determined crystallographically, thermal ellipsoids are shown at 50% probability.



View Article Online

## Communication

ChemComm

complex for its biological activity, and for immobilization of the complex onto solid supports to generate new electrocatalysts.

M. Schnierle and this project funded by Deutsche Forschungsgesellschaft SFB1333 C2. Calculations supported by the state of Baden-Württemberg through bwHPC and the German Research Foundation (DFG) through Grant INST 40/467-1 FUGG for access to the Justus cluster. The authors gratefully acknowledge Dr Wolfgang Frey and Dr Ingo Hartenbach for advice and crystallographic measurements.

## Conflicts of interest

There are no conflicts to declare.

## Notes and references

- 1 B. L. Oliveira, Z. Guo and G. J. L. Bernardes, *Chem. Soc. Rev.*, 2017, **46**, 4895–4950.
- 2 G. Linden, L. Zhang, F. Pieck, U. Linne, D. Kosenkov, R. Tonner and O. Vázquez, *Angew. Chem., Int. Ed.*, 2019, **58**, 12868–12873; A. Rondon and F. Degoul, *Bioconjugate Chem.*, 2020, **31**, 159–173; T. Cañeque, S. Müller and R. Rodríguez, *Nat. Rev. Chem.*, 2018, **2**, 202–215; E. Kim and H. Koo, *Chem. Sci.*, 2019, **10**, 7835–7851.
- 3 J. E. Hein and V. V. Fokin, *Chem. Soc. Rev.*, 2010, **39**, 1302–1315; L. Liang and D. Astruc, *Coord. Chem. Rev.*, 2011, **255**, 2933–2945.
- 4 J. E. Moses and A. D. Moorhouse, *Chem. Soc. Rev.*, 2007, **36**, 1249–1262.
- 5 P. Thirumurugan, D. Matosiuk and K. Jozwiak, *Chem. Rev.*, 2013, **113**, 4905–4979.
- 6 W. Chen, D. Wang, C. Dai, D. Hamelberg and B. Wang, *Chem. Commun.*, 2012, **48**, 1736–1738; J. Sauer, D. K. Heldmann, J. Hetzenegger, J. Krauthan, H. Sichert and J. Schuster, *Eur. J. Org. Chem.*, 1998, 2885–2896.
- 7 M. T. Taylor, M. L. Blackman, O. Dmitrenko and J. M. Fox, *J. Am. Chem. Soc.*, 2011, **133**, 9646–9649.
- 8 N. K. Devaraj and R. Weissleder, *Acc. Chem. Res.*, 2011, **44**, 816–827; H. Wu and N. K. Devaraj, *Top. Curr. Chem.*, 2015, **374**, 3; A. Darko, S. Wallace, O. Dmitrenko, M. M. Machovina, R. A. Mehl, J. W. Chin and J. M. Fox, *Chem. Sci.*, 2014, **5**, 3770–3776.
- 9 N. K. Devaraj, R. Weissleder and S. A. Hilderbrand, *Bioconjugate Chem.*, 2008, **19**, 2297–2299; K. Lang, L. Davis, J. Torres-Kolbus, C. Chou, A. Deiters and J. W. Chin, *Nat. Chem.*, 2012, **4**, 298–304.
- 10 W. Kaim, *Coord. Chem. Rev.*, 2002, **230**, 127–139.
- 11 M. Maekawa, T. Miyazaki, K. Sugimoto, T. Okubo, T. Kuroda-Sowa, M. Munakata and S. Kitagawa, *Inorg. Chim. Acta*, 2014, **410**, 46–53.
- 12 M. Glöckle and W. Kaim, *Angew. Chem., Int. Ed.*, 1999, **38**, 3072–3074; S. Kraft, E. Hanuschek, R. Beckhaus, D. Haase and W. Saak, *Chem. – Eur. J.*, 2005, **11**, 969–978.
- 13 T. S.-M. Tang, H.-W. Liu and K. K.-W. Lo, *Chem. Commun.*, 2017, **53**, 3299–3302.
- 14 K. K.-W. Lo, *Acc. Chem. Res.*, 2015, **48**, 2985–2995; E. B. Bauer, A. A. Haase, R. M. Reich, D. C. Crans and F. E. Kühn, *Coord. Chem. Rev.*, 2019, **393**, 79–117; M. S. Capper, H. Packman and M. Rehkämper, *ChemBioChem*, 2020, **21**, 2111–2115.
- 15 K. M. Knopf, B. L. Murphy, S. N. MacMillan, J. M. Baskin, M. P. Barr, E. Boros and J. J. Wilson, *J. Am. Chem. Soc.*, 2017, **139**, 14302–14314.
- 16 L. Suntrup, F. Stein, J. Klein, A. Wiltung, F. G. L. Parlange, C. M. Brown, J. Fiedler, C. P. Berlinguette, I. Siewert and B. Sarkar, *Inorg. Chem.*, 2020, **59**(7), 4215–4227; S. Sung, D. Kumar, M. Gil-Sepulcre and M. Nippe, *J. Am. Chem. Soc.*, 2017, **139**, 13993–13996; B. P. Sullivan, C. M. Bolinger, D. Conrad, W. J. Vining and T. J. Meyer, *J. Chem. Soc., Chem. Commun.*, 1985, 1414–1416, DOI: 10.1039/C39850001414.
- 17 A.-C. Knall and C. Slugovc, *Chem. Soc. Rev.*, 2013, **42**, 5131–5142.
- 18 A.-C. Knall, M. Hollauf and C. Slugovc, *Tetrahedron Lett.*, 2014, **55**, 4763–4766.
- 19 S. Choi, M. L. Personick, J. A. Bogart, D. Ryu, R. M. Redman and E. Laryea-Walker, *Dalton Trans.*, 2011, **40**, 2888–2897.
- 20 I. Martínez-Montero, S. Bruña, A. M. González-Vadillo and I. Cuadrado, *Macromolecules*, 2014, **47**, 1301–1315.
- 21 J. A. Bravo, F. M. Raymo, J. F. Stoddart, A. J. P. White and D. J. Williams, *Eur. J. Inorg. Chem.*, 1998, 2565–2571.





## 7.2 Publication Paper 2.

WILEY-VCH

FULL PAPER

## (Spectro)Electrochemistry of 3-(Pyrid-2-yl)-s-Tetrazine- or 1,2-(dihydro)pyridazine Tricarbonylrhenium(I)chloride

Marc Schnierle,<sup>[a]</sup> Mario Winkler,<sup>[c]</sup> Vasileios Filippou,<sup>[a][b]</sup> Joris van Slageren,<sup>\*[c]</sup> and Mark R. Ringenberg<sup>\*[a]</sup><sup>[a]</sup> Mr. M. Schnierle, Dr. V. Filippou, Dr. M.R. Ringenberg\*Institut für Anorganische Chemie  
Pfaffenwaldring 55, 70569 Stuttgart, Germany  
E-mail: mark.ringenberg@iac.uni-stuttgart.de<sup>[b]</sup> Dr. V. Filippou,  
TTI GmbH TGU Varimol  
Pfaffenwaldring 55, 70569 Stuttgart, Germany<sup>[c]</sup> Mr. M. Winkler, Prof. Dr. J. van Slageren\*  
Institut für Physikalische Chemie  
Pfaffenwaldring 55, 70569 Stuttgart, Germany  
E-mail: slageren@ipc.uni-stuttgart.de

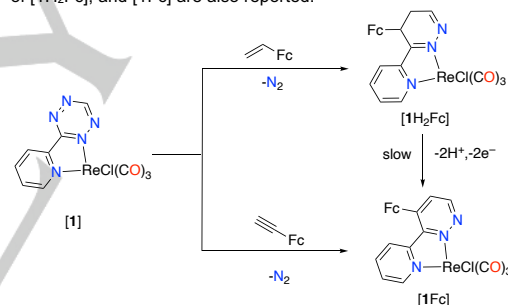
Supporting information for this article is given via a link at the end of the document.

**Abstract:** The electrochemistry and spectroelectrochemistry (SEC) of the three  $[\text{ReCl}(\text{CO})_3(\text{N}^*\text{N})]$ ,  $\text{N}^*\text{N} = 3\text{-(pyrid-2-yl)-1,2,4,5-tetrazine}$  [1],  $3\text{-(pyrid-2-yl)-4-ferrocenyl-4,5-dihydropyridazine}$  [ $1\text{H}_2\text{Fc}$ ], and  $3\text{-(pyrid-2-yl)-4-ferrocenyl-pyridazine}$  [1Fc] are reported. The ligand's conjugation affects the reduction potentials as well as intramolecular charge transfers observed in the UV-vis-NIR spectrum. The spectroscopic observations were further supported by DFT calculations.

## Introduction

Systems designed to retain a coordinated ligand in the inner sphere of the metal atom before, during, and after the chemical reaction offer a convenient approach to obtaining new ligand architectures.<sup>[1-2]</sup> The *fac*-tricarbonylhalorhenium core coordinated by nitrogen donor ligands ( $\text{N}^*\text{N}$ ) has found uses in medicine, photocatalysis, and electrocatalysis.<sup>[3-8]</sup> Changes to the  $\text{N}^*\text{N}$  ligand in  $\text{ReCl}(\text{CO})_3(\text{N}^*\text{N})$  provides a means to better catalytic activity for electrocatalytic  $\text{CO}_2$  reduction.<sup>[9-11]</sup> The heterocyclic 3-(pyrid-2-yl)-1,2,4,5-tetrazine (TzPy) ligand, isoelectronic to *bpy* = 2,2'-bipyridine,<sup>[12-13]</sup> can be modified post ligation by the addition of different dienophiles (olefins). Tetrazines have also found many applications in biorthogonal labeling<sup>[14-20]</sup>, as well as in materials and organic synthesis.<sup>[21-27]</sup> Recently we reported on the synthesis of  $[\text{ReCl}(\text{CO})_3(\text{TzPy})]$  [1] (TzPy = 3-(pyrid-2-yl)-1,2,4,5-tetrazine) and how the coordinated TzPy enhanced the rate of vinylferrocene's (ViFc) [4+2] cycloaddition to form the 4,5-dihydropyridazine moiety from the tetrazine giving complex [ $1\text{H}_2\text{Fc}$ ] (Scheme 1). The bulky ferrocenyl moiety was at the 5-position due to trapping of the kinetic product.<sup>[28]</sup> In a similar report on the addition of ViFc to  $[\text{CyRuCl}(\text{TzPy})]^+$ , Cy =  $\eta^5$ -cymene, we found that dihydropyridazine could be oxidized to the pyridazine state of the ligand,<sup>[29]</sup> where [ $1\text{H}_2\text{Fc}$ ] did not show this apparent reactivity, but did appear to slowly oxidize over the course of several weeks to [1Fc]. The pyridazine could, however, be generated by adding ethynylferrocene (EthFc) to [1] to give [1Fc] (Scheme 1). The reaction produced a single kinetically trapped product with the Fc at the 5-position. Here we investigate the electrochemical

response of [1], [ $1\text{H}_2\text{Fc}$ ], and [1Fc] and how the ligands geometry, especially the strain between the two heterocycles in the ligand, affects the redox properties and spectroscopic response. The three compounds were also investigated using IR, and UV-vis-NIR spectroelectrochemistry (SEC). The  $^{57}\text{Fe}$  Mößbauer spectra of [ $1\text{H}_2\text{Fc}$ ], and [1Fc] are also reported.



Scheme 1. [4+2] addition of ViFc and EthFc to [1].

## Results and Discussion

The addition of ethynylferrocene (EthFc) to [1] produced a single product according to the  $^1\text{H}$  NMR spectra following the reaction *in situ* (Figure S7). Crystals of [1Fc] suitable for X-ray crystallography were obtained from the reaction mixture and the molecular structure is shown in Figure 1. The pyridazine and pyridine are aromatic (Figure 1), however, the Fc placed at the 5-position causes the ligand to distort from coplanar, where the C-C-C torsion angle is  $26(1)^\circ$ , and the nitrogen chelate has a N-C-C-N torsion angle of  $18(1)^\circ$  (Figure 1). Such  $\text{N}^*\text{N}$  donor ligands with groups, especially the large ferrocenyl moiety, at the 5-position may otherwise be difficult to synthesize, and to the best of our knowledge, is the first example of such a ligand.

## FULL PAPER

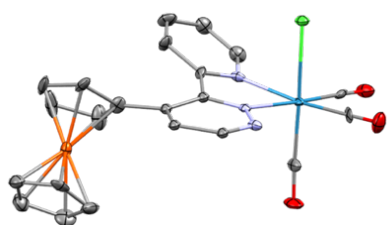


**Figure 1.** Molecular structure of [1Fc] found in the crystal state. Thermal ellipsoids are displayed at 50% probability. H-atoms omitted for clarity. Colors: C (gray), N (light blue), O (red), Cl (lime green), Re (teal), & Fe (orange).

Density functional theory (DFT) was performed starting from the molecular structures of [1], [1H<sub>2</sub>Fc], and [1Fc]. The frontier orbitals for [1] were presented in our previous report,<sup>[28]</sup> but briefly the HOMO was Re localized, while the LUMO was tetrazine based.<sup>[28]</sup> The cyclic voltammogram (CV) of [1], similar to the isostructural [ReCl(CO)<sub>3</sub>(bpy)]<sup>[9]</sup>, showed an irreversible oxidation ( $E_{pa}$ ) and a reversible reduction ( $E_{1/2}$ ) followed by an irreversible wave ( $E_{pc}$ ), see Figure 8 and Table 1 for values. The tetrazine moiety causes a large anodic shift for the reversible reduction relative to [ReCl(CO)<sub>3</sub>(bpy)]<sup>[9]</sup>  $\Delta E = 1.27$  V (122 kJ mol<sup>-1</sup>), due to the increase in electronegativity of the tetrazine moiety.

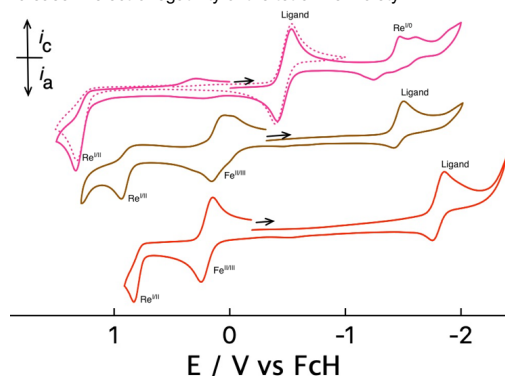


**Figure 2.** Electrochemistry of [1] (top, pink) [1H<sub>2</sub>Fc] (middle, brown), and [1Fc] (bottom, red). 0.1 M n-Bu<sub>4</sub>NPF<sub>6</sub>/CH<sub>2</sub>Cl<sub>2</sub>,  $\nu = 100$  mV s<sup>-1</sup>.

**Table 1.** Summary of Redox Potentials / V<sup>[a]</sup>

	$E_{1/2}$ L <sup>0/-1</sup> (Re <sup>0</sup> )	$E_{1/2}$ Fc <sup>0/+</sup>	$E_{pa}$ Re <sup>III</sup>
[ReCl(CO) <sub>3</sub> (bpy)] <sup>[9]</sup>	-1.73 (-2.11 <sup>[c]</sup> )	–	–
[1]	-0.46 (-1.49 <sup>[c]</sup> )	–	1.35 <sup>[c]</sup>
[1H <sub>2</sub> Fc]	-1.48	0.13	0.90 <sup>[b]</sup>
[1Fc]	-1.80	0.20	0.82 <sup>[c]</sup>

[a] potentials referenced against [Fe(C<sub>6</sub>H<sub>5</sub>)<sub>2</sub>]<sup>0/+</sup>, [b] quasi-reversible [c] irreversible

The cyclic voltammogram (CV) of [1H<sub>2</sub>Fc], and [1Fc] are depicted in Figure 2. The electrochemical response for the ligand-based reduction was cathodically shifted from [1] by >1 V, due to the increased electron density offered by the Fc moiety. Both [1H<sub>2</sub>Fc], and [1Fc] showed a new reversible Fc based oxidation,<sup>[9, 30-32]</sup> where [1Fc] showed a clearly reversible process but [1H<sub>2</sub>Fc] showed two possible processes. It is not evidently clear why multiple oxidation processes were observed but could be attributed to the presences of two isomers of [1H<sub>2</sub>Fc] described in our previous manuscript. The major isomer of [1H<sub>2</sub>Fc] is the one used for further calculations where the Fc moiety was pointed towards the CO-face while the minor product had it pointed towards the Cl-face.<sup>[28]</sup>

The frontier orbitals for [1H<sub>2</sub>Fc], and [1Fc] are depicted in Figure 3. The HOMO for both [1H<sub>2</sub>Fc] and [1Fc] resides at the Fc and differ in energy by 11 kJ mol<sup>-1</sup> (DFT). The difference in energies between the two Fc was confirmed electrochemically where the  $\Delta E = 0.07$  V is an energy difference of 6.75 kJ mol<sup>-1</sup>. The LUMO of [1Fc] was similar to [1H<sub>2</sub>Fc] but the former was 23 kJ mol<sup>-1</sup> higher in energy than the later (Figure 3). The LUMO's  $\Delta E$  was confirmed electrochemically  $\Delta E = 0.31$  V is 30 kJ mol<sup>-1</sup>. The lack of coplanarity found in the two heterocycles in [1Fc] breaks the ligands conjugation, while the aliphatic backbone in [1H<sub>2</sub>Fc] does not affect the conjugation of the C-N-N-C = 0.41°.

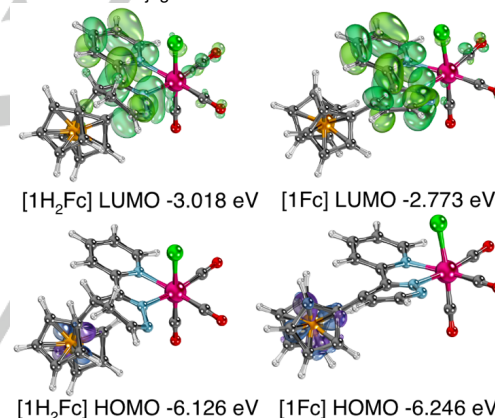


**Figure 3.** Depiction of HOMO (blue/purple), and LUMO (green/lime).

The IR, and UV–vis–NIR SEC spectra for [1], [1H<sub>2</sub>Fc] and [1Fc] were measured to understand how the ligand influences the ReCl(CO)<sub>3</sub>. The IR SEC spectra for the first reduction event for all three compounds showed a bathochromic shift  $\Delta\nu_{CO} \sim 30$  cm<sup>-1</sup> (Table 2), indicating ligand noninnocence because typically a shift of  $\Delta\nu_{CO} \sim 100$  cm<sup>-1</sup> is typical for metal-based redox events.<sup>[4]</sup> The IR SEC spectra are also very similar to the isoelectronic [ReCl(CO)<sub>3</sub>(bpy)], that showed  $\Delta\nu_{CO} = 28$  cm<sup>-1</sup> typical for such bpy noninnocence.<sup>[33]</sup> The change in the ligands architecture between [1H<sub>2</sub>Fc] and [1Fc] results in a minor change in the IR spectrum ( $\Delta\Delta\nu_{CO} = 7$  cm<sup>-1</sup>). The IR SEC for the reversible oxidation processes for [1H<sub>2</sub>Fc]<sup>0/+</sup> and [1Fc]<sup>0/+</sup> showed only small hypsochromic shifts (Table 2,  $\Delta\Delta\nu_{CO} = 2$  cm<sup>-1</sup>). The ferrocenium found in [1Fc]<sup>+</sup> was only slightly better at transmitting this increased charge to the ReCl(CO)<sub>3</sub>, than [1H<sub>2</sub>Fc]<sup>+</sup>. This, however,



## FULL PAPER

was not the case for the electronic communication between the two metals in the UV-vis-NIR SEC.

**Table 2.** Summary of IR SEC<sup>[a]</sup>

Compound	$\nu / \text{cm}^{-1}$	$\nu$ average	$\Delta$
[1]	2032 1948 1921	1967	
[1] <sup>-</sup>	2021 1906 1880	1937	30
[1H <sub>2</sub> Fc]	2023 1924 1900	1949	
[1H <sub>2</sub> Fc] <sup>+</sup>	2025 1927 1902	1951	2
[1H <sub>2</sub> Fc] <sup>-</sup>	2007 1897 1869	1924	23
[1Fc]	2023 1923 1898	1948	
[1Fc] <sup>+</sup>	2026 1927 1903	1952	4
[1Fc] <sup>-</sup>	1999 1893 1862	1918	30

[a] 0.1 M n-Bu<sub>4</sub>NPF<sub>6</sub> / CH<sub>2</sub>Cl<sub>2</sub>

The UV-vis-NIR spectrum of all three compounds was described by time dependence (TD)-DFT. The UV-vis-NIR spectrum of [1] showed a MLCT band at 529 nm (Table 3),<sup>[33]</sup> according to TD-DFT (Figure S17). The spectrum of [1H<sub>2</sub>Fc] showed two bands at 443 nm and 604 nm that were both described as MLCTs (Figure S19), where the former transition was from the Re and the latter was from the Fe, where similar Fe→L have been described elsewhere (Table 3).<sup>[30-32]</sup> The UV-vis-NIR spectrum of [1Fc] was similar but hypsochromically shifted from [1H<sub>2</sub>Fc] due to the increase in the LUMO's energy (Figure S22). Details concerning TD-DFT and electron density difference maps can be found in the supporting information.

The change in redox states was further analyzed by UV-vis-NIR SEC and the data is summarized in Table 3. The spectrum for the cathodic process [1]<sup>0/-1</sup> showed a bathochromic shift in absorption spectrum (Figure 4). The absorption bands were described as a MLCT from the Re to the tetrazine moiety (See ESI for depiction of electron density difference maps, Figure S18). The irreversible processes were not studied by SEC.

**Table 3.** Summary of UV-vis-NIR SEC<sup>[a]</sup>

	$\lambda_{\text{max}} / \text{nm} [10^3 / \text{cm}^{-1}] (\epsilon / \text{M}^{-1} \text{cm}^{-1})$
[1]	221 [45.3] (9808), 277 [36.1] (8659), 529 [18.9] (2835),
[1] <sup>-</sup>	224 [44.6] (10744), 262sh [38.2] (7662), 356 [28.1] (2564),
[1H <sub>2</sub> Fc]	298 [33.5] (5530), 443 [22.6] (2545), 604sh [16.5] (755),
[1H <sub>2</sub> Fc] <sup>+</sup>	256 [39.1] (10130), 290 [34.5] (8280), 460 [21.7] (1550), 630 [15.9] (215)
[1H <sub>2</sub> Fc] <sup>-</sup>	310 [32.3] (4150), 372 [26.9] (3320), 540 [18.5] (1300)
[1Fc]	306 [32.7] (3020), 405 [24.7] (1450), 495sh [20.2] (681)
[1Fc] <sup>+</sup>	265 [37.9] (4860), 298 [33.6] (4780), 419 [23.9] (1500), 653 [15.3] (128)
[1Fc] <sup>-</sup>	206 [32.7] (2800), 390 [25.6] (1450), 495 [20.2] (1010), 830 [12.0] (68), 1431 [6.99] (41)

[a] 0.1 M n-Bu<sub>4</sub>NPF<sub>6</sub> / CH<sub>2</sub>Cl<sub>2</sub>

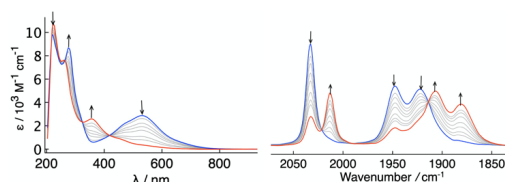


**Figure 4.** UV-vis-NIR and IR SEC of [1]<sup>0/-</sup> in 0.1 M n-Bu<sub>4</sub>NPF<sub>6</sub>/CH<sub>2</sub>Cl<sub>2</sub>. Blue denotes starting spectrum while red denotes final spectrum.

The UV-vis-NIR SEC spectra for [1H<sub>2</sub>Fc]<sup>0/+</sup> showed the two main MLCT feature (Table 3), that were red shifted upon oxidation, and a weak band at 630 nm was appears. This weak band is consistent with ferrocenium.<sup>[34-38]</sup> These features are also described by TD-DFT (Figure S20). The UV-vis-NIR SEC [1H<sub>2</sub>Fc]<sup>0/-1</sup> resulted in the MLCT band at 443 nm to decrease in intensity and the appearance of a new blue shifted band at 372 nm and a weak band at 540 nm to appear. The band at 540 nm was an intraligand (IL)CT from the diazine to the pyridine, while the higher energy bands were both MLCT (Figure S21). The UV-vis-NIR SEC spectrum of [1Fc]<sup>0/+</sup> was similar to [1H<sub>2</sub>Fc]<sup>0/+</sup> and TD-DFT described similar CT bands. The absence of pyridine-pyridazine conjugation resulted in higher energy LUMOs that precluded several CT bands often observed in ferrocene substituted by ligands.<sup>[30-32]</sup> The anodic process generated a stronger response, where the NIR bands were ILCTs. The higher energy bands can be described as MLCT, both Re and Fe contribute to these bands.

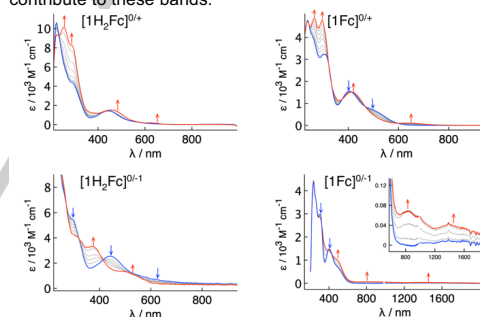


**Figure 5.** UV-vis-NIR SEC in 0.1 M n-Bu<sub>4</sub>NPF<sub>6</sub>/CH<sub>2</sub>Cl<sub>2</sub> for cathodic and anodic processes found in the CVs of [1H<sub>2</sub>Fc] and [1Fc]. blue denotes starting spectrum while red denotes final spectrum.

## FULL PAPER

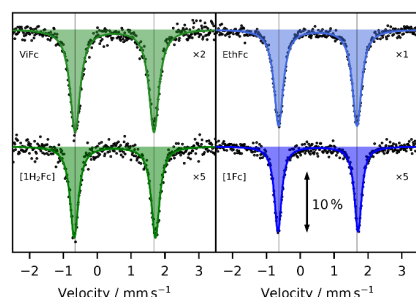


Figure 6. Mössbauer spectra of ViFc, EthFc, [1H<sub>2</sub>Fc], and [1Fc] in the solid state measured at 80 K. For better visibility the data was multiplied with the given factors.

Minor changes were observed in the Mössbauer spectra going from ViFc to EthFc and [1H<sub>2</sub>Fc] to [1Fc] (Figure 6 and Table 4), but the differences are not such that definitive conclusions can be based on them.

**Table 4.** Isomer shifts  $\delta$ , Quadrupole splittings  $\Delta E_Q$  and line widths  $\Gamma$  as were determined from Mössbauer measurements at 80 K in the solid state.

	$\delta / \text{mm s}^{-1}$	$\Delta E_Q / \text{mm s}^{-1}$	$\Gamma / \text{mm s}^{-1}$
ViFc	0.51	2.33	0.36
[1H <sub>2</sub> Fc]	0.52	2.40	0.30
EthFc	0.52	2.32	0.33
[1Fc] <sup>a</sup>	0.527(2)	2.366(3)	0.258(5)

## Conclusion

The addition of dienophiles to the tetrazine in [1] provides straightforward access to new ligands that may otherwise be unavailable due to kinetic trapping. This is the case for the synthesis of [1H<sub>2</sub>Fc] and [1Fc], where both ligands would likely be difficult to access by traditional synthesis due to the ligand strain imparted by the Fc, such as that found in [1Fc]. This approach to accessing strained ligands had a large influence on the electrochemical response of [1], [1H<sub>2</sub>Fc], and [1Fc]. This strain was observed in the difference in the geometry of [1Fc] versus [1H<sub>2</sub>Fc], where despite the aromatic pyridazine moiety in [1Fc], it is nearly 30 kJ mol<sup>-1</sup> higher in energy than [1H<sub>2</sub>Fc] due to the strain of the Fc moiety in the 5-position.

The ligands influence on the electrochemical response was substantial, where the addition of ferrocenyl-dienophiles, ViFc or EthFc, resulted in a nearly 1 V cathodic shift in the ligands reduction from [1]. The IR- and UV-vis-NIR SEC responses for [1], [1H<sub>2</sub>Fc], and [1Fc] was also performed. The data indicated the reversible reduction was ligand based for all three complexes, while [1H<sub>2</sub>Fc] and [1Fc] showed reversible Fc oxidations. [1] is currently under investigation for further functionalization and for generating new electrocatalysts bound to surfaces or materials.

## Experimental Section

Complexes [1] and [1H<sub>2</sub>Fc] were made according to our previous report.<sup>[28]</sup> Crystallographic data can be found on the CCDC entry: 2054871. Ethynylferrocene was purchased from Sigma-Aldrich and used without further purification. Details concerning DFT and measurements can be found in the supporting information. **[1Fc]:** Ethynylferrocene (34.8 mg, 0.166 mmol) and the TzPyRe(CO)<sub>3</sub>Cl (70 mg, 0.151 mmol) were stirred together in dry DCM (20 ml) for 24h at room temperature. The unreacted ethynylferrocene was removed by flash chromatography on silica with *n*-hexanes and [1Fc] was eluted with CH<sub>2</sub>Cl<sub>2</sub>. The red dition was collected and the solvent was removed under reduced pressure to yield a deep red solid. Yield: 30 mg (30 %). <sup>1</sup>H NMR (700 MHz, Dichloromethane -d<sub>2</sub>)  $\delta$  8.97 (d, *J* = 5.3 Hz, 1H), 8.96 – 8.95 (m, 1H), 8.10 (d, *J* = 5.3 Hz, 1H), 7.65 (td, *J* = 8.2, 1.6 Hz, 1H), 7.47 (d, *J* = 8.3 Hz, 1H), 7.38 (ddd, *J* = 7.5, 5.4, 1.2 Hz, 1H), 4.57 – 4.53 (m, 2H), 4.52 (q, *J* = 2.0 Hz, 1H), 4.47 (dt, *J* = 2.4, 1.2 Hz, 2H), 4.16 (s, 5H). Elemental analysis: Calc.: C<sub>22</sub>H<sub>17</sub>ClFeN<sub>3</sub>O<sub>3</sub>Re(CH<sub>2</sub>Cl<sub>2</sub>)<sub>0.25</sub> C, 39.88; H, 2.83; N, 6.27. Found: C: 40.06, H: 2.82, N: 6.81. ESI m/z: [M]<sup>+</sup> 669.9595, calcd 669.9593.

## Acknowledgements

The authors thank Dr. Wolfgang Frey for advice and crystallographic measurements. M.R.R. gratefully acknowledge support by the state of Baden-Württemberg through bwHPC and the German Research Foundation (DFG) through grant no. INST 40/467-1 FUGG for access to the Justus cluster. M.S. and M.W. are funded by the Deutsche Forschungsgemeinschaft SFB1333-C2.

## Additional Information

Dr. Filippou is founder of TGU Varimol which has commercialized the ligand TzPy and complex [1], <https://www.varimol.de>.

**Keywords:** DFT • Ferrocene • Electrochemistry • UV-vis-NIR • Spectroelectrochemistry

- [1] A. Blackman, in *Advances in Heterocyclic Chemistry*, Vol. 58 (Ed.: A. R. Katritzky), Academic Press, **1993**, pp. 123-170.
- [2] D. H. Busch, in *Reactions of Coordinated Ligands*, Vol. 37, American Chemical Society, **1962**, pp. 1-18.
- [3] A. Zarkadoulas, E. Koutsouri, C. Kefalidi, C. A. Mitsopoulou, *Coord. Chem. Rev.* **2015**, 304–305, 55-72.
- [4] T. Scheiring, A. Klein, W. Kaim, *J. Chem. Soc., Perkin Trans. 2* **1997**, 2569-2572.
- [5] E. B. Bauer, A. A. Haase, R. M. Reich, D. C. Crans, F. E. Kühn, *Coord. Chem. Rev.* **2019**, 393, 79-117.
- [6] K. M. Knopf, B. L. Murphy, S. N. MacMillan, J. M. Baskin, M. P. Barr, E. Boros, J. J. Wilson, *J. Am. Chem. Soc.* **2017**, 139, 14302-14314.
- [7] M. Waki, K.-i. Yamanaka, S. Shirai, Y. Maegawa, Y. Goto, Y. Yamada, S. Inagaki, *Chem. Eur. J.* **2018**, 24, 3846-3853.
- [8] N. Akabar, V. Chaturvedi, G. E. Shillito, B. J. Schwehr, K. C. Gordon, G. S. Huff, J. J. Sutton, B. W. Skelton, A. N. Sobolev, S. Stagni, D. J. Nelson, M. Massi, *Dalton Trans.* **2019**, 48, 15613-15624.
- [9] J. K. Nganga, C. R. Samanamu, J. M. Tanski, C. Pacheco, C. Saucedo, V. S. Batista, K. A. Grice, M. Z. Ertem, A. M. Angeles-Boza, *Inorg. Chem.* **2017**, 56, 3214-3226.
- [10] E. E. Benson, C. P. Kubiak, A. J. Sathrum, J. M. Smieja, *Chem. Soc. Rev.* **2009**, 38, 89-99.



WILEY-VCH

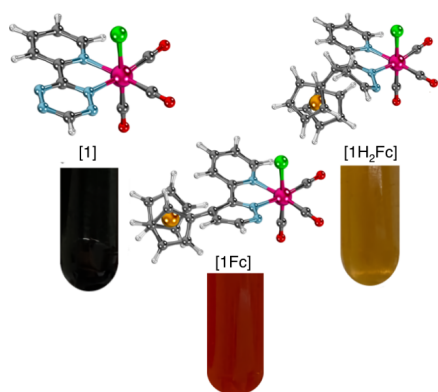
## FULL PAPER

- [11] J. M. Smieja, C. P. Kubiak, *Inorg. Chem.* **2010**, *49*, 9283-9289.
- [12] M. Schwach, H.-D. Hausen, W. Kaim, *Inorg. Chem.* **1999**, *38*, 2242-2243.
- [13] N. A. Maciulis, R. N. Schauggaard, Y. Losovyj, C.-H. Chen, M. Pink, K. G. Caulton, *Inorg. Chem.* **2018**, *57*, 12671-12682.
- [14] N. K. Devaraj, R. Weissleder, S. A. Hilderbrand, *Bioconjugate Chem.* **2008**, *19*, 2297-2299.
- [15] A.-C. Knall, C. Slugovc, *Chem. Soc. Rev.* **2013**, *42*, 5131-5142.
- [16] F. Ehret, H. Wu, S. C. Alexander, N. K. Devaraj, *J. Am. Chem. Soc.* **2015**, *137*, 8876-8879.
- [17] B. L. Oliveira, Z. Guo, G. J. L. Bernardes, *Chem. Soc. Rev.* **2017**, *46*, 4895-4950.
- [18] J. C. T. Carlson, H. Mikula, R. Weissleder, *J. Am. Chem. Soc.* **2018**, *140*, 3603-3612.
- [19] G. Linden, L. Zhang, F. Pieck, U. Linne, D. Kosenkov, R. Tonner, O. Vázquez, *Angew. Chem. Int. Ed.* **2019**, *58*, 12868-12873.
- [20] W. Mao, W. Shi, J. Li, D. Su, X. Wang, L. Zhang, L. Pan, X. Wu, H. Wu, *Angew. Chem. Int. Ed.* **2019**, *58*, 1106-1109.
- [21] J. W. Wijnen, S. Zavarise, J. B. F. N. Engberts, M. Charton, *J. Org. Chem.* **1996**, *61*, 2001-2005.
- [22] J. Sauer, D. K. Heldmann, *Tetrahedron* **1998**, *54*, 4297-4312.
- [23] G. Clavier, P. Audebert, *Chem. Rev.* **2010**, *110*, 3299-3314.
- [24] T. W. Myers, D. E. Chavez, S. K. Hanson, R. J. Scharff, B. L. Scott, J. M. Veauthier, R. Wu, *Inorg. Chem.* **2015**, *54*, 8077-8086.
- [25] S. D. Schnell, L. V. Hoff, A. Panchagnula, M. H. H. Wurzenberger, T. M. Klapötke, S. Sieber, A. Linden, K. Gademann, *Chem. Sci.* **2020**, *11*, 3042-3047.
- [26] S. D. Schnell, J. A. González, J. Sklyaruk, A. Linden, K. Gademann, *J. Org. Chem.* **2021**, *86*, 12008-12023.
- [27] S. D. Schnell, M. Schilling, J. Sklyaruk, A. Linden, S. Lubner, K. Gademann, *Org. Lett.* **2021**, *23*, 2426-2430.
- [28] M. Schnierle, S. Blicke, V. Filippou, M. R. Ringenberg, *Chem. Commun.* **2020**, *56*, 12033-12036.
- [29] M. Schnierle, M. Leimkühler, M. R. Ringenberg, *Inorg. Chem.* **2021**, *60*, 6367-6374.
- [30] S. Ø. Scottwell, K. J. Shaffer, C. J. McAdam, J. D. Crowley, *RSC Adv.* **2014**, *4*, 35726-35734.
- [31] J. E. Barnsley, J. A. Findlay, G. E. Shillito, W. S. Pelet, S. Ø. Scottwell, S. M. McIntyre, E. J. Tay, K. C. Gordon, J. D. Crowley, *Dalton Trans.* **2019**, *48*, 15713-15722.
- [32] J. A. Findlay, C. J. McAdam, J. J. Sutton, D. Preston, K. C. Gordon, J. D. Crowley, *Inorg. Chem.* **2018**, *57*, 3602-3614.
- [33] F. P. A. Johnson, M. W. George, F. Hartl, J. J. Turner, *Organometallics* **1996**, *15*, 3374-3387.
- [34] R. Prins, *J. Chem. Soc. D* **1970**, 280b-281.
- [35] T. Sixt, J. Fiedler, W. Kaim, *Inorg. Chem. Commun.* **2000**, *3*, 80-82.
- [36] K. Kowalski, M. Linseis, R. F. Winter, M. Zabel, S. Zálaiš, H. Kelm, H.-J. Krüger, B. Sarkar, W. Kaim, *Organometallics* **2009**, *28*, 4196-4209.
- [37] S. Hartmann, Rainer F. Winter, Birgit M. Brunner, B. Sarkar, A. Knödler, I. Hartenbach, *Eur. J. Inorg. Chem.* **2003**, *2003*, 876-891.
- [38] Y. Pan, M. Schnierle, D. Auweiler, M. R. Ringenberg, *Organometallics* **2021**, *40*, 760-765.

WILEY-VCH

FULL PAPER

## Entry for the Table of Contents



Tetrazine ligand modification through [4+2] cycloaddition of ferrocenyl olefins, color arises from dramatic change in the ligands LUMO energy.

Institute and/or researcher Twitter usernames: @varimolTGU, @JvanSlageren, @ringenber




## 7.3 Publication Paper 3.

## Inorganic Chemistry

pubs.acs.org/IC

Article

[( $\eta^6$ -*p*-Cymene)[3-(pyrid-2-yl)-1,2,4,5-tetrazine]chlororuthenium(II)]<sup>+</sup>,  
Redox Noninnocence and Dienophile Addition to Coordinated  
Tetrazine

Marc Schnierle,<sup>‡</sup> Marie Leimkühler,<sup>‡</sup> and Mark R. Ringenberg\*
 Cite This: *Inorg. Chem.* 2021, 60, 6367–6374

 Read Online

ACCESS |

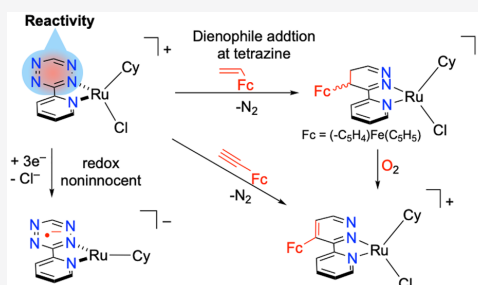
Metrics &amp; More

Article Recommendations

Supporting Information

**ABSTRACT:** The bidentate ligand 3-(pyrid-2-yl)-1,2,4,5-tetrazine (TzPy) coordinated in the complex [CyRuCl(TzPy)]PF<sub>6</sub> ([1]<sup>+</sup>; Cy =  $\eta^6$ -*p*-cymene) shows noninnocent behavior and can be modified through the addition of dienophiles, vinylferrocene (ViFc) or ethynylferrocene (EthFc). The kinetics and transition-state thermodynamic analysis of the reaction of [1]<sup>+</sup> + ViFc found  $\Delta G^\ddagger(298\text{ K}) = 67\text{ kJ mol}^{-1}$ , while that of [1]<sup>+</sup> + EthFc was  $\Delta G^\ddagger(298\text{ K}) = 83\text{ kJ mol}^{-1}$ . The room temperature second-order rate of [1]<sup>+</sup> + ViFc,  $k_2 = 1.51(4) \times 10^{-2}\text{ M}^{-1}\text{ s}^{-1}$ , was 3 orders of magnitude faster than that of EthFc + TzPy,  $k_2 = 1.05(15) \times 10^{-4}\text{ M}^{-1}\text{ s}^{-1}$ . The [1H<sub>2</sub>Fc]<sup>+</sup> complex was converted to [1Fc]<sup>+</sup> by oxidation with oxygen and 3,5-di-*tert*-butyl-*o*-quinone, and the molecular structure of [1Fc]<sup>+</sup> was determined by single-crystal X-ray diffraction. The title complex

[1]<sup>+</sup> showed a quasi-reversible reduction in the cyclic voltammogram, and the electrochemical reduction mechanism was determined by UV–vis spectroelectrochemistry (SEC) experiments, as well as supported by density functional theory (DFT) calculations. The dihydropyridazine [1H<sub>2</sub>Fc]<sup>+</sup> and pyridazine [1Fc]<sup>+</sup> states of the ligand showed ligand noninnocence similar to that of the parent tetrazine but at a cathodically shifted potential. The dihydropyridazine [1H<sub>2</sub>Fc]<sup>+</sup> showed a mixture of several products; however, upon oxidation, only a single product, [1Fc]<sup>+</sup>, was formed from the *endo* addition of the dienophile to [1]<sup>+</sup>. The electrochemical mechanism of [1Fc]<sup>+</sup> was also studied by cyclic voltammetry and UV–vis SEC experiments, as well as supported by DFT calculations.



## INTRODUCTION

Ruthenium half-sandwich complexes coordinated to N-donor ligands, such as 2,2'-bipyridine (bipy), have found uses as precatalysts for several transformations, including hydride transfer reactions or electrocatalysts for CO<sub>2</sub> reduction.<sup>1,2</sup> The substituents on the noninnocent N-donor ligand can be used to tune the reduction potential because they change the energy of the ligand's lowest unoccupied molecular orbital (LUMO).<sup>3–6</sup> The heterocyclic 3-(pyrid-2-yl)-1,2,4,5-tetrazine (TzPy) ligand, isoelectronic to bipy,<sup>7,8</sup> can be modified after coordination by the addition of different dienophiles (Scheme 1).<sup>9,10</sup>

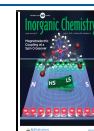
The inverse electron demand [4 + 2] pericyclic addition (Diels–Alder) between 1,2,4,5-tetrazines and electron-rich dienophiles provides a convenient method for generating new C–C bonds and heterocycles, and this technology has found applications in biological labeling.<sup>11–18</sup> Recently, we<sup>10</sup> and others<sup>19</sup> reported that tetrazine metalation increases the rate as well as the selectivity of the dienophile addition compared to the nonmetalated tetrazine.

The selectivity and rate of dienophile addition to octahedrally coordinated tetrazines have been discussed;<sup>10,19</sup>

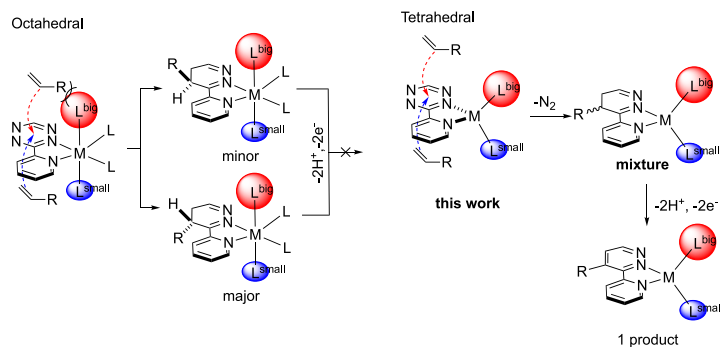
however, the addition of dienophiles to a three-legged-piano-stool compound has not been explored (Scheme 1). Herein we describe how coordinated TzPy ligand modification affects the redox chemistry of [(*p*-cymene)[3-(pyridin-2-yl)-1,2,4,5-tetrazine]chlororuthenium(II)]<sup>+</sup> ([1]<sup>+</sup>), relative to the pyridazine [(*p*-cymene)[3-(pyridin-2-yl)-4-ferrocenyl-1,2-pyridazine]chlororuthenium(II)]<sup>+</sup> ([1Fc]<sup>+</sup>). The synthesis of the pyridazine [1Fc]<sup>+</sup> is also discussed, in which it can be made directly by the addition of ethynylferrocene (EthFc) to [1]<sup>+</sup> or by adding vinylferrocene (ViFc) to [1]<sup>+</sup>, followed by chemical oxidation. Such a post addition oxidation is often performed on organic dihydropyridazines;<sup>20</sup> however, in our previous report on rhenium, rearomatization of the dihydropyridazine was not possible (Scheme 1).<sup>10</sup> A kinetic analysis of the

Received: January 11, 2021

Published: April 15, 2021



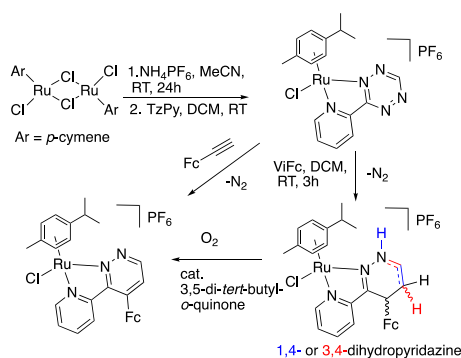
Scheme 1. Dienophile Addition to Octahedral versus Tetrahedral Metallotetrazine and Oxidation of Dihydropyridazine



respective addition of EthFc and ViFc to  $[1]^+$  was also performed.

## RESULTS AND DISCUSSION

**Synthesis.** The synthesis of  $[\text{CyRuCl}(\text{TzPy})]\text{PF}_6$  ( $[1]^+$ ; Cy = *p*-cymene) is shown in Scheme 2 and was performed by first

Scheme 2. Synthesis and Reactions of  $[1]^+$  + ViFc or EthFc

generating the intermediate  $[\text{CyRu}(\text{NCMe})_2\text{Cl}]\text{PF}_6$  from  $[\text{CyRuCl}_2]_2$  in acetonitrile (MeCN) with  $\text{NH}_4\text{PF}_6$ . Ligation of the TzPy ligand occurs through displacement of the MeCN ligands in  $\text{CH}_2\text{Cl}_2$ , as noted by a change in the solution color from yellow to dark brown. Any excess TzPy ligand can be recovered by extraction with diethyl ether ( $\text{Et}_2\text{O}$ ), as noted by its intense pink color in solution. The  $\text{PF}_6^-$  anion was exchanged by dissolving equimolar  $\text{Na}[\text{B}(\text{Ar}^F)_4]$  [ $\text{B}(\text{Ar}^F)_4^-$  = tetrakis[3,5-bis(trifluoromethyl)phenyl]borate] with  $[1]\text{PF}_6$  in  $\text{CH}_2\text{Cl}_2$ , followed by the precipitation of  $\text{NaPF}_6$  with  $\text{Et}_2\text{O}$ , concurrent with extraction of  $[1]\text{B}(\text{Ar}^F)_4$ . Crystals suitable for X-ray diffraction could only be obtained as the  $[1]\text{B}(\text{Ar}^F)_4$  salt; however, unless otherwise stated, the  $\text{PF}_6^-$  counterion was used throughout this work.

The molecular structure of  $[1]\text{B}(\text{Ar}^F)_4$  is shown in Figure 1, and it shows the expected three-legged-piano-stool geometry. The addition of ViFc to a solution of  $[1]^+$  in  $\text{CH}_2\text{Cl}_2$  showed a complicated mixture according to the  $^1\text{H}$  NMR spectrum. This is due to the formation of several dihydropyridazine products (Figures 2A and S38 and S39). These products are, as will be shown below, due to the *endo* addition of ViFc to  $[1]^+$ , where

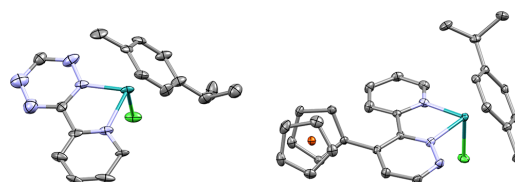


Figure 1. Molecular structures of  $[1]\text{B}(\text{Ar}^F)_4$  and  $[1\text{Fc}]\text{PF}_6$  determined by X-ray diffraction. Counteranion and H atoms removed for clarity, C (gray), N (blue), Ru (teal), Fe (orange), and Cl (green)

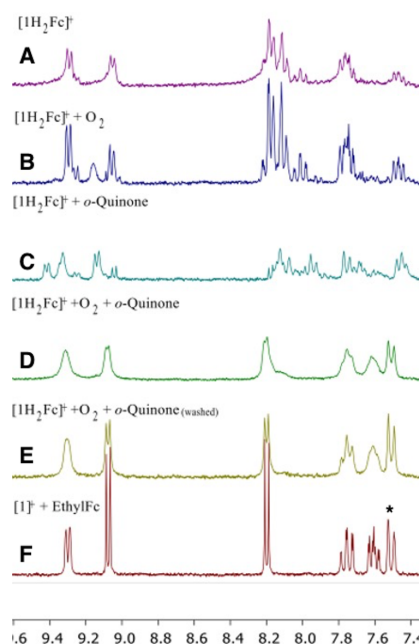


Figure 2.  $^1\text{H}$  NMR spectra for the oxidation of  $[1\text{H}_2\text{Fc}]^+$  to  $[1\text{Fc}]^+$  in the aromatic region. From top to bottom,  $[1\text{H}_2\text{Fc}]^+$  (A, purple),  $[1\text{H}_2\text{Fc}]^+ + \text{O}_2$  (B, blue),  $[1\text{H}_2\text{Fc}]^+ + o\text{-quinone}$  (C, teal),  $[1\text{H}_2\text{Fc}]^+ + o\text{-quinone} + \text{O}_2$  (D, green), isolated  $[1\text{H}_2\text{Fc}]^+$  (E, yellow), and isolated product from  $[1]^+ + \text{EthylFc}$  (F, red).

the products are due to the ViFc approach from the Cy or Cl face of  $[1]^+$  (Scheme 2), as well as the products from a 1,3-prototropic shift of 4,5-dihydropyridazine to 1,4-dihydropyridazine (Scheme 1).

The individual products of the reaction of  $[1]^+$  + ViFc could not be resolved. Crystals were, however, obtained from the slow evaporation (>48 h) of the reaction mixture  $[1]^+$  + ViFc in  $\text{CH}_2\text{Cl}_2$ . Instead of dihydropyridazine, the ligand had oxidized to 3-(pyridin-2-yl)-4-ferrocenylpyridazine to form  $[1\text{Fc}]^+$  (Figure 1). This oxidation process was slow, which was confirmed by the  $^1\text{H}$  NMR spectrum of the freshly prepared  $[1\text{H}_2\text{Fc}]^+$  that showed minimal amounts of  $[1\text{Fc}]^+$ . It is not without reason that the ruthenium complex could autocatalytically oxidize the dihydropyridazine to pyridazine,<sup>21,22</sup> however, it is more likely that atmospheric  $\text{O}_2$  acted as the oxidant, as will be shown below.

**Dihydropyridazine Oxidation.** In order to test if  $\text{O}_2$  was acting as the oxidant, the product mixture of freshly prepared  $[1\text{H}_2\text{Fc}]^+$  (Figure 2A) was saturated with  $\text{O}_2$ . The  $^1\text{H}$  NMR spectrum of  $[1\text{H}_2\text{Fc}]^+$  +  $\text{O}_2$  (Figure 2B) showed a minor change, primarily a new signal at 9.2 ppm and no signals for  $[1\text{Fc}]^+$  were observed over the course of several hours. A solution of  $[1\text{H}_2\text{Fc}]^+$  was treated with 3,5-di-*tert*-butyl-quinone (dtq), and a new signal formed around 9.4 ppm (Figure 2C); however, no further changes in the spectrum were observed after 24 h. The reaction between  $[1\text{H}_2\text{Fc}]^+$  and  $\text{O}_2$ , with a catalytic amount of dtq, generated the spectrum shown in Figure 2D after approximately 3 h of reaction time. The broad line shape found in the spectrum (Figure 2D) was attributed to the presence of a residual paramagnetic product; however, this was removed by titration with  $\text{Et}_2\text{O}$ , and the isolated product  $[1\text{Fc}]^+$  is shown in Figure 2E. The spectrum for  $[1\text{Fc}]^+$  from the reaction of  $[1]^+$  + EthFc (Figure 2F) confirms the spectrum of the oxidation product shown in Figure 2E. The oxidation of  $[1\text{H}_2\text{Fc}]^+$  to both  $[1\text{Fc}]^+$  and the isolated  $[1\text{Fc}]^+$  (Scheme 3) indicated that *only* the 5-ferrocenyl-substituted product was formed, consistent with the *endo* addition of dienophiles to  $[1]^+$ . These data are also

supported by our previous observation that tetrazine metal-ligation results in an enhancement of the *endo* effect.

**Kinetics of Dienophile Addition.** The addition rates of ViFc and EthFc to  $[1]^+$  were determined by following the reaction by time-resolved UV-vis or  $^1\text{H}$  NMR spectroscopy, respectively. The room temperature rate for the reaction between EthFc and TzPy was  $k_2 = 6.35 \times 10^{-5} \text{ M}^{-1} \text{ s}^{-1}$ , and because of the limited temperature range of  $\text{CD}_2\text{Cl}_2$ , an Eyring analysis was deemed impractically slow at lower temperatures; for comparison, the room temperature reaction between  $[1]^+$  and EthFc ( $k_2 = 1.40 \times 10^{-2} \text{ M}^{-1} \text{ s}^{-1}$ ) was nearly 3 orders of magnitude faster than the free ligand reaction.

Eyring analysis for the reaction of  $[1]^+$  + ViFc showed  $\Delta G^\ddagger(298 \text{ K}) = 67 \text{ kJ mol}^{-1}$ ; for comparison, the addition of ViFc to the rhenium complex  $[\text{ReCl}(\text{CO})_3(\text{TzPy})]$  was  $\Delta G^\ddagger(298 \text{ K}) = 68 \text{ kJ mol}^{-1}$ , while for the free ligand TzPy + ViFc,  $\Delta G^\ddagger(298 \text{ K}) = 84 \text{ kJ mol}^{-1}$ .<sup>10</sup> The lack of selectivity and similar rate of ViFc addition to  $[1]^+$  are somewhat unexpected because of the increased valency of  $\text{Ru}^{\text{II}}$  versus  $\text{Re}^{\text{I}}$  and the larger cymene ligand versus CO ligands in our previous report.<sup>10</sup> The geometry around the pyridyl moiety was expected to influence the selectivity of the dienophiles *endo* approach to the tetrazine moiety. Only minor structural differences around the TzPy ligand can be found between  $[1]^+$  and  $[\text{ReCl}(\text{CO})_3(\text{TzPy})]$ ; the distance between the C–H on the cymene and the pyridyl centroid is 4.370 Å, while  $\text{C}_{\text{CO}}\text{-centroid}_{\text{py}}$  is 4.272 Å. The  $\text{Cl}\text{-centroid}_{\text{py}}$  distance for  $[1]^+$  is 3.959 Å, which is shorter than the  $\text{Cl}\text{-centroid}_{\text{py}}$  distance of 4.101 Å for  $[\text{ReCl}(\text{CO})_3(\text{TzPy})]$ .

The valency and increased charge on  $[1]^+$  were expected to increase the addition rate because of increased tetrazine back-bonding; however, any charge effect appears to be compensated for by the electron-rich cymene ligand compared to the  $\pi$ -acceptor CO ligands in  $[\text{ReCl}(\text{CO})_3(\text{TzPy})]$  (Figure 3). Complex  $[1]^+$  and  $[\text{ReCl}(\text{CO})_3(\text{TzPy})]$  both show similar partial charges on the tetrazines C(3), while the back-bonding to N(4) is larger in  $[\text{ReCl}(\text{CO})_3(\text{TzPy})]$  with a symmetry match between M–CO and tetrazine (Table 1 and Figure 3). Several factors appear important to controlling the dienophiles

**Scheme 3.** Proposed *o*-Quinone-Catalyzed Oxidation of Dihydropyridazine with  $\text{O}_2$

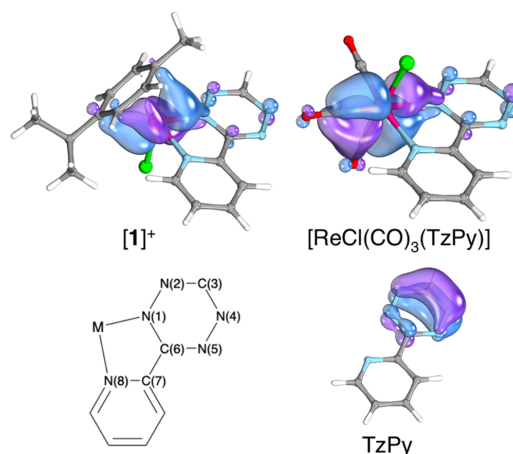
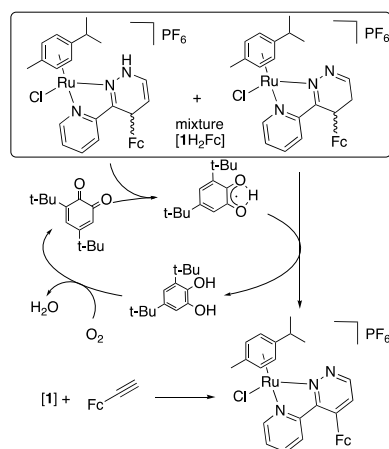


**Figure 3.** Intrinsic bonding orbitals (IBOs) for M-Tetrazine backbonding in  $[1]^+$ ,  $[\text{ReCl}(\text{CO})_3(\text{TzPy})]$  and TzPy.

Table 1. Partial Charge on Selected Atoms<sup>a</sup>

atom	[1] <sup>+</sup>	[Re] <sup>10</sup>	TzPy <sup>10</sup>
M	0.797	0.818	n/a
N1	-0.088	-0.118	-0.143
N2	-0.142	-0.143	-0.148
C3	0.103	0.108	0.090
N4	-0.112	-0.146	-0.149
N5	-0.111	-0.131	-0.155
C6	0.218	0.226	0.225
C7	0.114	0.114	0.109
N8	-0.214	-0.245	-0.300

<sup>a</sup>Partial charges determined from IBOView.<sup>23,24</sup>

addition rate and selectivity to metallotetrazines; however, it is clear that the ancillary ligands on the metal that also contribute in the reactivity.

Eyring analysis for the reaction of [1]<sup>+</sup> + EthFc found  $\Delta G^\ddagger(298\text{ K}) = 82\text{ kJ mol}^{-1}$ . Important values, as well as the previously reported values for the reaction between [ReCl(CO)<sub>3</sub>(TzPy)] and ViFc,<sup>10</sup> are listed in Table 2.  $\Delta H^\ddagger = 17\text{ kJ}$

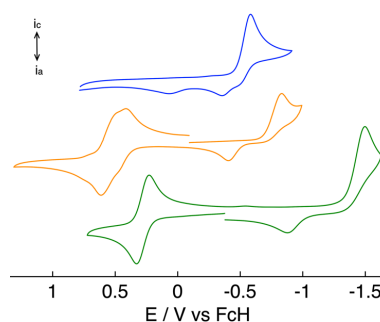
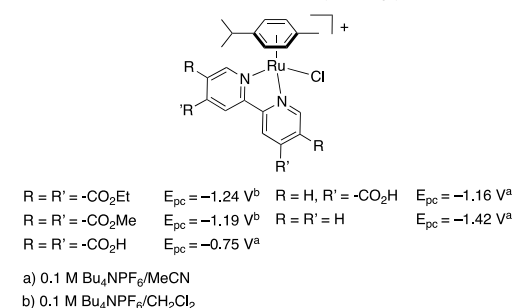
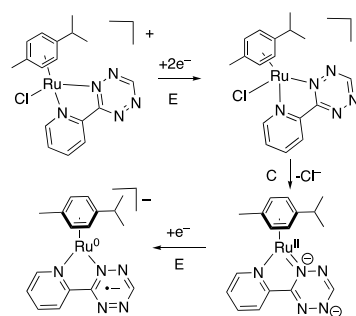
Table 2. Transition-State Thermodynamic Values Determined from an Eyring Plot

	reaction			
	[1] <sup>+</sup> + ViFc	[1] <sup>+</sup> + EthFc	[Re] <sup>+</sup> + ViFc <sup>10</sup>	TzPy + ViFc <sup>10</sup>
$\Delta H^\ddagger/\text{kJ mol}^{-1}$	17	46	23	27
$\Delta S^\ddagger/\text{J mol}^{-1}\text{K}^{-1}$	-170	-122	-150	-192
$\Delta G^\ddagger(298\text{ K})/\text{kJ mol}^{-1}$	67	82	68	84

$\text{mol}^{-1}$  for the addition of ViFc is 6 kJ mol<sup>-1</sup> lower for [1]<sup>+</sup> versus [ReCl(CO)<sub>3</sub>(TzPy)], while  $\Delta S^\ddagger = -170\text{ J mol}^{-1}\text{K}^{-1}$  is 20 J mol<sup>-1</sup> K<sup>-1</sup> lower for [1]<sup>+</sup>. It is surprising, but likely purely coincidental, that the difference in  $\Delta H^\ddagger$  and  $\Delta S^\ddagger$  between these two reactions results in very close  $\Delta G^\ddagger(298)$  values.

$\Delta H^\ddagger = 46\text{ kJ mol}^{-1}$  for the addition of EthFc to [1]<sup>+</sup> was 2.7 times that of ViFc to [1]<sup>+</sup> (Table 2), but  $\Delta S^\ddagger = -122\text{ J mol}^{-1}\text{K}^{-1}$  was ~50 J mol<sup>-1</sup> K<sup>-1</sup> lower because of the restricted rotational freedom of the ethynyl versus vinyl group. Several factors may account for the increased dienophile addition rate, such as coordination restricts the tetrazine, or inductive effects where the electron density can be pushed/pulled between the ligand and metal center through back-bonding. It is not evidently clear which factors, or a combination of these factors, results in the increased reaction rates.

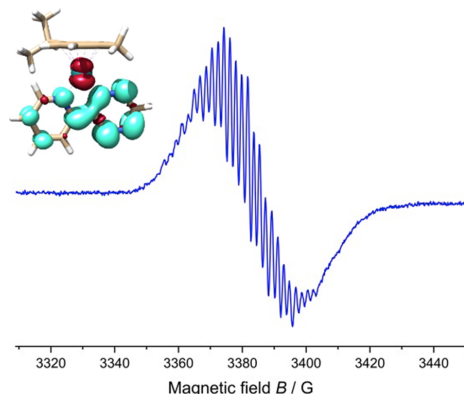
**Electrochemistry.** The products from the respective dienophiles' addition to [1]<sup>+</sup> were studied by electrochemistry to understand the impact that this modification had on the redox chemistry of the ligand (Chart 1). The cyclic voltammograms of the three complexes [1]<sup>+</sup>, [1H<sub>2</sub>Fc]<sup>+</sup>, and [1Fc]<sup>+</sup> are shown in Figure 4, and they were all recorded in 0.1 M *n*-Bu<sub>4</sub>NPF<sub>6</sub>/CH<sub>2</sub>Cl<sub>2</sub>. The cyclic voltammetry (CV) of [1]<sup>+</sup> shows a quasi-reversible reduction event at  $E_{pc} = -0.58\text{ V}$  versus [Fe(C<sub>5</sub>H<sub>5</sub>)<sub>2</sub>]<sup>+0</sup> (the internal standard for all potentials reported herein unless otherwise specified) followed by two small anodic events appearing at  $E_{pa} = -0.36$  and 0.01 V (Figure 4) process. The cathodic process for [1]<sup>+</sup> becomes more reversible when the electrolyte was switched to *n*-Bu<sub>4</sub>NCl (Figure S1), consistent with Cl–ligand dissociation (Scheme 4).

Chart 1. Reduction Potentials of [CyRu(bipy)]<sup>+</sup>Figure 4. CV curves of [1]<sup>+</sup> (blue), [1H<sub>2</sub>Fc]<sup>+</sup> (orange), and [1Fc]<sup>+</sup> (green) in 0.1 M *n*-Bu<sub>4</sub>NPF<sub>6</sub>/CH<sub>2</sub>Cl<sub>2</sub> at 100 mV s<sup>-1</sup>.Scheme 4. Proposed Electrochemical Mechanism of [1]<sup>+</sup>

The cathodic behavior of [CyRuCl(bipy)]<sup>+</sup> and its derivatives was previously reported (Chart 1).<sup>3,4</sup> The electrochemical mechanism was described as a 2e<sup>-</sup> reduction followed by chloride dissociation (EC mechanism) and a third electron transferred; this mechanism was confirmed here by performing Levich analysis using a rotating disk electrode.<sup>25</sup> Levich analysis found that 2.21e<sup>-</sup> were transferred when *n*-Bu<sub>4</sub>NCl was added to the cell (Figures S12–S14). In the absence of excess Cl<sup>-</sup>, the neutral species [CyRu(TzPy)] can then be further reduced by a third electron (E-type mechanism) to generate [CyRu(TzPy)<sup>•-</sup>]. Levich analysis of [1]<sup>+</sup> in *n*-Bu<sub>4</sub>NPF<sub>6</sub> (Figures S9–S11) found that 3.47e<sup>-</sup> were transferred, confirming this mechanism.<sup>25</sup> The ligand-based radical was also observed by electron paramagnetic resonance (EPR) spectroelectrochemistry (SEC) of [1]<sup>+</sup> under reducing



conditions, where the spectrum showed an organic radical ( $g = 2.00$ ; Figure 5). This mechanism was finally supported by DFT calculations (see below).



**Figure 5.** Spin density of  $[1]^\bullet$  spin up shown in green and spin down shown in red. EPR SEC spectrum in the X band of  $[1]^\bullet$  under reducing potential in  $n\text{-Bu}_4\text{NPF}_6/\text{CH}_2\text{Cl}_2$ .

The CV of  $[\text{1H}_2\text{Fc}]^+$  showed a reduction event at  $E_{\text{pc}} = -0.83$  V with an anodically shifted return wave at  $E_{\text{pa}} = -0.411$  V, while  $[\text{1Fc}]^+$  showed  $E_{\text{pc}} = -1.50$  V with the anodically shifted return wave at  $E_{\text{pa}} = -0.88$  V. This wave did not become reversible even in 0.1 M  $n\text{-Bu}_4\text{NCl}/\text{CH}_2\text{Cl}_2$  (Figure S8). The large differences in the reduction potential  $\Delta E_{\text{pc}} = 0.43$  V between  $[1]^\bullet$  and  $[\text{1H}_2\text{Fc}]^+$  or  $\Delta E_{\text{pc}} = 1.1$  V between  $[1]^\bullet$  and  $[\text{1Fc}]^+$  are consistent with the increased electron density offered to the diazo-ligand, and this is reflected by an increase in the energy of the ligand LUMO energies (Figures S36–S39). The LUMOs of the four likely isomers of  $[\text{1H}_2\text{Fc}]^+$  are delocalized over the pyridyl and the diazodiimine  $\text{C}=\text{N}$  bond of the dihydropyridazine moiety (Figures S38 and S39). The CV curves of both  $[\text{1H}_2\text{Fc}]^+$  and  $[\text{1Fc}]^+$  showed new oxidation waves at  $E_{1/2} = 0.5$  and 0.27 V, respectively. The anodic event for  $[\text{1H}_2\text{Fc}]^+$  appears as two possible waves, which could be a result of the multiple isomers; however, this phenomenon could not be studied because the multiple products formed in the reaction could not be isolated (Scheme 2). Redox-induced C–H activation and hydrogen release from the ligands have been reported for  $[\text{CyRu}(\eta^2\text{-S}=\text{PPh}_2)_2\text{CH}_2]^+$ , which formed  $[\text{CyRu}(\eta^3\text{-S}=\text{PPh}_2)_2\text{CH}]^+ + \text{H}_2$  upon reduction.<sup>5</sup>

**Spectroelectrochemistry.** SEC was used to help assign the redox processes observed in the CV curves of  $[1]^\bullet$ ,  $[\text{1H}_2\text{Fc}]^+$ , and  $[\text{1Fc}]^+$ . The UV–vis SEC spectrum for the process  $[1]^{+/0}$  showed only a broad featureless absorption at  $\lambda_{\text{max}} = 370$  nm (Figure S33), and the ECE mechanism makes it difficult to study it by means of UV–vis SEC. The EPR SEC spectrum of  $[1]^\bullet$  under reducing conditions did, however, provide some insight into the electron structure of the reduced species (Figure 5). The  $g$  value of 2.002 along with the narrow line width and fine structure are consistent with an organic radical.<sup>4</sup> Attempts to simulate the spectrum were not possible because of the multiple hyperfine interactions and the low resolution of the spectrum at the low/high magnetic fields. The open-shell DFT calculations found that the ligand supported the radical in which the spin was located over both the ligand and Ru. This spin-density analysis is consistent with the observed EPR spectrum shown in Figure 5, and further discussion on the DFT calculations is found below.

The UV–vis SEC of  $[\text{1H}_2\text{Fc}]^+$  was complicated because of the likely C–H activation of the dihydropyridazine moiety.<sup>5</sup> The UV–vis SEC spectra of both  $[\text{1H}_2\text{Fc}]^{+/2+}$  and  $[\text{1H}_2\text{Fc}]^{+/0}$  can be found in Figures S34 and S35, but only a cursory analysis will be presented here. The reduction event shows only featureless, nonisobestic behavior and no reversibility, and because of the lack of clear structural information, this process was not further analyzed. The UV–vis SEC spectrum for the oxidation of  $[\text{1H}_2\text{Fc}]^{+/2+}$  showed that the absorption at 220 nm increased, while the absorption at 237 and 380 nm decreased; the process was reversible by SEC, and the absorption bands at 237 and 380 nm could be regenerated. The UV–vis SEC spectrum of  $[\text{1Fc}]^+$  was, however, better defined because of the aromaticity of the pyridazine moiety.

The UV–vis SEC spectrum for the  $[\text{1Fc}]^{+/2+}$  process and the reduction are shown in Figure 6. The band at 520 nm for  $[\text{1Fc}]^+$  was described by time-dependent (TD-)DFT as a  $\text{Ru} \rightarrow$  pyridazine transition (Figure S52). A similar ferrocenyl-2,2'-bipyridine ligand in  $\text{Ru}(\text{bipy})_2(\text{FcCCbipy})$  ( $\text{FcCCbipy} = 4\text{-ethynylferrocenyl-2,2'-bipyridine}$ ) shows a metal-to-ligand charge transfer (MLCT;  $\text{Ru} \rightarrow \text{bipy}$ ) at 538 nm,<sup>26</sup> and other complexes coordinating 5-ferrocenyl-2,2'-bipyridine describe absorption between 540 and 470 nm depending on the coordinated metal atom.<sup>27,28</sup> The transition at 520 nm was consumed upon oxidation to form new bands at 290, 300, 440, and 670 nm. The bands at 290, 300, and 670 nm were described by TD-DFT as  $\text{Ru}^{2+} \rightarrow$  pyridazine transitions, while the band at 440 nm was an  $\text{Ru}^{2+} \rightarrow \text{Fe}^{3+}$  intravalence charge

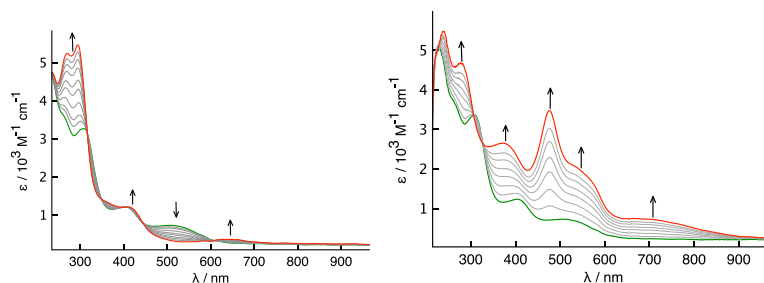


**Figure 6.** UV–vis–near-IR SEC of  $[\text{1Fc}]^\bullet$  in 0.1 M  $n\text{Bu}_4\text{NPF}_6/\text{CH}_2\text{Cl}_2$ : anodic process  $[\text{1Fc}]^\bullet+/2+$  (left); cathodic process  $[\text{1Fc}]^\bullet+/^\bullet$  (right).



transfer. The reduced species was somewhat complicated by the multiple bands generated in the spectrum (Figure 6). The broad band at 700 nm was assigned as a (Ru)MLCT, and the band at 500 nm was a (Fe)MLCT. The band at 380 nm was a ligand-to-metal charge transfer in which both metals were involved in the transition (Figure S53). The aromatic pyridazine offers better electron coupling throughout the bimetallic system.

**Computational Procedures.** Starting from the molecular structure of  $[1]^+$ , a geometry-optimized model was generated using DFT calculations. The frontier Kohn–Sham molecular orbitals for  $[1]^+$  are depicted in Figure 7. The highest occupied

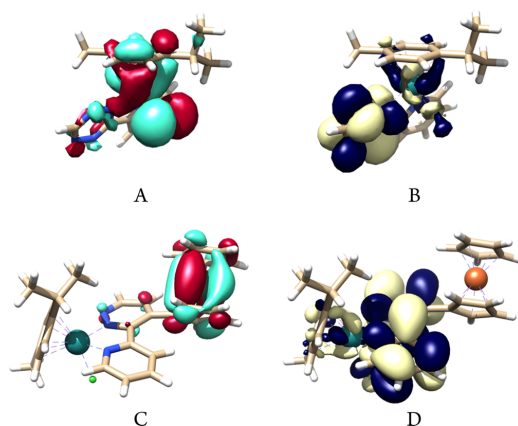


**Figure 7.** Molecule structures of  $[1]^+$  [HOMO (A)/LUMO (B)] and  $[1Fc]^+$  [HOMO (C)/LUMO (D)] determined by DFT calculations using B3LYP/def2-TZVP/J. Orbital isovalue = 0.02.

molecular orbital (HOMO) is located over the Ru–Cl bond, and the LUMO is located in the  $\pi^*$  system of the tetrazine chelate ligand (Figure 7). The frontier orbitals of  $[1]^+$  are generally representative of similar pyridyl-based ligands bound to  $CyRuCl$ ; however, the tetrazine moiety has a localized LUMO. This observation is different from the bipy ligand, where the LUMO is located over the entire  $\pi^*$  system. TD-DFT analysis described the low-energy band at 490 nm as a (Ru)MLCT (see the Supporting Information). The close-shell structure of the doubly reduced  $[1-Cl]^-$  found that the  $Cl^-$  ligand spontaneously dissociates from the Ru, forming the structure shown in Figure 8. For the open-shell structure  $[1]^-$ , the result of the addition of a third electron, it was found that the unpaired electron is located on the  $\pi^*$  system of TzPy over the entire  $\pi^*$  system of the ligand with some spin density located at the Ru center (Figure 5).

A similar DFT analysis was performed on  $[1Fc]^+$ , and the HOMO was located on the Fc moiety, which is consistent with the anodic sweep of CV, while the LUMO was located at the pyridazine–pyridine moiety. The LUMO for  $[1Fc]^+$  was delocalized over the  $\pi^*$  of the ligand, in contrast to the LUMO of  $[1]^+$ . The open-shell calculations on the reduced  $[1Fc]^-$  found a delocalized electron spin located over the entire  $\pi^*$  system of the pyridazine–pyridine moiety (see the Supporting Information). This delocalization was also observed in the EPR SEC spectrum of  $[1Fc]^+$  under reducing conditions, which showed only a broad unresolved spectrum with  $g = 2.002$ .

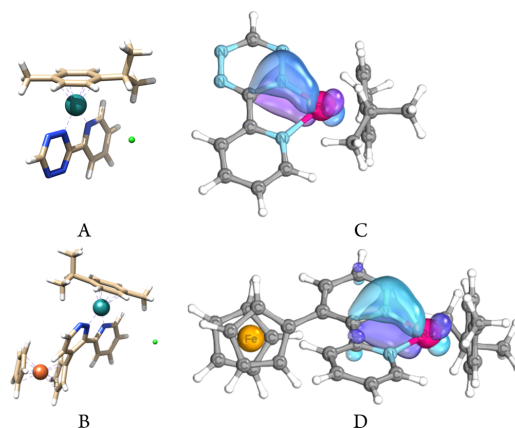


**Figure 8.** Molecule structures of  $[1-Cl]^-$  (A) and  $[1Fc-Cl]^-$  (B). IBOs of the  $N= Ru$   $\pi$  bond of  $[1]^0$  (C) and  $[1Fc]^0$  (D).

## CONCLUSIONS

The work presented herein describes the synthesis of the title complex  $[1]^+$ . The tetrazine moiety of  $[1]^+$  could be modified through the addition of two different dienophiles, ViFc and EthFc, to form the dihydropyridazine  $[1H_2Fc]^+$  and the pyridazine  $[1Fc]^+$  of the ligand. The dihydropyridazine form could be oxidized to the pyridazine form by the addition of  $O_2$  and catalytic *o*-quinone. The redox reactivity of the three complexes was also measured by CV, where the electrochemical mechanisms for  $[1]^+$  and  $[1Fc]^+$  were determined with the aid of SEC and supported by DFT calculations. The ligand-focused reactivity of these complexes allows for a module approach to ligand design, which is currently under further exploration in the development of new and novel ruthenium catalysts.

## EXPERIMENTAL SECTION

The ligand TzPy was purchased from TTI GmbH/TGU Varimol ([www.varimol.de](http://www.varimol.de)). Vinylferrocene, ethynylferrocene, and  $[CyRuCl_2]_2$  were purchased from Sigma Aldrich and used without further purification.

**$[CyRu(TzPy)Cl]PF_6$  ( $[1]PF_6$ ).**  $NH_4PF_6$  (84 mg, 0.514 mmol) was added to an orange solution of  $[CyRuCl_2]_2$  (150 mg, 0.245 mmol) in MeCN (20 mL) and stirred for 24 h at room temperature. The solvent was removed under reduced pressure, the residue was suspended with dichloromethane (DCM; 20 mL) and filtered over Celite to remove the white precipitate. The ligand TzPy (78 mg, 0.490 mmol) was dissolved in DCM (10 mL), and the solution was added to the filtrate and stirred for 2 h. After removal of the solvent under reduced pressure, a dark-brown solid was obtained. For purification, the solid was washed with  $Et_2O$ . Yield: 269 mg of a dark-brown solid (0.468 mmol, 96%). Elem anal. Calcd for  $C_{17}H_{19}ClF_6N_3PRu(O(C_2H_5)_2)_{0.25}$ : C, 36.43; H, 3.65; N, 11.80. Found: C, 36.14; H, 3.65; N, 11.70.  $^1H$  NMR (250 MHz,  $CD_2Cl_2$ ):  $\delta$  10.26 (s, 1H), 9.34 (d,  $J = 5.2$  Hz, 1H), 8.90 (d,  $J = 7.9$  Hz, 1H), 8.32 (s, 1H), 7.97 (s, 1H), 6.09 (dd,  $J = 10.8$  and 6.4 Hz, 2H), 5.92 (s, 2H), 2.95 (dt,  $J = 13.8$  and 6.9 Hz, 1H), 2.21 (s, 3H), 1.28 (d,  $J = 6.9$  Hz, 6H).

**$[1H_2Fc]^+$ .** To a solution of  $[1]PF_6$  (70 mg, 0.122 mmol) in DCM (20 mL) was added ViFc (28 mg, 0.134 mmol). After the solution was stirred for 24 h, the solvent was removed under reduced pressure. The residue was washed several times with *n*-hexane. Yield: 78 mg of a dark-brown solid (0.103 mmol, 84%). Elem anal. Calcd for  $C_{29}H_{31}ClF_6FeN_3PRu(O(C_2H_5)_2)_{0.5}$ : C, 46.78; H, 4.56; N, 5.28.

Found: C, 47.36; H, 4.44; N, 5.48. See Figures S7 and S8 for the  $^1\text{H}$  NMR spectra.

**[1Fc]PF<sub>6</sub>.** To a solution of [1]PF<sub>6</sub> (70 mg, 0.122 mmol) in DCM (20 mL) was added EthFc (30 mg, 0.134 mmol). After the solution was stirred for 24 h, the solvent was removed under reduced pressure. The residue was washed several times with *n*-hexane. Yield: 82 mg of a red-brown solid (0.109 mmol, 89%). Elem. anal. Calcd for C<sub>29</sub>H<sub>29</sub>ClF<sub>6</sub>FeN<sub>3</sub>PRu: C, 43.66; H, 3.86; N, 5.55. Found: C, 43.96; H, 3.81; N, 5.58.  $^1\text{H}$  NMR (250 MHz, CD<sub>2</sub>Cl<sub>2</sub>):  $\delta$  9.33–9.26 (m, 1H), 9.08 (d,  $J$  = 5.3 Hz, 1H), 8.20 (d,  $J$  = 5.3 Hz, 1H), 7.76 (td,  $J$  = 7.9 and 1.6 Hz, 1H), 7.61 (ddd,  $J$  = 7.5, 5.6, and 1.5 Hz, 1H), 7.51 (d,  $J$  = 8.2 Hz, 1H), 5.87 (t,  $J$  = 6.1 Hz, 2H), 5.69 (t,  $J$  = 6.9 Hz, 2H), 4.67–4.61 (m, 2H), 4.59 (dt,  $J$  = 2.4 and 1.5 Hz, 1H), 4.52 (dt,  $J$  = 2.6 and 1.4 Hz, 1H), 4.24 (s, 5H), 2.82 (p,  $J$  = 7.0 Hz, 1H), 2.25 (s, 3H), 1.17 (dd,  $J$  = 9.3 and 6.9 Hz, 6H).

**Kinetics.** First-order kinetics were fitted using eq 2-33 (p 23) and second-order kinetics using eq 2-35 (p 24) from *Chemical Kinetics and Reaction Mechanisms* by J. H. Espenson (1981 McGraw-Hill Education). The data were fitted using the corresponding equation on a MacBook Pro 2019 using the *Plot2 Pro*, version 2.6.6 (9980), graphing program; for more information, see [micw.org](http://micw.org).

First-order kinetics

$$\ln(P_t - P_\infty)P_0 - P_\infty = -kt \quad P_t = (P_0 - P_\infty)e^{-kt} + P_\infty \quad (2-33)$$

where  $P_t$  = absorption at time  $t$ ,  $P_0$  = initial absorption at time 0,  $P_\infty$  = absorption at time infinity (reaction end point),  $k$  = rate constant, and  $t$  = time.

Second-order kinetics

$$\Delta_0 = [B]_0 - [A]_0$$

$$\ln(1 + \Delta_0[A]_0P_0 - P_\infty P_t - P_\infty) = \ln[B]_0[A]_0 + \Delta_0 kt$$

$$P_t = [(P_0 - P_\infty)([B]_0\Delta_0 + [A]_0\Delta_0e^{\Delta_0 kt}) - 1] + P_\infty \quad (2-35)$$

where  $P_t$  = absorption at time  $t$ ,  $P_0$  = initial absorption at time 0,  $P_\infty$  = absorption at time infinity (reaction end point),  $k$  = rate constant,  $t$  = time,  $[A]_0$  = initial concentration of [1]<sup>+</sup>, and  $[B]_0$  = initial concentration of ViFc.

## ■ ASSOCIATED CONTENT

### Supporting Information

The Supporting Information is available free of charge at <https://pubs.acs.org/doi/10.1021/acs.inorgchem.1c00094>. Raw data will also be freely accessible on the DaRUS repository at <http://dx.doi.org/10.18419/darus-1181>

XYZ coordinates determined by DFT (ZIP)

Computational details, crystallographic tables, kinetic plots, UV–vis spectra, and TD-DFT (PDF)

### Accession Codes

CCDC 2054095 and 2054096 contain the supplementary crystallographic data for this paper. These data can be obtained free of charge via [www.ccdc.cam.ac.uk/data\\_request/cif](http://www.ccdc.cam.ac.uk/data_request/cif), or by emailing [data\\_request@ccdc.cam.ac.uk](mailto:data_request@ccdc.cam.ac.uk), or by contacting The Cambridge Crystallographic Data Centre, 12 Union Road, Cambridge CB2 1EZ, UK; fax: +44 1223 336033.

## ■ AUTHOR INFORMATION

### Corresponding Author

Mark R. Ringenberg – *Institut für Anorganische Chemie, Universität Stuttgart, 70569 Stuttgart, Germany*;  
[orcid.org/0000-0001-7585-5757](https://orcid.org/0000-0001-7585-5757);  
 Email: [mark.ringenberg@iac.uni-stuttgart.de](mailto:mark.ringenberg@iac.uni-stuttgart.de)

## Authors

Marc Schnierle – *Institut für Anorganische Chemie, Universität Stuttgart, 70569 Stuttgart, Germany*

Marie Leimkühler – *Institut für Anorganische Chemie, Universität Stuttgart, 70569 Stuttgart, Germany*

Complete contact information is available at:

<https://pubs.acs.org/10.1021/acs.inorgchem.1c00094>

## Author Contributions

These authors contributed equally. The manuscript was written through contribution and approval of the final version from all authors.

## Funding

M.R.R. gratefully acknowledges support by the state of Baden-Württemberg through bwHPC and the German Research Foundation through Grant INST 40/467-1 FUGG for accessing the Justus cluster. M.S. and this project was funded by Grant SFB1333 C2.

## Notes

The authors declare no competing financial interest.

## ■ ACKNOWLEDGMENTS

This manuscript is dedicated to Prof. Wolfgang Kaim on the occasion of his 70th birthday, whose continued support and friendship have made me the chemist I am today.

## ■ REFERENCES

- Blakemore, J. D.; Schley, N. D.; Balcells, D.; Hull, J. F.; Olack, G. W.; Incarvito, C. D.; Eisenstein, O.; Brudvig, G. W.; Crabtree, R. H. Half-Sandwich Iridium Complexes for Homogeneous Water-Oxidation Catalysis. *J. Am. Chem. Soc.* **2010**, *132*, 16017–16029.
- Caix, C.; Chardon-Noblat, S.; Deronzier, A. Electrocatalytic reduction of CO<sub>2</sub> into formate with [( $\eta^3$ -Me<sub>3</sub>C<sub>5</sub>)M(L)Cl]<sup>+</sup> complexes (L = 2,2'-bipyridine ligands; M = Rh(III) and Ir(III)). *J. Electroanal. Chem.* **1997**, *434*, 163–170.
- Rüther, T.; Woodward, C. P.; Jones, T. W.; Coghlan, C. J.; Hebling, Y.; Cordiner, R. L.; Dawson, R. E.; Robinson, D. E. J. E.; Wilson, G. J. Synthesis, characterisation, and properties of *p*-cymene Ruthenium(II) tetracarboxylate bipyridine complexes [( $\eta^6$ -*p*-cymene)Ru(R<sub>n</sub>R<sub>n'</sub>-tcby)Cl][Cl]. *J. Organomet. Chem.* **2016**, *823*, 136–146.
- Kaim, W.; Reinhardt, R.; Sieger, M. Chemical and Electrochemical Generation of Hydride-Forming Catalytic Intermediates (bpy)M(C<sub>n</sub>R<sub>n</sub>): M = Rh, Ir (n = 5); M = Ru, Os (n = 6). Coordinatively Unsaturated Ground State Models of MLCT Excited States? *Inorg. Chem.* **1994**, *33*, 4453–4459.
- Valderrama, M.; Contreras, R.; Arancibia, V.; Muñoz, P. Synthesis and electrochemical properties of *p*-cymene-ruthenium(II) complexes with (EPPH<sub>2</sub>)<sub>2</sub>CHR (E = S, Se; R = H, Me) and their anionic derivatives as ligands. Crystal structure of [( $\eta^6$ -MeC<sub>6</sub>H<sub>4</sub>Pr)<sup>+</sup>Ru( $\eta^3$ -SPPH<sub>2</sub>)<sub>2</sub>CMe-C,S,S'}]PF<sub>6</sub>. *Inorg. Chim. Acta* **1997**, *255*, 221–227.
- Thirumala Prasad, K.; Gupta, G.; Chandra, A. K.; Phani Pavan, M.; Mohan Rao, K. Spectral, structural and DFT studies of platinum group metal 3,6-bis(2-pyridyl)-4-phenylpyridazine complexes and their ligand bonding modes. *J. Organomet. Chem.* **2010**, *695*, 707–716.
- Schwach, M.; Hausen, H.-D.; Kaim, W. The First Crystal Structure of a Metal-Stabilized Tetrazine Anion Radical: Formation of a Dicopper Complex through Self-Assembly in a Comproportionation Reaction. *Inorg. Chem.* **1999**, *38*, 2242–2243.
- Maciulis, N. A.; Schaugaard, R. N.; Losovyj, Y.; Chen, C.-H.; Pink, M.; Caulton, K. G. Seeking Redox Activity in a Tetrazinyl Pincer Ligand: Installing Zerovalent Cr and Mo. *Inorg. Chem.* **2018**, *57*, 12671–12682.

- (9) Prokhorov, A. M.; Prokhorova, P. E. Triazines and Tetrazines. In *Progress in Heterocyclic Chemistry*; Gribble, G. W., Joule, J. A., Eds.; Elsevier, 2015; Vol. 27, Chapter 6.3, pp 451–464.
- (10) Schmierle, M.; Blickle, S.; Filippou, V.; Ringenberg, M. R. Tetrazine metallation boosts rate and regioselectivity of inverse electron demand Diels–Alder (iEDDA) addition of dienophiles. *Chem. Commun.* **2020**, *56*, 12033–12036.
- (11) Kaim, W. The coordination chemistry of 1,2,4,5-tetrazines. *Coord. Chem. Rev.* **2002**, *230*, 127–139.
- (12) Oliveira, B. L.; Guo, Z.; Bernardes, G. J. L. Inverse electron demand Diels–Alder reactions in chemical biology. *Chem. Soc. Rev.* **2017**, *46*, 4895–4950.
- (13) Devaraj, N. K.; Weissleder, R. Biomedical Applications of Tetrazine Cycloadditions. *Acc. Chem. Res.* **2011**, *44*, 816–827.
- (14) Clavier, G.; Audebert, P. s-Tetrazines as Building Blocks for New Functional Molecules and Molecular Materials. *Chem. Rev.* **2010**, *110*, 3299–3314.
- (15) Zhang, J.; Shukla, V.; Boger, D. L. Inverse Electron Demand Diels–Alder Reactions of Heterocyclic Azadienes, 1-Aza-1,3-Butadienes, Cyclopropenone Ketals, and Related Systems. A Retrospective. *J. Org. Chem.* **2019**, *84*, 9397–9445.
- (16) Zhu, Z.; Glinkerman, C. M.; Boger, D. L. Selective N1/N4 1,4-Cycloaddition of 1,2,4,5-Tetrazines Enabled by Solvent Hydrogen Bonding. *J. Am. Chem. Soc.* **2020**, *142*, 20778–20787.
- (17) Salmain, M.; Fischer-Durand, N.; Rudolf, B. Bioorthogonal Conjugation of Transition Organometallic Complexes to Peptides and Proteins: Strategies and Applications. *Eur. J. Inorg. Chem.* **2020**, *2020*, 21–35.
- (18) Connell, T. U.; Donnelly, P. S. Labelling proteins and peptides with phosphorescent d<sup>6</sup> transition metal complexes. *Coord. Chem. Rev.* **2018**, *375*, 267–284.
- (19) Tang, T. S.-M.; Liu, H.-W.; Lo, K. K.-W. Monochromophoric iridium(III) pyridyl–tetrazine complexes as a unique design strategy for bioorthogonal probes with luminogenic behavior. *Chem. Commun.* **2017**, *53*, 3299–3302.
- (20) Knall, A.-C.; Slugovc, C. Inverse electron demand Diels–Alder (iEDDA)-initiated conjugation: a (high) potential click chemistry scheme. *Chem. Soc. Rev.* **2013**, *42*, 5131–5142.
- (21) Yan, Y. K.; Melchart, M.; Habtemariam, A.; Peacock, A. F.; Sadler, P. J. Catalysis of regioselective reduction of NAD<sup>+</sup> by ruthenium(II) arene complexes under biologically relevant conditions. *JBC, J. Biol. Inorg. Chem.* **2006**, *11*, 483–8.
- (22) Ohtsu, H.; Fujii, S.; Tsuge, K.; Tanaka, K. Novel synthesis of a four-electron-reduced ruthenium(II) NADH-type complex under water-gas-shift reaction conditions. *Dalton Trans.* **2016**, *45*, 16130–16133.
- (23) Knizia, G. *IboView*; Universität Stuttgart, 2015.
- (24) Knizia, G. Intrinsic Atomic Orbitals: An Unbiased Bridge between Quantum Theory and Chemical Concepts. *J. Chem. Theory Comput.* **2013**, *9*, 4834–4843.
- (25) Bard, A. J.; Faulkner, L. R. *Electrochemical Methods: Fundamentals and Applications*; Wiley, 2000.
- (26) Barnsley, J. E.; Findlay, J. A.; Shillito, G. E.; Pelet, W. S.; Scottwell, S. Ø.; McIntyre, S. M.; Tay, E. J.; Gordon, K. C.; Crowley, J. D. Long-lived MLCT states for Ru(II) complexes of ferrocene-appended 2,2'-bipyridines. *Dalton Trans.* **2019**, *48*, 15713–15722.
- (27) Scottwell, S. Ø.; Shaffer, K. J.; McAdam, C. J.; Crowley, J. D. Ferrocenyl-2,2'-bipyridine ligands: synthesis, palladium(II) and copper(I) complexes, optical and electrochemical properties. *RSC Adv.* **2014**, *4*, 35726–35734.
- (28) Findlay, J. A.; McAdam, C. J.; Sutton, J. J.; Preston, D.; Gordon, K. C.; Crowley, J. D. Metallosupramolecular Architectures Formed with Ferrocene-Linked Bis-Bidentate Ligands: Synthesis, Structures, and Electrochemical Studies. *Inorg. Chem.* **2018**, *57*, 3602–3614.



## 7.4 Manuscript Paper 4.

Manuscript, 1st draft by Schnierle

## Immobilization by iEDDA [4+2] cycloaddition of a 3-(pyrid-2-yl)-methyl-tetrazine-tricarbonylrhenium(I)-chloride derivative onto a norbonene-trimethoxysilane functionalized SBA-15.

Marc Schnierle<sup>‡[1]</sup>, Laura Neumüller<sup>‡[1]</sup>, Felix Ziegler<sup>[3]</sup>, Kim-I. Mehnert<sup>[1,5]</sup>, Osman Bunjaku<sup>[2]</sup>, Mario Winkler<sup>[4]</sup>, Kevin Wanek, Indro Biswas<sup>[5]</sup>, Johanna Bruckner<sup>[4]</sup>, Joris van Slageren<sup>[4]</sup>, Michael Buchmeiser<sup>[3]</sup>, Deven P. Estes<sup>\*[2]</sup>, Mark R. Ringenberg<sup>\*[1]</sup>

[1] Institut für Anorganische Chemie, Universität Stuttgart, Pfaffenwaldring 55, 70569 Stuttgart, Germany.

[2] Institut für Technische Chemie, Universität Stuttgart, Pfaffenwaldring 55, 70569 Stuttgart, Germany.

[3] Institut für Polymer Chemie, Universität Stuttgart, Pfaffenwaldring 55, 70569 Stuttgart, Germany.

[4] Institut für Physikalische Chemie, Universität Stuttgart, Pfaffenwaldring 55, 70569 Stuttgart, Germany.

[5] Institut für Technische Thermodynamik, Deutsches Zentrum für Luft- und Raumfahrt Stuttgart, Pfaffenwaldring 38-40, 70569 Stuttgart, Germany.

**KEYWORDS.** Kinetics • Electrochemistry • Immobilization • solid-state UV/Vis / IR • XPS

**ABSTRACT:** The divers substituted bidentate ligand 3-(pyrid-2-yl)-1,2,4,5-tetrazines (MeTzPy) coordinated in the complex (MeTzPy)Re(CO)<sub>3</sub>Cl shows an increased reactivity compared to the ligand itself. The complexation accelerates the reaction by a factor of about 2.9 to 4.2 for the reaction with TCO. Also the different substituents in third position of the pyrid-2-yl. Thus, the electron pushing substituents such as OMe and Me show a lower reaction rate  $k_2$  than when CF<sub>3</sub> is used as an electron pulling substituent. In the reaction of the complexes with the TCO, reaction rates  $k_2$  were in the range of 59 l·mol<sup>-1</sup>·s<sup>-1</sup> for OMe to 119 l·mol<sup>-1</sup>·s<sup>-1</sup> for CF<sub>3</sub> were determined. In a reaction with norbonene,  $k_2$  were determined from 0.021 l·mol<sup>-1</sup>·s<sup>-1</sup> to 0.048 l·mol<sup>-1</sup>·s<sup>-1</sup>. Electrochemical, UV/Vis, and IR measurements support the assumption that reduced electron density provides accelerated [4+2] cycloaddition by their trends of displacement. Furthermore, the immobilization of the complex in a norbonene trimethoxysilane functionalized SBA-15 is shown. Successful immobilization was confirmed by solid-state UV/Vis, solid-state IR, and XPS measurements.

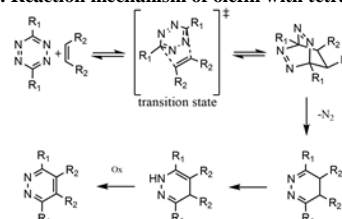
## INTRODUCTION

Catalytic processes are standard in industrial chemistry, to improve them, the development of heterogeneous asymmetric catalyst systems is one novel aspect. [1-8]

One of the key points is the immobilization technique on the surface. The immobilization via a trimethoxysilane linker on a silica surface presented by Soai et al. 1990 is one of the possibilities and gained high popularity. [4,6,9,10]

Immobilization itself is already one of the most important points in the preparation of heterogeneous asymmetric catalysts. Therefore, all types of coupling reactions are potentially interesting. The inverse electron demand [4+2] pericyclic addition (Diels-Alder) between electron arm 1,2,4,5-tetrazines and electron rich dienophiles provide a convenient method for generating new C-C bonds and heterocycles. This technology has found applications in biological labeling. Recently, we and others showed that metallotetrazine complexes themselves are active for [4+2] cycloaddition. This offers the possibility of binding the complex to the surface via ligand. The mechanism of [4+2] cycloaddition is shown in **scheme 1**. [11-19]

**Scheme 1. Reaction mechanism of olefin with tetrazine.**



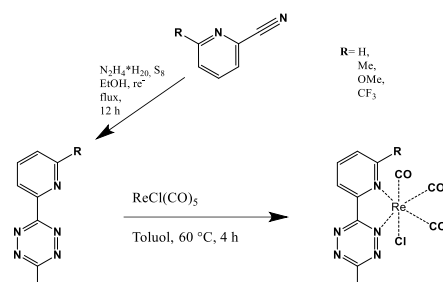
We describe how the different substituents on a MeTzPy ligand affect the kinetics of the free tetrazine, as well as of their metal complex with norbonene or trans-cyclooctene. Furthermore, immobilization on a SBA-15-surface is discussed.

## RESULTS AND DISCUSSION

**Synthesis.** The 3-(pyrid-2-yl)-methyl-tetrazine derivatives ([L]-R) were synthesized to Caulton, published in 2014. [20] The synthesis of different 3-(pyrid-2-yl)-methyl-tetrazine-tricarbonylrhenium(I)-chloride derivatives ([C]-R) starting from the nitrile, is shown in **scheme 2** and was performed by dissolving the

respective [L]-R in toluol. Pentacarbonylrhenium(I)-chloride was added and the mixture was heated to 60 °C for 4 h. A good indicator is the color change from a light pink to a dark purple.[21]

**Scheme 2. Synthesis of the different 3-(pyrid-2-yl)-methyl-tetrazine-tricarbonylrhenium(I)-chloride derivatives.**



The molecular structure of [L]-CF<sub>3</sub> and [C]-CF<sub>3</sub> are shown in **figure 1** as examples for all 8 compounds in figure 1. The twisting of the two six-membered rings to each other is clearly visible. Depending on the substituent, this twisting differs. Complexation and the formation of the [C]-R compounds force the rings of the ligand to approximate planarity. The remaining molecular data of the compounds [L]-H, [L]-Me, [L]-OMe, [L]-CF<sub>3</sub>, [C]-H, [C]-Me, [C]-OMe and [C]-CF<sub>3</sub> are shown in **table S1-S4**.

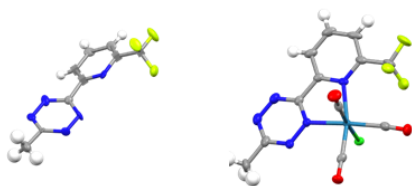


**Figure 1.** Molecular structure of [L]-CF<sub>3</sub> and [C]-CF<sub>3</sub> determined by X-ray diffraction.

For the immobilization on the surface, the compound [C]-CF<sub>3</sub> was chosen because of the CF<sub>3</sub> group, which is a probe for successful immobilization due to the fluorine atoms. The SBA-15 material prepared by the Cruden method was first functionalized with a bi-cyclo[2.2.1]hept-5-en-2-yltrimethoxysilane linker and finally reacted with the [C]-R compounds. All treatment steps of the SBA-15, up to immobilization are outlined in **scheme 3**.<sup>[22]</sup>

Additionally, for comparison of the solid state analytics, the compound [C]-CF<sub>3</sub> reacted with the linker molecule itself. The molecular structure of linker-[C]-CF<sub>3</sub> is shown in **figure 1**.

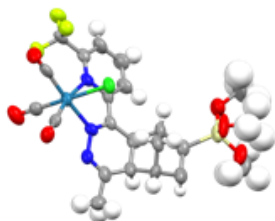
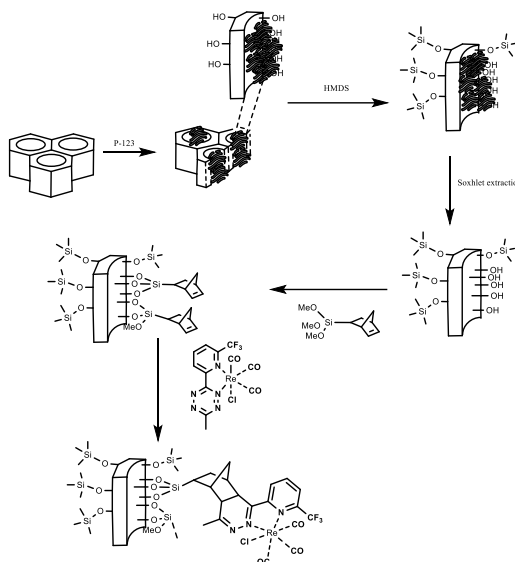


**Figure 2.** Molecular structure of linker-[C]-CF<sub>3</sub> determined by X-ray diffraction.

Manuscript, 1st draft by Schnierle  
**Scheme 3. Immobilization of [C]-CF<sub>3</sub> into a norbornyltri-methoxysilane functionalized SBA-15.**



**Kinetics of dienophile addition.** The addition rate of the different [C]-R as well as of the different [L]-R to TCO or NBE were determined by following the reaction by time-resolved UV/Vis or <sup>1</sup>H NMR spectroscopy, respectively. All the UV/Vis and NMR kinetics measurements culminate in **table 1** and show the *k*<sub>2</sub> of the 8 compounds studied with TCO and NBE, respectively. In the addition of TCO, the complexes have a *k*<sub>2</sub> 2.9 to 4.2 times higher compare to the ligand, which is due to the electron density in the tetrazine unit. The reaction with NBE is similar, except that the difference between the reaction with free tetrazine and the complexed one is only 1.7 to 2.8 times higher.

**Table 1. Kinetic 2.order values for the [4+2] cycloadditionreaction of the [L]-R and [C]-R with TCO or NBE.**

	<i>k</i> <sub>2</sub> [l·mol <sup>-1</sup> ·s <sup>-1</sup> ] + TCO	<i>k</i> <sub>2</sub> [l·mol <sup>-1</sup> ·s <sup>-1</sup> ] + NBE
[L]-H	21	0.012
[L]-Me	17	0.008
[L]-OMe	19	0.010
[L]-CF <sub>3</sub>	41	0.027
[C]-H	90	0.032
[C]-Me	63	0.022
[C]-OMe	59	0.021
[C]-CF <sub>3</sub>	119	0.048

The [4+2] cycloaddition of the compounds presented here with the TCO was subjected to a more detailed investigation. For these reactions, the Δ*H*<sup>‡</sup>, Δ*S*<sup>‡</sup> and Δ*G*<sup>‡</sup>(298 K) were determined with the aid of the Eyring analysis.

**Table 2. Transition State Thermodynamic Values Determined from Eyring plot.**

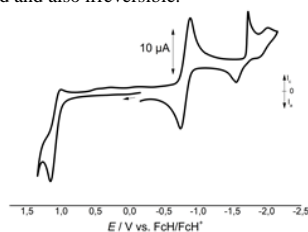
	[L]-H + TCO	[L]-Me + TCO	[L]-OMe + TCO	[L]-CF <sub>3</sub> + TCO
$\Delta H^\ddagger$ / kJ mol <sup>-1</sup>	13.35	17.96	18.71	19.50
$\Delta S^\ddagger$ / J mol <sup>-1</sup> K <sup>-1</sup>	- 136	- 122	- 119	- 114
$\Delta G^\ddagger$ (298 K)/kJ mol <sup>-1</sup>	53.88	54.32	54.17	53.47
	[C]-H + TCO	[C]-Me + TCO	[C]-OMe + TCO	[C]-CF <sub>3</sub> + TCO
$\Delta H^\ddagger$ / kJ mol <sup>-1</sup>	13.00	13.79	13.76	7.97
$\Delta S^\ddagger$ / J mol <sup>-1</sup> K <sup>-1</sup>	- 125	- 125	- 126	- 140
$\Delta G^\ddagger$ (298 K)/kJ mol <sup>-1</sup>	50.25	51.04	51.31	49.69

**Electrochemistry.** In order to investigate the influence of the shift the substituents are studied more in detail. The compounds were investigated electrochemically, for which CV experiments were carried out. Basically, the four tetrazines and the four complexes would act identically in CV. Only the potentials are slightly different due to the electron pushing or pulling properties of the substituents. The free tetrazines show a single reversible reduction in the range of -1.44 V to -1.32 V against FcH/FcH<sup>+</sup> (see figure S63 – S66). The complexes each exhibit complexing behavior with an irreversible oxidation, a reversible reduction, and a pseudo reversible second reduction (see figure 3 and figure S67 – S70). The potentials of the respective processes are listed in table 3.

**Table 3. Potentials of the CV measurements of the four complexes in 0.1 M n-Bu<sub>4</sub>NPF<sub>6</sub>/CH<sub>2</sub>Cl<sub>2</sub> at 100 mV s<sup>-1</sup> and referenced against FcH/FcH<sup>+</sup>.**

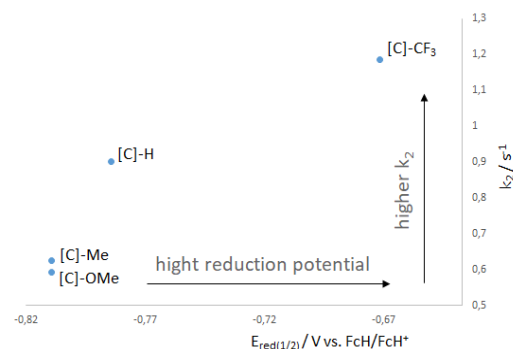
	E <sub>off-set Ox</sub> [V]	E <sub>1/2 Red1</sub> [V]	E <sub>off-set Red2</sub> [V]
[C]-H	0.92	-0.78	-1.64
[C]-Me	0.91	-0.81	-1.68
[C]-OMe	0.80	-0.81	-1.85
[C]-CF <sub>3</sub>	0.90	-0.67	-1.59

The reversible first reduction can be assigned to the tetrazine unit. Due to the complexation, an enormous shift of 0.5 - 0.6 V is to be forgiven for the reduction of the tetrazines. The second reduction also belongs to the tetrazine unit, but is irreversible. The oxidation is metal based and also irreversible.<sup>[23]</sup>

**Figure 3.** CVs of [C]-CF<sub>3</sub> in 0.1 M n-Bu<sub>4</sub>NPF<sub>6</sub>/CH<sub>2</sub>Cl<sub>2</sub> at 100 mV s<sup>-1</sup>.

Manuscript, 1st draft by Schnierle

Comparing the  $k_2$  values from the kinetic measurements and the potentials from the CV measurements, a clear trend and dependence can be seen. A higher reduction potential is accompanied by higher kinetics.

**Figure 4.** Reduction potential  $E$  vs. kinetics  $k_2$  of the compounds [C]-H, [C]-Me, [C]-OMe and [C]-CF<sub>3</sub>.

**IR and UV/Vis spectroscopy.** For a better understanding of the analytics on the SBA-15 surface with the immobilized [C]-CF<sub>3</sub>, the individual compounds were also investigated in solution IR and UV/Vis spectroscopy. As expected, the IR spectra show three characteristic CO vibrational abundances for all complexes in the range at around 2000 cm<sup>-1</sup>. The influence of the substituents makes the bands shift slightly. What stands out from the list is [C]-CF<sub>3</sub> with its electron-withdrawing group, whose CO bands clearly deviate from the others. They are shifted by an average of approx. 10 wavenumbers. The exact data are listed in table 4.<sup>[23]</sup>

**Table 4. Summary of IR measurements of the complexes.**

	$\nu$ / cm-1			$\nu$ average
	[C]-H	2033	1946	1917
[C]-Me	2031	1944	1914	1963
[C]-OMe	2032	1946	1911	1963
[C]-CF <sub>3</sub>	2040	1958	1923	1974

The UV–vis–NIR spectra showed for all [C]-R a band from 520 nm to 530 nm and can be assigned to a MLCT transition. The exact values are listed in table 5.<sup>[23]</sup>

**Table 5. Summary of UV/Vis-NIR measurements of the complexes.**

	$\lambda_{\max}$ / nm ( $\epsilon$ / 10 <sup>3</sup> M <sup>-1</sup> cm <sup>-1</sup> )
[C]-H	522 (4.871)
[C]-Me	520 (4.524)
[C]-OMe	530 (5.678)
[C]-CF <sub>3</sub>	522 (4.435)



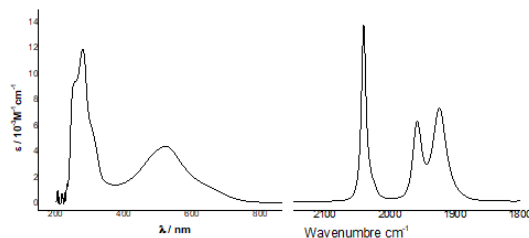


**Figure 5.** UV/Vis-NIR and IR spectra [C]-CF<sub>3</sub> CH<sub>2</sub>Cl<sub>2</sub>.

**Solid-state analytics.** The immobilized compound [C]-CF<sub>3</sub> (SBA-15-[C]-CF<sub>3</sub>), linker-[C]-CF<sub>3</sub> and the compound [C]-CF<sub>3</sub> itself was studied by solid-state IR, and solid-state UV/Vis.

**Scheme 4.** Illustration of SBA-15-[C]-CF<sub>3</sub>.

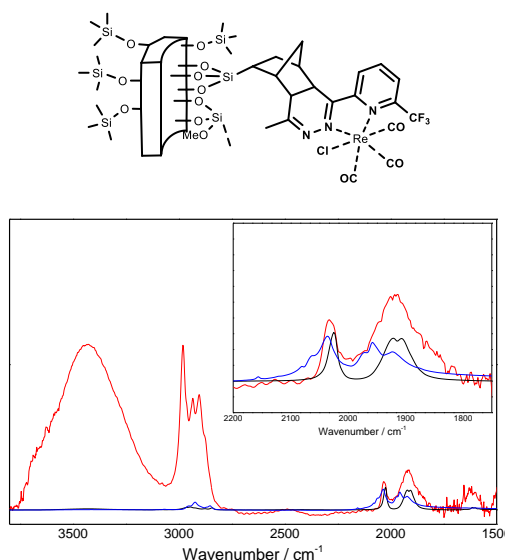


**Figure 6.** Solid state IR spectra of [C]-CF<sub>3</sub> (blue), linker-[C]-CF<sub>3</sub> (black) and SBA-15-[C]-CF<sub>3</sub> (red).

**Table 6.** Summary of IR solid-state measurements.

	ν / cm <sup>-1</sup>			ν average
[C]-CF <sub>3</sub>	2036	1957	1921	1971
Linker-[C]-CF <sub>3</sub>	2025	1923	1905	1951
SBA-15-[C]-CF <sub>3</sub>	2033	1927	1913	1958

As the IR solid state measurements in **figure 6** show, the SBA-15 is loaded with [C]-CF<sub>3</sub>, because the CO bands are clearly visible. Also the MLCT transition of [C]-CF<sub>3</sub> is still visible in the solid state UV/Vis. The solid state UV/Vis spectra of the compounds [C]-CF<sub>3</sub>, linker-[C]-CF<sub>3</sub> and SBA-15-[C]-CF<sub>3</sub> are shown in **figure S81-S83**. **Table 7** lists the detected bands of the three compounds. <sup>[24]</sup>

Manuscript, 1st draft by Schnierle

**Table 7.** Summary of UV/Vis-NIR solid-state measurements.

	λ <sub>max</sub> / nm
[C]-CF <sub>3</sub>	486
Linker-[C]-CF <sub>3</sub>	436
SBA-15-[C]-CF <sub>3</sub>	468

Furthermore, XPS measurements of the NBE functionalized SBA-15 and the SBA-15-[C]-CF<sub>3</sub> were performed. The two spectra are shown in **figure 7** and **S84**. Both show characteristic O1s and O-Auger signals for SBA-15 at around 500 to 600 eV and 950 to 1200 eV. The XPS measurement of the [4+2] cycloaddition product also shows an F1s signal at 695 eV, indicating successful loading with [C]-CF<sub>3</sub>.<sup>[25]</sup>

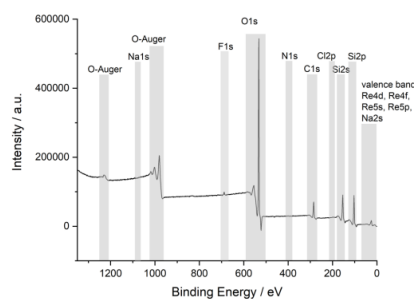


**Figure 6.** XPS spectra of SBA-15-[C]-CF<sub>3</sub>.

## CONCLUSIONS

The work presented here describes the synthesis of various 3-(pyrid-2-yl)-methyl-tetrazine derivatives and 3-(pyrid-2-yl)-methyl-tetrazine-tricarbonylrhenium(I)-chloride derivatives. Also shown is the kinetics with NBE and TCO, spectroscopy and electrochemistry. Finally, the immobilization on an SBA-15 surface via a norbornic trimethoxysilane linker is also shown.

## EXPERIMENTAL

**3-(pyrid-2-yl)-methyl-tetrazine derivatives ([L]-R).** Analogous to the synthesis of Caulton, [L] is prepared by dissolving the corresponding nitrile derivative (1eq) in degassed EtOH and add mono-hydrated hydrazine (10eq) in excess.<sup>[20]</sup> The reaction solution is heated to 6°C for 4 h. The solution is then cooled in an ice bath and acetonitrile is added in excess (60eq). The reaction solution is heated to reflux and stirred overnight at this temperature. After cooling, a solution of acetic acid and demineralized water (3:1) is added and NaNO<sub>2</sub> is added to the reaction solution until no more brown gas is formed. The resulting [L] is purified by acid chromatography with diethyl ether over silica gel.

**[L]-H.** Yield: 23 %. <sup>1</sup>H NMR (500 MHz, Chloroform-*d*) δ = 8.88 (ddd, *J* = 4.7, 1.7, 0.9 Hz, 1H), 8.58 (dt, *J* = 8.0, 1.1 Hz, 1H), 7.91 (td, *J* = 7.8, 1.8 Hz, 1H), 7.49 (ddd, *J* = 7.6, 4.7, 1.2 Hz, 1H), 3.10 (s, 3H). <sup>13</sup>C NMR (126 MHz, CDCl<sub>3</sub>) δ 168.15, 163.63, 150.90, 150.32, 137.44, 126.34, 123.89, 21.37. Elemental anal. calcd: C 55.48; H 4.07; N 40.44. Found: C 55.01; H 4.397; N 39.17. ESI-MS *m/z*: [M]<sup>+</sup>Na: 196.0594, calcd: 196.0594.

**[L]-Me.** Yield: 26 %. <sup>1</sup>H NMR (500 MHz, Chloroform-*d*) δ 8.36 (d, *J* = 7.7 Hz, 1H), 7.78 (t, *J* = 7.8 Hz, 1H), 7.34 (d, *J* = 7.8 Hz, 1H), 3.08 (s, 3H), 2.69 (s, 3H). <sup>13</sup>C NMR (126 MHz, CDCl<sub>3</sub>) δ 167.93, 163.84,



160.10, 149.80, 137.48, 126.17, 121.24, 24.85, 21.33. Elemental anal. calcd: C 57.74; H 4.85; N 37.41. Found: C 57.69; H 4.970; N 37.38. ESI-MS *m/z*: [M]<sup>+</sup>Na: 210.0751, calcd: 210.0750.

**[L]-OMe.** Yield: 29 %. <sup>1</sup>H NMR (500 MHz, Chloroform-*d*) δ 8.13 (dd, *J* = 7.3, 0.8 Hz, 1H), 7.75 (dd, *J* = 8.3, 7.3 Hz, 1H), 6.93 (dd, *J* = 8.4, 0.8 Hz, 1H), 4.04 (s, 3H), 3.07 (s, 3H). <sup>13</sup>C NMR (126 MHz, CDCl<sub>3</sub>) δ 167.61, 164.71, 163.82, 147.80, 139.45, 117.46, 114.59, 53.83, 21.29. Elemental anal. calcd: C 53.20; H 4.46; N 34.47. Found: C 52.92; H 4.543; N 33.42. ESI-MS *m/z*: [M]<sup>+</sup>Na 226.0699, calcd: 226.0699.

**[L]-CF<sub>3</sub>.** Yield: 19 %. <sup>1</sup>H NMR (500 MHz, Chloroform-*d*) δ 8.73 (d, *J* = 7.9 Hz, 1H), 8.12 (t, *J* = 7.9 Hz, 1H), 7.88 (dd, *J* = 7.9, 1.0 Hz, 1H), 3.11 (s, 3H). <sup>13</sup>C NMR (126 MHz, CDCl<sub>3</sub>) δ 168.40, 163.08, 151.07, 139.09, 126.32, 122.87, 21.42. <sup>19</sup>F NMR (235 MHz, CDCl<sub>3</sub>) δ -67.72. Elemental anal. calcd: C 44.82; H 2.51; N 29.04. Found: C 44.73; H 2.655; N 28.51. ESI-MS *m/z*: [M]<sup>+</sup>H 242.0648, calcd: 242.0648.

**3-(pyrid-2-yl)-methyl-tetrazine-tricarbonylrhenium(I)-chloride derivatives ([C]-R).** [C] was synthesised by refluxing the 1.05 eq ReCl(CO)<sub>3</sub> with 1 eq of the respective [L] in toluene for 4 h. After the reaction solution was cooled to room temperature, hexanes was overlaid and allowed to slowly diffuse into the solution to produce crystals of [C].

**[C]-H.** Yield: %. <sup>1</sup>H NMR (700 MHz, Chloroform-*d*) δ 9.02 (dt, *J* = 5.4, 1.0 Hz, 1H), 8.90 (dt, *J* = 7.9, 1.0 Hz, 1H), 8.20 (td, *J* = 7.9, 1.5 Hz, 1H), 7.74 (ddd, *J* = 7.6, 5.4, 1.4 Hz, 1H), 3.18 (s, 3H). <sup>13</sup>C NMR (176 MHz, CDCl<sub>3</sub>) δ 168.80, 164.55, 152.68, 149.27, 138.64, 129.09, 125.43, 20.70. Elemental anal. calcd: C 27.59; H 1.47; N 14.63. Found: C 27.44; H 1.556; N 14.40. ESI-MS *m/z*: [M]<sup>+</sup>Na 501.9679, calcd: 501.9678.

**[C]-Me.** Yield: %. <sup>1</sup>H NMR (700 MHz, Chloroform-*d*) δ 8.77 (d, *J* = 7.8 Hz, 1H), 8.02 (t, *J* = 7.8 Hz, 1H), 7.70 (d, *J* = 7.8 Hz, 1H), 3.21 – 3.10 (m, 3H), 3.01 (t, *J* = 1.4 Hz, 3H). <sup>13</sup>C NMR (176 MHz, CDCl<sub>3</sub>) δ 196.39, 191.88, 185.83, 168.46, 165.24, 162.25, 149.83, 138.65, 129.09, 122.95, 29.19, 20.58. Elemental anal. calcd: C 29.24; H 1.84; N 14.21. Found: C 30.08; H 2.201; N 13.12. ESI-MS *m/z*: [M]<sup>+</sup>Na 515.9835, calcd: 515.9835.

**[C]-OMe.** Yield: %. <sup>1</sup>H NMR (700 MHz, Chloroform-*d*) δ 8.51 (d, *J* = 7.5 Hz, 1H), 8.11 (t, *J* = 8.0 Hz, 1H), 7.21 (d, *J* = 8.5 Hz, 1H), 4.15 (s, 3H), 3.14 (s, 3H). <sup>13</sup>C NMR (176 MHz, CDCl<sub>3</sub>) δ 195.64, 192.80, 186.30, 168.43, 165.25, 164.00, 148.50, 141.52, 118.13, 110.03, 56.37, 20.60. Elemental anal. calcd: C 28.32; H 1.78; N 13.76. Found: C 28.23; H 1.870; N 13.40. ESI-MS *m/z*: [M]<sup>+</sup>Na 531.9786, calcd: 531.9784.

**[C]-CF<sub>3</sub>.** Yield: %. <sup>1</sup>H NMR (700 MHz, Chloroform-*d*) δ 9.24 (dd, *J* = 8.0, 1.4 Hz, 1H), 8.40 (t, *J* = 8.0 Hz, 1H), 8.27 (dd, *J* = 7.9, 1.4 Hz, 1H), 3.20 (s, 3H). <sup>13</sup>C NMR (176 MHz, CDCl<sub>3</sub>) δ 168.65, 164.31, 152.84, 140.39, 127.71, 125.95, 20.67. <sup>19</sup>F NMR (235 MHz, CDCl<sub>3</sub>) δ -62.24. Elemental anal. calcd: C 24.80; H 0.76; N 13.14. Found: C 29.45; H 1.889; N 10.87. ESI-MS *m/z*: [M]<sup>+</sup>Na 569.9558, calcd: 569.9552.

**Linker-[C]-CF<sub>3</sub>.** [C]-CF<sub>3</sub> was diluted in DCM and the linker bicyclo[2.2.1]hept-5-en-2-yltrimethoxysilane was added in small excess (1.05eq). The DCM solution was overcoated with *n* hexane and the product was obtained as a crystalline solid. ESI-MS *m/z*: [M]<sup>+</sup>Na 756.0519, calcd: 756.0525.

**Immobilization.** The reaction was done in a double schlenk flask bridged with a filter. The functionalized SBA-15 is stored in the first flask. In the other flask, an excess of [C]-CF<sub>3</sub> dissolved in DCM was introduced and fed in with the aid of liquid nitrogen. Vacuum was applied to the double schlenk flask. After 1 h of vacuum of 1x10<sup>-3</sup> mbar, the solution was thawed and the two flask contents were added together and reacted for 36 h. The product was washed 5 times with DCM using a centrifuge.

## ASSOCIATED CONTENT

Manuscript, 1st draft by Schnierle

Supporting Information

## AUTHOR INFORMATION

Corresponding Author\*

Dr. Mark R. Ringenberg, Institut für Anorganische Chemie, Universität Stuttgart, Pfaffenwaldring 55, 70569 Stuttgart, Germany. Email: [mark.ringenberg@iac.uni-stuttgart.de](mailto:mark.ringenberg@iac.uni-stuttgart.de)

Dr. Deven P. Estes, Institut für Technische Chemie, Universität Stuttgart, Pfaffenwaldring 55, 70569 Stuttgart, Germany. Email: [deven.estes@itc.uni-stuttgart.de](mailto:deven.estes@itc.uni-stuttgart.de)

## Author Contributions

The manuscript was written through contribution and approval of the final version from all authors. †These authors contributed equally.

## Funding Sources

M.R.Ringenberg gratefully acknowledge support by the state of Baden-Württemberg through bwHPC and the German Research Foundation (DFG) through grant no. INST 40/467-1 FUGG for access to the Justus cluster. M. Schnierle and this project funded by Deutsche Forschungsgesellschaft SFB1333 C2.

**Keywords:** Kinetics • Electrochemistry • Immobilization • Surface Spectroscopy

## ACKNOWLEDGMENT

The authors gratefully acknowledge Dr. Wolfgang Frey and Dr. Falk Lissner for performing crystallographic measurements. Also a thanks to Prof. Dr. Roger Alberto and Dr. Henrik Braband for the use of the temperature-controlled, externally triggered stop flow UV/Vis reactor for the time-resolved measurements.

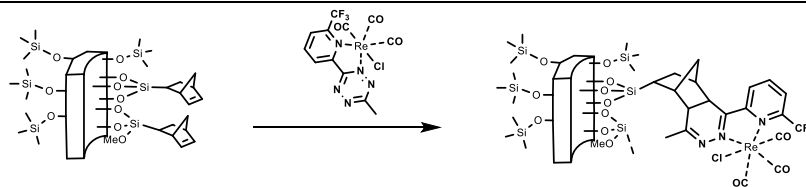
## REFERENCES

- [1] S. S. Joshi, V. V. Ranade, *Industrial Catalytic Processes for Fine and Specialty Chemicals*, 1. Aufl., Elsevier Reference Monographs, s.l., 2016, 782 pp.
- [2] H.-U. Blaser, *Catalysis Today* 2000, 60, PII: S0920586100003321, 161–165.
- [3] A. Corma, H. Garcia, *Topics in Catalysis* 2008, 48, PII: 9056, 8–31.
- [4] M. Heitbaum, F. Glorius, I. Escher, *Angewandte Chemie (International ed. in English)* 2006, 45, *Journal Article Research Support, Non-U.S. Gov't Review*, 4732–4762.
- [5] C. Martínez, A. Corma, *Coordination Chemistry Reviews* 2011, 255, PII: S0010854511001214, 1558–1580.
- [6] P. McMorn, G. J. Hutchings, *Chemical Society reviews* 2004, 33, *Journal Article Review*, 108–122.
- [7] J. A. Widegren, R. G. Finke, *Journal of Molecular Catalysis A: Chemical* 2003, 198, PII: S1381116902007288, 317–341.
- [8] B. Yilmaz, U. Müller, *Topics in Catalysis* 2009, 52, PII: 9226, 888–895.
- [9] K. Soai, M. Watanabe, A. Yamamoto, *The Journal of Organic Chemistry* 1990, 55, 4832–4835.
- [10] J. D. Webb, T. Seki, J. F. Goldston, M. Pruski, C. M. Cruden, *Microporous and Mesoporous Materials* 2015, 203, PII: S138718111400612X, 123–131.
- [11] Schnierle, M.; Blicke, S.; Filippou, V.; Ringenberg, M. R. *Chem. Commun.* 2020, 56, 12033–12036.

- [12] Kaim, W. *Coord. Chem. Rev.* 2002, 230, 127–139.
- [13] Oliveira, B. L.; Guo, Z.; Bernardes, G. J. L. *Chem. Soc. Rev.* 2017, 46, 4895–4950.
- [14] Devaraj, N. K.; Weissleder, R. *Chem. Res.* 2011, 44, 816–827.
- [15] Clavier, G.; Audebert, P. *Chem. Rev.* 2010, 110, 3299–3314.
- [16] Zhang, J.; Shukla, V.; Boger, D. L. *J. Org. Chem.* 2019, 84, 9397–9445.
- [17] Zhu, Z.; Glinkerman, C. M.; Boger, D. L. *J. Am. Chem. Soc.* 2020, 142, 20778–20787.
- [18] Salmain, M.; Fischer-Durand, N.; Rudolf, B. *ur. J. Inorg. Chem.* 2020, 2020, 21–35.
- [19] M. Schnierle, M. Leimkühler, M. R. Ringenberg, *Inorg. Chem.* 2021, 60, 6367–6374.
- [20] C. R. Benson, A. K. Hui, K. Parimal, B. J. Cook, C.-H. Chen, R. L. Lord, A. H. Flood, K. G. Caulton, *Dalton transactions (Cambridge England : 2003)* 2014, 43, Journal Article, 6513–6524.
- [21] S. Sato, T. Morimoto and O. Ishitani *Inorg. Chem.* 2007, 46, 22, 9051–9053.
- [22] J. D. Webb, T. Seki, J. F. Goldston, M. Pruski, C. M. Crudden, *Microporous and Mesoporous Materials* 2015, 203, PII: S138718111400612X, 123–131.
- [23] M. Schnierle, M. Winkler, V. Filippou, J. van Slageren and M. R. Ringenberg, *Eur. J. Inorg. Chem* 202100998 (1), 5.
- [24] J. J. Rack, J. D. Webb, and S. H. Strauss, *Inorg. Chem.* 1996, 35, 2, 277–278
- [25] J. L. Smith, R. G. Herman, C. R. Terenna, M. R. Galler, and K. Klier *J. Phys. Chem. A* 2004, 108, 1, 39–46

Manuscript, 1st draft by Schnierle

SYNOPSIS TOC. Inverse electron demand [4+2] pericyclic addition (Diels–Alder) for click onto surface.



## References

- [1] S. S. Joshi, V. V. Ranade, *Industrial Catalytic Processes for Fine and Specialty Chemicals*, 1. Aufl., Elsevier Reference Monographs, s.l., **2016**, 782 pp.
- [2] H.-U. Blaser, *Catalysis Today* **2000**, *60*, PII: S0920586100003321, 161–165.
- [3] A. Corma, H. Garcia, *Topics in Catalysis* **2008**, *48*, PII: 9056, 8–31.
- [4] M. Heitbaum, F. Glorius, I. Escher, *Angewandte Chemie (International ed. in English)* **2006**, *45*, Journal Article Research Support, Non-U.S. Gov't Review, 4732–4762.
- [5] C. Martínez, A. Corma, *Coordination Chemistry Reviews* **2011**, *255*, PII: S0010854511001214, 1558–1580.
- [6] P. McMorn, G. J. Hutchings, *Chemical Society reviews* **2004**, *33*, Journal Article Review, 108–122.
- [7] J. A. Widegren, R. G. Finke, *Journal of Molecular Catalysis A: Chemical* **2003**, *198*, PII: S1381116902007288, 317–341.
- [8] B. Yilmaz, U. Müller, *Topics in Catalysis* **2009**, *52*, PII: 9226, 888–895.
- [9] O. Beeck, *Reviews of Modern Physics* **1948**, *20*, 127–130.
- [10] G.-M. Schwab, *Transactions of the Faraday Society* **1946**, *42*, 689–697.
- [11] K. J. Laidler, *Discussions of the Faraday Society* **1950**, *8*, 47–54.
- [12] R. Schlögl, *Angewandte Chemie (International ed. in English)* **2015**, *54*, Journal Article, 3465–3520.
- [13] B. C. Gates, **01/1991**.
- [14] J. Čejka, A. Corma, S. Zones, *Zeolites and Catalysis*, Wiley, **2010**.
- [15] I. W. Davies, L. Matty, D. L. Hughes, P. J. Reider, *Journal of the American Chemical Society* **2001**, *123*, Journal Article, 10139–10140.
- [16] R. A. Sheldon in *Heterogeneous Catalysis and Fine Chemicals II, Proceedings of the 2nd International Symposium*, Studies in Surface Science and Catalysis, Elsevier, **1991**, pp. 33–54.
- [17] J. M. Thomas, R. Raja, *Topics in Catalysis* **2006**, *40*, PII: 105, 3–17.
- [18] Q.-H. Xia, H.-Q. Ge, C.-P. Ye, Z.-M. Liu, K.-X. Su, *Chemical reviews* **2005**, *105*, Journal Article, 1603–1662.

- [19] K. Kakaei, M. D. Esrafil, A. Ehsani in *Graphene Surfaces - Particles and Catalysts*, Interface Science and Technology, Elsevier, **2019**, pp. 1–21.
- [20] Z. Ma, F. Zaera in *Encyclopedia of Inorganic Chemistry*, (Eds.: R. B. King, R. H. Crabtree, C. M. Lukehart, D. A. Atwood, R. A. Scott), John Wiley & Sons, Ltd, Chichester, UK, **2006**.
- [21] J. L. Williams, *Catalysis Today* **2001**, *69*, PII: S0920586101003480, 3–9.
- [22] F. Ziegler, J. Teske, I. Elser, M. Dyballa, W. Frey, H. Kraus, N. Hansen, J. Rybka, U. Tallarek, M. R. Buchmeiser, *Journal of the American Chemical Society* **2019**, *141*, Journal Article Research Support, Non-U.S. Gov't, 19014–19022.
- [23] H. Zhong, R. Sa, H. Lv, S. Yang, D. Yuan, X. Wang, R. Wang, *Advanced Functional Materials* **2020**, *30*, 2002654.
- [24] M. J. Climent, A. Corma, S. Iborra, *RSC advances* **2012**, *2*, 16–58.
- [25] M Kim, S. Salley, K. Ng, *Energy & Fuels* **2008**, *22*, 3594–3599.
- [26] A. Ruhul, M. Kalam, H. Masjuki, I. R. Fattah, S. Reham, M. Rashed, *RSC Advances* **2015**, *5*, 101023–101044.
- [27] N. S. Talha, S. Sulaiman, et al., *ARPN Journal of Engineering and Applied Sciences* **2016**, *11*, 439–442.
- [28] M. Á. Navarro, J. Amaro-Gahete, J. R. Ruiz, C. Jiménez-Sanchidrián, F. J. Romero-Salguero, D. Esquivel, *Dalton transactions (Cambridge England : 2003)* **2022**, *51*, Journal Article, 4884–4897.
- [29] R. H. Crabtree, *The organometallic chemistry of the transition metals*, 6. Aufl., Wiley, Hoboken, N.J., **2014**, 504 pp.
- [30] F. Jensen, *Introduction to computational chemistry*, 2nd ed., John Wiley & Sons, Chichester, England and Hoboken, NJ, **2007**, 599 pp.
- [31] C. E. Housecroft, A. G. Sharpe, *Inorganic chemistry*, 3. ed., Pearson Prentice Hall, Harlow and Munich, **2008**, 1098 pp.
- [32] Gary L. Miessler, Donald A. Tarr, *Inorganic Chemistry 4th Ed.*
- [33] A. E. Martell, R. D. Hancock, *Metal Complexes in Aqueous Solutions*, Springer US, Boston, MA, **1996**.
- [34] R. Reinhardt, W. Kaim, *Zeitschrift für anorganische und allgemeine Chemie* **1993**, *619*, 1998–2005.

- [35] F. P. A. Johnson, M. W. George, F. Hartl, J. J. Turner, *Organometallics* **1996**, *15*, 3374–3387.
- [36] J. Hawecker, J.-M. Lehn, R. Ziessel, *Helvetica Chimica Acta* **1986**, *69*, 1990–2012.
- [37] J. Hawecker, J.-M. Lehn, R. Ziessel, *Journal of the Chemical Society Chemical Communications* **1984**, 328–330.
- [38] R. Arevalo, R. López, L. R. Falvello, L. Riera, J. Perez, *Chemistry (Weinheim an der Bergstrasse Germany)* **2021**, *27*, Journal Article, 379–389.
- [39] H. Takeda, K. Koike, T. Morimoto, H. Inumaru, O. Ishitani in *Inorganic Photochemistry*, Advances in Inorganic Chemistry, Elsevier, **2011**, pp. 137–186.
- [40] H. Hartmann, T. Scheiring, J. Fiedler, W. Kaim, *Journal of Organometallic Chemistry* **2000**, *604*, PII: S0022328X00002825, 267–272.
- [41] A. Klein, C. Vogler, W. Kaim, *Organometallics* **1996**, *15*, 236–244.
- [42] W. Kaim, S. Kohlmann, *Inorganic Chemistry* **1990**, *29*, 2909–2914.
- [43] E. E. Benson, C. P. Kubiak, *Chemical communications (Cambridge England)* **2012**, *48*, Journal Article, 7374–7376.
- [44] R. Anwander, *Chemistry of materials* **2001**, *13*, 4419–4438.
- [45] Z. Thiam, E. Abou-Hamad, B. Dereli, L. Liu, A.-H. Emwas, R. Ahmad, H. Jiang, A. A. Isah, P. B. Ndiaye, M. Taoufik, et al., *Journal of the American Chemical Society* **2020**, *142*, 16690–16703.
- [46] A. Domnick, C. Winter, L. Sušac, L. Hennecke, M. Hensen, N. Zitzmann, S. Trowitzsch, C. Thomas, R. Tampé, *Nature Communications* **2022**, *13*, 4701.
- [47] K. Soai, M. Watanabe, A. Yamamoto, *The Journal of Organic Chemistry* **1990**, *55*, 4832–4835.
- [48] J. D. Webb, T. Seki, J. F. Goldston, M. Pruski, C. M. Crudden, *Microporous and Mesoporous Materials* **2015**, *203*, PII: S138718111400612X, 123–131.
- [49] H. C. Kolb, M. G. Finn, K. B. Sharpless, *Angewandte Chemie (International ed. in English)* **2001**, *40*, 2004–2021.
- [50] W. Xi, T. F. Scott, C. J. Kloxin, C. N. Bowman, *Advanced Functional Materials* **2014**, *24*, 2572–2590.
- [51] W. H. Binder, R. Sachsenhofer, *Macromolecular Rapid Communications* **2007**, *28*, 15–54.

- [52] K. Nwe, M. W. Brechbiel, *Cancer Biotherapy and Radiopharmaceuticals* **2009**, *24*, 289–302.
- [53] C. S. McKay, M. Finn, *Chemistry & biology* **2014**, *21*, 1075–1101.
- [54] B. A. Kashemirov, J. L. F. Bala, X. Chen, F. H. Ebetino, Z. Xia, R. G. G. Russell, F. P. Coxon, A. J. Roelofs, M. J. Rogers, C. E. McKenna, *Bioconjugate chemistry* **2008**, *19*, Journal Article Research Support, Non-U.S. Gov't, 2308–2310.
- [55] C. Spiteri, J. E. Moses, *Angewandte Chemie (International ed. in English)* **2010**, *49*, Comment Journal Article Research Support, Non-U.S. Gov't, 31–33.
- [56] C. E. Hoyle, C. N. Bowman, *Angewandte Chemie (International ed. in English)* **2010**, *49*, Journal Article Research Support, N.I.H., Extramural Research Support, Non-U.S. Gov't Research Support, U.S. Gov't, Non-P.H.S. Review, 1540–1573.
- [57] T. Posner, *Berichte der deutschen chemischen Gesellschaft* **1905**, *38*, 646–657.
- [58] V. V. Rostovtsev, L. G. Green, V. V. Fokin, K. B. Sharpless, *Angewandte Chemie* **2002**, *114*, 2708–2711.
- [59] T. J. Del Castillo, S. Sarkar, K. A. Abboud, A. S. Veige, *Dalton transactions (Cambridge England : 2003)* **2011**, *40*, Journal Article, 8140–8144.
- [60] L. Henry, C. Schneider, B. Mützel, P. V. Simpson, C. Nagel, K. Fucke, U. Schatzschneider, *Chemical communications (Cambridge England)* **2014**, *50*, Journal Article Research Support, Non-U.S. Gov't, 15692–15695.
- [61] W. E. Bachmann, N. C. Deno, *Journal of the American Chemical Society* **1949**, *71*, 3062–3072.
- [62] R. A. A. Foster, M. C. Willis, *Chemical Society reviews* **2013**, *42*, Journal Article, 63–76.
- [63] Z. M. Png, H. Zeng, Q. Ye, J. Xu, *Chemistry an Asian journal* **2017**, *12*, Journal Article Review, 2142–2159.
- [64] R. L. Cobb, V. C. Vives, J. E. Mahan, *The Journal of Organic Chemistry* **1978**, *43*, 931–936.
- [65] S. N. Kessler, M. Neuburger, H. A. Wegner, *Journal of the American Chemical Society* **2012**, *134*, 17885–17888.
- [66] A.-C. Knall, C. Slugovc, *Chemical Society reviews* **2013**, *42*, Journal Article, 5131–5142.

- [67] H. C. Kolb, K. B. Sharpless, *Drug discovery today* **2003**, *8*, Journal Article Review, 1128–1137.
- [68] A. M. Prokhorov, D. N. Kozhevnikov in *Progress in Heterocyclic Chemistry*, Elsevier, **2013**, pp. 391–408.
- [69] J. Cioslowski, J. Sauer, J. Hetzenegger, T. Karcher, T. Hierstetter, *Journal of the American Chemical Society* **1993**, *115*, 1353–1359.
- [70] J. Sauer, D. K. Heldmann, *Tetrahedron* **1998**, *54*, PII: S0040402098001276, 4297–4312.
- [71] B. L. Oliveira, Z. Guo, G. J. L. Bernardes, *Chemical Society reviews* **2017**, *46*, Journal Article Review, 4895–4950.
- [72] J. Yang, M. R. Karver, W. Li, S. Sahu, N. K. Devaraj, *Angewandte Chemie (International ed. in English)* **2012**, *51*, Journal Article Research Support, N.I.H., Extramural Research Support, Non-U.S. Gov't Research Support, U.S. Gov't, Non-P.H.S., 5222–5225.
- [73] C. R. Benson, A. K. Hui, K. Parimal, B. J. Cook, C.-H. Chen, R. L. Lord, A. H. Flood, K. G. Caulton, *Dalton transactions (Cambridge England : 2003)* **2014**, *43*, Journal Article, 6513–6524.
- [74] Y. Qu, F.-X. Sauvage, G. Clavier, F. Miomandre, P. Audebert, *Angewandte Chemie* **2018**, *130*, 12233–12237.
- [75] W. Kaim, *Coordination Chemistry Reviews* **2002**, *230*, PII: S0010854502000449, 127–139.
- [76] Neumüller-Schnierle, *University Stuttgart unpublished results*.
- [77] L. Neumüller, *University Stuttgart* **2022**, Bachelorthesis.
- [78] *Chemical Rocket Propulsion*, (Eds.: L. T. de Luca, T. Shimada, V. P. Sinditskii, M. Calabro), Springer International Publishing, Cham, **2017**.
- [79] D. E. Chavez, M. A. Hiskey, D. L. Naud, *Propellants Explosives Pyrotechnics* **2004**, *29*, 209–215.
- [80] I. N. Zyuzin, I. Y. Gudkova, D. B. Lempert, *Russian Journal of Physical Chemistry B* **2021**, *15*, PII: 8401, 611–621.
- [81] K. Kang, J. Park, E. Kim, *Proteome science* **2016**, *15*, Journal Article Review, 15.
- [82] M. A. Kassem, G. O. El-Sayed, *Journal of Environmental Analytical Chemistry* **2014**, *01*, DOI 10.4172/jreac.1000102.



- [83] K. Gustav, J.-C. Schmidt, *Zeitschrift für Chemie* **1969**, *9*, 32–33.
- [84] A. A. Schilt, W. E. Dunbar, B. W. Gandrud, S. E. Warren, *Talanta* **1970**, *17*, Journal Article, 649–653.
- [85] M. A. Lemes, G. Brunet, A. Pialat, L. Ungur, I. Korobkov, M. Murugesu, *Chemical communications (Cambridge England)* **2017**, *53*, Journal Article, 8660–8663.
- [86] A. M.-H. Yip, C. K.-H. Lai, K. S.-M. Yiu, K. K.-W. Lo, *Angewandte Chemie* **2022**, *134*, DOI 10.1002/ange.202116078.
- [87] T. S.-M. Tang, H.-W. Liu, K. K.-W. Lo, *Chemical communications (Cambridge England)* **2017**, *53*, Journal Article, 3299–3302.
- [88] B. Oliveira, Z Guo, G. Bernardes, *Chemical Society Reviews* **2017**, *46*, 4895–4950.
- [89] M. L. Blackman, M. Royzen, J. M. Fox, *Journal of the American Chemical Society* **2008**, *130*, 13518–13519.
- [90] T. S.-M. Tang, H.-W. Liu, K. K.-W. Lo, *Chemical Communications* **2017**, *53*, 3299–3302.
- [91] W. Kaim, *Coordination Chemistry Reviews* **2002**, *230*, 127–139.
- [92] N. K. Devaraj, R. Weissleder, *Accounts of chemical research* **2011**, *44*, 816–827.
- [93] M. Meldal, C. W. Tornøe, *Chemical reviews* **2008**, *108*, 2952–3015.
- [94] S. Mushtaq, S.-J. Yun, J. Jeon, *Molecules* **2019**, *24*, 3567.
- [95] G. I. Anderton, A. S. Bangerter, T. C. Davis, Z. Feng, A. J. Furtak, J. O. Larsen, T. L. Scroggin, J. M. Heemstra, *Bioconjugate Chemistry* **2015**, *26*, 1687–1691.
- [96] W. Chen, D. Wang, C. Dai, D. Hamelberg, B. Wang, *Chemical communications* **2012**, *48*, 1736–1738.
- [97] B. Sarkar, R. H. Laye, B. Mondal, S. Chakraborty, R. L. Paul, J. C. Jeffery, V. G. Puranik, M. D. Ward, G. K. Lahiri, *Journal of the Chemical Society Dalton Transactions* **2002**, 2097–2101.
- [98] G. Clavier, P. Audebert, *Chemical reviews* **2010**, *110*, 3299–3314.
- [99] K. Soai, M. Watanabe, A. Yamamoto, *The Journal of Organic Chemistry* **1990**, *55*, 4832–4835.
- [100] J. D. Webb, T. Seki, J. F. Goldston, M. Pruski, C. M. Crudden, *Microporous and Mesoporous Materials* **2015**, *203*, 123–131.

- [101] F. Ziegler, J. Teske, I. Elser, M. Dyballa, W. Frey, H. Kraus, N. Hansen, J. Rybka, U. Tallarek, M. R. Buchmeiser, *Journal of the American Chemical Society* **2019**, *141*, 19014–19022.
- [102] M. Á. Navarro, J. Amaro-Gahete, J. R. Ruiz, C. Jiménez-Sanchidrián, F. J. Romero-Salguero, D. Esquivel, *Dalton Transactions* **2022**, *51*, 4884–4897.
- [103] P. Delahay, G. Mamantov, *Analytical Chemistry* **1955**, *27*, 478–483.
- [104] S. S. Gwebu, G. H. Mhlongo, N. W. Maxakato, *Voltammetry*, Sandile Surprise Gwebu (VerfasserIn) Gugu Hlengiwe Mhlongo (VerfasserIn) Nobanathi Wendy Maxakato (VerfasserIn), IntechOpen, Erscheinungsort nicht ermittelbar, **2019**, 116 pp.
- [105] J. F. Rusling, S. L. Suib, *Advanced Materials* **1994**, *6*, 922–930.
- [106] N. Elgrishi, K. J. Rountree, B. D. McCarthy, E. S. Rountree, T. T. Eisenhart, J. L. Dempsey, *Journal of Chemical Education* **2018**, *95*, 197–206.
- [107] J. Heinze, *Angewandte Chemie International Edition in English* **1984**, *23*, 831–847.
- [108] M. Ebihara, M. Iiba, H. Matsuoka, T. Kawamura, *Inorganica Chimica Acta* **2004**, *357*, PII: S0020169303006583, 1236–1242.
- [109] M. Schnierle, M. Leimkühler, M. R. Ringenberg, *Inorganic chemistry* **2021**, *60*, Journal Article, 6367–6374.
- [110] C. G. Zoski, *Handbook of Electrochemistry*, Zoski, Cynthia G (VerfasserIn), Elsevier Science & Technology, Oxford, **2007**, 935 pp.
- [111] *Spectroelectrochemistry*, (Eds.: W. Kaim, A. Klein), Royal Society of Chemistry, Cambridge, **2008**, 248 pp.
- [112] J. H. Espenson, *Chemical kinetics and reaction mechanisms*, MacGraw-Hill, New York, NY, **1981**, 218 pp.
- [113] J. F. Corbett, *Journal of Chemical Education* **1972**, *49*, 663.



## 8 Appendices

### Supporting Infos of Paper 1.

Electronic Supplementary Material (ESI) for ChemComm.  
This journal is © The Royal Society of Chemistry 2020

#### SUPPLEMENTARY INFORMATION

#### TETRAZINE METALLATION BOOSTS RATE AND REGIOSELECTIVITY OF INVERSE ELECTRONIC DEMAND DIELS-ALDER (IEDDA) ADDITION OF DIENOPHILES

Marc Schnierle<sup>†</sup>, Svenja Blickle<sup>†</sup>, Vasileios Filippou<sup>†\*</sup>, and Mark R. Ringenberg<sup>†\*</sup>

<sup>†</sup> Institut für Anorganische Chemie, Universität Stuttgart, Pfaffenwaldring 55, 70569  
Stuttgart, Germany

## Contents

<b>1</b>	<b>Experimental</b>	<b>S3</b>
<b>2</b>	<b>DFT Calculations</b>	<b>S3</b>
<b>3</b>	<b>References</b>	<b>S4</b>
<b>4</b>	<b>Kinetics</b>	<b>S8</b>
<b>5</b>	<b>NMR Spectroscopy</b>	<b>S20</b>
<b>6</b>	<b>Crystallography</b>	<b>S38</b>
<b>7</b>	<b>XYZ Coordinates from DFT calculations</b>	<b>S40</b>

## List of Figures

S1	4,5- and 1,4-dhp isomers of <b>1</b> Fe . . . . .	S4
S2	4,5- and 1,4-dhp isomers of <b>1</b> Cl . . . . .	S5
S3	PES of iEDDA Reaction . . . . .	S5
S4	PES of Cl vs. CO-approach of Ci . . . . .	S6
S5	PES of Cl vs. CO-approach of ViFc . . . . .	S7
S6	PES of TzPy + ViFc . . . . .	S8
S7	Eyring Plot of ViFc + 1 . . . . .	S9
S8	Kinetics Trace of ViFc + 1, 22C . . . . .	S10
S9	Kinetics Trace of ViFc + 1, 0 C . . . . .	S11
S10	Kinetics Trace of ViFc + 1, 10 C . . . . .	S12
S11	Kinetics Trace of ViFc + 1, 40 C . . . . .	S13
S12	Eyring Plot of Ci + 1 . . . . .	S14
S13	Kinetics Trace of Ci + 1 . . . . .	S15
S14	Kinetics Trace of TCO + 1 . . . . .	S16
S15	Kinetics Trace of TCO + 1 at 0C . . . . .	S16
S16	Kinetics Trace of TCO + 1 at 10 C . . . . .	S17
S17	Eyring Plot of TCO + 1 . . . . .	S17
S18	Eyring Plot of ViFc + TzPy . . . . .	S18
S19	Kinetics Trace of TzPy + ViFc . . . . .	S19
S20	<sup>1</sup> H NMR of <b>1</b> . . . . .	S20
S21	<sup>1</sup> H NMR of <b>1</b> Fe . . . . .	S21
S22	<sup>1</sup> H NMR of <b>1</b> Fe zoom . . . . .	S21

S23	COSY NMR of <b>1Fc</b> . . . . .	S22
S24	<sup>1</sup> H NMR of <b>1Ci</b> . . . . .	S23
S25	<sup>1</sup> H NMR of <b>1Ci</b> zoom . . . . .	S24
S26	COSY NMR of <b>1Ci</b> . . . . .	S25
S27	<sup>1</sup> H NMR of <b>1TCO</b> . . . . .	S26
S28	<sup>1</sup> H NMR of <b>1TCO</b> zoom . . . . .	S27
S29	COSY NMR of <b>1TCO</b> . . . . .	S28
S30	<sup>1</sup> H NMR of <b>1Allyltrimethylsilane</b> . . . . .	S29
S31	<sup>1</sup> H NMR of <b>1Allyltrimethylsilane</b> zoom . . . . .	S30
S32	COSY NMR of <b>1Allyltrimethylsilane</b> . . . . .	S31
S33	<sup>1</sup> H NMR of <b>1Vinyltrimethoxysilane</b> . . . . .	S32
S34	<sup>1</sup> H NMR of <b>1Vinyltrimethoxysilane</b> zoom . . . . .	S33
S35	COSY NMR of <b>1Vinyltrimethoxysilane</b> . . . . .	S34
S36	<sup>1</sup> H NMR of <b>1Quinine</b> . . . . .	S35
S37	<sup>1</sup> H NMR of <b>1PhCCH</b> . . . . .	S36
S38	<sup>1</sup> H NMR of <b>ViFc</b> . . . . .	S37
S39	<sup>1</sup> H NMR of <b>ViFc + TzPy</b> . . . . .	S38
S40	Molecular Structure of <b>TzPy</b> . . . . .	S38

## List of Tables

S1	Crystallographic Information for Complexes Reported Herein . . . . .	S39
S2	Crystallographic Information 2 for Complexes Reported Herein . . . . .	S39

## 1 Experimental

The ligand TzPy and the *trans*-cyclooctene were purchased or generously provided from TTI GmbH/TGU Varimol ([www.varimol.de](http://www.varimol.de))

**[ReCl(CO)3(TzPy)]** was made by refluxing the  $\text{ReCl}(\text{CO})_5$  (100 mg, 0.277 mmol) with TzPy (44 mg, 0.277 mmol) in toluene for 3 h. After the reaction solution was cooled to room temperature, hexanes was over-layered and allowed to slowly diffuse into the solution to produce crystals of **[1]**. Yield: 97 mg (76.1%). IR ( $\text{CH}_2\text{Cl}_2$ ):  $\nu_{\text{CO}} = 2033, 1948, 1920 \text{ cm}^{-1}$ .  $\lambda_{\text{max}}(\epsilon) = 522 \text{ nm}$  ( $2924 \text{ M}^{-1} \text{ cm}^{-1}$ ). Elemental anal. Calcd (%) for  $\text{C}_{10}\text{H}_5\text{ClN}_5\text{O}_3\text{Re} - 0.2\text{C}_7\text{H}_8 - 0.2\text{H}_2\text{O}$ : C, 28.1; H, 1.53; N, 14.44. Found: C, 28.12; H, 1.45; N, 14.38 (max. diff: 0.08).

## 2 DFT Calculations

**Calculations.** All calculations reported herein were done with the ORCA program package. **[1]** The structure of **[1]**, **[1Fc]** and **[1Ci]** was calculated using the molecular structure as a base. The structure of 1,4- and 4,5-dihydropyridazine of **[1Fc]** and **[1Ci]** were determined respectively by shifting the proton and finding the energy minimum structure, using the the same basis sets and level of theory as for the structures determined from the molecular structures. The geometry optimizations were carried out at the TPSS level of DFT.<sup>[2,3]</sup> Accurate triplet- $\zeta$  valence basis sets with one set of polarization functions on all atoms were used (def2-TZVP) and J-approximation as an auxiliary basis set with RI approximation. The SCF calculations were of spin-polarized type with Tight convergence ( $1 \times 10^{-9}$  Eh in energy).

A DFT potential energy surface scan was performed in which the olefin was brought to the tetrazine moiety of **[1]**. The first energy minima was found after the dearomatization of the tetrazine moiety. This energy minima was then used to determine the energy of  $\text{N}_2$  release by increasing the distance between the one of the uncoordinated nitrogen atoms and the carbon atom from 1.58 Å to 3.5 Å. The activation energy of the approach of the olefin to the tetrazine was confirmed by increasing the distance between the  $\beta\text{C}$  of the olefin and the carbon atom in the tetrazine from 1.5 Å to 3.5 Å. Only the *endo*- approach of the olefin was considered because attempt to calculate the *exo*-approach resulted in unreasonable activation energies. The Cl-face versus CO-face approach of the olefin to **[1]** was determined only for the first step to show the difference in activation energy.

### 3 References

1. F. Neese, "The orca program system," Wiley Interdisciplinary Reviews: Computational Molecular Science **2012**, 2, 73-78.
2. A. D. Becke, "Density-functional exchange-energy approximation with correct asymptotic behavior," *Phys. Rev. A*, **1988**, 38, 3098-3100.
3. J. P. Perdew, "Density-functional approximation for the correlation energy of the inhomogeneous electron gas," *Phys. Rev. B*, **1986**, 33, 8822-8824.

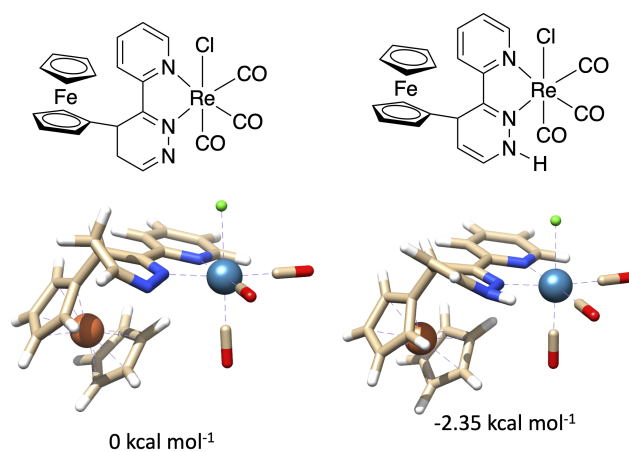


Figure S1: Molecular structures of 4,5-dhp (left) and 1,4-dhp (right) of [1Fc], difference in energy shown in kcal. Calculations were performed using TPSS basis set at def2-TZVP/J level of theory with TightSCF, in the gas-phase.



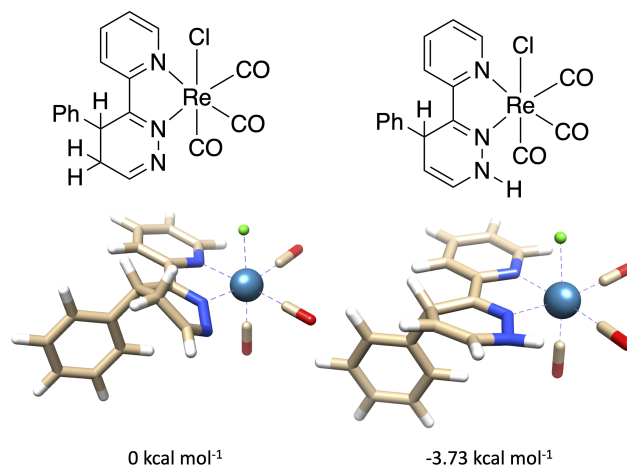


Figure S2: Molecular structures of 4,5-dhp (left) and 1,4-dhp (right) of [1Ci], difference in energy shown in kcal. Calculations were performed using TPSS basis set at def2-TZVP/J level of theory with TightSCF, in the gas-phase.

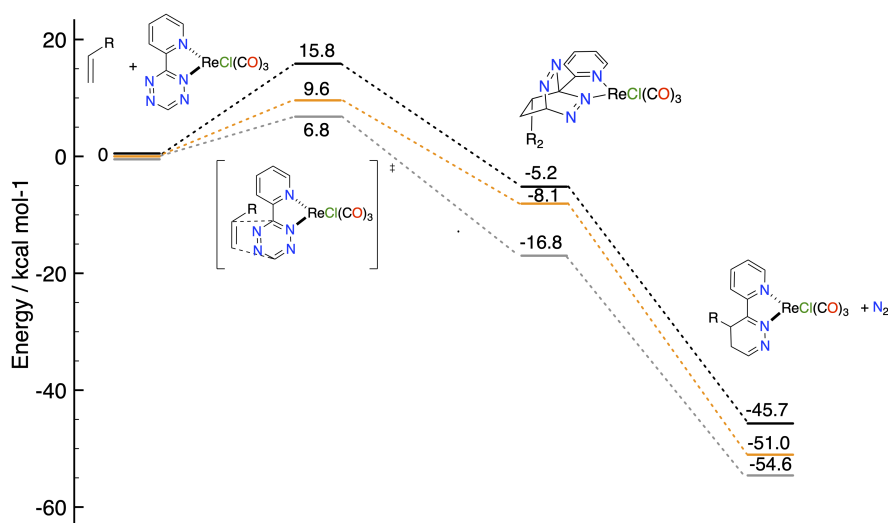


Figure S3: Potential energy surface scan between olefin and [1], and the three olefins discussed in the manuscript, styrene (gray), vinylferrocene (orange) and *trans*-cyclooctene (black). Calculations were performed using TPSS basis set at def2-TZVP/J level of theory with TightSCF, in the gas-phase.

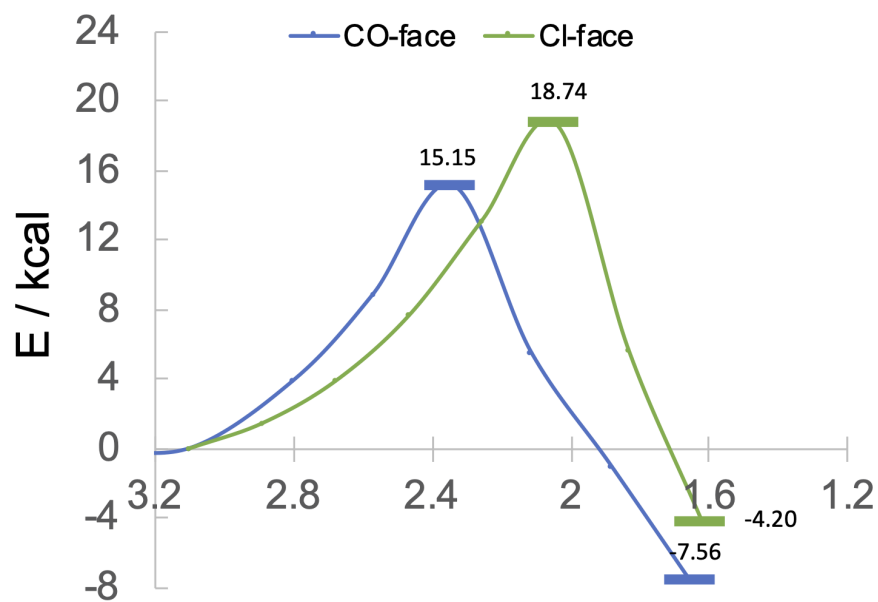


Figure S4: Potential energy surface scan between Ci and [1], from Cl-face (green) and CO-face (blue). Calculations were performed using TPSS basis set at def2-TZVP/J level of theory with TightSCF, in the gas-phase.

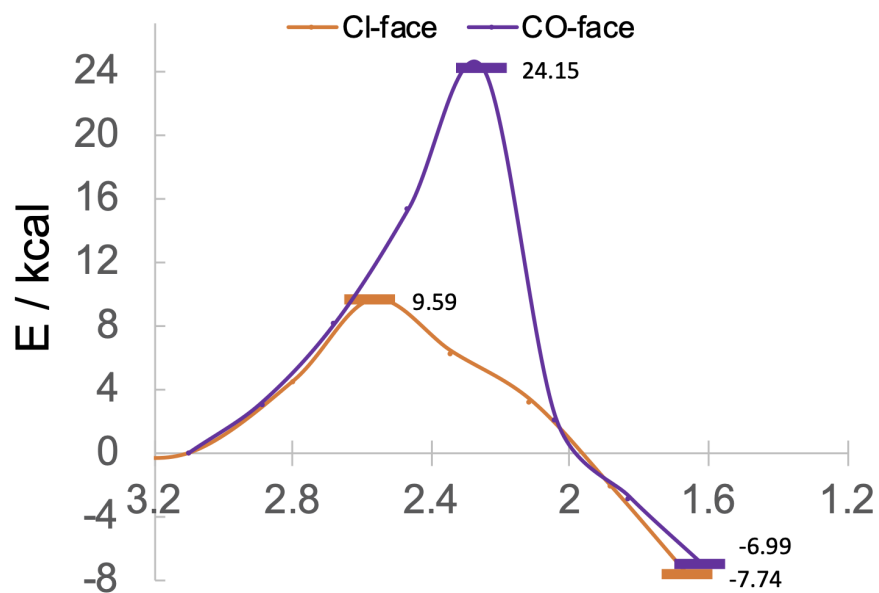


Figure S5: Potential energy surface scan between ViFc and [1], from Cl-face (orange) and CO-face (purple). Calculations were performed using TPSS basis set at def2-TZVP/J level of theory with TightSCF, in the gas-phase.

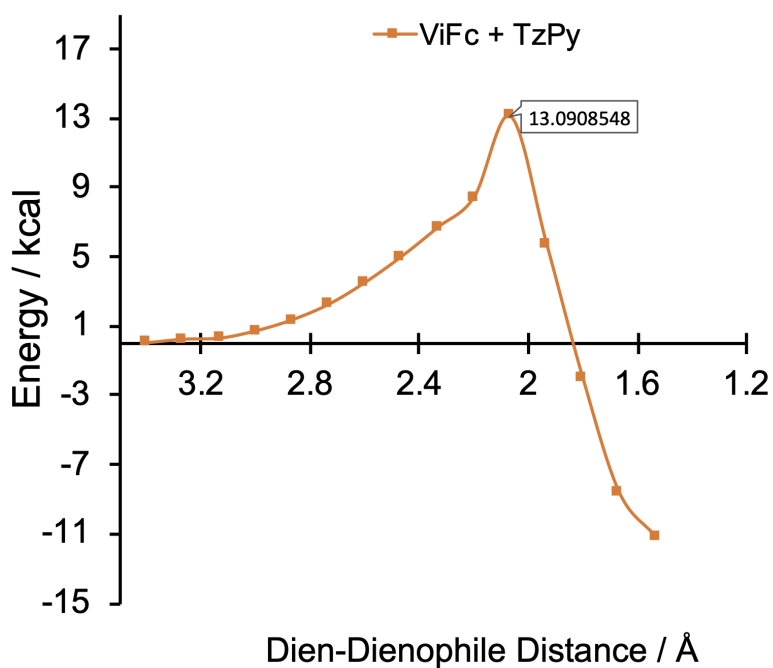


Figure S6: Potential energy surface scan between ViFc and TzPy. Calculations were performed using TPSS basis set at def2-TZVP/J level of theory with TightSCF, in the gas-phase.

## 4 Kinetics

1<sup>st</sup> order kinetics fitted using equation 2-33 (p 23) and 2<sup>nd</sup> order kinetics fitted using equation 2-35 (p 24) from Espenson "Chemical Kinetics" 1981 McGraw-Hill Education. The data was fitted using the corresponding equation on a MacBook Pro 2019 using Plot2 Pro Version 2.6.6 (9980) graphing program, for more information see micw.org.

$P_t$  = absorption at time  $t$

$P_0$  = initial absorption at time 0

$P_\infty$  = absorption at time infinity (reaction end point)

$k$  = rate constant

$t$  = time

$$\ln \frac{P_t - P_\infty}{P_0 - P_\infty} = -kt \quad (2-33)$$

$$P_t = (P_0 - P_\infty)e^{-kt} + P_\infty$$

$P_t$  = absorption at time  $t$

$P_0$  = initial absorption at time 0

$P_\infty$  = absorption at time infinity (reaction end point)

$k$  = rate constant

$t$  = time

$[A]_0$  = initial concentration of [1]

$[B]_0$  = initial concentration of ViFc

$$\Delta_0 = [B]_0 - [A]_0$$

$$\ln\left(1 + \frac{\Delta_0}{[A]_0} * \frac{P_0 - P_\infty}{P_t - P_\infty}\right) = \ln\frac{[B]_0}{[A]_0} + \Delta_0 kt \quad (2-35)$$

$$P_t = [(P_0 - P_\infty) * \left(\frac{[B]_0}{\Delta_0} + \frac{[A]_0}{\Delta_0} e^{\Delta_0 kt}\right)^{-1}] + P_\infty$$

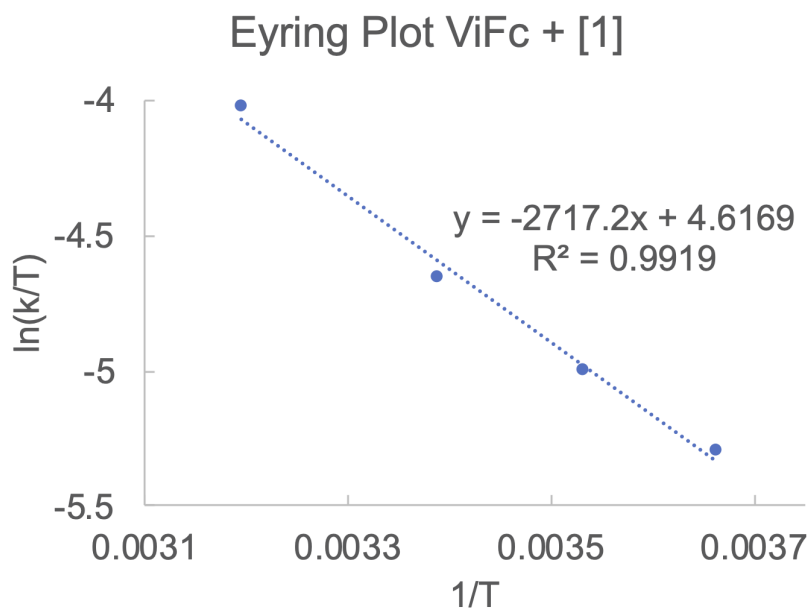


Figure S7: Eyring Plot of ViFc + [1]

Equations used for Eyring analysis

$$y = mx + b$$

$$m = \frac{-\Delta H^\ddagger}{R}$$

$$b = \ln\left(\frac{k'}{h}\right) + \frac{\Delta S^\ddagger}{R}$$

$$\ln\left(\frac{k'}{h}\right) = 23.7638$$

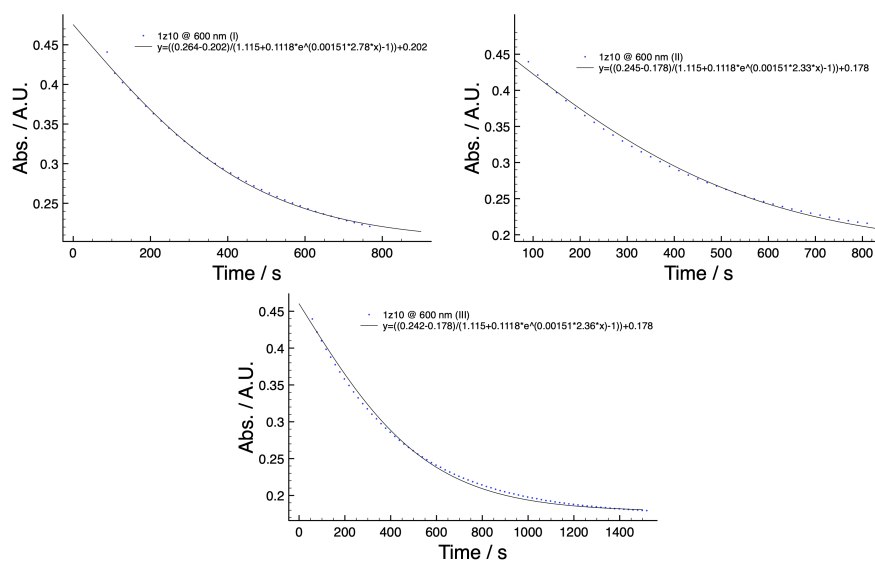


Figure S8: 2<sup>nd</sup> order kinetics trace of ViFc + [1], 22C. Signal at 600 nm, 2nd order equation used to fit the data. Concentration of [1] = 0.000168 M, [ViFc] = 0.00167 M.

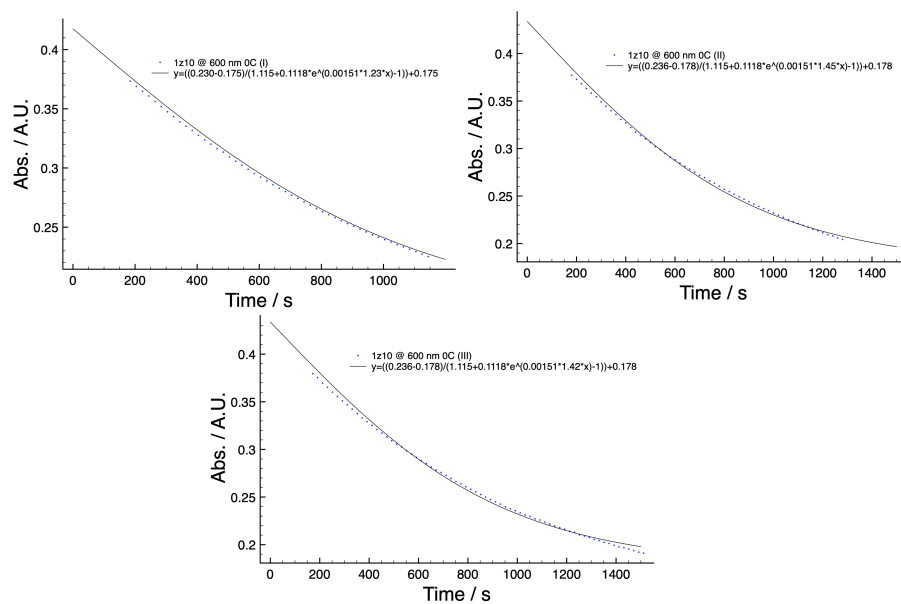


Figure S9: 2<sup>nd</sup> order kinetics trace of ViFc + [1], 0 C. Signal at 545 normalized and the 2nd order equation used to fit the data. Concentration of [1] = 0.000168 M, [ViFc] = 0.00167 M.

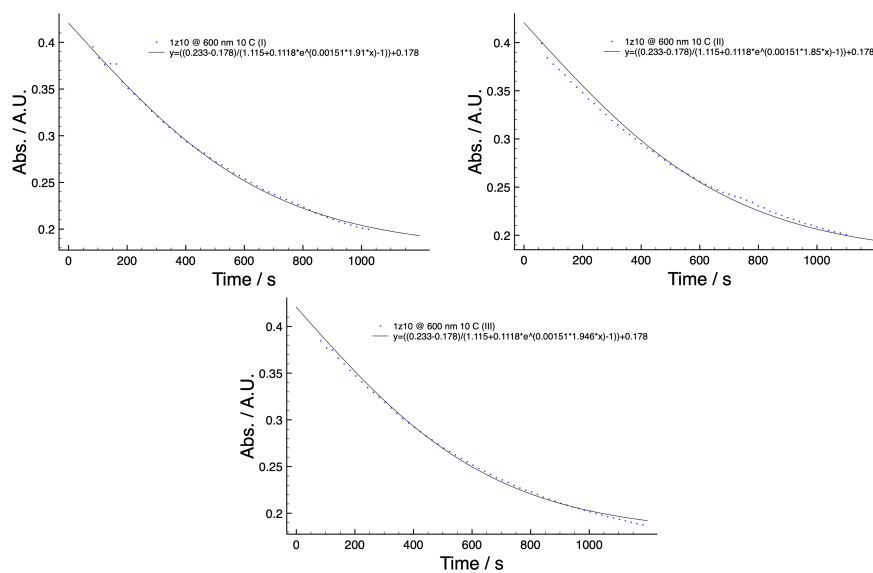


Figure S10: 2<sup>nd</sup> order kinetics trace off ViFc + [1], 10 C. Signal at 545 normalized and the 2<sup>nd</sup> order equation used to fit the data. Concentration of [1] = 0.000168 M, [ViFc] = 0.00167 M.



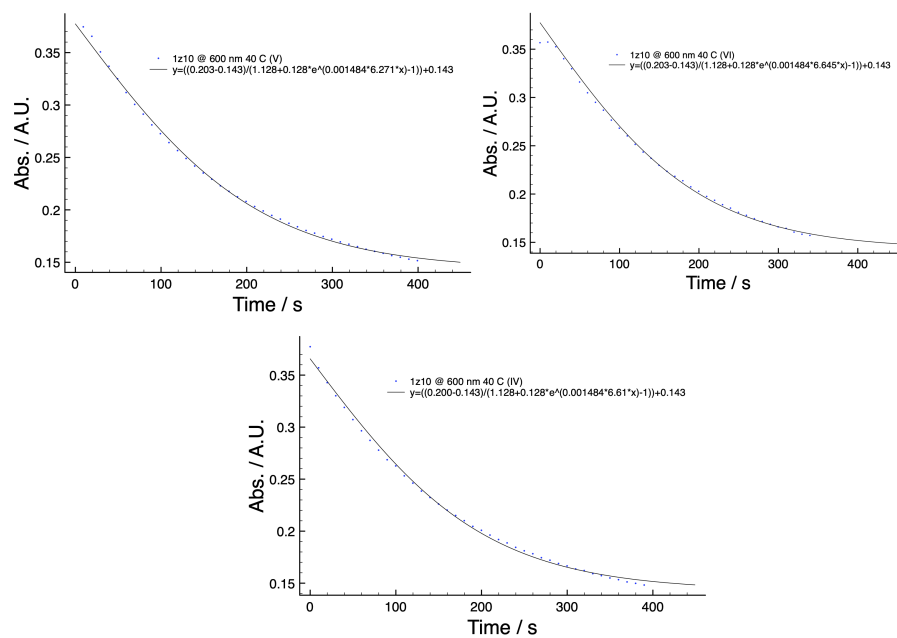


Figure S11: 2<sup>nd</sup> order kinetics trace of ViFc + [1], 44C. Signal at 545 normalized and the 2<sup>nd</sup> order equation used to fit the data. Concentration of [1] = 0.000190 M, [ViFc] = 0.00167 M.

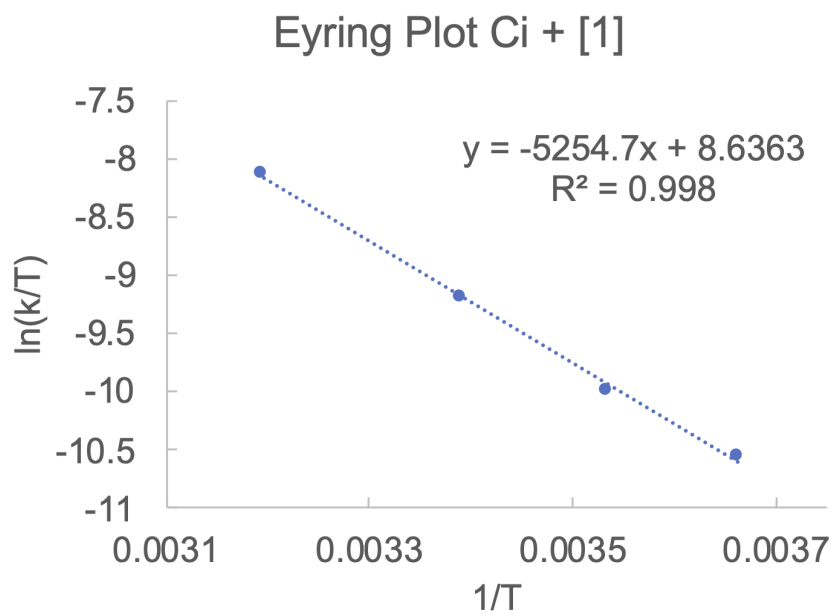


Figure S12: Eyring Plot of Ci + [1]

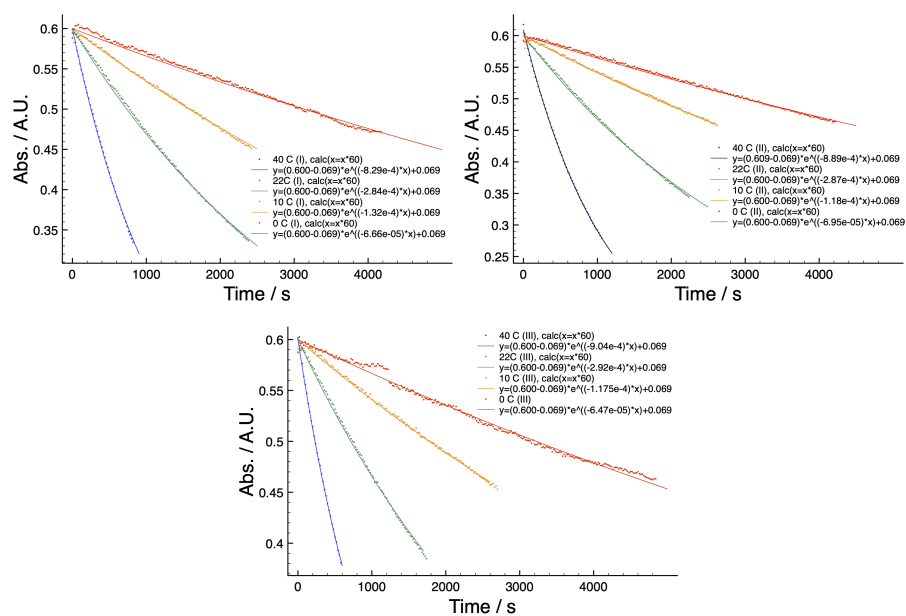


Figure S13: Pseudo 1<sup>st</sup> order kinetics trace of  $C_i + [1]$ , at different temperatures. Signal at 545 normalized and the 1st order equation used to fit the data, run at 50 equiv.  $C_i$ . Concentration of  $[1] = 0.000190$  M,  $[C_i] = 0.00949$  M.

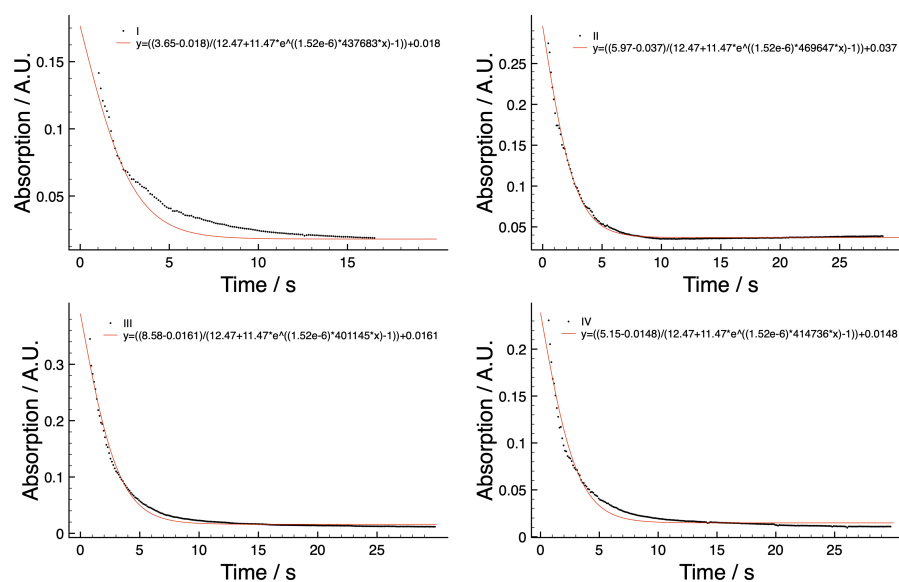


Figure S14: 2<sup>nd</sup> order kinetics trace of TCO + [1], at room temperature. 2<sup>nd</sup> order equation used to fit the data, Concentration [1] = 3.45 x 10<sup>-5</sup> M, [TCO] = 3.79 x 10<sup>-5</sup>.

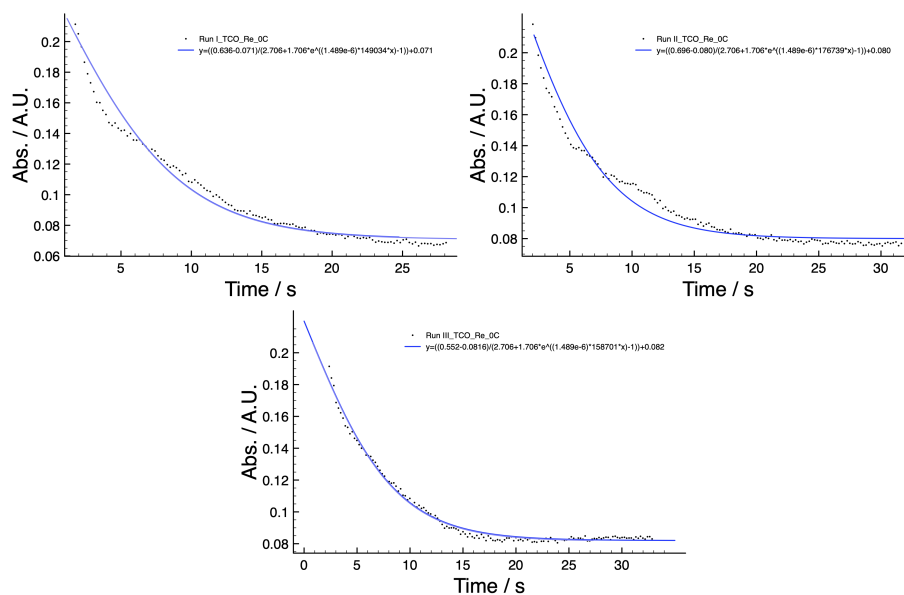


Figure S15: 2<sup>nd</sup> order kinetics trace of TCO + [1], at 0 C. 2<sup>nd</sup> order equation used to fit the data, Concentration [1] = 2.54 x 10<sup>-6</sup> M, [TCO] = 4.03 x 10<sup>-6</sup>.

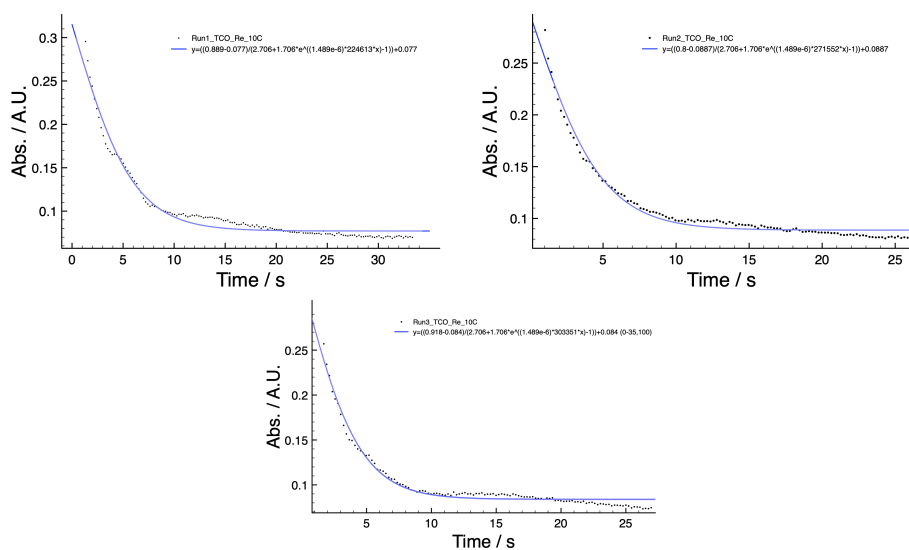


Figure S16: 2<sup>nd</sup> order kinetics trace of TCO + [1], at 10 C. 2nd order equation used to fit the data, Concentration [1] =  $2.54 \times 10^{-6}$  M, [TCO] =  $4.03 \times 10^{-6}$ .

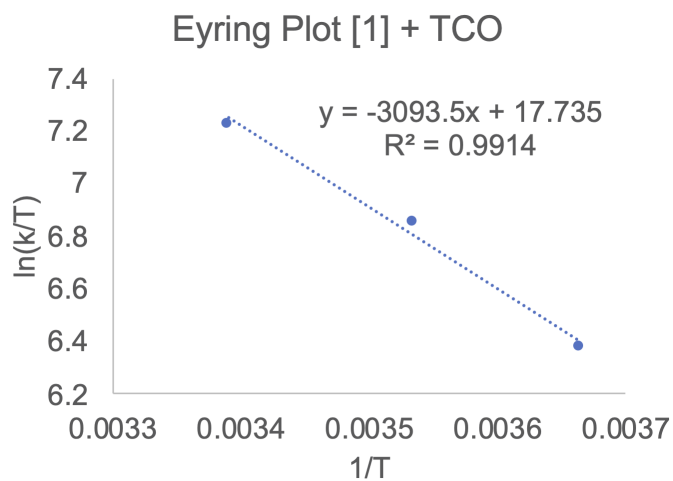


Figure S17: Eyring Plot of TCO + [1]

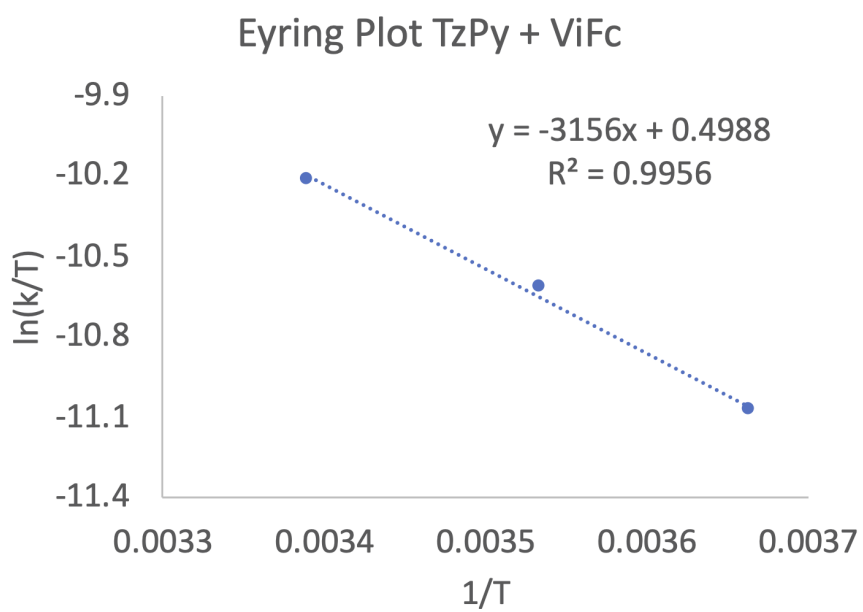


Figure S18: Eyring Plot of ViFc + TzPy

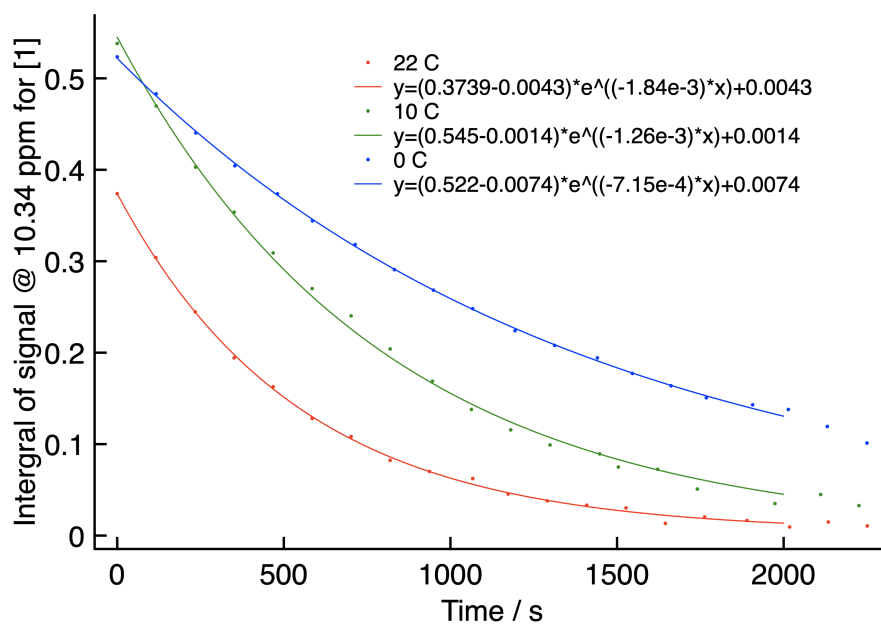


Figure S19: Pseudo 1<sup>st</sup> order kinetics trace of TzPy + ViFc (xs), at different temperatures. Signal at 9 ppm normalized and the 1st order equation used to fit the data, run at 4 equiv. ViFc. Concentration of TzPy = 0.042439M M, ViFc = 0.169747M

## 5 NMR Spectroscopy

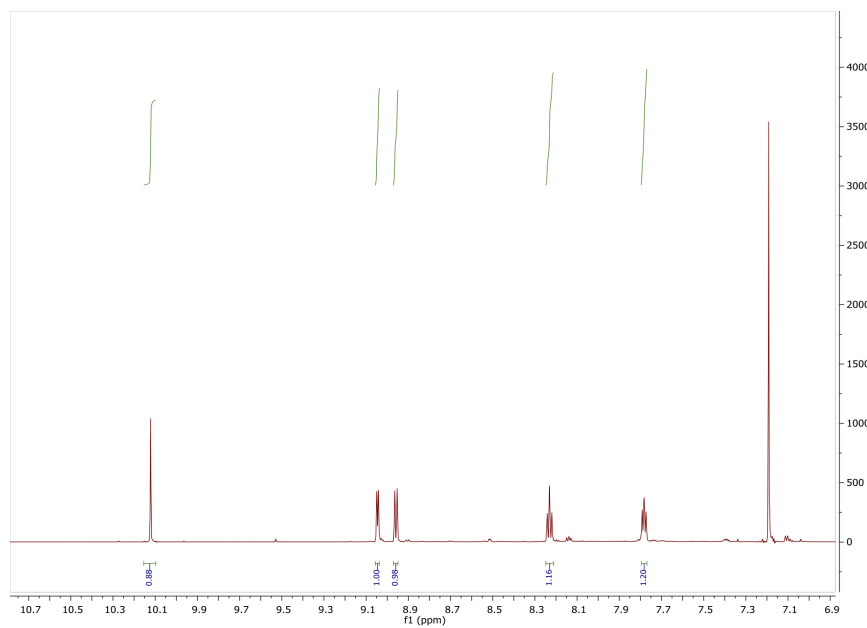


Figure S20:  $^1\text{H}$  NMR of [1] (700 MHz, Chloroform- $d$ )  $\delta$  10.19 (s, 1H), 9.11 (d,  $J = 5.3$  Hz, 1H), 9.03 (d,  $J = 7.9$  Hz, 1H), 8.30 (t,  $J = 7.8$  Hz, 1H), 7.85 (t,  $J = 6.5$  Hz, 1H).



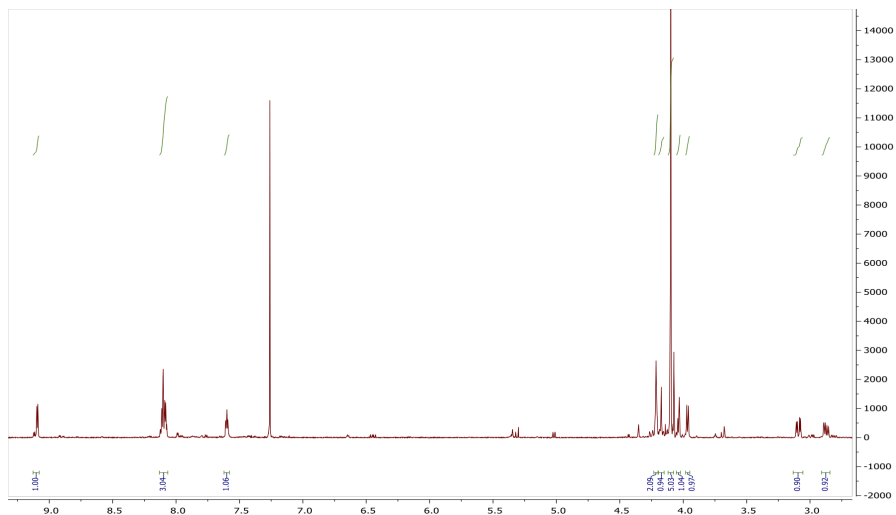


Figure S21:  $^1\text{H}$  NMR of [1Fc] (700 MHz, Chloroform- $d$ )  $\delta$  9.09 (d,  $J = 5.3$  Hz, 1H), 8.13 – 8.07 (m, 3H), 7.60 (ddd,  $J = 7.2, 5.5, 2.1$  Hz, 1H), 4.22 – 4.20 (m, 2H), 4.17 (s, 1H), 4.10 (s, 5H), 4.04 – 4.02 (m, 1H), 3.97 (d,  $J = 8.9$  Hz, 1H), 3.09 (dd,  $J = 18.3, 5.4$  Hz, 1H), 2.87 (ddd,  $J = 18.1, 8.7, 1.3$  Hz, 1H). Major Product

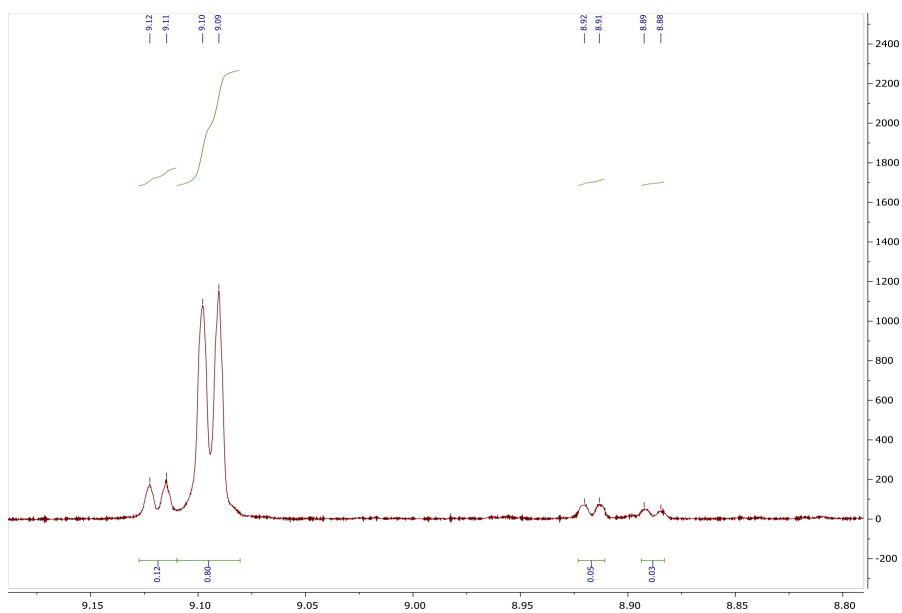


Figure S22:  $^1\text{H}$  NMR of [1Fc] (700 MHz, Chloroform- $d$ ) zoom of low field signals showing signals from minor products, ratio 0.12:0.8:0.08

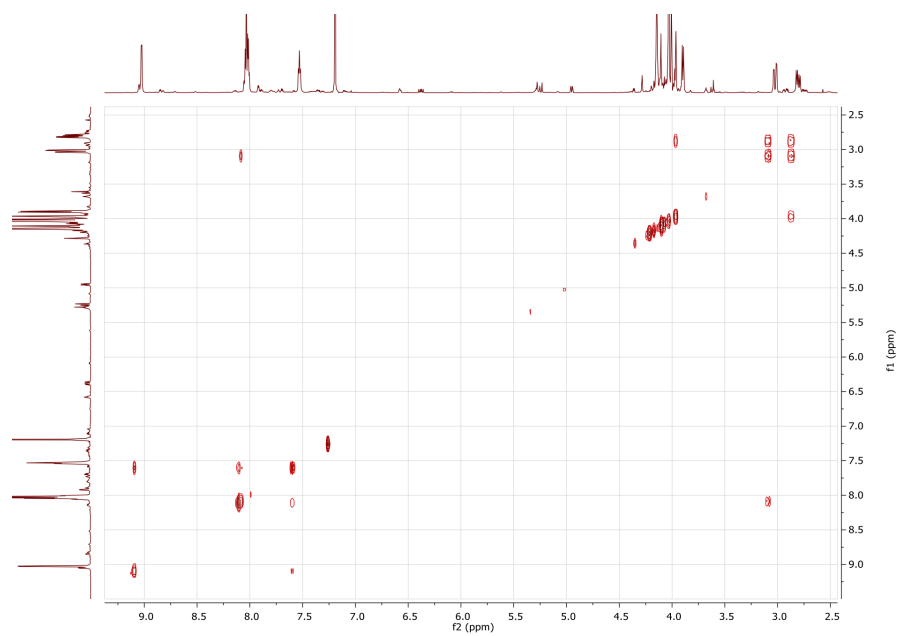


Figure S23: COSY NMR of [1Fc] (700 MHz, Chloroform-d) cross signals of major product

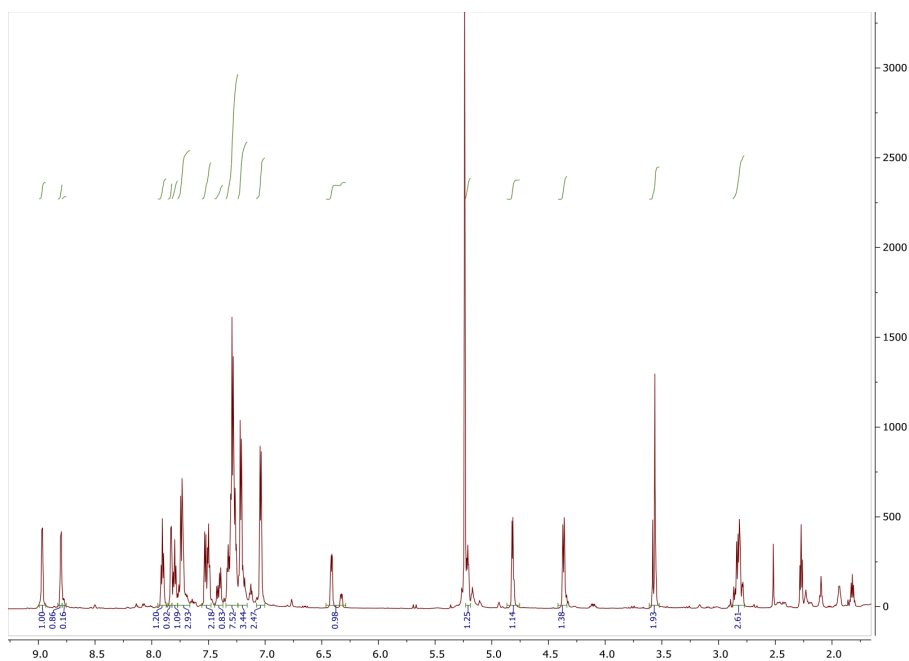


Figure S24: <sup>1</sup>H NMR of [1Ci] (700 MHz, Methylene Chloride-d<sub>2</sub>) δ 8.97 (d, J = 5.4 Hz, 1H), 8.80 (d, J = 5.4 Hz, 1H), 7.91 (t, J = 7.8 Hz, 1H), 7.86 – 7.82 (m, 1H), 7.80 (t, J = 7.9 Hz, 1H), 7.74 (q, J = 8.4, 5.7 Hz, 3H), 7.56 – 7.48 (m, 2H), 7.41 (dd, J = 17.3, 8.0 Hz, 1H), 7.29 (tt, J = 19.5, 7.1 Hz, 8H), 7.24 – 7.16 (m, 3H), 7.04 (d J = 7.2 Hz, 2H), 6.37 (ddd, J = 60.5, 7.7, 3.4 Hz, 1H), 5.23 – 5.19 (m, 1H), 4.81 (dd, J = 8.3, 5.2 Hz, 1H), 4.37 (d, J = 9.0 Hz, 1H), 3.61 – 3.52 (m, 2H), 2.87 – 2.77 (m, 3H).

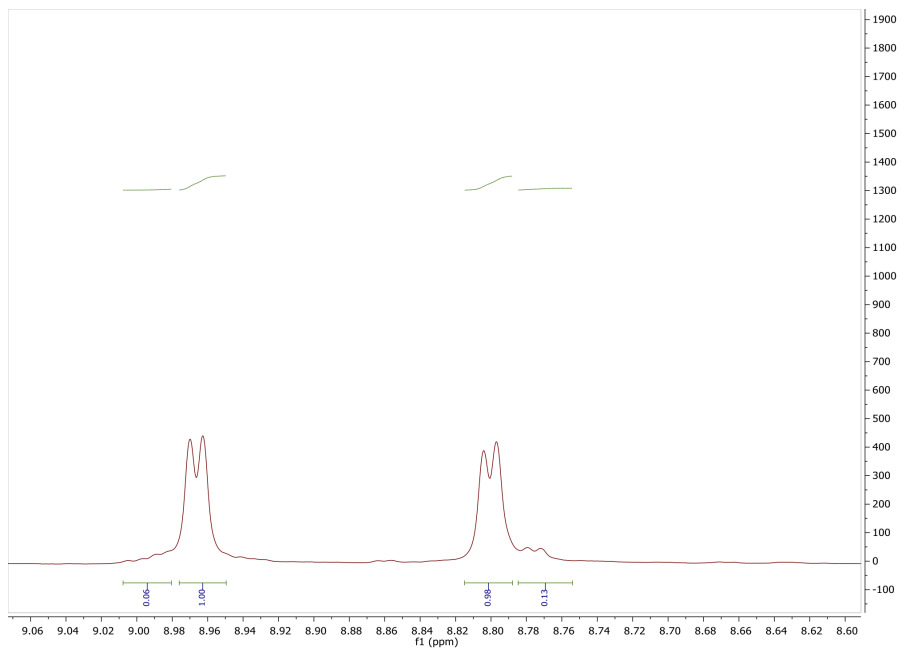


Figure S25:  $^1\text{H}$  NMR of [1Ci] (700 MHz, Chloroform-d) zoom of low field signals showing signals from minor products product ratio 0.03:0.46:0.46:0.05



Figure S26: COSY NMR of [1Ci] (700 MHz, Chloroform-d)

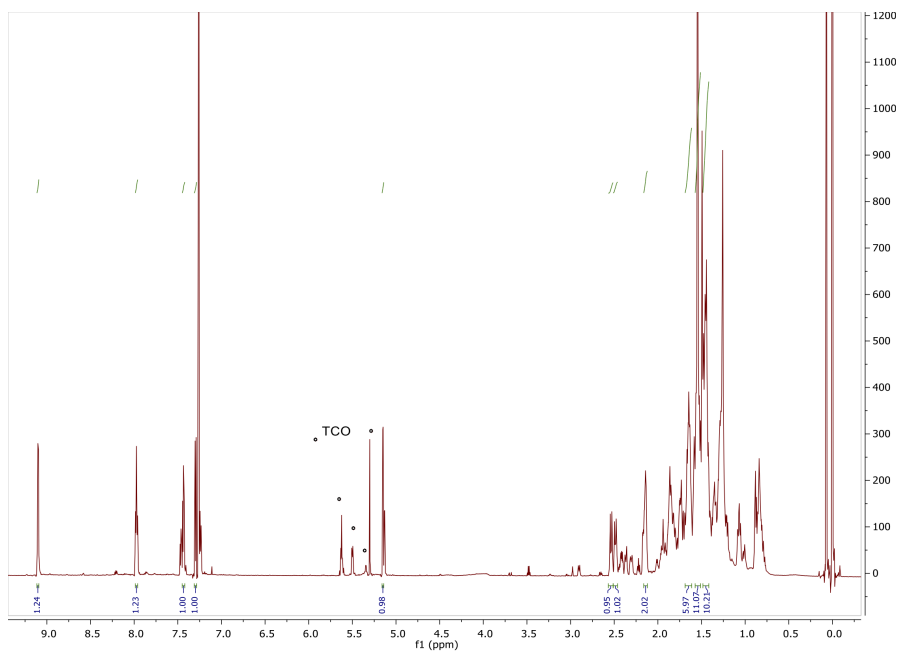


Figure S27:  $^1\text{H}$  NMR of [1TCO] (700 MHz, Chloroform- $d$ )  $\delta$  9.10 (d,  $J = 4.9$  Hz, 1H), 7.97 (t,  $J = 7.8$  Hz, 1H), 7.43 (t,  $J = 6.0$  Hz, 1H), 7.30 (d,  $J = 8.1$  Hz, 1H), 5.15 (d,  $J = 2.5$  Hz, 1H), 2.54 (dt,  $J = 11.7, 5.4$  Hz, 1H), 2.49 (dt,  $J = 12.0, 4.7$  Hz, 1H), 2.16 – 2.12 (m, 2H), 1.90 – 1.79 (m, 1H), 1.64 (m, 1H), 1.61 – 1.50 (m, 4H), 1.50 – 1.40 (m, 4H). TCO signals based on reported spectrum, *J. Am. Chem. Soc.*, **2008**, *130*, 3760-3761

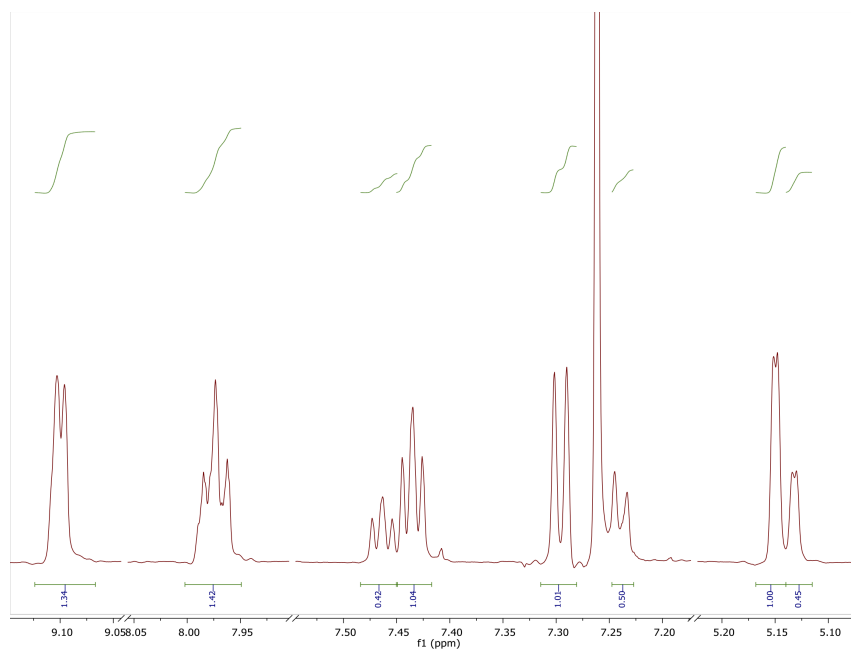


Figure S28: <sup>1</sup>H NMR of [1TCO] (700 MHz, Chloroform-d) zoom of low field signals showing signals from minor products 0.71:0.29



Figure S29: COSY NMR of [1TCO] (700 MHz, Chloroform-d)



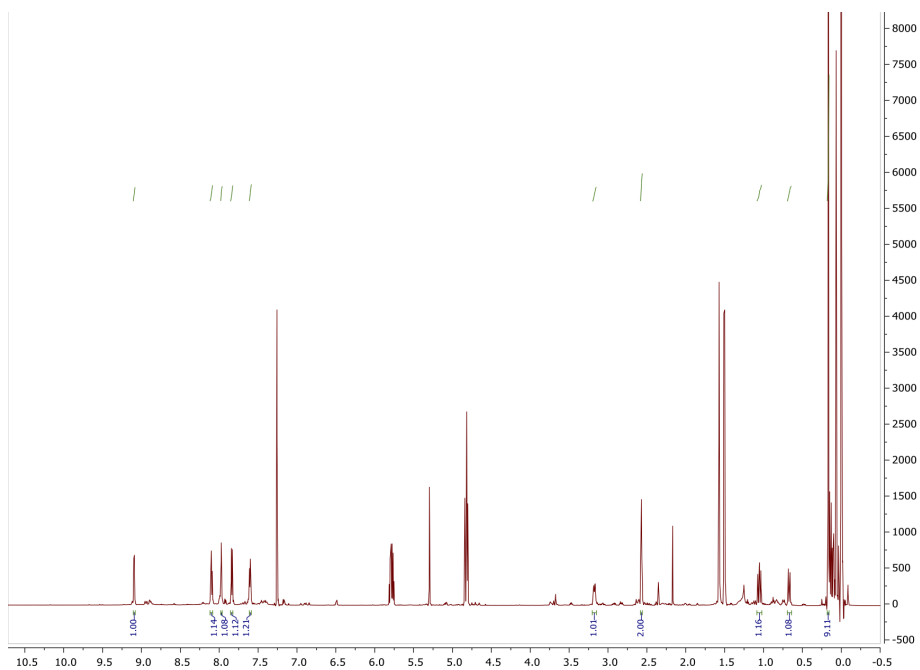


Figure S30:  $^1\text{H}$  NMR of [1Allyl-TMS] (700 MHz, Chloroform- $d$ )  $\delta$  9.09 (d,  $J = 5.2$  Hz, 1H), 8.10 (t,  $J = 7.8$  Hz, 1H), 7.97 (t,  $J = 3.1$  Hz, 1H), 7.84 (d,  $J = 7.9$  Hz, 1H), 7.61 – 7.59 (m, 1H), 3.20 – 3.15 (m, 1H), 2.59 – 2.56 (t,  $J = 2.6$  Hz, 2H), 1.05 (dd,  $J = 15.0, 13.1$  Hz, 1H), 0.67 (dd,  $J = 15.2, 2.6$  Hz, 1H), 0.17 (s, 9H).

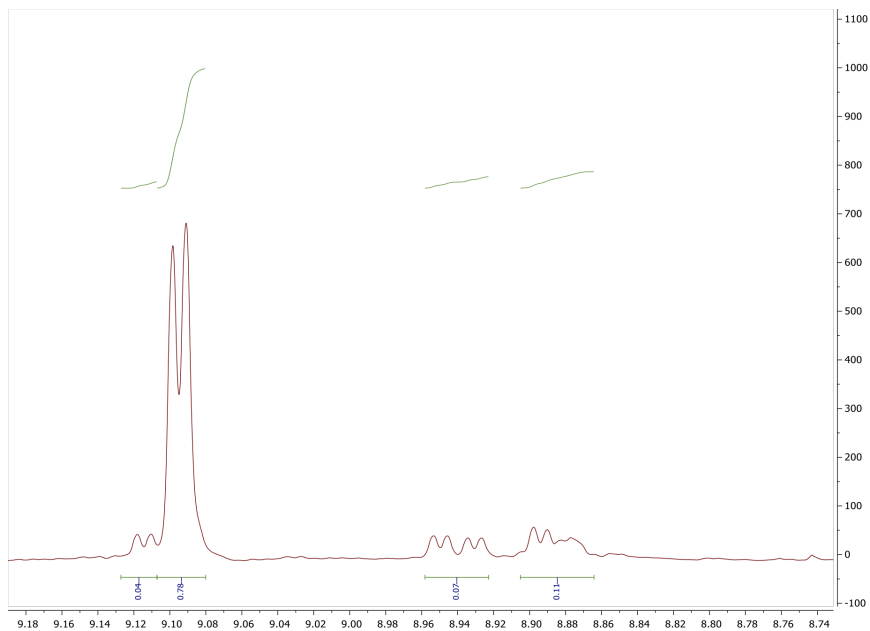


Figure S31: <sup>1</sup>H NMR of [1Allyltrimethylsilane] (700 MHz, Chloroform-d) zoom of low field signals showing signals from minor products 0.72:0.04:0.07:0.11

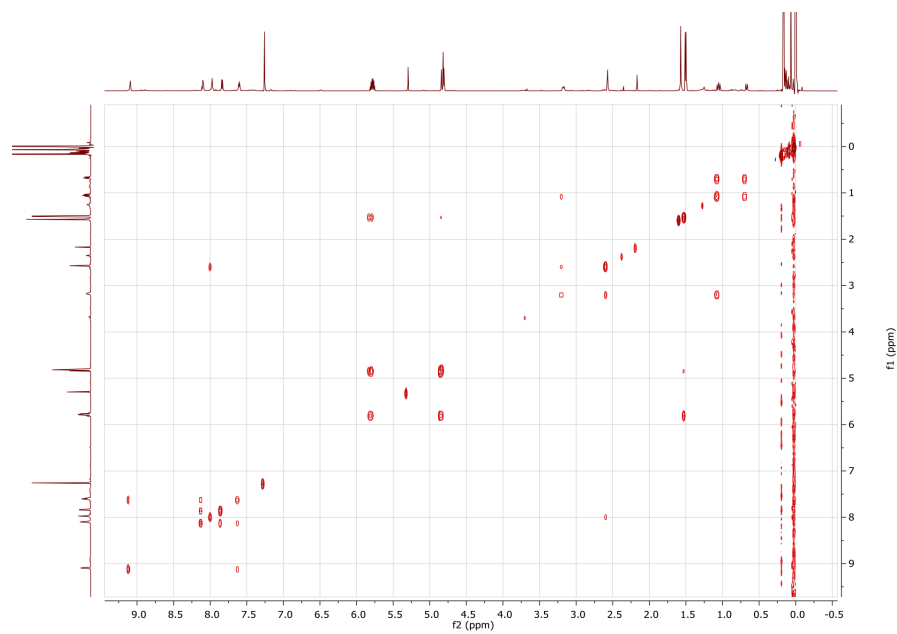


Figure S32: COSY NMR of [1Allyltrimethylsilane] (700 MHz, Chloroform-d)

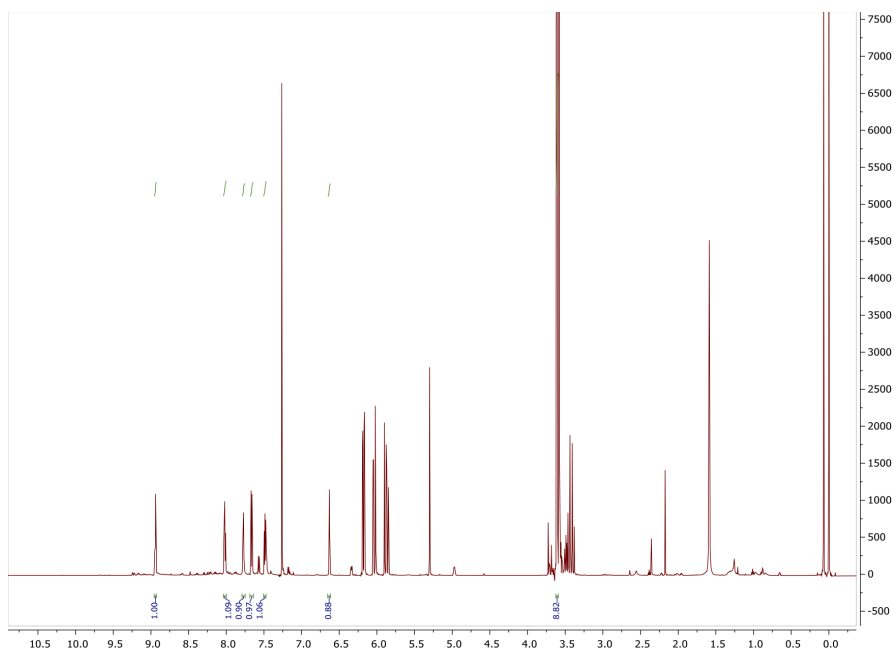


Figure S33:  $^1\text{H}$  NMR of [1Vinyltrimethoxysilane] (700 MHz, Chloroform- $d$ )  $\delta$  8.94 (d,  $J = 5.3$  Hz, 1H), 8.02 (t,  $J = 7.9$  Hz, 1H), 7.77 (d,  $J = 2.7$  Hz, 1H), 7.66 (d,  $J = 8.0$  Hz, 1H), 7.49 (t,  $J = 6.8, 5.6$  Hz, 1H), 6.63 (d,  $J = 3.1$  Hz, 1H), 3.61 (s, 9H).

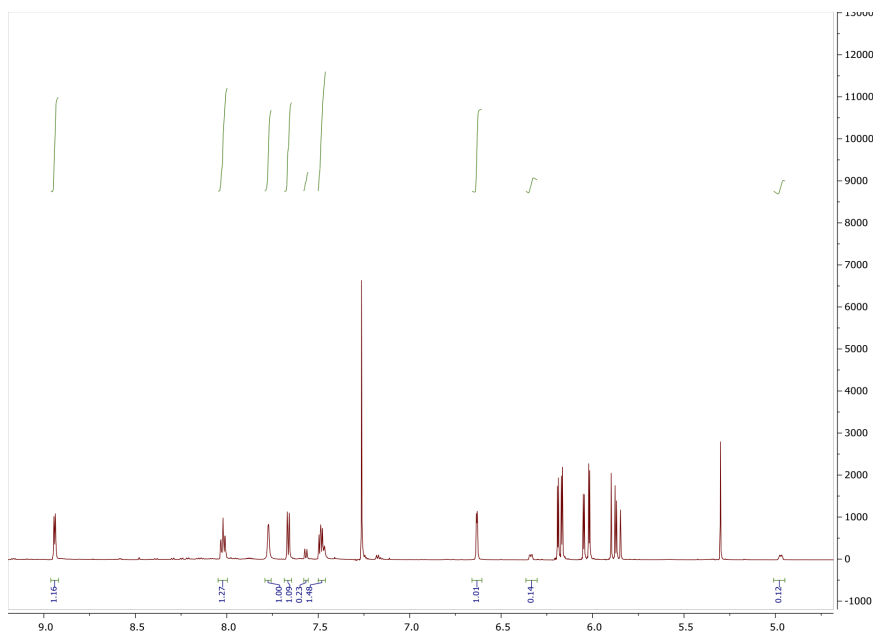


Figure S34: <sup>1</sup>H NMR of [1Vinyltrimethoxysilane] (700 MHz, Chloroform-d) zoom of low field signals showing signals from minor products 0.82:0.18

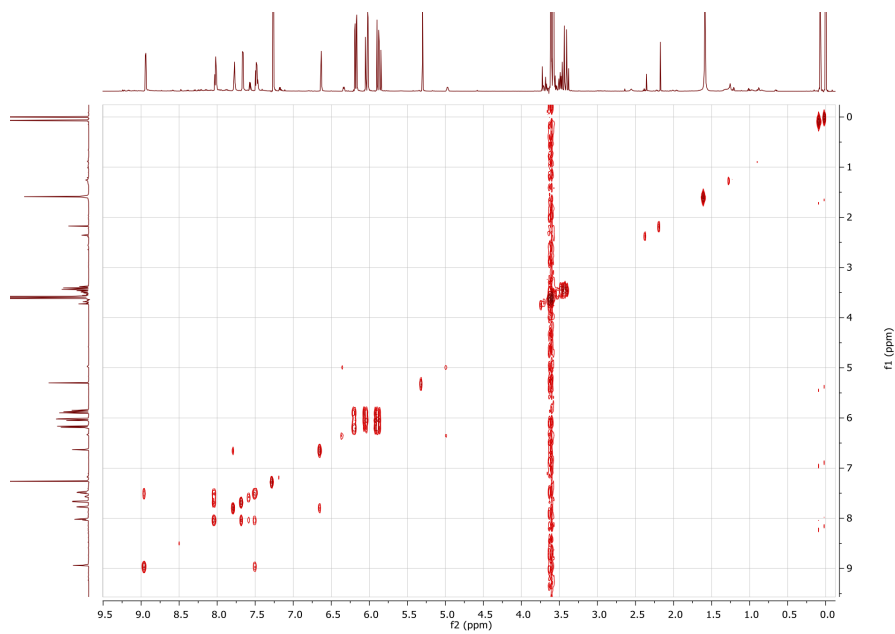


Figure S35: COSY NMR of [1Vinyltrimethoxysilane] (700 MHz, Chloroform-d)

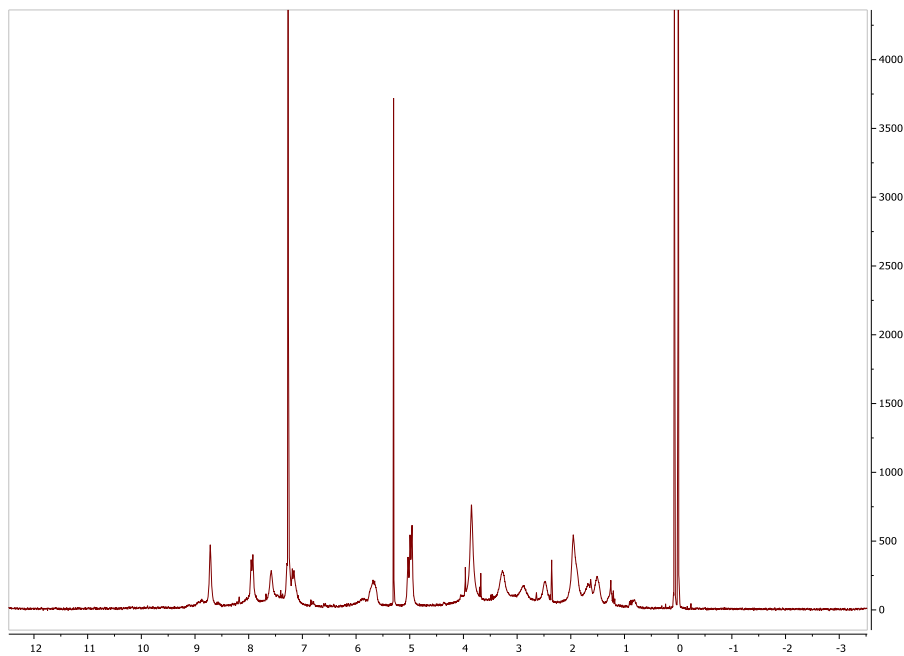


Figure S36: <sup>1</sup>H NMR of [1Quinine] from reaction of [1] and quinine at 40 C

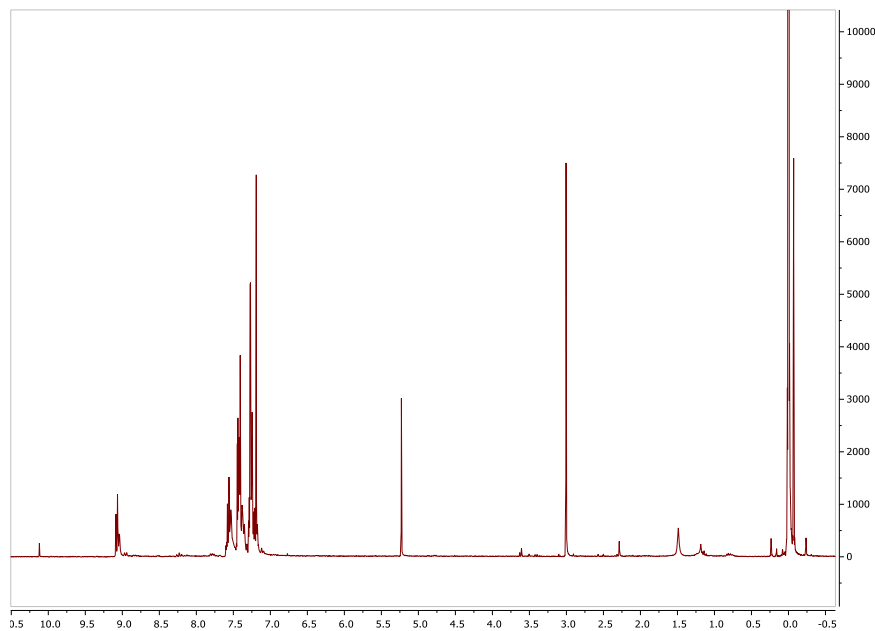


Figure S37: <sup>1</sup>H NMR of [1PhCCH] from the reaction between [1] and phenylacetylene at 50 C for 60 h, approx. 85 % conversion



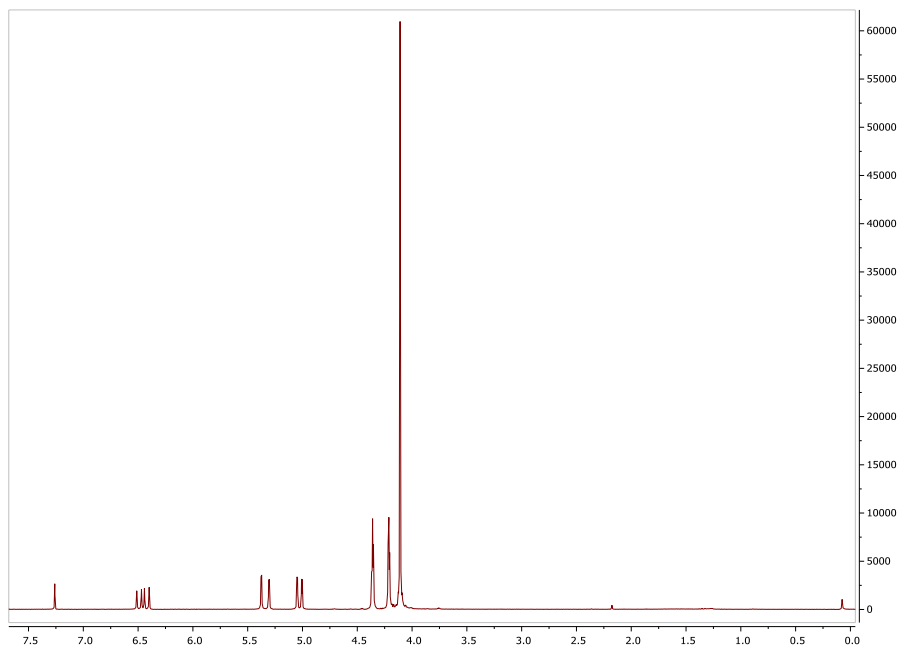


Figure S38:  $^1\text{H}$  NMR of ViFc (400 MHz, Chloroform-d)

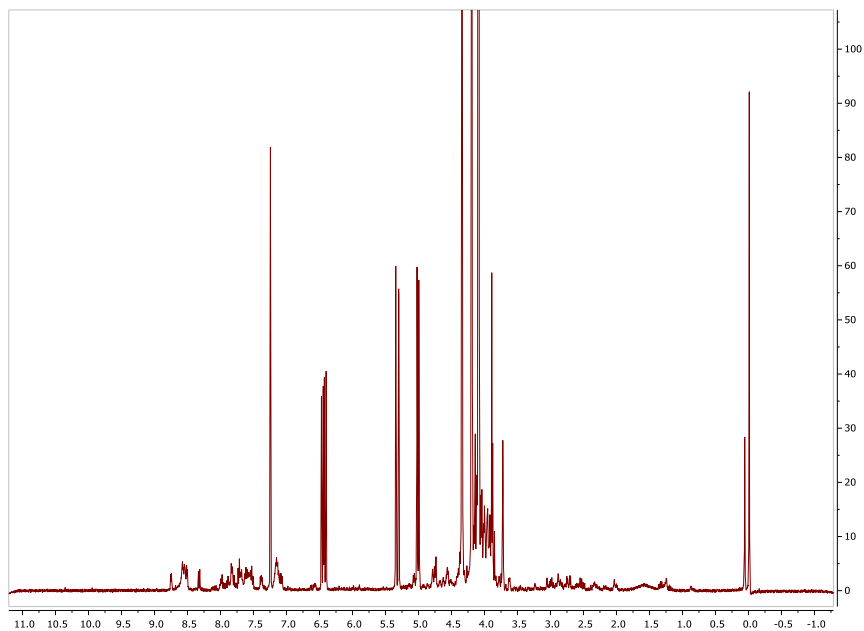


Figure S39: <sup>1</sup>H NMR of *in situ* reaction between TzPy and ViFc (400 MHz, Chloroform-d) after 1 h

## 6 Crystallography

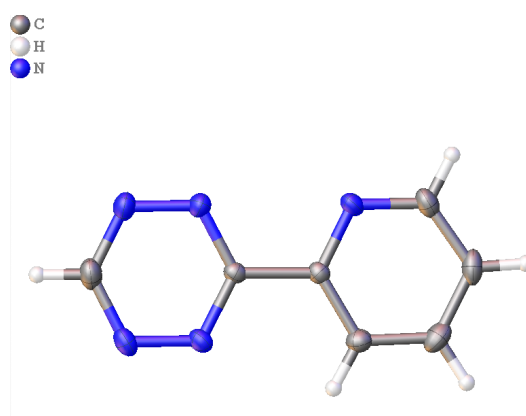


Figure S40: Molecular structure of TzPy determined crystallographically. Ellipsoids are shown at 50% probability.

Table S1: Crystallographic Information for Complexes Reported Herein

Identification code	ac488 [1]	ac479a [1Fc]
Empirical formula	C <sub>10</sub> H <sub>5</sub> N <sub>5</sub> O <sub>3</sub> ClRe	C <sub>22</sub> H <sub>17</sub> ClFeN <sub>3</sub> O <sub>3</sub> Re
Formula weight	464.842	648.90
Temperature/K	135.0	135.02
Crystal system	monoclinic	monoclinic
Space group	C2/c	P2 <sub>1</sub> /c
a/Å	16.0600(8)	12.9074(3)
b/Å	13.0072(8)	12.0184(3)
c/Å	13.9753(7)	14.9765(4)
$\alpha$ /°	90	90
$\beta$ /°	99.720(6)	113.9810(10)
$\gamma$ /°	90	90
Volume/Å <sup>3</sup>	2877.5(3)	2122.71(9)
Z	8	4
$\rho_{\text{calc}}/(\text{g}/\text{cm}^3)$	2.146	2.0303
$\mu/\text{mm}^{-1}$	18.383	6.537
F(000)	1698.7	1247.1
Crystal size/mm <sup>3</sup>	0.146 × 0.065 × 0.029	0.286 × 0.105 × 0.035
Radiation	Cu K $\alpha$ ( $\lambda$ = 1.54178)	Mo K $\alpha$ ( $\lambda$ = 0.71073)
2 $\theta$ range/° for data collection	10.32 to 132.66	3.46 to 66.34
Index ranges	-18 ≤ h ≤ 18 -10 ≤ k ≤ 15 -16 ≤ l ≤ 16	-19 ≤ h ≤ 19 -18 ≤ k ≤ 18 -22 ≤ l ≤ 23
Reflections collected	17080	58206
Independent reflections	2412	8110
Data/restraints/parameters	[R <sub>int</sub> = 0.0685, R <sub>sigma</sub> = 0.0440] 2412/0/195	[R <sub>int</sub> = 0.0419, R <sub>sigma</sub> = 0.0268] 8110/0/280
Goodness-of-fit on F <sup>2</sup>	1.046	0.994
Final R indexes [I >= 2 $\sigma$ (I)]	R <sub>1</sub> = 0.0750, wR <sub>2</sub> = 0.1901	R <sub>1</sub> = 0.0197, wR <sub>2</sub> = 0.0374
Final R indexes [all data]	R <sub>1</sub> = 0.0888, wR <sub>2</sub> = 0.2250	R <sub>1</sub> = 0.0329, wR <sub>2</sub> = 0.0415
Largest diff. peak/hole/eÅ <sup>-3</sup>	6.27/-2.57	0.83/-0.85

Table S2: Crystallographic Information 2 for Complexes Reported Herein

Identification code	ac484 [1Ci]	TzPy	stams02 [1TCO]
Empirical formula	C <sub>18</sub> H <sub>13</sub> ClN <sub>3</sub> O <sub>3</sub> Re	C <sub>7</sub> H <sub>5</sub> N <sub>5</sub>	C <sub>36</sub> H <sub>38</sub> Cl <sub>2</sub> N <sub>6</sub> O <sub>6</sub> Re <sub>2</sub>
Formula weight	540.981	159.16	1094.02
Temperature/K	135.0	135(2)	100
Crystal system	monoclinic	monoclinic	monoclinic
Space group	P2 <sub>1</sub> /n	P2 <sub>1</sub> /c	C2/c
a/Å	9.0781(7)	7.2794(4)	17.9274(18)
b/Å	10.9568(10)	9.3608(4)	12.2202(9)
c/Å	22.080(2)	10.4528(5)	17.9025(19)
$\alpha$ /°	90	90	90
$\beta$ /°	92.870(2)	96.970(3)	103.284(8)
$\gamma$ /°	90	90	90
Volume/Å <sup>3</sup>	2193.5(3)	707.00(6)	3817.1(6)
Z	4	4	4
$\rho_{\text{calc}}/(\text{g}/\text{cm}^3)$	1.638	1.495	1.904
$\mu/\text{mm}^{-1}$	5.681	0.103	6.529
F(000)	1030.6	328	2112.0
Crystal size/mm <sup>3</sup>	0.149 × 0.127 × 0.085	0.647 × 0.248 × 0.165	
Radiation	Mo K $\alpha$ ( $\lambda$ = 0.71073)	Mo K $\alpha$ ( $\lambda$ = 0.71073)	Mo K $\alpha$ ( $\lambda$ = 0.71073)
2 $\theta$ range/° for data collection	3.7 to 56.62	2.819 to 28.338	4.07 to 63.838
Index ranges	-9 ≤ h ≤ 12 -14 ≤ k ≤ 14 -29 ≤ l ≤ 29	-9 ≤ h ≤ 9 -12 ≤ k ≤ 12 -13 ≤ l ≤ 13	-25 ≤ h ≤ 26 -17 ≤ k ≤ 17 -26 ≤ l ≤ 25
Reflections collected	22804	13031	24957
Independent reflections	5438	1759	6069
Data/restraints/parameters	[R <sub>int</sub> = 0.0703, R <sub>sigma</sub> = 0.0744] 5438/36/211	[R <sub>int</sub> = 0.0262] 1759/0/110	[R <sub>int</sub> = 0.2298, R <sub>sigma</sub> = 0.3791] 6069/36/235
Goodness-of-fit on F <sup>2</sup>	0.957	1.079	0.948
Final R indexes [I >= 2 $\sigma$ (I)]	R <sub>1</sub> = 0.0395, wR <sub>2</sub> = 0.0731	R <sub>1</sub> = 0.0432, wR <sub>2</sub> = 0.1227	R <sub>1</sub> = 0.0675, wR <sub>2</sub> = 0.1271
Final R indexes [all data]	R <sub>1</sub> = 0.0630, wR <sub>2</sub> = 0.0785	R <sub>1</sub> = 0.0611, wR <sub>2</sub> = 0.1396	R <sub>1</sub> = 0.1927, wR <sub>2</sub> = 0.1503
Largest diff. peak/hole/eÅ <sup>-3</sup>	2.20/-1.69	0.434/-0.222	3.83/-1.60

## 7 XYZ Coordinates from DFT calculations

25

```
Coordinates from ORCA-job TPSS-Re-tzpy
Re 0.45312857971257 9.5054885528947 4.36894768089622
Cl -1.15399358688330 11.36181241617654 4.01369499166142
C 1.25116725081583 10.37301756215786 5.91061448436461
O 1.70647549292669 10.87838284941238 6.85071267770601
O 2.50269950964509 10.88873419914539 2.47376549845189
O 2.41950544599235 7.14207213609889 4.73091200995003
C 1.74770263087134 10.37876401247920 3.18940574407375
C -2.08808746135165 7.94431526553578 4.68968568344493
N -3.18148591052866 7.38814144049383 5.21797324204466
N -3.32448658878812 7.40714448445461 6.53665883778184
C -2.33612901600564 7.98489791213714 7.24411227372241
H -2.43902286567569 7.98680714602697 8.32353464388922
N -1.24529608612629 8.57390327583050 6.75346901679622
N -1.11570959925189 8.55874780351854 5.4268904286478
C -1.87663653766782 7.9105443104493 3.24577620726812
N -0.72998565175394 8.51124195655138 2.82564392804747
C -0.45268178161498 8.50728618999339 1.50868461599515
H 0.46550803661249 8.99693306462370 1.20935009883169
C -1.2960981399070 7.91269504124572 0.57610327629191
H -1.02542699551762 7.93879589138762 -0.47325325020143
C -2.47085515810148 7.29970301761300 1.00773184136395
H -3.14535305969810 6.83168482557462 0.29907542857590
C -2.76596504517789 7.29729344180766 2.36733082052897
H -3.66383375940376 6.83459916604284 2.75895602574743
C 1.67431197096113 8.02612391535802 4.59489381990288
```

48

Coordinates from ORCA-job TPSS-Re-Fc

Cl	0.18506648428448	3.42122874274687	2.37172639840736
Re	2.22737466596789	4.42327635795717	3.39591800713869
Fe	1.43300403995904	9.87644711039803	4.63049781825045
N	0.79448516353345	5.12838345065919	4.87995962126592
N	1.41469265774342	6.25101417726888	2.62161369572687
N	1.94857111717107	6.80087844611940	1.43594308355795
O	3.94767051284486	3.70956414963615	0.91691507427927
O	2.97819193506709	1.74565635492876	4.77574691335317
O	4.74222196322722	5.69397727454627	4.66022476546823
C	3.31018810710239	3.96117440926495	1.85590830545138
C	2.70745398417633	2.74471261989844	4.24303159279017
C	3.77832978927707	5.23111741539400	4.18802758232102
C	0.54326672556538	4.53566444677405	6.06169949786620
H	1.17683453378633	3.69598771767171	6.31974861369018
C	-0.47023423155839	4.96510562112339	6.91054702268779
H	-0.62631282006818	4.45388432759609	7.85350949743076
C	-1.26897846735625	6.03961491524205	6.52281881956456
H	-2.07306208816891	6.39253769730084	7.15958102266574
C	-1.01761738117111	6.65814985150897	5.30328667969521
H	-1.62199122451858	7.49492174480699	4.97719163396085
C	0.02473671150415	6.19461118508862	4.49939632893614
C	0.39827261158778	6.80661314624178	3.23233602230492
C	-0.35086481249832	7.96834672751861	2.63370660328478
H	-1.39815112769356	7.87148864185846	2.92789606997869
C	-0.26864270817345	7.81221649102815	1.10323752354818
H	-0.91812428568241	6.98571407611627	0.78262895310182
H	-0.60852828300989	8.71795436793290	0.59672647805410
C	1.14022039396773	7.49807857838809	0.71744248412602
H	1.56026588006825	7.88689500725299	-0.20819261336962
C	0.14296703025518	9.31604441289558	3.12328781203716
C	1.25323649084852	10.07765047121335	2.61482793430375
H	1.97279618130582	9.74672014596102	1.87890185405257
C	1.24425708610187	11.35842648335701	3.25362108859701
H	1.96704866369714	12.14769809464944	3.09621251327280
C	0.14935823127169	11.38899783310134	4.17466656672301
H	-0.10595386257669	12.20707509231319	4.83469273603917
C	-0.52538180835356	10.13046357391614	4.09854800000443
H	-1.39968345945149	9.84236658300189	4.66735281096197
C	2.33814853808139	8.25376000592948	5.50648490656935
H	2.24717840462632	7.21506519836525	5.22938868638274
C	3.31496248113259	9.16201289433031	4.99323368411958
H	4.05744973178189	8.93479981665295	4.24041770096251
C	3.11697118001489	10.42779717772203	5.63264220407231
H	3.67636026912532	11.33308480769109	5.43827443617293
C	2.01242754610704	10.29995082864123	6.53657348980869
H	1.59634500783786	11.09089728314819	7.14618134455327
C	1.52631974453519	8.95516957330203	6.45461747622283
H	0.68945369672416	8.54684367149037	7.00426625761112

48

Coordinates from ORCA-job TPSS-Re-Fc-tH

Cl	0.34564263366766	3.31878125651867	2.27450205004789
Re	2.29202190699586	4.43663184074747	3.35856484882548
Fe	1.46320864549179	9.89320524615512	4.71230361751859
N	0.79817594182267	5.09335344130777	4.80159652293330
N	1.37516203367355	6.21983703441998	2.51632200590007
N	1.67696546918145	6.65791357388724	1.26624081265933
O	4.17558823509742	3.72739138273111	1.00026211734426
O	3.15640747960945	1.83148417746677	4.79509989307592
O	4.66821109826900	5.88733036744934	4.69471005117509
C	3.47118669916481	3.98356592374757	1.89203264126208
C	2.84248489754490	2.80777910456443	4.24516637609977
C	3.75481643805592	5.35562424353996	4.19631999539078
C	0.53907535487829	4.48102051364937	5.97355942276233
H	1.15708252545369	3.62334843595449	6.20949315958542
C	-0.45741027394220	4.91269092637931	6.83774607499144
H	-0.62460671188146	4.38160670866670	7.76761808845682
C	-1.21882608757829	6.02666537762274	6.48327348891335
H	-2.00197345474636	6.39442833708704	7.13792343196106
C	-0.95515218644659	6.67041982767244	5.28138384901697
H	-1.51870749231147	7.54885802391672	4.99536855708038
C	0.05618194977246	6.18744918186501	4.44400792362772
C	0.39746111141868	6.80253246087288	3.17481489141849
C	-0.33197523358937	8.02094790769919	2.65281674080250
H	-1.37064734958043	7.96387081663897	2.99159181164077
C	-0.29624184392265	7.96710937906645	1.14382852151789
H	-1.06788853331596	8.47238911275172	0.57589186832940
C	0.72502233809545	7.35782928833106	0.52919326398714
H	0.89184164717015	7.34085193891802	-0.54086917559172
C	0.22974164778461	9.34367719184999	3.15393014073858
C	1.41590704650597	10.00217931163979	2.67851762658755
H	2.14159104802903	9.58269015854307	1.99495506390960
C	1.46198632765159	11.30980005086397	3.25781009852184
H	2.24701875873677	12.04017746102386	3.11335509644251
C	0.31810367594586	11.46044249774078	4.10734610536824
H	0.08584089785719	12.32585311971288	4.71370619678705
C	-0.43828067132280	10.24773273770182	4.04594102756193
H	-1.36026789593793	10.04176578167371	4.57462064111159
C	2.21373448042692	8.26798855363865	5.72188725299103
H	2.07659003052617	7.22409296371757	5.48849448387703
C	3.27258131437630	9.09425150876137	5.23245407078872
H	4.04827543166630	8.78908419754321	4.54373566512433
C	3.10849289789493	10.39966366471135	5.79764789612175
H	3.73116595020543	11.26178283262347	5.59898487245173
C	1.94232636669312	10.37898065359012	6.63042591393362
H	1.53463518689756	11.22153169178796	7.17300013825415
C	1.38515965799322	9.06019669470074	6.57953765389265
H	0.49188277838103	8.72600677213997	7.08936342082605
H	2.31905783164033	6.04513632640814	0.78040378397750

39

Coordinates from ORCA-job TPSS-RePh

Re	6.89105283696937	7.22458141202392	-0.06295340986764
Cl	4.92662458137780	7.63855887782010	-1.48253117854742
C	8.11536969219838	7.23730848008968	-1.56882052228602
C	6.72313829617657	5.30240368625229	-0.24466585888967
C	8.37169726314148	6.98479966025638	1.15327765179797
C	5.18615140999834	8.73438745892209	1.94113262095716
C	4.21819789511823	9.05600422522366	3.06165784814094
H	3.63052884795612	9.93699782027597	2.76842815022404
C	3.28509210098784	7.88337578150841	3.25039970029021
H	2.36648532397389	8.03079731405715	3.80528956888416
C	3.60662786516611	6.67288871176695	2.78450200758995
H	3.00650275156859	5.78258273817300	2.92840254220972
C	4.95724497935758	9.40962088408533	4.35321523531426
C	4.47126630858280	10.42134418100895	5.18677858288191
H	3.57517185296865	10.96863929360141	4.89967666827383
C	5.12524124242656	10.73261408468202	6.37843230841232
H	4.73893209801998	11.52113255339399	7.01814711099737
C	6.27767118287915	10.03597021440936	6.74373623279754
H	6.79152881568678	10.28010056222149	7.66886648828861
C	6.77045748787628	9.02757371222774	5.91415745630605
H	7.67021596434963	8.48534135966645	6.18996863245070
C	6.11257443821873	8.71442605132512	4.72624383793231
H	6.50547040227282	7.93079034649111	4.08355323916782
N	6.80431059644939	9.36717578549403	0.29791199933847
C	7.50715497573113	10.29339623943798	-0.37872375842756
H	8.16816951517534	9.91381666885523	-1.14876066572872
C	7.40022468440671	11.65299480512700	-0.11913051857406
H	7.98831125178514	12.35567774559327	-0.69872284432867
C	6.53895282540330	12.08061069006645	0.89123851120060
H	6.44273526173373	13.13519463753096	1.12916272401437
C	5.80728409292026	11.13433966494738	1.59563429295125
C	5.14726329213998	11.43257044735286	2.40135148862670
C	5.93868219284137	9.77826181468508	1.273849583664519
N	5.45155989217174	7.51541093541877	1.53056745150656
N	4.77598835381458	6.46541314947870	2.06063514063966
H	4.87976162776429	5.62895797549016	1.50016235776653
O	8.84851250900037	7.28295607039207	-2.46720974824314
O	6.59036721627884	4.14911520012032	-0.31830948441094
O	9.25692007511214	6.85040176422712	1.90090355669765

39

Coordinates from ORCA-job TPSS-RePh008

Re	0.53170039229605	9.24918329245092	4.88281412771571
Cl	-1.78317902640154	9.57885356308625	5.66235755564654
C	1.25916313142971	9.74481323976439	6.62509297580367
O	1.68147032463724	10.00849360354930	7.66943942251896
O	0.72637501954494	12.16908182771469	3.83269370728179
O	3.41228177091741	8.71348742907327	3.87553244709015
C	0.66582142837705	11.09034608453969	4.25631097739870
C	-0.77500344943389	6.58858646148313	4.59697799231497
C	-0.10158296500698	5.74636311165821	7.08468122194539
H	0.33399765272931	5.29041202398760	7.97170734310426
N	0.64341677907633	6.60531889836098	6.48836122501640
N	0.09666343359091	7.22181849547444	5.35025428439984
C	-1.07212317496472	7.22602751430280	3.33162795728325
N	-0.46766645229564	8.44000928927459	3.13891156849929
C	-0.64953227716470	9.06898478601185	1.96290021572976
H	-0.16161240682519	10.03140110294641	1.86311333704420
C	-1.42062384880654	8.53447702585431	0.93992295107552
H	-1.53401490469037	9.08707287553504	0.01389028953188
C	-2.03907807675630	7.29665792665235	1.12888299492313
H	-2.64692209243989	6.85470773791360	0.34602854836706
C	-1.86086843664295	6.63804389159452	2.33702511378717
H	-2.31329285236365	5.66885746608393	2.51489637137389
C	2.32902997896181	8.91529402130646	4.25424450661363
C	-1.45443768055170	5.34114100132645	6.58687495872019
H	-1.74628618580348	4.37184963180629	6.99783411612095
H	-2.19432376408060	6.08919039835124	6.90313208649436
C	-1.40679169991476	5.29710936920389	5.04006981417041
C	-0.71364890091001	4.05904703261940	4.48906637307613
C	-1.44976115184596	2.87896514047853	4.32817787452214
H	-2.51061970347651	2.87067412318903	4.57072816185979
C	-0.83732805668002	1.71901637938198	3.85789703249636
H	-1.42139154196084	0.81160390523484	3.73371821984310
C	0.52219071047278	1.72679128648329	3.54207573805661
H	1.00114024255003	0.82445089950622	3.17365891093454
C	1.26098604955940	2.89945234905646	3.69558106651603
H	2.31845362842801	2.91427228902793	3.44873436222346
C	0.64664660267210	4.06065696474707	4.16465985081942
H	1.23049052003485	4.97003726924921	4.27674402946890
H	-2.44086287211658	5.29620501335475	4.68003546608577



37

Coordinates from ORCA-job TPSS-RePh-H

Re	6.41570146318435	7.39300985919715	-0.16627945323268
Cl	4.12766557053690	8.16305556357702	-0.71312700031688
C	7.02690464734859	7.74234554727203	-1.98159068619912
C	6.02947154594971	5.53627801910191	-0.62734804977434
C	8.20317964501872	6.87038934702610	0.34113987365711
C	5.12210421901139	8.51271803987318	2.27896864996614
C	4.10918823304092	8.55541115826354	3.26148680462434
C	3.78183998501883	7.34325089685113	3.85996982638456
H	3.00570405359298	7.29802119781880	4.61742739962774
C	4.41140192987832	6.18272286101678	3.41299113958489
H	4.20958016266764	5.21220838517987	3.85581361913273
C	3.33183554542309	9.77544748371250	3.56490596152546
C	2.75508711744005	10.49751546432772	2.50689320029900
H	2.91242916229634	10.15979306171946	1.48540563021166
C	1.97848360486106	11.62051314885835	2.77488965092224
H	1.52523445626048	12.16770850957048	1.95370684995374
C	1.77647182136708	12.03935930364682	4.09243453141178
H	1.17463872412774	12.91994818039014	4.29697514512101
C	2.34228124291291	11.32128384778202	5.14629886385348
H	2.18651448505419	11.64334058594608	6.17170184866757
C	3.10985396596422	10.18693989774646	4.88573241383200
H	3.56004559689035	9.63212594597656	5.70465466831571
N	6.58965712178901	9.39595454461146	0.61382339748962
C	7.34349770472162	10.37483422527641	0.07499712775207
H	7.90695429775571	10.09820357692076	-0.80811835149011
C	7.39906477941956	11.65219586785614	0.60917714344833
H	8.01781033262256	12.40512102543396	0.13370160164826
C	6.66304607742080	11.93117704256843	1.76137820019795
H	6.70193693823840	12.91298876251662	2.22211634992848
C	5.88097403014071	10.93025658327164	2.32061983762086
H	5.31308511142742	11.11740189210662	3.22195424279512
C	5.83453643618735	9.66846368895205	1.71721352885488
N	5.56164868803297	7.31185833935899	1.79671442508151
N	5.23285699091557	6.15254189604517	2.36413612110899
O	7.40312936878001	8.00015462450892	-3.04892431598857
O	5.78576257671053	4.43062523299212	-0.86571935238148
O	9.28566236799191	6.56314639272667	0.64450915636593



## **Supporting Infos of Paper 2.**

### SUPPORTING INFORMATION

## Contents

<b>1</b>	<b>Experimental</b>	<b>S3</b>
<b>2</b>	<b>Crystallography</b>	<b>S5</b>
<b>3</b>	<b>Cyclic Voltammetry</b>	<b>S6</b>
<b>4</b>	<b>NMR Spectroscopy</b>	<b>S7</b>
<b>5</b>	<b>Infrared Spectroscopy</b>	<b>S10</b>
<b>6</b>	<b>Absorption Spectroscopy</b>	<b>S13</b>
<b>7</b>	<b>TD DFT</b>	<b>S16</b>

## List of Figures

S1	CV of <b>1</b> . . . . .	S6
S2	CV of <b>1Fc</b> . . . . .	S6
S3	CV of <b>1H<sub>2</sub>Fc</b> . . . . .	S7
S4	<sup>1</sup> H NMR of <b>1Fc</b> . . . . .	S7
S5	<sup>13</sup> C NMR of <b>1Fc</b> . . . . .	S8
S6	COSY NMR of <b>1Fc</b> . . . . .	S8
S7	Reaction NMR <b>1+</b> <b>EthFc</b> . . . . .	S9
S8	Zoom in Reaction NMR <b>1+</b> <b>EthFc</b> . . . . .	S10
S9	IR SEC of <b>1</b> reduction . . . . .	S10
S10	IR SEC of <b>1H<sub>2</sub>Fc</b> oxidation . . . . .	S11
S11	IR SEC of <b>1H<sub>2</sub>Fc</b> reduction . . . . .	S11
S12	IR SEC of <b>1Fc</b> oxidation . . . . .	S12
S13	IR SEC of <b>1Fc</b> reduction . . . . .	S12
S14	UV-vis NIR SEC of <b>1</b> <sup>0/-1</sup> . . . . .	S13
S15	UV-vis NIR SEC of <b>1H<sub>2</sub>Fc</b> <sup>0/+</sup> . . . . .	S13
S16	UV-vis NIR SEC of <b>1H<sub>2</sub>Fc</b> <sup>0/-1</sup> . . . . .	S14
S17	UV-vis NIR SEC of <b>1Fc</b> <sup>0/+</sup> . . . . .	S14
S18	UV-vis NIR SEC of <b>1Fc</b> <sup>0/-1</sup> . . . . .	S15
S19	TDDFT Transitions <b>1</b> . . . . .	S16
S20	TDDFT Transitions <b>1</b> <sup>-1</sup> . . . . .	S17
S21	TDDFT Transitions <b>1H<sub>2</sub>Fc</b> . . . . .	S18
S22	TDDFT Transitions <b>1H<sub>2</sub>Fc</b> <sup>+</sup> . . . . .	S19

---

S23	TDDFT Transitions <b>1H<sub>2</sub>Fe<sup>-1</sup></b> . . . . .	S20
S24	TDDFT Transitions <b>1Fe</b> . . . . .	S21
S25	TDDFT Transitions <b>1Fe<sup>-1</sup></b> . . . . .	S22
S26	TDDFT Transitions <b>1Fe<sup>+</sup></b> . . . . .	S23

## List of Tables

S1	Crystallographic Information for <b>1Fe</b> . . . . .	S5
----	---	----

## 1 Experimental

$^1\text{H}$  NMR spectra were recorded on a Bruker AC 250 spectrometer.  $^1\text{H}$  NMR spectra were referenced against remanent solvent peak. IR spectra were recorded on a Bruker FTIR INVENIO. UV-vis-NIR absorption spectra were obtained on J&M TIDAS spectrophotometer. Cyclic voltammetry was carried out in 0.1 M  $^n\text{Bu}_4\text{NPF}_6$  in acetonitrile solutions using a three-electrode configuration (glassy carbon working, Pt wire counter, and Ag reference electrode) on a Metrohm Autolab potentiostat. The couple  $[\text{FeCp}_2]/[\text{FeCp}_2]^+$  (Fc/Fc+) served as internal reference in all experiments. All solvents were degassed by passing through argon prior to use. Spectroelectrochemistry was performed at  $-30\text{ }^\circ\text{C}$  using an optically transparent thin-layered electrode (OTTLE).<sup>[1]</sup> Single crystals of suitable crystal was selected and measured on an Apex II, Bruker diffractometer. Using Olex2<sup>[2]</sup> the structure was solved with the ShelXS structure solution program using Direct Methods and refined with the least squared refinement.<sup>[3]</sup>

Density functional theory (DFT) calculations were performed using the molecular structure of  $[\mathbf{1}]^+$ . A computational analysis was performed by means of restricted Kohn-Sham density functional theory (DFT) using TPSS<sup>[4]</sup> functional in combination with the D3 dispersion correction<sup>[5]</sup> with the def2-TZVP and Weigend J auxiliary basis set.<sup>[6,7]</sup> Geometry optimizations were realized with the ORCA program package with TightSCF convergence ( $10^{-7}$  a.u.).<sup>[8]</sup> Solvation in  $\text{CH}_2\text{Cl}_2$  was modeled using the CPCM solvation model.<sup>[9]</sup> Open-shell calculations on the structure  $[\mathbf{1}]^0$ ,  $[\mathbf{1}]^{-1}$  ( $S = 3$ ) and compared to restricted KS for and  $[\mathbf{1}]^{-1}$  were determined by adding the requisite number of electrons, and calculations were performed by means of (un)restricted Kohn-Sham DFT using the same basis set, functionals, and solvent models as  $[\mathbf{1}]^+$ .

## References

- [1] M. Krejčík, M. Danek, and F. Hartl, "Simple construction of an infrared optically transparent thin-layer electrochemical cell: Applications to the redox reactions of ferrocene,  $\text{Mn}_2(\text{CO})_{10}$  and  $\text{Mn}(\text{CO})_3(3,5\text{-di-}t\text{-butyl-catecholate})^-$ ," *J. Electroanal. Chem. Interfacial Electrochem.*, vol. 317, no. 1-2, pp. 179-187, 1991.
- [2] O. V. Dolomanov, L. J. Bourhis, R. J. Gildea, J. A. K. Howard, and H. Puschmann, "Olex2: a complete structure solution, refinement and analysis program," *J. Appl. Cryst.*, vol. 42, pp. 339-341, 2009.
- [3] G. M. Sheldrick, "Shelxl-97: Program for crystal structure determination," 1997.

- 
- [4] J. P. Perdew, K. Burke, and M. Ernzerhof, "Generalized gradient approximation made simple [phys. rev. lett. 77, 3865 (1996)]," *Phys. Rev. Lett.*, vol. 78, no. 7, pp. 1396–1396, 1997.
- [5] S. Grimme, J. Antony, S. Ehrlich, and H. Krieg, "A consistent and accurate ab initio parametrization of density functional dispersion correction (dft-d) for the 94 elements h-pu," *J. Chem. Phys.*, vol. 132, no. 15, p. 154104, 2010.
- [6] F. Weigend and R. Ahlrichs, "Balanced basis sets of split valence, triple zeta valence and quadruple zeta valence quality for h to rn: Design and assessment of accuracy," *Phys. Chem. Chem. Phys.*, vol. 7, no. 18, pp. 3297–3305, 2005.
- [7] F. Weigend, M. Häser, H. Patzelt, and R. Ahlrichs, "Ri-mp2: optimized auxiliary basis sets and demonstration of efficiency," *Chem. Phys. Lett.*, vol. 294, no. 1–3, pp. 143–152, 1998.
- [8] F. Neese, "The orca program system," *WIREs Comput Mol Sci*, vol. 2, no. 1, pp. 73–78, 2012.
- [9] Y. Takano and K. N. Houk, "Benchmarking the conductor-like polarizable continuum model (cpcm) for aqueous solvation free energies of neutral and ionic organic molecules," *J. Chem. Theory Comput.*, vol. 1, no. 1, pp. 70–77, 2005.

## 2 Crystallography

Table S1: Crystallographic Information for 1Fc

**Table 1 Crystal data and structure refinement for stams05.**

Identification code	stams05
Empirical formula	C <sub>22</sub> H <sub>15</sub> ClFeN <sub>3</sub> O <sub>3</sub> Re
Formula weight	646.89
Temperature/K	100
Crystal system	monoclinic
Space group	P2 <sub>1</sub> /c
a/Å	10.4369(5)
b/Å	19.7530(7)
c/Å	12.2664(7)
$\alpha$ /°	90
$\beta$ /°	91.649(4)
$\gamma$ /°	90
Volume/Å <sup>3</sup>	2527.8(2)
Z	4
$\rho_{\text{calc}}/\text{g/cm}^3$	1.6997
$\mu/\text{mm}^{-1}$	5.489
F(000)	1239.1
Crystal size/mm <sup>3</sup>	0.023 × 0.012 × 0.033
Radiation	Mo K $\alpha$ ( $\lambda$ = 0.71073)
2 $\Theta$ range for data collection/°	3.9 to 64.36
Index ranges	-15 ≤ h ≤ 15, -28 ≤ k ≤ 29, -18 ≤ l ≤ 17
Reflections collected	78058
Independent reflections	8386 [R <sub>int</sub> = 0.1821, R <sub>sigma</sub> = 0.1085]
Data/restraints/parameters	8386/39/280
Goodness-of-fit on F <sup>2</sup>	0.916
Final R indexes [I >= 2 $\sigma$ (I)]	R <sub>1</sub> = 0.0698, wR <sub>2</sub> = 0.1723
Final R indexes [all data]	R <sub>1</sub> = 0.0992, wR <sub>2</sub> = 0.1912
Largest diff. peak/hole / e Å <sup>-3</sup>	8.74/-5.50



### 3 Cyclic Voltammetry

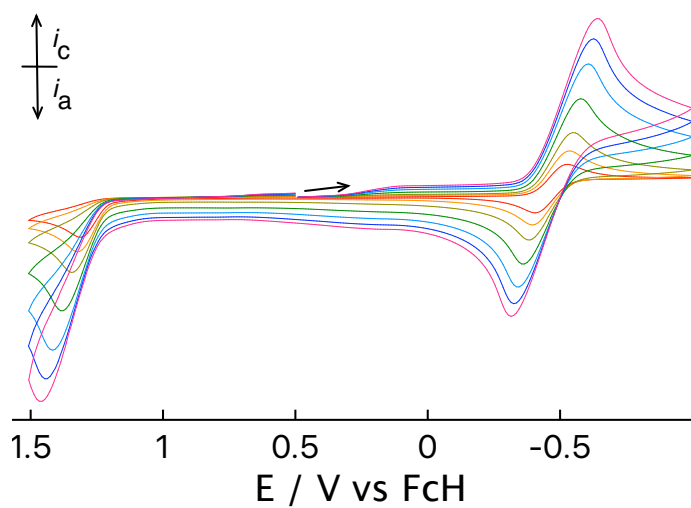


Figure S1: Cyclicvoltammogram of [1] in 0.1 M n-Bu<sub>4</sub>N[PF<sub>6</sub>]/CH<sub>2</sub>Cl<sub>2</sub>

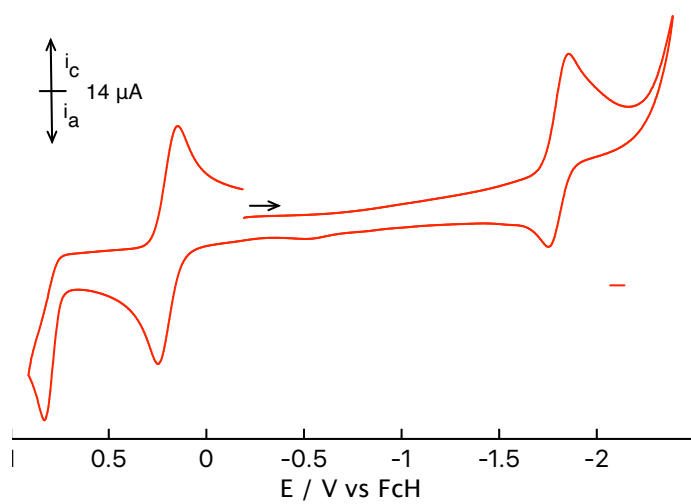


Figure S2: Cyclicvoltammogram of [1Fc] in 0.1 M n-Bu<sub>4</sub>N[PF<sub>6</sub>]/CH<sub>2</sub>Cl<sub>2</sub>

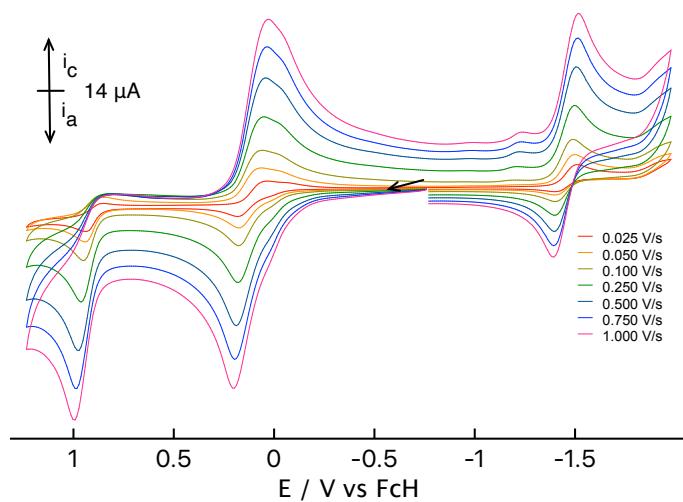


Figure S3: Cyclicvoltammogram of  $[1H_2Fc]$  in 0.1 M  $n\text{-Bu}_4N[PF_6]/CH_2Cl_2$

## 4 NMR Spectroscopy

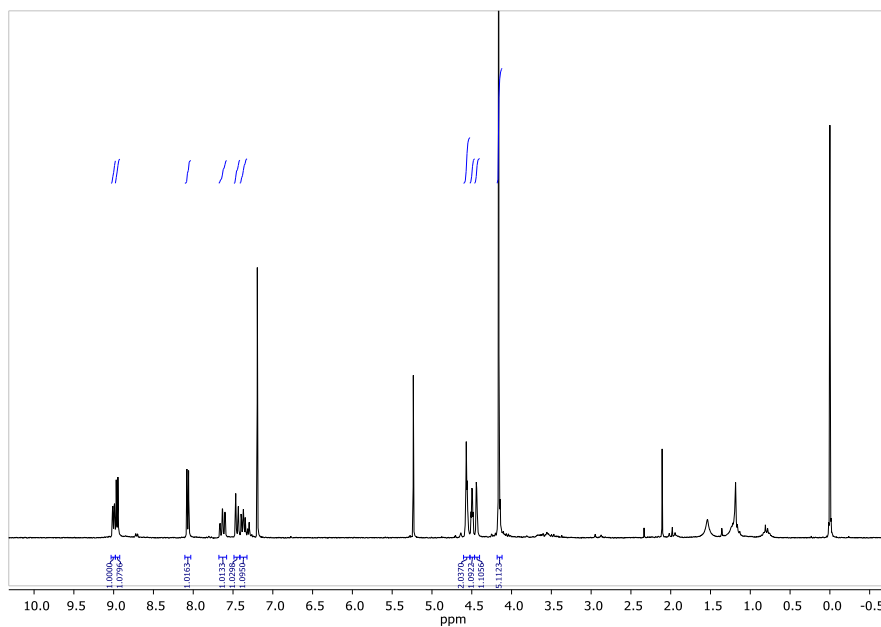
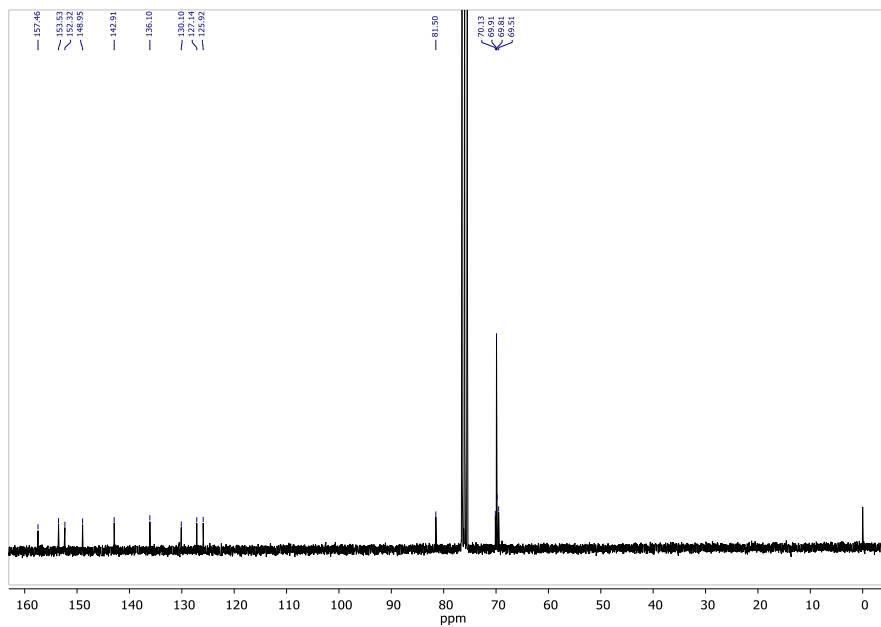
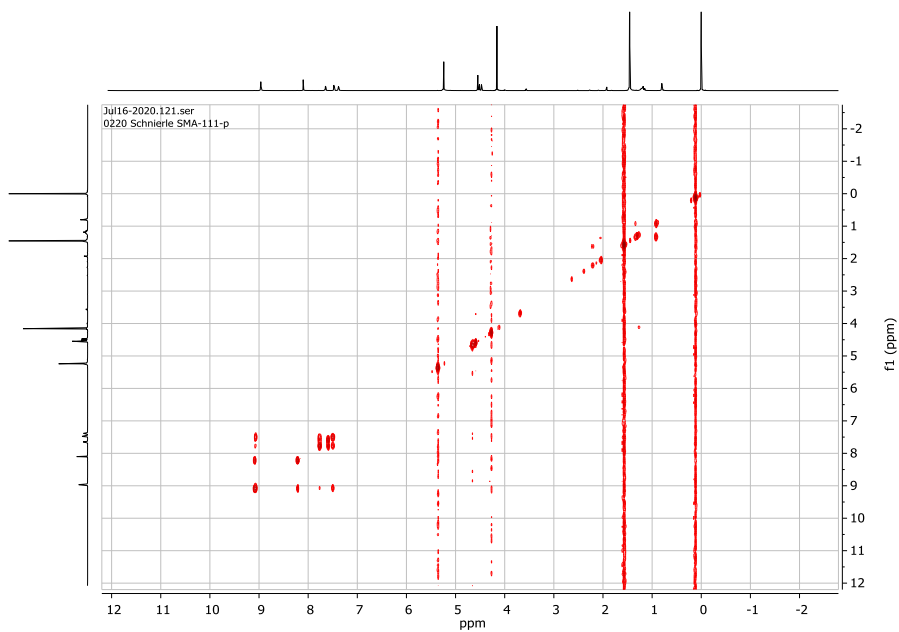


Figure S4:  $^1H$  NMR of  $[1Fc]$  in  $d_2$ -dichloromethane.

Figure S5:  $^{13}\text{C}$  NMR of [1Fc] in  $\text{d}_3$ -chloroform.Figure S6: COSY NMR of [1Fc] in  $\text{d}_2$ -dichloromethane.

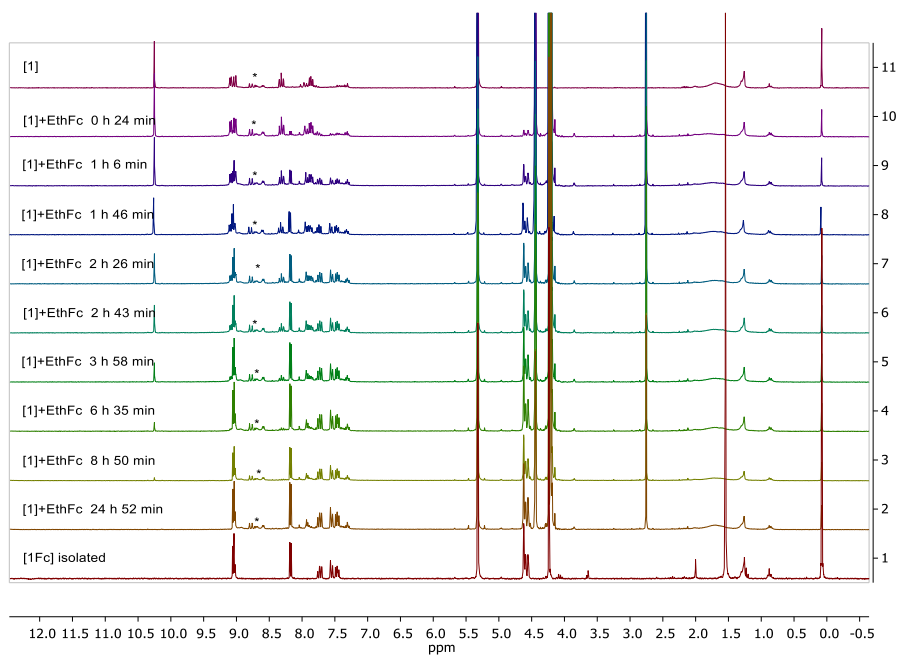


Figure S7: Reaction between [1] + excess EthFc 1H NMR d3-chloroform. \*denotes minor impurity detecting in [1].

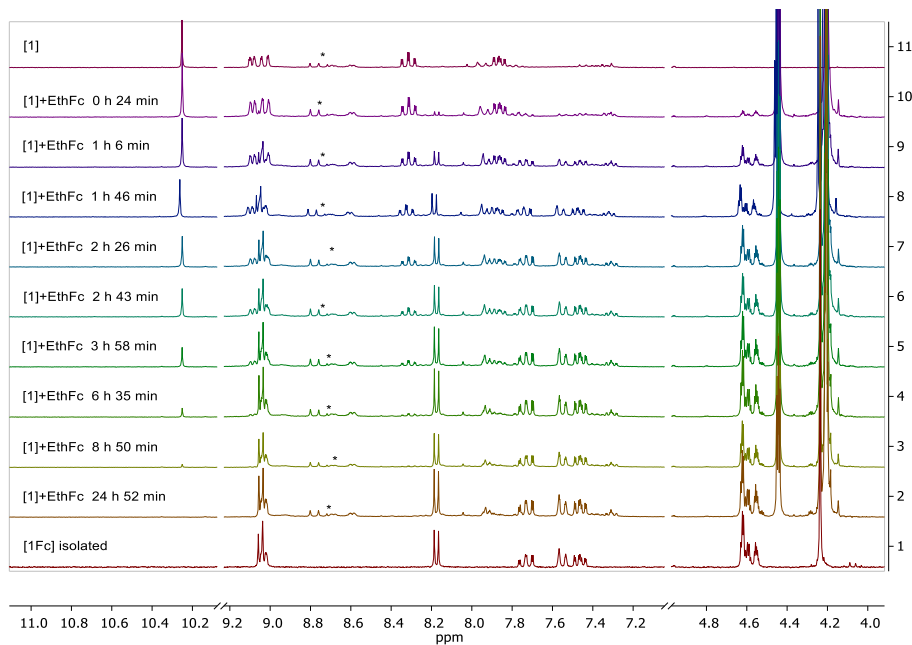


Figure S8: Highlighted peaks during reaction between [1] + excess EthFc 1H NMR d<sub>3</sub>-chloroform. \*denotes minor impurity detecting in [1].

## 5 Infrared Spectroscopy

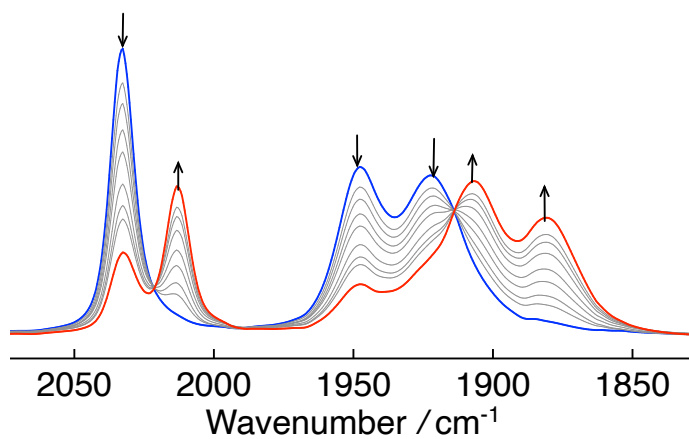


Figure S9: IR SEC of [1]<sup>0/-1</sup> in 0.1 M n-Bu<sub>4</sub>N[PF<sub>6</sub>]/CH<sub>2</sub>Cl<sub>2</sub>.

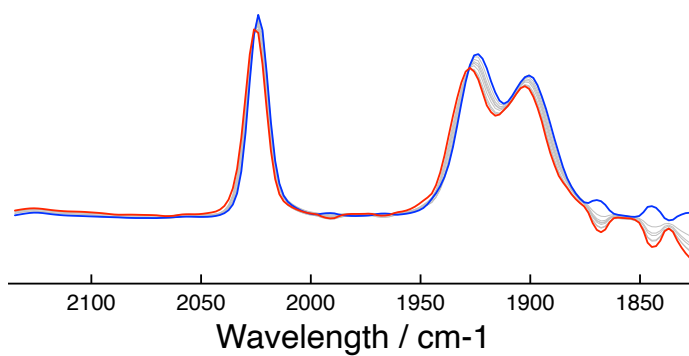


Figure S10: IR SEC of  $[1\text{H}_2\text{Fc}]^{0/+}$  in 0.1 M  $n\text{-Bu}_4\text{N}[\text{PF}_6]/\text{CH}_2\text{Cl}_2$ .

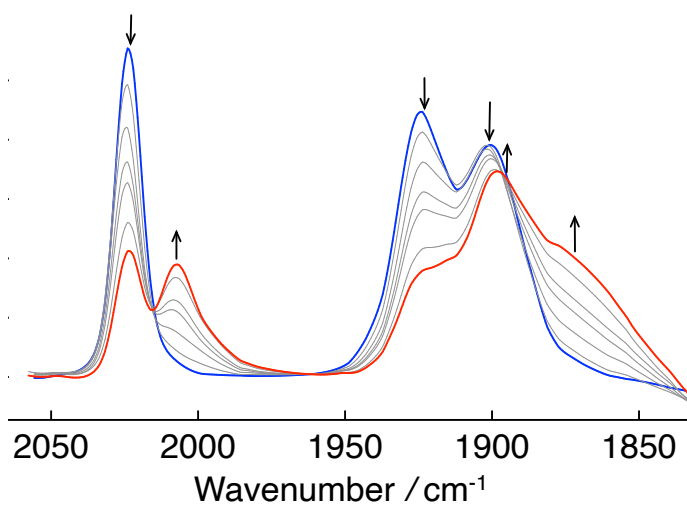


Figure S11: IR SEC of  $[1\text{H}_2\text{Fc}]^{0/-1}$  in 0.1 M  $n\text{-Bu}_4\text{N}[\text{PF}_6]/\text{CH}_2\text{Cl}_2$ .

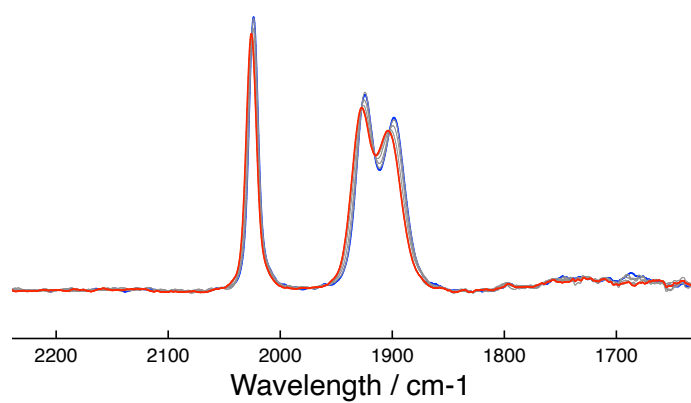


Figure S12: IR SEC of  $[1Fc]^{0/+}$  in 0.1 M  $n\text{-Bu}_4\text{N}[\text{PF}_6]/\text{CH}_2\text{Cl}_2$ .

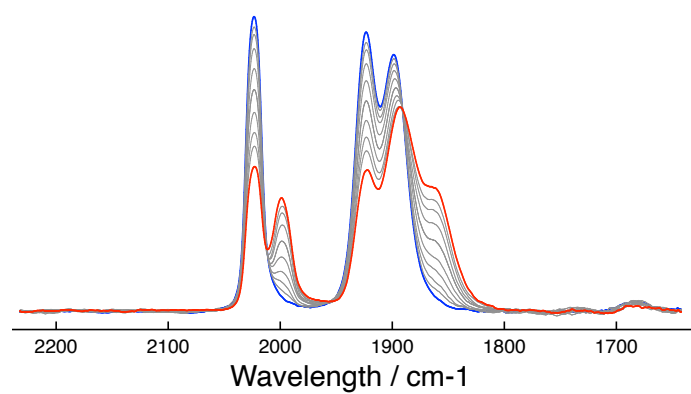


Figure S13: IR SEC of  $[1Fc]^{0/-}$  in 0.1 M  $n\text{-Bu}_4\text{N}[\text{PF}_6]/\text{CH}_2\text{Cl}_2$ .

## 6 Absorption Spectroscopy

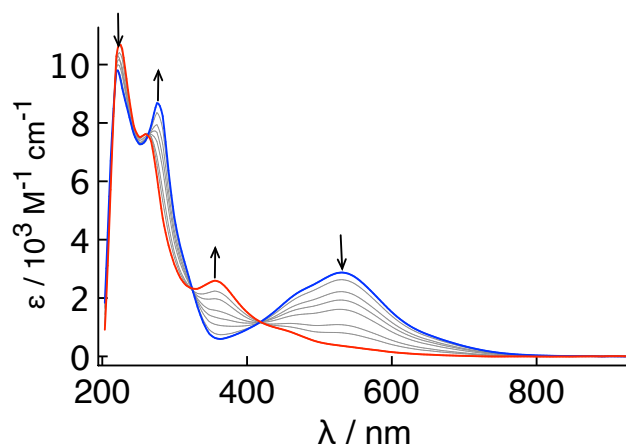


Figure S14: UV-vis NIR SEC of  $[1]^{0/-1}$  in 0.1 M  $\text{Bu}_4\text{NPF}_6 / \text{CH}_2\text{Cl}_2$ .

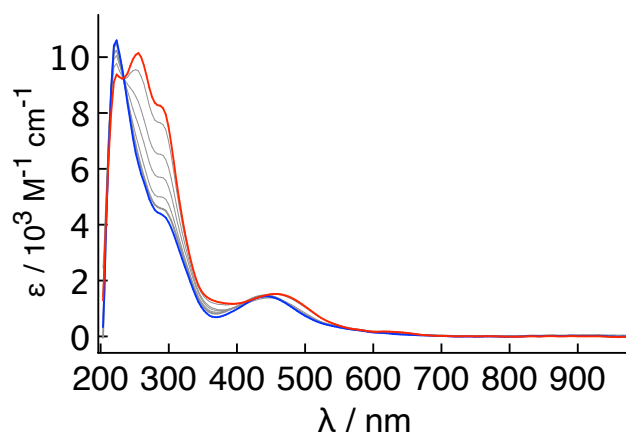


Figure S15: UV-vis NIR SEC of  $[1_2\text{Fc}]^{0/+}$  in 0.1 M  $\text{Bu}_4\text{NPF}_6 / \text{CH}_2\text{Cl}_2$ .



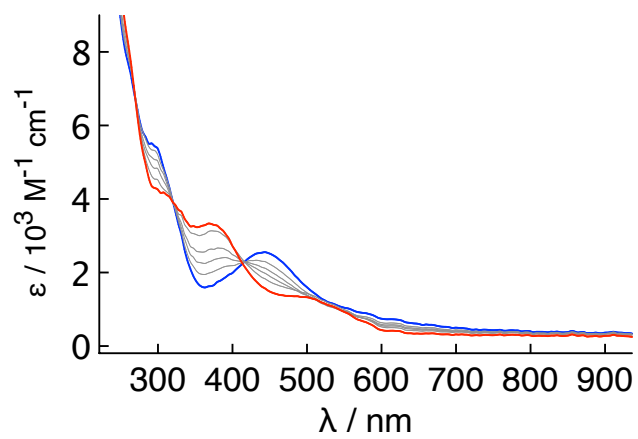


Figure S16: UV-vis NIR SEC of  $[1_2\text{Fc}]^{0/-1}$  in 0.1 M  $\text{Bu}_4\text{NPF}_6 / \text{CH}_2\text{Cl}_2$ .

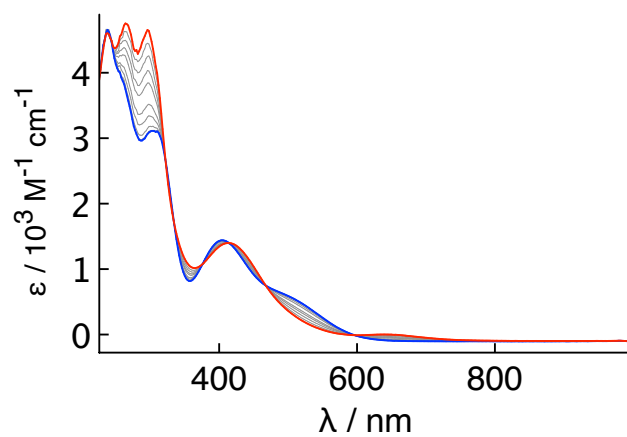


Figure S17: UV-vis NIR SEC of  $[1\text{Fc}]^{0/+}$  in 0.1 M  $\text{Bu}_4\text{NPF}_6 / \text{CH}_2\text{Cl}_2$ .

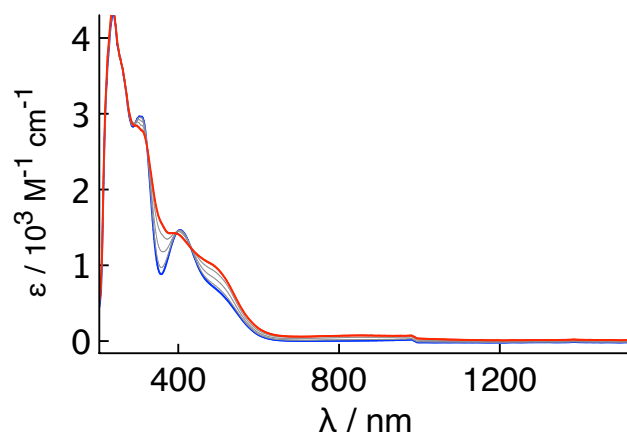


Figure S18: UV-vis NIR SEC of [1Fc]<sup>0/-1</sup> in 0.1 M Bu<sub>4</sub>NPF<sub>6</sub> / CH<sub>2</sub>Cl<sub>2</sub>.

## 7 TD DFT

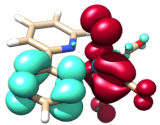
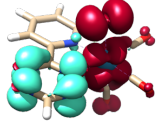
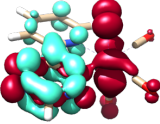
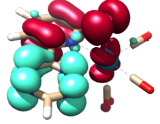
<p>[1]<sup>0</sup>  ! RKS PBE0 RIJCOSX def2-TZVP def2/J D3BJ NormalPrint Grid6 TightSCF CPCM(CH2Cl2)  Isosurface = 0.002, green denotes gain of electron density  Transitions below 5% were omitted</p>	
	<p>STATE 1: E= 0.052103 au 1.418 eV 11435.4 cm<sup>**</sup>-1  77a -&gt; 78a : 0.956230 (c= -0.97786991)</p>
	<p>STATE 3: E= 0.075747 au 2.061 eV 16624.5 cm<sup>**</sup>-1  74a -&gt; 78a : 0.049700 (c= -0.22293585)  75a -&gt; 78a : 0.067009 (c= 0.25886007)  76a -&gt; 78a : 0.741459 (c= 0.86108021)  77a -&gt; 79a : 0.074542 (c= 0.27302371)</p>
	<p>STATE 4: E= 0.092986 au 2.530 eV 20408.1 cm<sup>**</sup>-1  74a -&gt; 78a : 0.391136 (c= -0.62540837)  77a -&gt; 79a : 0.555033 (c= -0.74500555)</p>
	<p>STATE 11: E= 0.133817 au 3.641 eV 29369.4 cm<sup>**</sup>-1  71a -&gt; 78a : 0.727627 (c= 0.85301035)  72a -&gt; 78a : 0.058195 (c= 0.24123633)  72a -&gt; 79a : 0.056514 (c= -0.23772588)  77a -&gt; 80a : 0.077977 (c= -0.27924294)</p>

Figure S19: TDDFT transitions for [1] green denotes gain, red denotes loss.

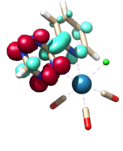
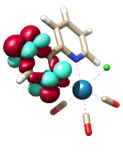
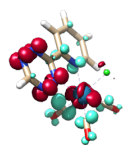
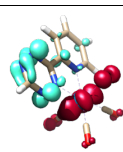
$[1]^{-1}$ ! UKS PBE0 RIJCOSX def2-TZVP def2/J D3BJ NormalPrint Grid6 TightSCF CPCM(CH2Cl2) Isosurface = 0.002, green denotes gain of electron density Transitions below 5% were omitted	
	STATE 1: E= 0.043139 au 1.174 eV 9468.0 cm <sup>**</sup> -1 78a -> 79a : 0.926469 (c= 0.96253236)
	STATE 3: E= 0.105018 au 2.858 eV 23048.7 cm <sup>**</sup> -1 74b -> 79b : 0.051047 (c= -0.22593516) 75b -> 78b : 0.172493 (c= -0.41532308) 75b -> 79b : 0.559844 (c= 0.74822756) 75b -> 80b : 0.054156 (c= -0.23271496)
	STATE 10: E= 0.122506 au 3.334 eV 26886.9 cm <sup>**</sup> -1 78a -> 82a : 0.558744 (c= -0.74749194) 76b -> 78b : 0.214445 (c= -0.46308181)
	STATE 15: E= 0.123213 au 3.353 eV 27042.1 cm <sup>**</sup> -1 77b -> 79b : 0.781123 (c= 0.88381188)

Figure S20: TDDFT transitions for  $[1]^{2+}$  green denotes gain, red denotes loss.

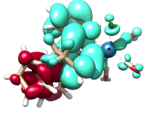
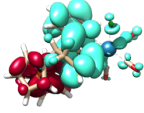
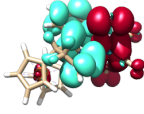
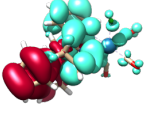
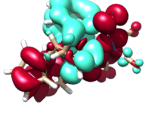
[1H <sub>2</sub> Fc] ! RKS PBE0 RIJCOSX def2-TZVP def2/J D3BJ NormalPrint Grid6 TightSCF CPCM(CH <sub>2</sub> Cl <sub>2</sub> ) Isosurface = 0.002, green denotes gain of electron density Transitions below 5% were omitted	
	STATE 1: E= 0.067510 au 1.837 eV 14816.8 cm <sup>**</sup> -1 124a -> 126a : 0.396810 (c= -0.62992831) 124a -> 132a : 0.010052 (c= 0.10025919) 125a -> 126a : 0.562709 (c= -0.75013957) 125a -> 131a : 0.013319 (c= -0.11540683)
	STATE 2: E= 0.067870 au 1.847 eV 14895.7 cm <sup>**</sup> -1 124a -> 126a : 0.564835 (c= -0.75155503) 124a -> 131a : 0.014555 (c= -0.12064570) 125a -> 126a : 0.393460 (c= 0.62726403) 125a -> 132a : 0.011273 (c= -0.10617326)
	STATE 8: E= 0.093215 au 2.536 eV 20458.2 cm <sup>**</sup> -1 120a -> 126a : 0.040649 (c= -0.20161489) 122a -> 126a : 0.872670 (c= 0.93416788) 123a -> 126a : 0.040539 (c= -0.20134403)
	STATE 11: E= 0.113133 au 3.078 eV 24829.7 cm <sup>**</sup> -1 119a -> 126a : 0.974233 (c= -0.98703235)
	STATE 18: E= 0.137962 au 3.754 eV 30279.1 cm <sup>**</sup> -1 112a -> 126a : 0.020032 (c= 0.14153609) 116a -> 126a : 0.279852 (c= -0.52901034) 117a -> 126a : 0.353630 (c= -0.59466811) 122a -> 127a : 0.190589 (c= 0.43656520) 123a -> 127a : 0.098324 (c= -0.31356632)

Figure S21: TDDFT transitions for 1H<sub>2</sub>Fc green denotes gain, red denotes loss.

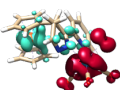
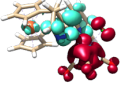
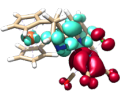
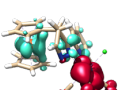
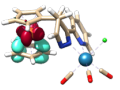
<p>[1H<sub>2</sub>Fc]<sup>+</sup>  ! UKS PBE0 RIJCOSX def2-TZVP def2/J D3BJ NormalPrint Grid6 TightSCF CPCM(CH<sub>2</sub>Cl<sub>2</sub>)  Isosurface = 0.002, green denotes gain of electron density  Transitions below 5% were omitted</p>	
	<p>STATE 8: E= 0.071496 au 1.946 eV 15691.7 cm<sup>**</sup>-1  124a -&gt; 126a : 0.210983 (c= -0.45932877)  123b -&gt; 125b : 0.397969 (c= 0.63084809)  123b -&gt; 126b : 0.054195 (c= -0.23279755)  124b -&gt; 125b : 0.104507 (c= 0.32327530)  124b -&gt; 126b : 0.186574 (c= -0.43194158)</p>
	<p>STATE 13: E= 0.088681 au 2.413 eV 19463.3 cm<sup>**</sup>-1  123a -&gt; 126a : 0.568244 (c= 0.75381979)  124a -&gt; 126a : 0.128133 (c= 0.35795727)  123b -&gt; 126b : 0.266542 (c= -0.51627721)</p>
	<p>STATE 14: E= 0.091984 au 2.503 eV 20188.1 cm<sup>**</sup>-1  123a -&gt; 126a : 0.354412 (c= 0.59532484)  124a -&gt; 126a : 0.180541 (c= -0.42490148)  122b -&gt; 125b : 0.073772 (c= -0.27161003)  123b -&gt; 126b : 0.348659 (c= 0.59047338)</p>
	<p>STATE 18: E= 0.086979 au 2.367 eV 19089.6 cm<sup>**</sup>-1  122b -&gt; 125b : 0.297062 (c= -0.54503439)  122b -&gt; 126b : 0.682648 (c= 0.82622486)</p>
	<p>STATE 25: E= 0.117369 au 3.194 eV 25759.5 cm<sup>**</sup>-1  112b -&gt; 125b : 0.208305 (c= 0.45640481)  114b -&gt; 125b : 0.066920 (c= 0.25868882)  117b -&gt; 125b : 0.174500 (c= 0.41773256)  118b -&gt; 125b : 0.096991 (c= 0.31143316)  119b -&gt; 125b : 0.244860 (c= -0.49483282)</p>

Figure S22: TDDFT transitions for 1H<sub>2</sub>Fc<sup>+</sup> green denotes gain, red denotes loss.

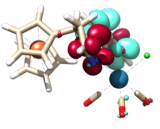
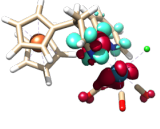
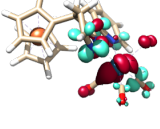
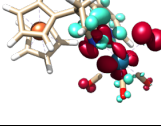
$[1\text{H}_2\text{Fc}]^{-1}$ ! UKS PBE0 RIJCOSX def2-TZVP def2/J D3BJ NormalPrint Grid6 TightSCF CPCM(CH2Cl2) Isosurface = 0.002, green denotes gain of electron density Transitions below 5% were omitted	
	STATE 5: E= 0.066121 au 1.799 eV 14512.0 cm <sup>**</sup> -1 126a -> 127a : 0.931796 (c= 0.96529587) 126a -> 129a : 0.017632 (c= 0.13278638)
	STATE 10: E= 0.094557 au 2.573 eV 20752.9 cm <sup>**</sup> -1 126a -> 128a : 0.095300 (c= 0.30870619) 126a -> 129a : 0.213103 (c= 0.46163064) 123b -> 126b : 0.057911 (c= -0.24064623) 125b -> 126b : 0.494297 (c= -0.70306277)
	STATE 14: E= 0.105471 au 2.870 eV 23148.3 cm <sup>**</sup> -1 126a -> 129a : 0.539957 (c= 0.73481756) 125b -> 126b : 0.240186 (c= 0.49008772)
	STATE 22: E= 0.128698 au 3.502 eV 28246.0 cm <sup>**</sup> -1 126a -> 129a : 0.054978 (c= 0.23447472) 126a -> 132a : 0.047459 (c= 0.21785120) 126a -> 133a : 0.012910 (c= 0.11362396) 120b -> 126b : 0.744587 (c= 0.86289449)

Figure S23: TDDFT transitions for  $1\text{H}_2\text{Fc}^{-1}$  green denotes gain, red denotes loss.

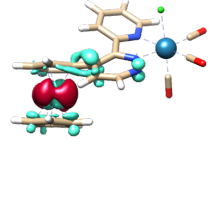
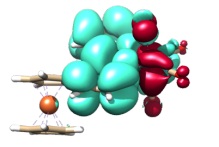
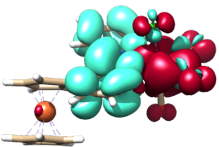
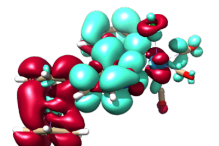
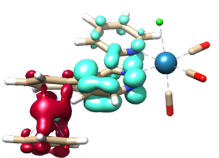
[1Fc] ! RKS PBE0 RIJCOSX def2-TZVP def2/J D3BJ NormalPrint Grid6 TightSCF CPCM(CH2Cl2) Isosurface = 0.002, green denotes gain of electron density Transitions below 5% were omitted	
	STATE 2: E= 0.087666 au 2.386 eV 19240.4 cm <sup>-1</sup> 122a -> 130a : 0.072724 (c= 0.26967435) 122a -> 131a : 0.054570 (c= -0.23360286) 122a -> 132a : 0.086173 (c= -0.29355162) 123a -> 126a : 0.087211 (c= -0.29531515) 123a -> 131a : 0.091726 (c= -0.30286259) 124a -> 126a : 0.175241 (c= -0.41861832) 124a -> 131a : 0.192112 (c= -0.43830530) 124a -> 132a : 0.082985 (c= 0.28807135)
	STATE 3: E= 0.084888 au 2.310 eV 18630.9 cm <sup>-1</sup> 123a -> 125a : 0.655172 (c= 0.80942686) 124a -> 125a : 0.280820 (c= -0.52992415)
	STATE 9: E= 0.100400 au 2.732 eV 22035.2 cm <sup>-1</sup> 120a -> 125a : 0.911082 (c= -0.95450624)
	STATE 18: E= 0.130883 au 3.562 eV 28725.6 cm <sup>-1</sup> 118a -> 125a : 0.806671 (c= 0.89814870)
	STATE 22: E= 0.141330 au 3.846 eV 31018.4 cm <sup>-1</sup> 117a -> 125a : 0.223878 (c= 0.47315775) 118a -> 126a : 0.055319 (c= 0.23520088) 119a -> 126a : 0.376345 (c= -0.61346963) 119a -> 131a : 0.081370 (c= 0.28525398) 119a -> 132a : 0.060817 (c= -0.24661191)

Figure S24: TDDFT transitions for 1Fc green denotes gain, red denotes loss.



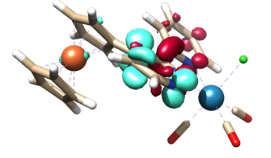
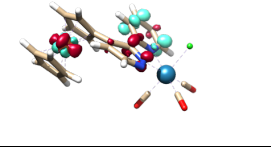
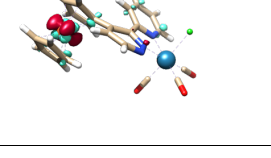
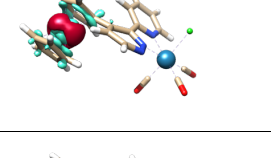
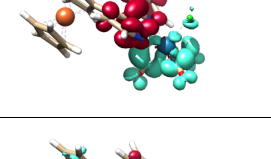
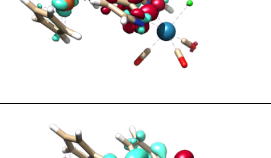
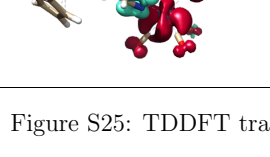
[1Fc] <sup>-1</sup> ! UKS PBE0 RIJCOSX def2-TZVP def2/J D3BJ NormalPrint Grid6 TightSCF CPCM(CH2Cl2) Isosurface = 0.002, green denotes gain of electron density Transitions below 5% were omitted	
	STATE 1: E= 0.032869 au 0.894 eV 7214.0 cm <sup>**</sup> -1 125a -> 126a : 0.955662 (c= -0.97757942)
	STATE 2: E= 0.061034 au 1.661 eV 13395.3 cm <sup>**</sup> -1 123a -> 131a : 0.109935 (c= -0.33156511) 125a -> 127a : 0.484792 (c= 0.69627007) 123b -> 131b : 0.097014 (c= 0.31147085)
	STATE 4: E= 0.063291 au 1.722 eV 13890.8 cm <sup>**</sup> -1 122a -> 126a : 0.077793 (c= 0.27891475) 122a -> 131a : 0.226371 (c= -0.47578498) 125a -> 127a : 0.182867 (c= -0.42762940) 122b -> 126b : 0.072307 (c= -0.26890050) 122b -> 129b : 0.067740 (c= -0.26026955) 122b -> 131b : 0.193027 (c= -0.43934883)
	STATE 9: E= 0.088377 au 2.405 eV 19396.5 cm <sup>**</sup> -1 122a -> 130a : 0.069300 (c= 0.26324953) 123a -> 131a : 0.113658 (c= -0.33713275) 122b -> 131b : 0.069609 (c= -0.26383508) 123b -> 129b : 0.092365 (c= -0.30391616) 123b -> 131b : 0.091886 (c= -0.30312634)
	STATE 12: E= 0.082582 au 2.247 eV 18124.8 cm <sup>**</sup> -1 125a -> 129a : 0.860449 (c= 0.92760411) 125a -> 130a : 0.064864 (c= 0.25468332)
	STATE 15: E= 0.102846 au 2.799 eV 22572.0 cm <sup>**</sup> -1 125a -> 130a : 0.383221 (c= 0.61904875) 125a -> 131a : 0.111115 (c= 0.33333946) 125a -> 132a : 0.328046 (c= -0.57275303)
	STATE 19: E= 0.115908 au 3.154 eV 25438.8 cm <sup>**</sup> -1 121b -> 125b : 0.779479 (c= 0.88288094) 123b -> 125b : 0.099981 (c= -0.31619762)

Figure S25: TDDFT transitions for 1Fc<sup>-1</sup> green denotes gain, red denotes loss.

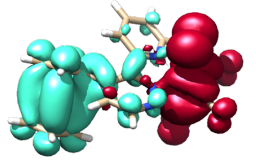
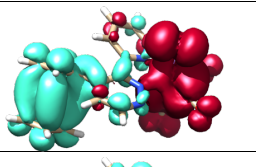
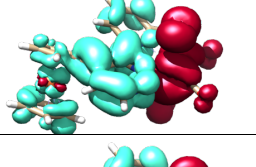
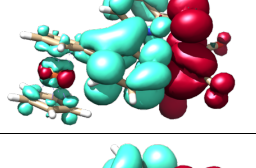
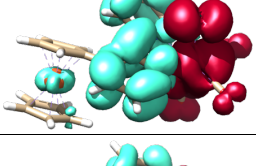
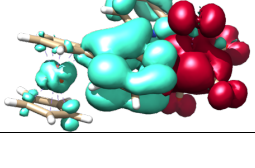
[1Fc] <sup>+</sup> ! UKS PBE0 RIJCOSX def2-TZVP def2/J D3BJ NormalPrint Grid6 TightSCF CPCM(CH2Cl2) Isosurface = 0.002, green denotes gain of electron density Transitions below 5% were omitted	
	STATE 5: E= 0.045085 au 1.227 eV 9895.0 cm <sup>-1</sup> 123b -> 124b : 0.971534 (c= 0.98566407) 123b -> 125b : 0.013840 (c= 0.11764352)
	STATE 6: E= 0.048772 au 1.327 eV 10704.3 cm <sup>-1</sup> 122b -> 124b : 0.971396 (c= -0.98559420) 122b -> 125b : 0.010465 (c= -0.10229793)
	STATE 10: E= 0.077726 au 2.115 eV 17058.9 cm <sup>-1</sup> 124a -> 125a : 0.659935 (c= -0.81236362) 123b -> 125b : 0.086823 (c= 0.29465741)
	STATE 12: E= 0.083885 au 2.283 eV 18410.6 cm <sup>-1</sup> ) 124a -> 125a : 0.161178 (c= 0.40146919) 124a -> 126a : 0.159339 (c= 0.39917346) 124a -> 127a : 0.174826 (c= 0.41812176) 123b -> 125b : 0.340935 (c= 0.58389661)
	STATE 15: E= 0.092620 au 2.520 eV 20327.7 cm <sup>-1</sup> 123a -> 126a : 0.196577 (c= -0.44337015) 123a -> 127a : 0.181876 (c= -0.42646865) 122b -> 125b : 0.440844 (c= -0.66396106)
	STATE 22: E= 0.097175 au 2.644 eV 21327.4 cm <sup>-1</sup> 122a -> 125a : 0.104346 (c= -0.32302619) 122a -> 126a : 0.109500 (c= -0.33090806) 122a -> 127a : 0.114672 (c= -0.33863207) 121b -> 125b : 0.399669 (c= -0.63219353) 122b -> 126b : 0.181598 (c= -0.42614362)

Figure S26: TDDFT transitions for 1Fc<sup>+</sup> green denotes gain, red denotes loss.



**Supporting Infos of Paper 3.**

## SUPPORTING INFORMATION

[[ $\eta^6$ -CYMENE)(3-(PYRID-2-YL)-1,2,4,5-TETRAZINE)CHLORORUTHENIUM(II)]<sup>+</sup>, REDOX NONINNOCENCE AND DIENOPHILE ADDITION TO COORDINATED TETRAZINE

Marc Schnierle, Marie Leimkühler, and Mark R. Ringenberg\*

† Insitut für Anorganische Chemie, Universität Stuttgart, Pfaffenwaldring 55, 70569  
Stuttgart, Germany

Raw data will be published to the data repository DARUS at  
<https://doi.org/10.18419/darus-1181> upon acceptance of this publication

## Contents

<b>1</b>	<b>Experimental</b>	<b>S4</b>
<b>2</b>	<b>Crystallography</b>	<b>S6</b>
<b>3</b>	<b>Cyclic Voltammetry</b>	<b>S7</b>
3.1	Rotating Disk Electrode . . . . .	S10
<b>4</b>	<b>NMR Spectroscopy</b>	<b>S14</b>
<b>5</b>	<b>Kinetics</b>	<b>S18</b>
<b>6</b>	<b>Absorption Spectroscopy</b>	<b>S21</b>
<b>7</b>	<b>DFT Calculations</b>	<b>S22</b>
7.1	TD-DFT . . . . .	S28
<b>8</b>	<b>XYZ Coordinates from DFT calculations</b>	<b>S40</b>

## List of Figures

S1	CV of $\mathbf{1}^+$ with Bu <sub>4</sub> NPF <sub>6</sub> , and Bu <sub>4</sub> NCl . . . . .	S7
S2	Randles-Sevcik Plot of $\mathbf{1}^+$ . . . . .	S7
S3	CV of $\mathbf{1}^+$ with Bu <sub>4</sub> NPF <sub>6</sub> . . . . .	S8
S4	Randles-Sevcik Plot of $\mathbf{1}^+$ . . . . .	S8
S5	CV compare $\mathbf{1}^+$ Bu <sub>4</sub> NCl or Bu <sub>4</sub> NPF <sub>6</sub> . . . . .	S9
S6	CV of $\mathbf{1}^+$ in DMF . . . . .	S9
S7	CV of $\mathbf{1H}_2\text{Fc}^+$ . . . . .	S9
S8	CV of $\mathbf{1Fc}^+$ , Bu <sub>4</sub> NCl . . . . .	S10
S9	LSV-RDE of $\mathbf{1}^+$ PF <sub>6</sub> . . . . .	S10
S10	Levich Plot of $\mathbf{1}^+$ . . . . .	S11
S11	Koutecky-Levich Plot of $\mathbf{1}^+$ . . . . .	S11
S12	LSV-RDE of $\mathbf{1}^+$ PF <sub>6</sub> /Cl . . . . .	S12
S13	Levich Plot of $\mathbf{1}^+$ + Cl . . . . .	S13
S14	Koutecky-Levich Plot of $\mathbf{1}^+$ + Cl . . . . .	S13
S15	<sup>1</sup> H NMR of $\mathbf{1}^+$ . . . . .	S14
S16	COSY NMR of $\mathbf{1}^+$ . . . . .	S15
S17	<sup>1</sup> H NMR of $\mathbf{1H}_2\text{Fc}^+$ . . . . .	S15
S18	<sup>1</sup> H NMR of $\mathbf{1H}_2\text{Fc}^+$ . . . . .	S16
S19	<sup>1</sup> H NMR of $\mathbf{1Fc}^+$ . . . . .	S16

S20	COSY NMR of $1\text{Fc}^+$ . . . . .	S17
S21	$^1\text{H}$ NMR from oxidation of $1\text{H}_2\text{Fc}^+$ to $1\text{Fc}^+$ . . . . .	S17
S22	$^1\text{H}$ NMR from oxidation of $1\text{H}_2\text{Fc}^+$ to $1\text{Fc}^+$ . . . . .	S18
S23	Kinetics of $\text{TzPy} + \text{EthFc}$ 22C . . . . .	S18
S24	Kinetics of $1^+ + \text{EthFc}$ 20C . . . . .	S18
S25	Kinetics of $1^+ + \text{EthFc}$ 10C . . . . .	S19
S26	Kinetics of $1^+ + \text{EthFc}$ 0C . . . . .	S19
S27	Kinetics of $1^+ + \text{EthFc}$ -20C . . . . .	S19
S28	Eyring Plot of $\text{EthFc} + 1^+$ . . . . .	S20
S29	Kinetics of $1^+ + \text{ViFc}$ 0C . . . . .	S20
S30	Kinetics of $1^+ + \text{ViFc}$ 22C . . . . .	S20
S31	Kinetics of $1^+ + \text{ViFc}$ 40C . . . . .	S21
S32	Eyring Plot of $\text{ViFc} + 1^+$ . . . . .	S21
S33	UV-vis NIR SEC of $1^{+/n}$ . . . . .	S21
S34	UV-vis NIR SEC of $1\text{H}_2\text{Fc}^{+/2+}$ . . . . .	S22
S35	UV-vis NIR SEC of $1\text{H}_2\text{Fc}^{+/n}$ . . . . .	S22
S36	DFT (HOMO/LUMO of four $1^+$ . . . . .	S22
S37	DFT (HOMO/LUMO of four $1\text{Fc}^+$ . . . . .	S23
S38	DFT (HOMO/LUMO of four $1(4,5)\text{H}_2\text{Fc}$ isomers . . . . .	S23
S39	DFT (HOMO/LUMO of four $1(2,5)\text{H}_2\text{Fc}$ isomers . . . . .	S24
S40	IBO of $1\text{-Cl}^0$ . . . . .	S25
S41	Spin Density of $1^0$ . . . . .	S25
S42	Spin Density of $1\bullet\text{Cl}^{-1}$ . . . . .	S26
S43	Spin Density of $1\text{Fc}^0$ . . . . .	S26
S44	Spin Density of $1\text{Fc}^{2+}$ . . . . .	S27
S45	DFT structured of $1\text{Fc}\bullet\text{Cl}^{-1}$ . . . . .	S27
S46	IBO of $1\text{Fc}\bullet\text{Cl}^0$ . . . . .	S27
S47	Spin Density of $1\text{Fc}\bullet\text{Cl}^{-1}$ . . . . .	S28
S48	EDDM of $\text{CyRuCl}(\text{TzPy})^+$ . . . . .	S28
S49	EDDM of $\text{CyRuCl}(\text{TzPy})^0$ . . . . .	S30
S50	EDDM of $\text{CyRu}(\text{TzPy})^0$ . . . . .	S31
S51	EDDM of $\text{CyRu}(\text{TzPy})^{-1}$ . . . . .	S32
S52	EDDM of $\text{CyRuCl}(\text{DzFcPy})^+$ . . . . .	S33
S53	EDDM of $\text{CyRuCl}(\text{DzFcPy})^{2+}$ . . . . .	S35
S54	EDDM of $\text{CyRuCl}(\text{DzFcPy})^0$ . . . . .	S36
S55	EDDM of $\text{CyRu}(\text{DzFcPy})^0$ . . . . .	S37
S56	EDDM of $\text{CyRu}(\text{DzFcPy})^{-1}$ . . . . .	S38

**List of Tables**

S1	Crystallographic Information for $[1]^+$ and $[1\mathbf{Fc}]^+$ . . . . .	S6
S2	TDDFT transitions of $\text{CyRuCl}(\text{TzPy})^+$ . . . . .	S29
S3	TDDFT transitions of $\text{CyRuCl}(\text{TzPy})^0$ . . . . .	S30
S4	TDDFT transitions of $\text{CyRu}(\text{TzPy})^0$ . . . . .	S31
S5	TDDFT transitions of $\text{CyRu}(\text{TzPy})^{-1}$ . . . . .	S32
S6	TDDFT transitions of $\text{CyRuCl}(\text{DzFcPy})^+$ . . . . .	S34
S7	TDDFT transitions of $\text{CyRuCl}(\text{DzFcPy})^{2+}$ . . . . .	S35
S8	TDDFT transitions of $\text{CyRuCl}(\text{DzFcPy})^0$ . . . . .	S36
S9	TDDFT transitions of $\text{CyRu}(\text{DzFcPy})^0$ . . . . .	S37
S10	TDDFT transitions of $\text{CyRu}(\text{DzFcPy})^{-1}$ . . . . .	S39
S11	XYZ file generated for B3LYP $\text{CyRuClTzPy}^+$ . . . . .	S40
S12	XYZ file generated for B3LYP $\text{CyRuClTzPy}^0$ . . . . .	S41
S13	XYZ file generated for B3LYP $\text{CyRuClTzPy}^{-1}$ . . . . .	S42
S14	XYZ file generated for B3LYP $\text{CyRuTzPy}^0$ . . . . .	S43
S15	XYZ file generated for B3LYP $\text{CyRuTzPy}^{-1}$ . . . . .	S44
S16	XYZ file generated for B3LYP $\text{CyRuCl}(\text{DzFcPy})^+$ . . . . .	S45
S17	XYZ file generated for B3LYP $\text{CyRuCl}(\text{DzFcPy})^{2+}$ . . . . .	S46
S18	XYZ file generated for B3LYP $\text{CyRuCl}(\text{DzFcPy})^0$ . . . . .	S47
S19	XYZ file generated for B3LYP $\text{CyRuCl}(\text{DzFcPy})^{-1}$ . . . . .	S48
S20	XYZ file generated for B3LYP $\text{CyRu}(\text{DzFcPy})^0$ . . . . .	S49
S21	XYZ file generated for B3LYP $\text{CyRu}(\text{DzFcPy})^{-1}$ . . . . .	S50
S22	XYZ file generated for B3LYP $[1(2,5)\text{H}_2\text{Fc-a}]^+$ . . . . .	S51
S23	XYZ file generated for B3LYP $[1(2,5)\text{H}_2\text{Fc-b}]^+$ . . . . .	S52
S24	XYZ file generated for B3LYP $[1(4,5)\text{H}_2\text{Fc-a}]^+$ . . . . .	S53
S25	XYZ file generated for B3LYP $[1(4,5)\text{H}_2\text{Fc-b}]^+$ . . . . .	S54

## 1 Experimental

$^1\text{H}$  spectra were taken on a Bruker AC 250, 400, or 700 MHz spectrometer.  $^1\text{H}$  NMR spectra were referenced versus residual solvent peak. UV-vis-NIR absorption spectra were recorded on J&M TIDAS spectrophotometer. Cyclic voltammetry was carried out in 0.1 M  $\text{Bu}_4\text{NPF}_6/\text{CH}_2\text{Cl}_2$  solutions using a three-electrode configuration (glassy carbon working, Pt wire counter, and Ag quasi-reference) and were performed using a Metrohm Autolab potentiostat. Rotating disk electrode from Metrohm (AUT.RDE.S) was equipped with a Pt working, 10 second resting period was done between different rotation speeds. The ferrocene/ferrocenium ( $[\text{Fc}]^{0/+}$ ) couple served as internal reference to all potentials reported herein. Spectroelectrochemistry was performed using an optically transparent thin-layered electrode (OTTLE) cell. [1] Low temperature spectroelectrochemistry was performed using a liquid nitrogen cooled cell previously described. [2] X-ray diffraction data were collected using a Bruker Kappa Apex2duo diffractometer. The structures were solved using charge flipping and refined by full-matrix least-squares techniques on F2 using the OLEX2 program [3] The absorption corrections were done by multiscan technique. All non-hydrogen atoms were refined anisotropically. Hydrogen atoms were included in the refinement process as per the riding model.

Density functional theory (DFT) calculations were performed using the solid-state structure of  $[\mathbf{1}]^+$  and  $[\mathbf{1Fc}]^+$ . A computational analysis was performed by means of restricted Kohn-Sham density functional theory (DFT) using B3LYP [4] functional in combination with the D3 dispersion correction [5] with the def2-TZVP and Weigend J auxiliary basis set. [6, 7] Geometry optimizations were realized with the ORCA program package with TightSCF convergence ( $1.0\text{e-}7$  a.u.). [8] Solvation in  $\text{CH}_2\text{Cl}_2$  was modeled using the CPCM solvation model. [9] Open-shell calculations on the structure  $[\mathbf{1}]^0$ ,  $[\mathbf{1Fc}]^0$ ,  $[\mathbf{1}]^{-1}$  and  $[\mathbf{1Fc}]^{-1}$  were determined by adding the requisite number of electrons and removing the chloride ligand where relevant, and calculations were performed by means of (un)restricted Kohn-Sham DFT using the same basis set, functionals, and solvent models as  $[\mathbf{1}]^+$ .

## References

- [1] M. Krejčík, M. Danek, and F. Hartl, "Simple construction of an infrared optically transparent thin-layer electrochemical cell: Applications to the redox reactions of ferrocene,  $\text{Mn}_2(\text{CO})_{10}$  and  $\text{Mn}(\text{CO})_3(3,5\text{-di-}t\text{-butyl-catecholate})^-$ ," *J. Electroanal. Chem. Interfacial Electrochem.*, vol. 317, no. 1–2, pp. 179–187, 1991.
- [2] T. Mahabiersing, H. Luyten, R. C. Nieuwendam, and F. Hartl, "Synthesis, spectroscopy and spectroelectrochemistry of chlorocarbonyl 1,2-Bis[(2,6-



- diisopropylphenyl)imino]acenaphthene- $\kappa^2$ -N,N'rhodium(i)," *Collect. Czech. Chem. Commun.*, vol. 68, no. 9, pp. 1687–1709, 2003.
- [3] O. V. Dolomanov, L. J. Bourhis, R. J. Gildea, J. A. K. Howard, and H. Puschmann, "Olex2: a complete structure solution, refinement and analysis program," *J. Appl. Cryst.*, vol. 42, pp. 339–341, 2009.
- [4] J. P. Perdew, K. Burke, and M. Ernzerhof, "Generalized gradient approximation made simple [phys. rev. lett. 77, 3865 (1996)]," *Phys. Rev. Lett.*, vol. 78, no. 7, pp. 1396–1396, 1997.
- [5] S. Grimme, J. Antony, S. Ehrlich, and H. Krieg, "A consistent and accurate ab initio parametrization of density functional dispersion correction (dft-d) for the 94 elements h-pu," *J. Chem. Phys.*, vol. 132, no. 15, p. 154104, 2010.
- [6] F. Weigend and R. Ahlrichs, "Balanced basis sets of split valence, triple zeta valence and quadruple zeta valence quality for h to rn: Design and assessment of accuracy," *Phys. Chem. Chem. Phys.*, vol. 7, no. 18, pp. 3297–3305, 2005.
- [7] F. Weigend, M. Häser, H. Patzelt, and R. Ahlrichs, "Ri-mp2: optimized auxiliary basis sets and demonstration of efficiency," *Chem. Phys. Lett.*, vol. 294, no. 1–3, pp. 143–152, 1998.
- [8] F. Neese, "The orca program system," *WIREs Comput Mol Sci*, vol. 2, no. 1, pp. 73–78, 2012.
- [9] Y. Takano and K. N. Houk, "Benchmarking the conductor-like polarizable continuum model (cpcm) for aqueous solvation free energies of neutral and ionic organic molecules," *J. Chem. Theory Comput.*, vol. 1, no. 1, pp. 70–77, 2005.
- [10] G. Knizia, "Intrinsic atomic orbitals: An unbiased bridge between quantum theory and chemical concepts," *J. Chem. Theory Comput.*, vol. 9, no. 11, pp. 4834–4843, 2013.

## 2 Crystallography

Table S1: Crystallographic Information for [1]<sup>+</sup> and [1Fc]<sup>+</sup>

<b>Crystal data and structure refinement:</b>		
Identification code	stams06 – [1] <sup>+</sup>	stams09 – [1Fc] <sup>+</sup>
Empirical formula	C <sub>24.5</sub> H <sub>15.5</sub> B <sub>0.5</sub> Cl <sub>0.5</sub> F <sub>11.98</sub> N <sub>2.5</sub> Ru <sub>0.5</sub>	C <sub>30</sub> H <sub>31</sub> Cl <sub>3</sub> F <sub>6</sub> FeN <sub>3</sub> PRu
Formula weight	646.23	841.82
Temperature/K	293(2)	100 k
Crystal system	triclinic	triclinic
Space group	P-1	P-1
a/Å	12.7973(10)	10.4460(7)
b/Å	13.4628(12)	11.0953(7)
c/Å	16.1756(12)	14.2019(9)
α/°	71.250(6)	86.266(5)
β/°	85.691(6)	84.375(5)
γ/°	73.409(6)	74.855(5)
Volume/Å <sup>3</sup>	2528.7(4)	1579.86(18)
Z	4	2
ρ <sub>calc</sub> /cm <sup>3</sup>	1.697	1.770
μ/mm <sup>-1</sup>	0.494	1.305
F(000)	1283.0	844.0
Crystal size/mm <sup>3</sup>	0.178 × 0.1275 × 0.0781	0.48 × 0.18 × 0.15
Radiation	MoKα (λ = 0.71073)	MoKα (λ = 0.71073)
2θ range for data collection/°	2.66 to 51.362	3.806 to 63.79
Index ranges	-15 ≤ h ≤ 15, -16 ≤ k ≤ 16, -19 ≤ l ≤ 19	-14 ≤ h ≤ 15, -16 ≤ k ≤ 15, -20 ≤ l ≤ 20
Reflections collected	18764	32771
Independent reflections	9583 [R <sub>int</sub> = 0.1385, R <sub>sigma</sub> = 0.1757]	9708 [R <sub>int</sub> = 0.0467, R <sub>sigma</sub> = 0.0771]
Data/restraints/parameters	9583/372/640	9708/0/409
Goodness-of-fit on F <sup>2</sup>	1.116	1.033
Final R indexes [I >= 2σ (I)]	R <sub>1</sub> = 0.1242, wR <sub>2</sub> = 0.3013	R <sub>1</sub> = 0.0458, wR <sub>2</sub> = 0.0891
Final R indexes [all data]	R <sub>1</sub> = 0.1770, wR <sub>2</sub> = 0.3456	R <sub>1</sub> = 0.0952, wR <sub>2</sub> = 0.1077
Largest diff. peak/hole / e Å <sup>-3</sup>	2.37/-2.11	1.07/-0.88

### 3 Cyclic Voltammetry

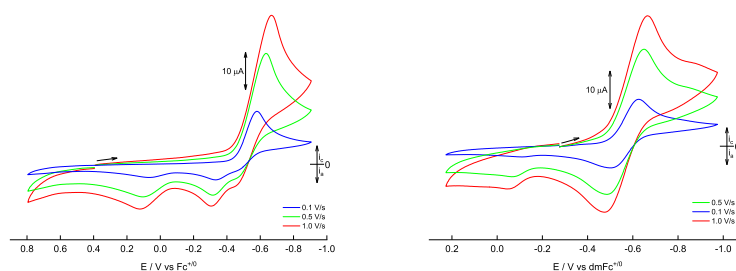


Figure S1: CV of cathodic process  $[1]^+$  in 0.1M  $\text{Bu}_4\text{NPF}_6/\text{CH}_2\text{Cl}_2$  (left) and 0.1M  $\text{Bu}_4\text{NCl}/\text{CH}_2\text{Cl}_2$  (right) at 0.1, 0.5, and 1  $\text{V s}^{-1}$ .

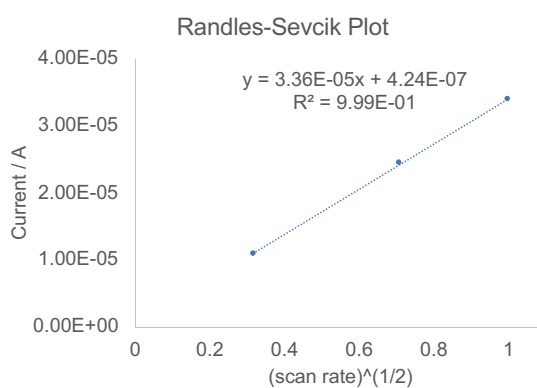


Figure S2: Randles-Sevcik Plot of cathodic process  $[1]^+$  in 0.1M  $\text{Bu}_4\text{NCl}/\text{CH}_2\text{Cl}_2$  (left) at 0.1, 0.5, and 1  $\text{V s}^{-1}$ .

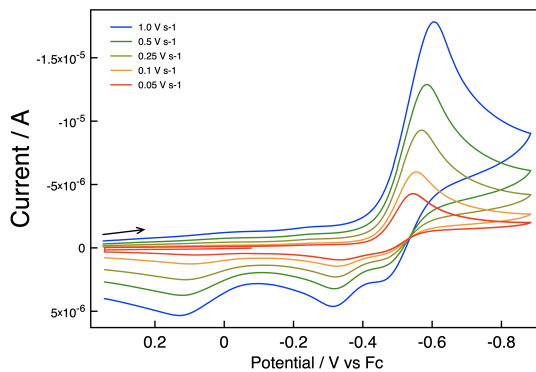


Figure S3: CV of cathodic process  $[1]^+$  in  $0.1\text{M Bu}_4\text{NPF}_6/\text{CH}_2\text{Cl}_2$  (left) at 0.05, 0.1, 0.25, 0.5, and  $1\text{ V s}^{-1}$ .

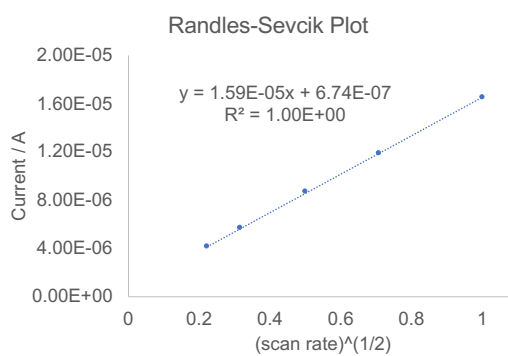


Figure S4: Randles-Sevcik Plot of cathodic process  $[1]^+$  in  $0.1\text{M Bu}_4\text{NPF}_6/\text{CH}_2\text{Cl}_2$  (left) at 0.05, 0.1, 0.25, 0.5, and  $1\text{ V s}^{-1}$ .

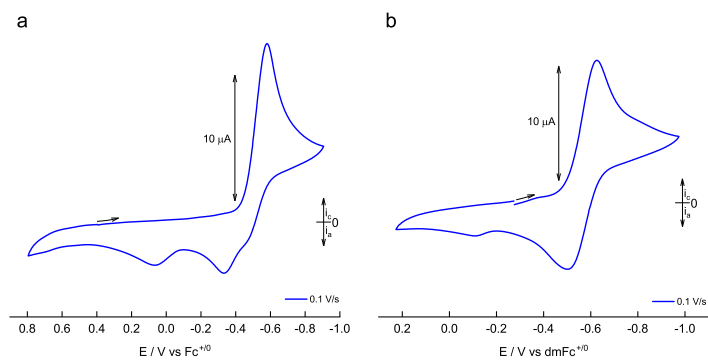


Figure S5: CV of cathodic process  $[1]^+$  in 0.1M  $\text{Bu}_4\text{NPF}_6/\text{CH}_2\text{Cl}_2$  (left) 0.1M  $\text{Bu}_4\text{NCl}/\text{CH}_2\text{Cl}_2$  (right) at  $0.1 \text{ V s}^{-1}$ .

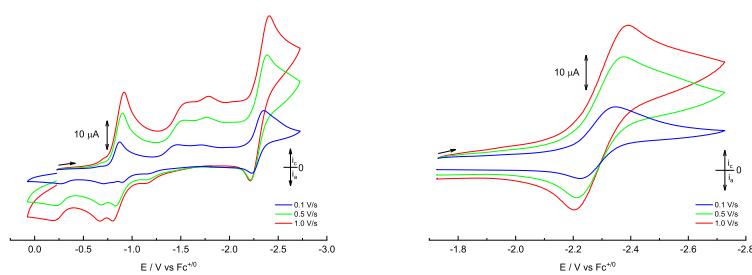


Figure S6: CV of  $[1]^+$  in 0.1M  $\text{Bu}_4\text{NPF}_6/\text{DMF}$  at 0.1, 0.5, and  $1 \text{ V s}^{-1}$ .

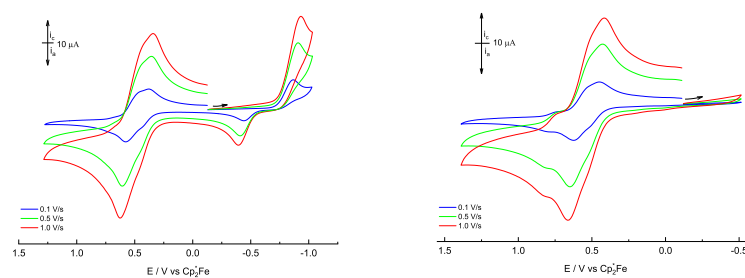


Figure S7: CV of  $[1\text{H}_2\text{Fc}]^+$  in 0.1M  $\text{Bu}_4\text{NPF}_6/\text{CH}_2\text{Cl}_2$  at 0.1, 0.5, and  $1 \text{ V s}^{-1}$ .

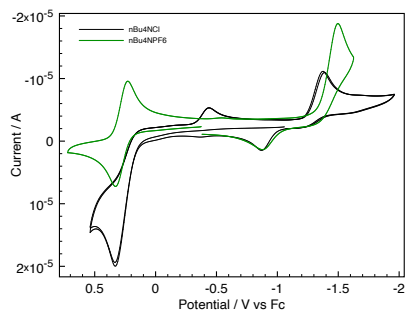


Figure S8: CV of  $[1Fc]^+$  in 0.1M  $Bu_4NCl/CH_2Cl_2$  at  $0.1 V s^{-1}$ .

### 3.1 Rotating Disk Electrode

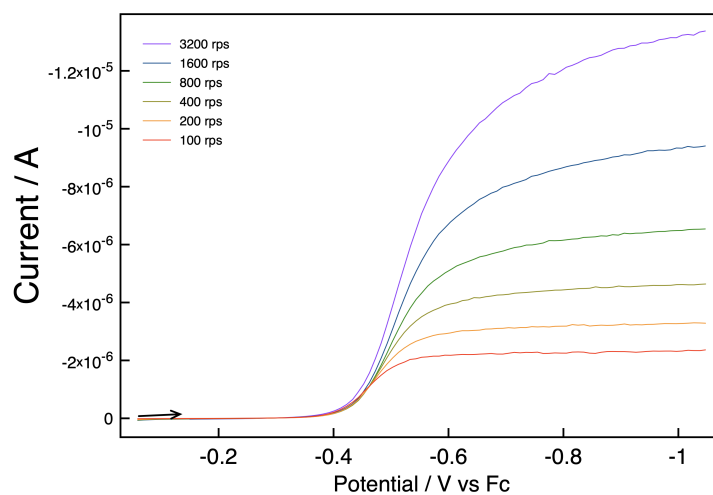


Figure S9: Linear Sweep Voltammogram at  $10 mV s^{-1}$  concentration  $2.43 e^{-07} mol cm^{-3} [1]^+$  in 0.1M  $Bu_4NPF_6/CH_2Cl_2$  at  $\omega / rad s^{-1} = 100, 200, 400, 800, 1600, 3200$

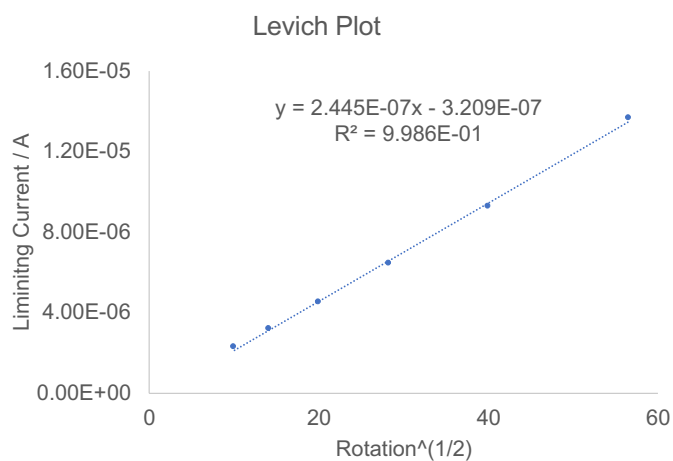


Figure S10: Levich Plot of cathodic process  $[1]^+$  in 0.1M  $\text{Bu}_4\text{NPF}_6/\text{CH}_2\text{Cl}_2$  at  $\omega$  /rad  $\text{s}^{-1}$ = 100, 200, 400, 800, 1600, 3200

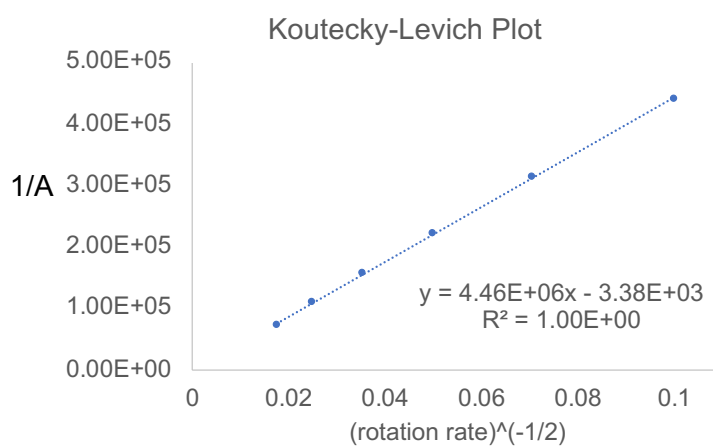


Figure S11: Koutecky-Levich Plot of cathodic process  $[1]^+$  in 0.1M  $\text{Bu}_4\text{NPF}_6/\text{CH}_2\text{Cl}_2$  at  $\omega$  /rad  $\text{s}^{-1}$ = 100, 200, 400, 800, 1600, 3200

Levich equation

$$I_L = (0.620)nFAD^{(2/3)}\nu^{(-1/6)}C\omega^{(1/2)}B = (0.620)nFAD^{(2/3)}\nu^{(-1/6)}C$$

Koutecký-Levich equation

$$\frac{1}{i_m} = \frac{1}{i_K} + \frac{1}{B_L\omega^{0.5}}$$

$$n = x$$

$$F = \text{Faraday constant} = 9.6485 \times 10^4 \text{ C mol}^{-1}$$

$$A = \text{Electrode Area} = 0.148 \text{ cm}^2$$

$$D = \text{Diffusion Coefficient} = 1.59 \times 10^{-5} \text{ cm}^2 \text{ s}^{-1}$$

$$\nu = \text{kinematic viscosity} = 1.318 \text{ g cm}^{-3}$$

$$C = \text{concentration} = 2.43 \times 10^{-7} \text{ mol cm}^{-3}$$

$$B/n = 1.299 \times 10^{-6}$$

$$n/B = 7.7 \times 10^5$$

$$(n/B)/4.46 \times 10^6 = 3.47 \text{ electrons}$$

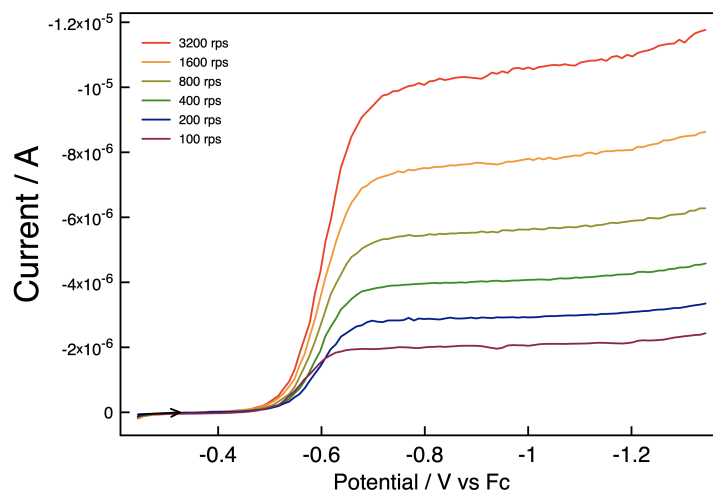


Figure S12: Linear Sweep Voltammogram at  $10 \text{ mV s}^{-1}$  concentration  $2.43 \times 10^{-7} \text{ mol cm}^{-3}$   $[1]^+$  in  $0.1 \text{ M Bu}_4\text{NPF}_6 + 0.1 \text{ M BuNCl} / \text{CH}_2\text{Cl}_2$  at  $\omega / \text{rad s}^{-1} = 100, 200, 400, 800, 1600, 3200$



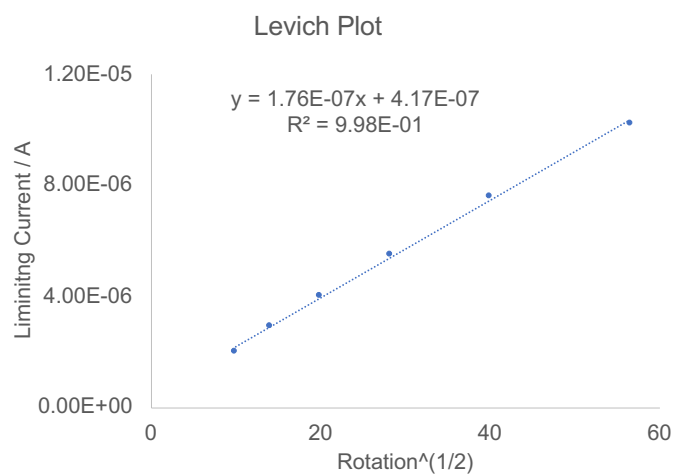


Figure S13: Levich Plot of cathodic process  $[1]^+$  in 0.1M  $Bu_4NPF_6/CH_2Cl_2$  at  $\omega$  /rad  $s^{-1}$  = 100, 200, 400, 800, 1600, 3200

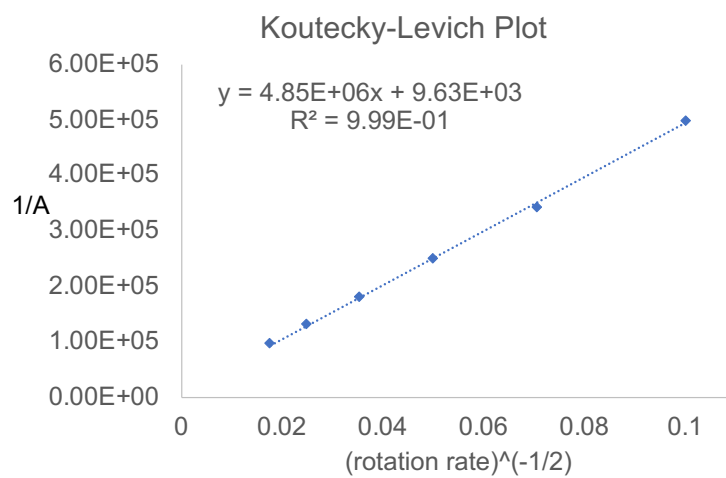


Figure S14: Koutecky-Levich Plot of cathodic process  $[1]^+$  in 0.1M  $Bu_4NPF_6/CH_2Cl_2$  at  $\omega$  /rad  $s^{-1}$  = 100, 200, 400, 800, 1600, 3200

$$n = x$$

$$F = \text{Faraday constant} = 9.6485 \times 10^4 \text{ C mol}^{-1}$$

$$A = \text{Electrode Area} = 0.148 \text{ cm}^2$$

$$D = \text{Diffusion Coefficient} = 3.36 \times 10^{-5} \text{ cm}^2 \text{ s}^{-1}$$

$$\nu = \text{kinematic viscosity} = 1.318 \text{ g cm}^{-3}$$

$$C = \text{concentration} = 2.48 \times 10^{-7} \text{ mol cm}^{-3}$$

$$B/n = 2.19 \times 10^{-6}$$

$$n/B = 4.56 \times 10^5$$

$$(n/B)/4.85 \times 10^6 = 2.21 \text{ electrons}$$

## 4 NMR Spectroscopy

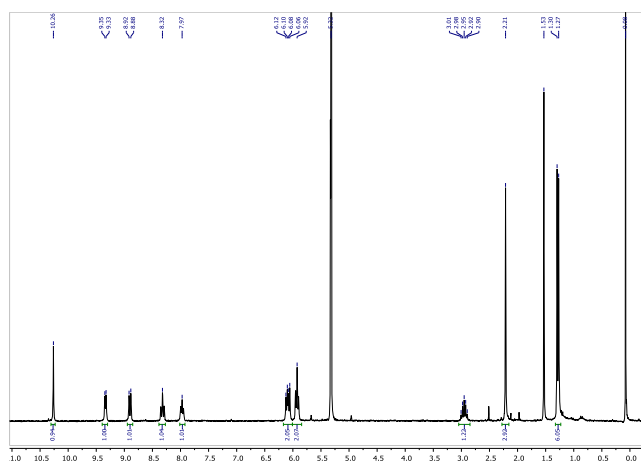
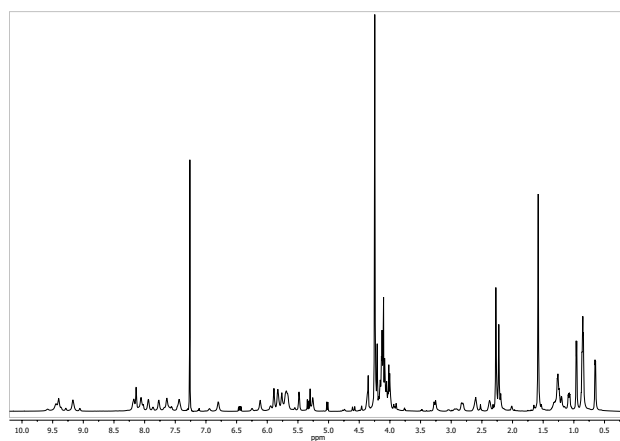
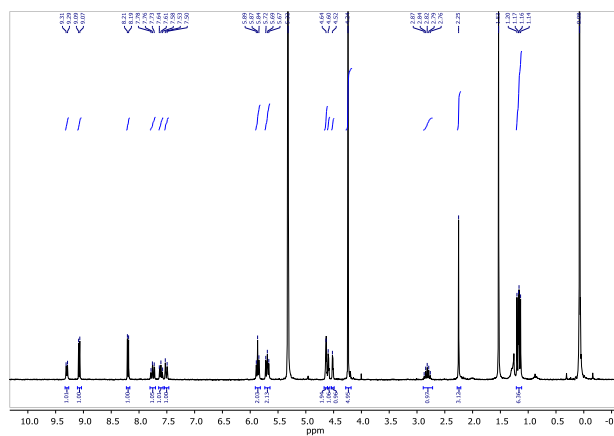
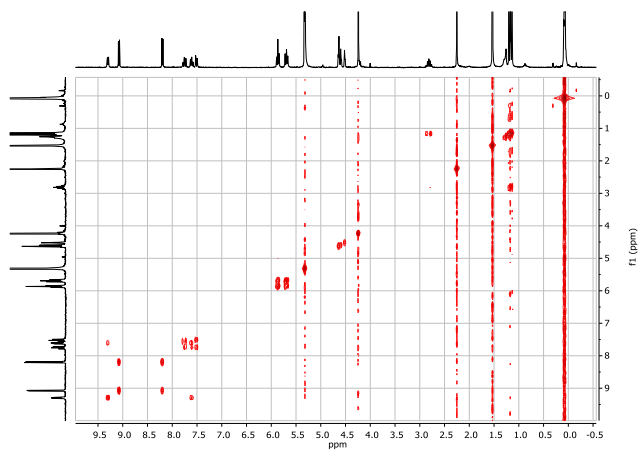
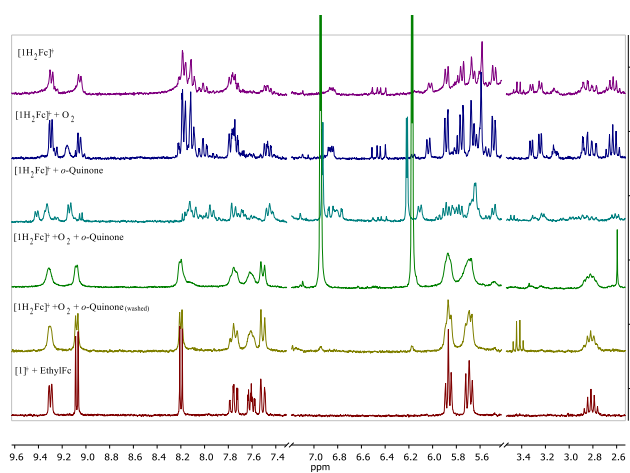


Figure S15:  $^1\text{H}$  NMR of  $1^+$  in  $\text{CD}_2\text{Cl}_2$ .



Figure S18:  $^1\text{H}$  NMR of  $[\text{1H}_2\text{Fc}]^+$  in  $\text{CD}_2\text{Cl}_2$ .Figure S19:  $^1\text{H}$  NMR of  $[\text{1Fc}]^+$  in  $\text{CD}_2\text{Cl}_2$ .

Figure S20: COSY NMR of  $[1\text{Fc}]^+$  in  $\text{CD}_2\text{Cl}_2$ .Figure S21:  $^1\text{H}$  NMR from oxidation of  $[1\text{H}_2\text{Fc}]^+$  to  $[1\text{Fc}]^+$  in  $\text{CD}_2\text{Cl}_2$ .

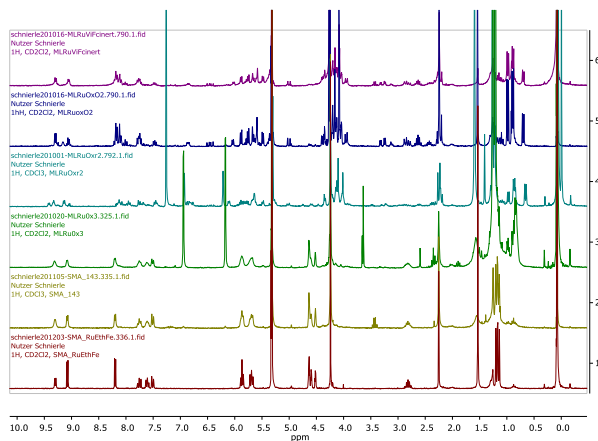


Figure S22:  $^1\text{H}$  NMR from oxidation of  $[\mathbf{1H}_2\text{Fc}]^+$  to  $[\mathbf{1Fc}]^+$  in  $\text{CD}_2\text{Cl}_2$ .

## 5 Kinetics

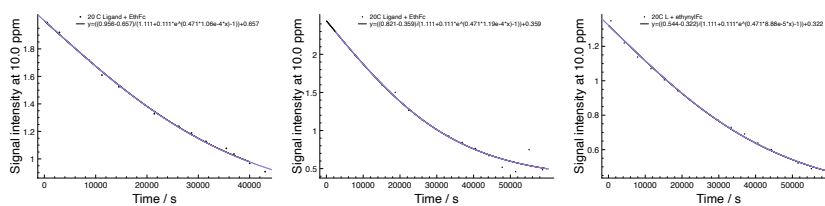


Figure S23: Kinetics of  $\text{TzPy} + \text{EthFc}$  at 20 C determined from  $^1\text{H}$  NMR of Reaction in  $\text{CD}_2\text{Cl}_2$ .

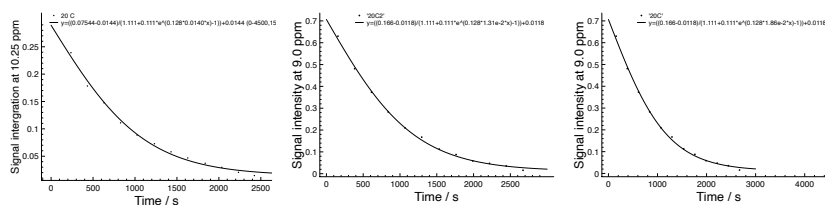


Figure S24: Kinetics of  $\mathbf{1}^+ + \text{EthFc}$  at 20 C determined from  $^1\text{H}$  NMR of Reaction in  $\text{CD}_2\text{Cl}_2$ .

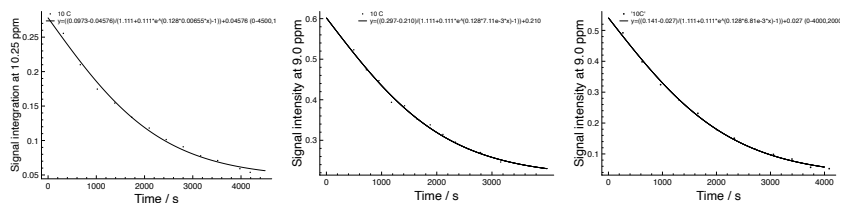


Figure S25: Kinetics of  $1^+$ +EthFc at 10 C determined from  $^1\text{H}$  NMR of Reaction in  $\text{CD}_2\text{Cl}_2$ .

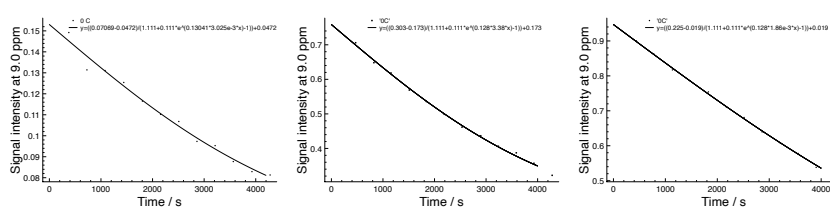


Figure S26: Kinetics of  $1^+$ +EthFc at 0 C determined from  $^1\text{H}$  NMR of Reaction in  $\text{CD}_2\text{Cl}_2$ .

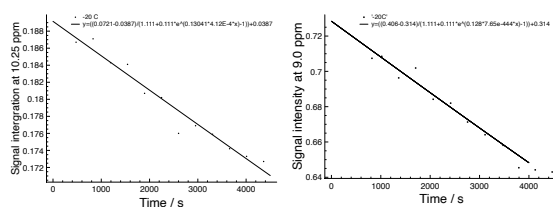
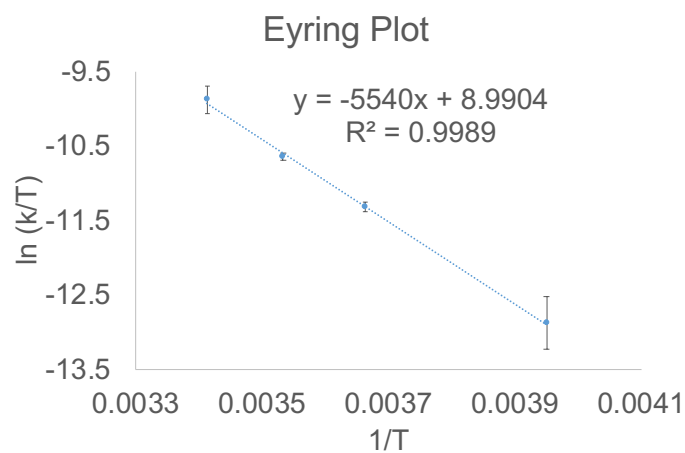


Figure S27: Kinetics of  $1^+$ +EthFc at -20 C determined from  $^1\text{H}$  NMR of Reaction in  $\text{CD}_2\text{Cl}_2$ .

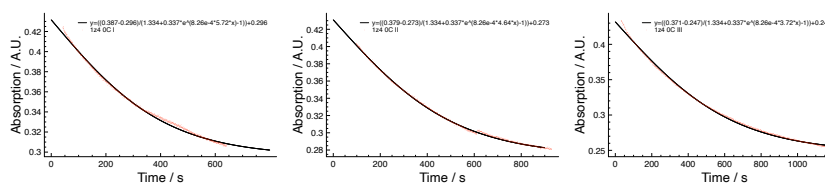
Figure S28: Eyring Plot of EthFc +  $[1]^+$ 

Equations used for Eyring analysis  $y = mx + b$

$$m = \frac{-\Delta H^\ddagger}{R}$$

$$b = \ln\left(\frac{k'}{h}\right) + \frac{\Delta S^\ddagger}{R}$$

$$\ln\left(\frac{k'}{h}\right) = 23.7638$$

Figure S29: Kinetics of  $1^+$ +ViFc at 0 C determined from UV vis NIR of Reaction in  $C_2H_4Cl_2$ .Figure S30: Kinetics of  $1^+$ +ViFc at 22 C determined from UV vis NIR of Reaction in  $C_2H_4Cl_2$ .



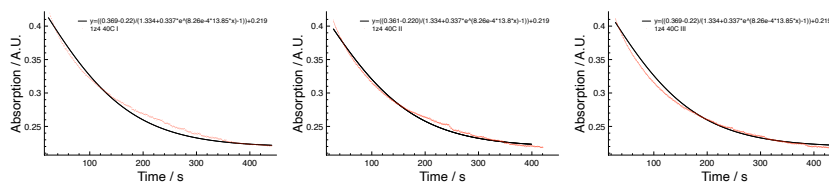


Figure S31: Kinetics of  $1^+ + \text{ViFc}$  at 40 C determined from UV vis NIR of Reaction in  $\text{C}_2\text{H}_4\text{Cl}_2$ .

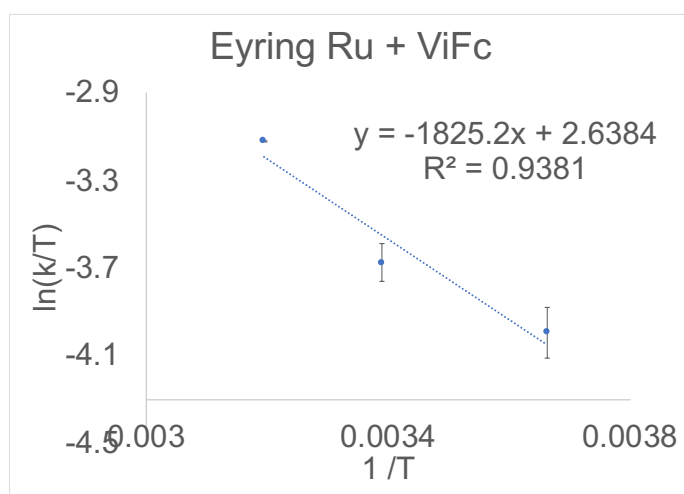


Figure S32: Eyring Plot of  $\text{ViFc} + 1^+$

## 6 Absorption Spectroscopy

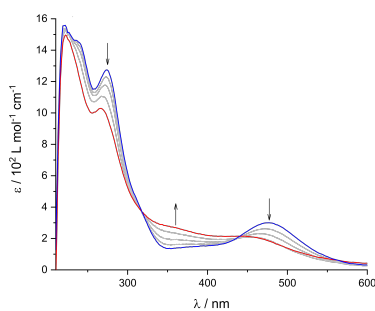


Figure S33: UV-vis NIR SEC of cathodic process  $[1]^{+}/n$  in 0.1 M  $\text{Bu}_4\text{NPF}_6 / \text{CH}_2\text{Cl}_2$ .

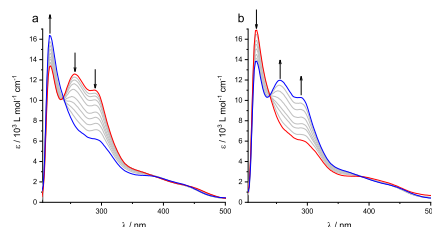


Figure S34: UV-vis NIR SEC of  $[1H_2Fc]^{+/2+}$  in 0.1 M  $Bu_4NPF_6 / CH_2Cl_2$ .

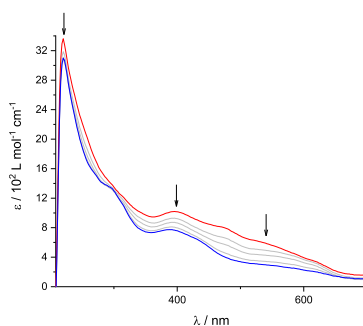
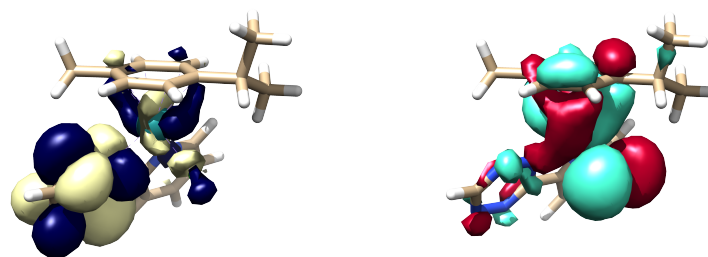


Figure S35: UV-vis NIR SEC of cathodic process  $[1H_2Fc]^{+/n}$  in 0.1 M  $Bu_4NPF_6 / CH_2Cl_2$ .

## 7 DFT Calculations



(a) LUMO (-6.6606 eV)  $1^+$

(b) HOMO (-9.2932 eV)  $1^+$

Figure S36: Molecular orbitals isosurface = 0.02, HOMO (green/red), LUMO (yellow/blue) of  $[1]^+$ . B3LYP/def2-TZVP/J level of theory

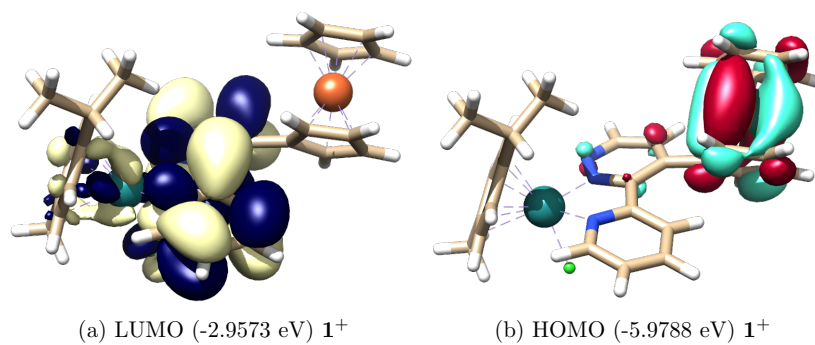


Figure S37: Molecular orbitals isosurface = 0.02, HOMO (green/red), LUMO (yellow/blue) of  $[1\text{Fc}]^+$ . B3LYP/def2-TZVP/J level of theory

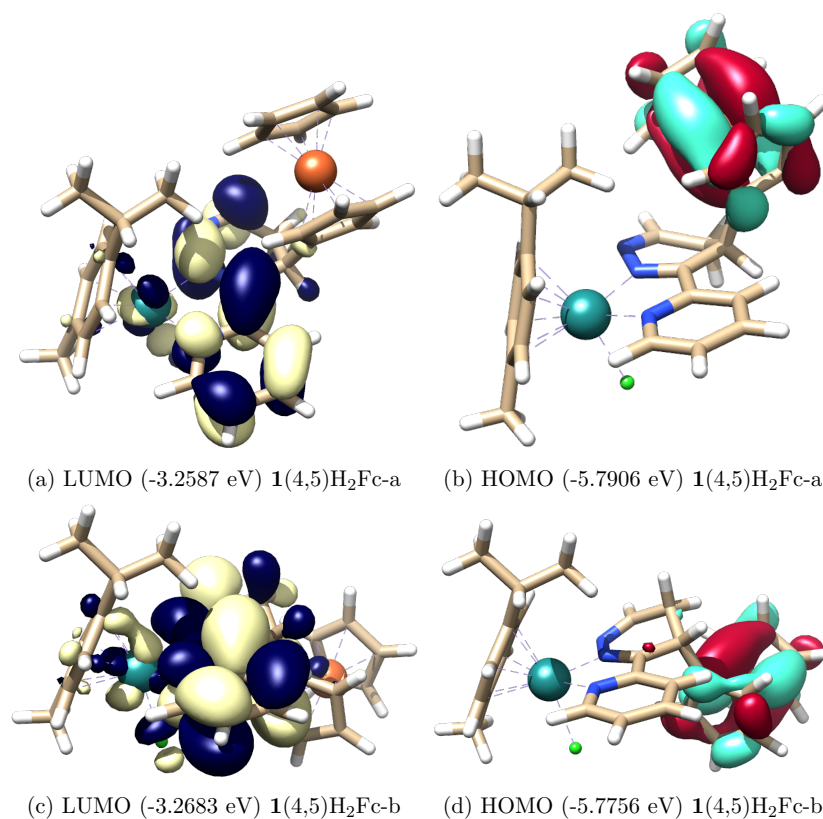


Figure S38: Molecular orbitals isosurface = 0.02, HOMO (green/red), LUMO (yellow/blue) of  $[1(4,5)\text{H}_2\text{Fc}]^+$ . B3LYP/def2-TZVP/J level of theory

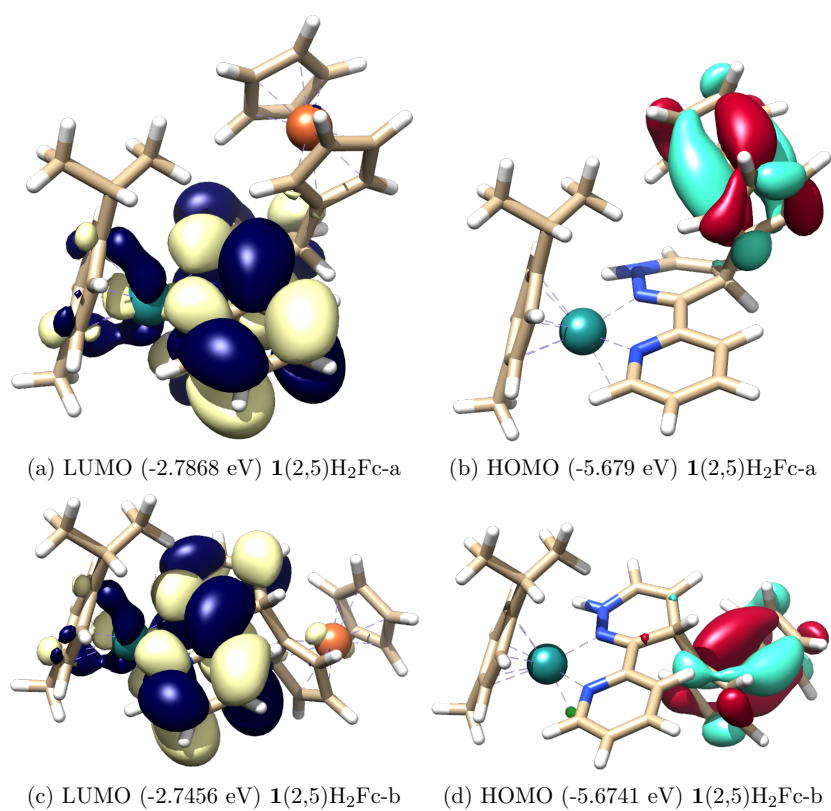


Figure S39: Molecular orbitals isosurface = 0.02, HOMO (green/red), LUMO (yellow/blue) of [1(2,5)H<sub>2</sub>Fc]<sup>+</sup>. B3LYP/def2-TZVP/J level of theory

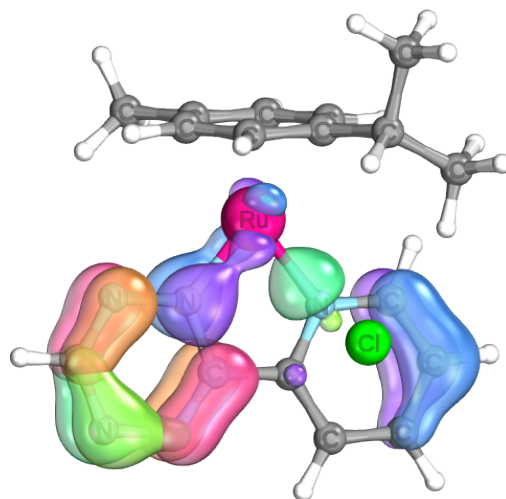


Figure S40: IBO <sup>[10]</sup> of  $[1\bullet\text{Cl}]^0$  determined from Kohn-Sham orbitals, using B3LYP/def2-TZVP/J level of theory. On tetrazine moiety: Blue/purple orbital showing Ru-N  $\pi$  bond, orange/red showing C-C  $\pi$  bond, green/teal show  $\pi$  orbital on N. On pyridyl moiety: green/teal shows  $\sigma$  bond between N-R, purple/blue shows typical aromatic orbital.

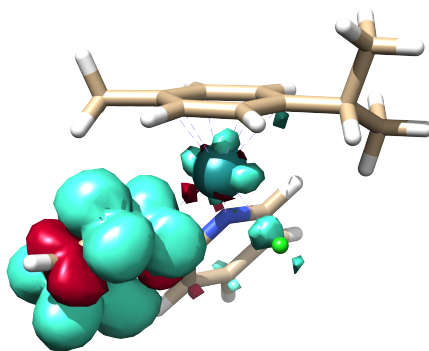


Figure S41: Unrestricted Kohn-Sham MOs of  $[1]^0$  determined from unrestricted Kohn-Sham orbitals, using B3LYP/def2-TZVP/J level of theory. Spin up shown in green, spin down shown in red.

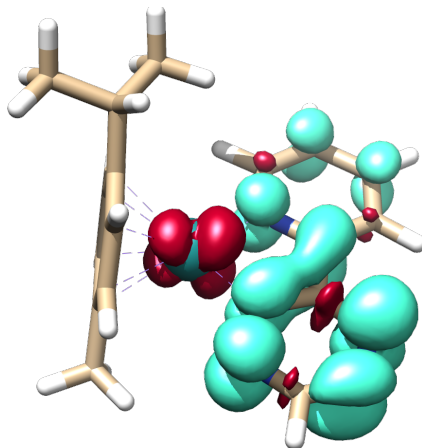


Figure S42: Unrestricted Kohn-Sham MOs of  $[1\bullet\text{Cl}]^{-1}$  determined from unrestricted Kohn-Sham orbitals, using B3LYP/def2-TZVP/J level of theory. Spin up shown in green, spin down shown in red.

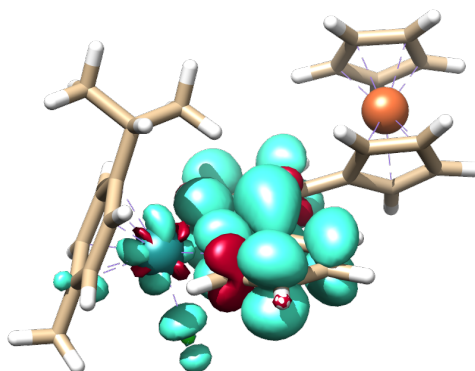


Figure S43: Unrestricted Kohn-Sham MOs of  $[1\text{Fc}]^0$  determined from unrestricted Kohn-Sham orbitals, using B3LYP/def2-TZVP/J level of theory. Spin up shown in green, spin down shown in red.

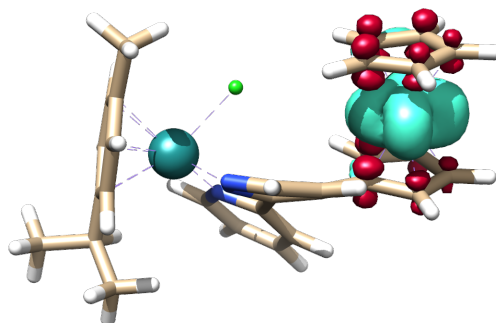


Figure S44: Unrestricted Kohn-Sham MOs of  $[1\text{Fc}]^{2+}$  determined from unrestricted Kohn-Sham orbitals, using B3LYP/def2-TZVP/J level of theory. Spin up shown in green, spin down shown in red.

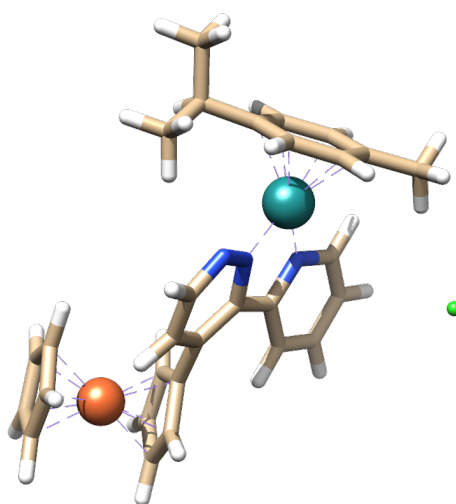


Figure S45: Molecular structure of  $[1\text{Fc}] \bullet \text{Cl}^{-1}$  determined using B3LYP/def2-TZVP/J level of theory.

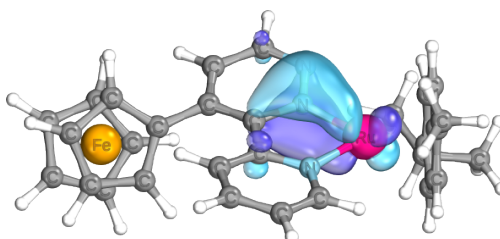


Figure S46: IBO<sup>[10]</sup> of  $[1\text{Fc} \bullet \text{Cl}]^0$  determined from Kohn-Sham orbitals, using B3LYP/def2-TZVP/J level of theory showing Ru-N  $\pi$  bond.

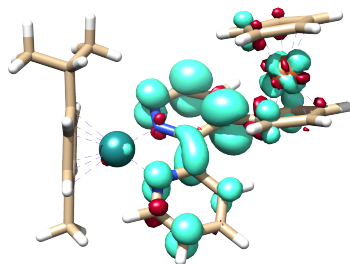


Figure S47: Unrestricted Kohn-Sham MOs of  $[1\text{Fe}\bullet\text{Cl}]^{-1}$  determined from unrestricted Kohn-Sham orbitals, using B3LYP/def2-TZVP/J level of theory. Spin up shown in green, spin down shown in red.

## 7.1 TD-DFT

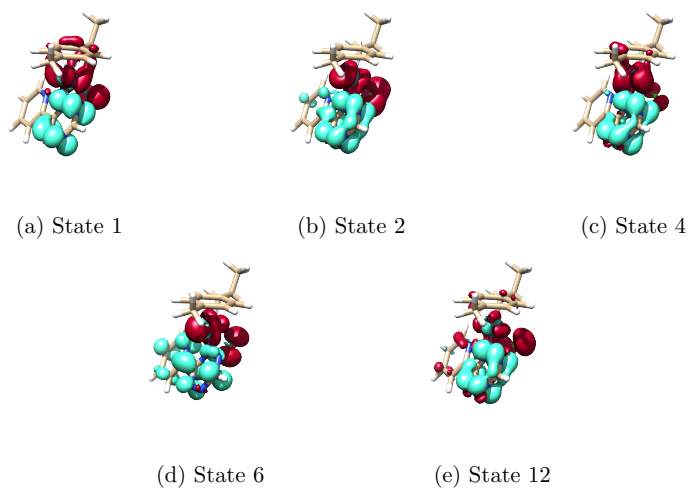


Figure S48: Electron density difference map shown at isosurface = 0.002, of the major transitions found in the UV-Vis NIR spectrum of  $\text{CyRuCl}(\text{TzPy})^+$ . Green denotes gain in electron density and red loss of electron density



Table S2: Transitions\* Determined by TD-DFT of closed-shell structure  $\text{CyRuCl}(\text{TzPy})^+$ 

STATE 1:	E= 0.056720 au	1.543 eV	12448.6 $\text{cm}^{-1}$
	92a $\longrightarrow$ 94a :	0.086368 (c= -0.29388455)	
	93a $\longrightarrow$ 94a :	0.885110 (c= 0.94080298)	
STATE 2:	E= 0.081507 au	2.218 eV	17888.7 $\text{cm}^{-1}$
	91a $\longrightarrow$ 94a :	0.063974 (c= -0.25293157)	
	92a $\longrightarrow$ 94a :	0.534984 (c= -0.73142624)	
	93a $\longrightarrow$ 95a :	0.319882 (c= 0.56558146)	
STATE 4:	E= 0.087231 au	2.374 eV	19145.1 $\text{cm}^{-1}$
	91a $\longrightarrow$ 94a :	0.550861 (c= -0.74219989)	
	92a $\longrightarrow$ 94a :	0.194877 (c= 0.44144852)	
	93a $\longrightarrow$ 95a :	0.111220 (c= 0.33349615)	
STATE 6:	E= 0.099670 au	2.712 eV	21875.1 $\text{cm}^{-1}$
	92a $\longrightarrow$ 95a :	0.866300 (c= -0.93075213)	
STATE 12:	E= 0.118122 au	3.214 eV	25924.9 $\text{cm}^{-1}$
	88a $\longrightarrow$ 94a :	0.095599 (c= 0.30919113)	
	89a $\longrightarrow$ 94a :	0.642384 (c= 0.80148866)	
	90a $\longrightarrow$ 95a :	0.142874 (c= 0.37798664)	

\*transitions below 5% were omitted

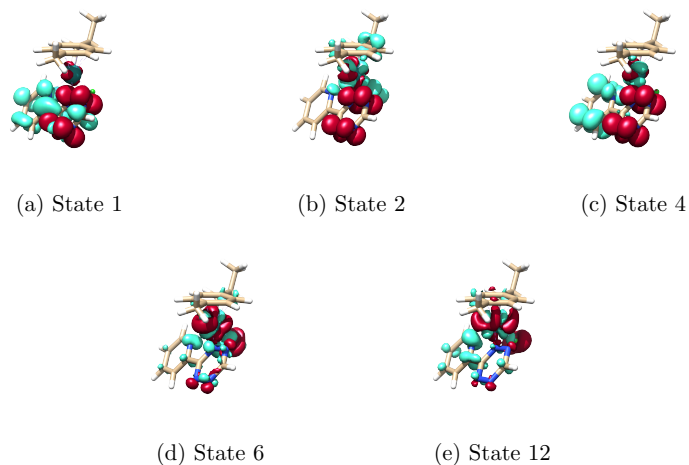


Figure S49: Electron density difference map shown at isosurface = 0.002, of the major transitions found in the UV-Vis NIR spectrum of  $\text{CyRuCl}(\text{TzPy})^0$ . Green denotes gain in electron density and red loss of electron density

Table S3: Transitions\* Determined by TD-DFT of closed-shell structure  $\text{CyRuCl}(\text{TzPy})^0$

STATE 1:	E= 0.039048 au	1.063 eV	8570.1 $\text{cm}^{-1}$
	94a $\rightarrow$ 95a :	0.949352 (c= 0.97434689)	
STATE 2:	E= 0.066186 au	1.801 eV	14526.1 $\text{cm}^{-1}$
	92a $\rightarrow$ 97a :	0.062945 (c= 0.25088751)	
	94a $\rightarrow$ 97a :	0.780090 (c= -0.88322681)	
STATE 4:	E= 0.072045 au	1.960 eV	15812.1 $\text{cm}^{-1}$
	94a $\rightarrow$ 96a :	0.435146 (c= 0.65965608)	
	94a $\rightarrow$ 98a :	0.475776 (c= -0.68976505)	
STATE 6:	E= 0.101405 au	2.759 eV	22255.9 $\text{cm}^{-1}$
	92a $\rightarrow$ 97a :	0.065347 (c= 0.25563084)	
	93a $\rightarrow$ 97a :	0.074394 (c= -0.27275229)	
	92b $\rightarrow$ 94b :	0.063858 (c= -0.25270208)	
	92b $\rightarrow$ 96b :	0.051219 (c= -0.22631692)	
	93b $\rightarrow$ 94b :	0.297654 (c= 0.54557714)	
STATE 12:	E= 0.113960 au	3.101 eV	25011.3 $\text{cm}^{-1}$
	92a $\rightarrow$ 97a :	0.159001 (c= -0.39874947)	
	93a $\rightarrow$ 95a :	0.095636 (c= 0.30924999)	
	93a $\rightarrow$ 97a :	0.193508 (c= 0.43989524)	
	93b $\rightarrow$ 94b :	0.050815 (c= 0.22542198)	
	93b $\rightarrow$ 95b :	0.061638 (c= 0.24826946)	
	93b $\rightarrow$ 96b :	0.068088 (c= -0.26093595)	
	93b $\rightarrow$ 97b :	0.083301 (c= -0.28861975)	

\*transitions below 5% were omitted

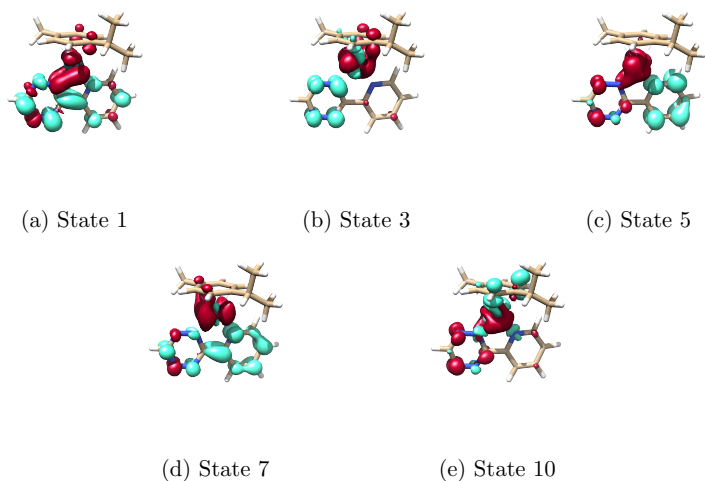


Figure S50: Electron density difference map shown at isosurface = 0.002, of the major transitions found in the UV-Vis NIR spectrum of  $\text{CyRu}(\text{TzPy})^0$ . Green denotes gain in electron density and red loss of electron density

Table S4: Transitions\* Determined by TD-DFT of closed-shell structure  $\text{CyRu}(\text{TzPy})^0$

STATE 1:	E= 0.070683 au	1.923 eV	15513.0 $\text{cm}^{-1}$
	85a $\rightarrow$ 86a :	0.749177 (c= 0.86554986)	
	85a $\rightarrow$ 87a :	0.172371 (c= 0.41517555)	
STATE 3:	E= 0.091102 au	2.479 eV	19994.5 $\text{cm}^{-1}$
	83a $\rightarrow$ 86a :	0.372202 (c= -0.61008324)	
	83a $\rightarrow$ 87a :	0.205898 (c= 0.45376008)	
	85a $\rightarrow$ 87a :	0.311289 (c= 0.55793311)	
STATE 5:	E= 0.100268 au	2.728 eV	22006.2 $\text{cm}^{-1}$
	83a $\rightarrow$ 87a :	0.179703 (c= -0.42391339)	
	84a $\rightarrow$ 86a :	0.081968 (c= 0.28630018)	
	85a $\rightarrow$ 86a :	0.051893 (c= -0.22780030)	
	85a $\rightarrow$ 88a :	0.528628 (c= -0.72706815)	
STATE 7:	E= 0.110249 au	3.000 eV	24196.9 $\text{cm}^{-1}$
	83a $\rightarrow$ 86a :	0.280584 (c= 0.52970195)	
	83a $\rightarrow$ 87a :	0.444060 (c= 0.66637860)	
	85a $\rightarrow$ 88a :	0.154470 (c= -0.39302698)	
STATE 10:	E= 0.129034 au	3.511 eV	28319.7 $\text{cm}^{-1}$
	82a $\rightarrow$ 87a :	0.112214 (c= -0.33498431)	
	83a $\rightarrow$ 86a :	0.075595 (c= 0.27494616)	
	85a $\rightarrow$ 87a :	0.079790 (c= 0.28247054)	
	85a $\rightarrow$ 89a :	0.367578 (c= -0.60628236)	
	85a $\rightarrow$ 91a :	0.165445 (c= -0.40674919)	

\*transitions below 5% were omitted

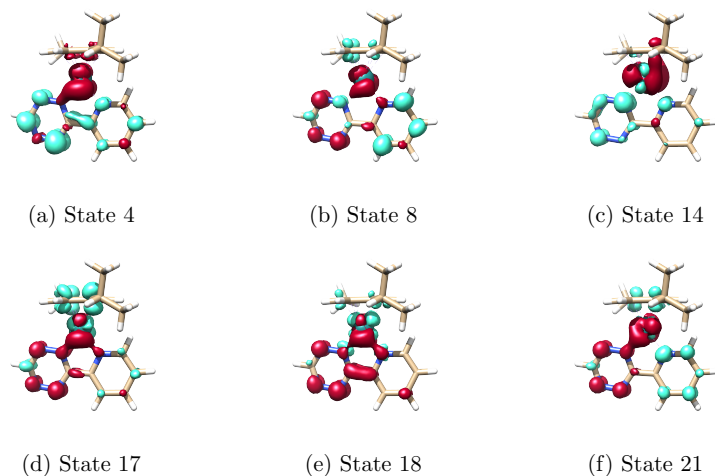


Figure S51: Electron density difference map shown at isosurface = 0.002, of the major transitions found in the UV-Vis NIR spectrum of  $\text{CyRu}(\text{TzPy})^{-1}$ . Green denotes gain in electron density and red loss of electron density

Table S5: Transitions\* Determined by TD-DFT of closed-shell structure  $\text{CyRu}(\text{TzPy})^{-1}$

STATE 4:	E= 0.070929 au    1.930 eV    15567.1 $\text{cm}^{-1}$
	85b $\rightarrow$ 86b : 0.802421 (c= -0.89577934)
STATE 8:	E= 0.094430 au    2.570 eV    20725.0 $\text{cm}^{-1}$
	85a $\rightarrow$ 87a : 0.176310 (c= 0.41989301)
	85a $\rightarrow$ 88a : 0.168810 (c= 0.41086541)
	86a $\rightarrow$ 90a : 0.197961 (c= 0.44492770)
	86a $\rightarrow$ 93a : 0.052711 (c= 0.22958891)
	85b $\rightarrow$ 87b : 0.164180 (c= 0.40519184)
STATE 14:	E= 0.107887 au    2.936 eV    23678.4 $\text{cm}^{-1}$
	85a $\rightarrow$ 87a : 0.062321 (c= -0.24964203)
	85a $\rightarrow$ 88a : 0.093557 (c= 0.30587035)
	83b $\rightarrow$ 87b : 0.582096 (c= -0.76295222)
	85b $\rightarrow$ 87b : 0.063511 (c= -0.25201486)
STATE 17:	E= 0.112869 au    3.071 eV    24771.8 $\text{cm}^{-1}$
	86a $\rightarrow$ 92a : 0.054383 (c= -0.23320199)
	86a $\rightarrow$ 93a : 0.186333 (c= 0.43166267)
	85b $\rightarrow$ 90b : 0.425468 (c= -0.65227936)
STATE 18:	E= 0.114823 au    3.124 eV    25200.8 $\text{cm}^{-1}$
	86a $\rightarrow$ 91a : 0.239327 (c= -0.48921050)
	86a $\rightarrow$ 92a : 0.163524 (c= -0.40438158)
	86a $\rightarrow$ 95a : 0.060346 (c= 0.24565390)
	85b $\rightarrow$ 91b : 0.062019 (c= 0.24903579)
	85b $\rightarrow$ 92b : 0.220549 (c= 0.46962651)
STATE 21:	E= 0.118912 au    3.236 eV    26098.1 $\text{cm}^{-1}$
	85a $\rightarrow$ 88a : 0.126814 (c= 0.35611008)
	85a $\rightarrow$ 90a : 0.068339 (c= -0.26141734)
	86a $\rightarrow$ 93a : 0.165555 (c= -0.40688402)
	83b $\rightarrow$ 86b : 0.091642 (c= -0.30272409)
	85b $\rightarrow$ 88b : 0.079469 (c= -0.28190212)
	85b $\rightarrow$ 90b : 0.074626 (c= -0.27317830)

\*transitions below 5% were omitted

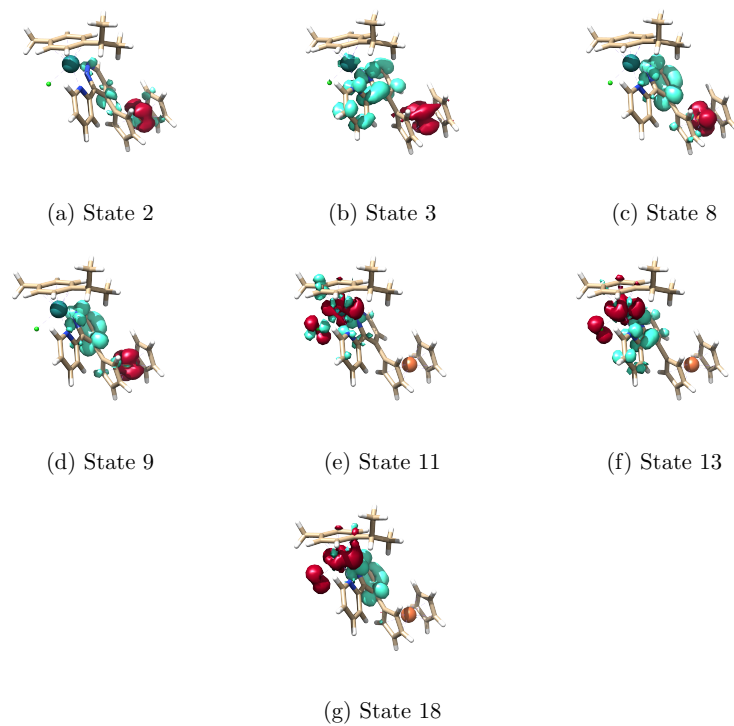


Figure S52: Electron density difference map shown at isosurface = 0.002, of the major transitions found in the UV-Vis NIR spectrum of  $\text{CyRuCl}(\text{DzFcPy})^+$ . Green denotes gain in electron density and red loss of electron density

Table S6: Transitions\* Determined by TD-DFT of closed-shell structure CyRuCl(DzFcPy)<sup>+</sup>

STATE 2:	E= 0.078701 au	2.142 eV	17272.9 cm <sup>-1</sup>
	139a → 148a :	0.197396 (c= -0.44429323)	
	140a → 142a :	0.267567 (c= -0.51726855)	
	140a → 147a :	0.067125 (c= -0.25908444)	
	140a → 149a :	0.290365 (c= -0.53885504)	
STATE 3:	E= 0.064636 au	1.759 eV	14186.0 cm <sup>-1</sup>
	139a → 141a :	0.058641 (c= -0.24215897)	
	140a → 141a :	0.926877 (c= 0.96274474)	
STATE 8:	E= 0.094614 au	2.575 eV	20765.4 cm <sup>-1</sup>
	136a → 142a :	0.058757 (c= 0.24239777)	
	136a → 149a :	0.092460 (c= 0.30407269)	
	139a → 142a :	0.350553 (c= -0.59207480)	
	139a → 148a :	0.076445 (c= 0.27648697)	
	139a → 149a :	0.050782 (c= 0.22534818)	
	140a → 142a :	0.223630 (c= -0.47289521)	
STATE 9:	E= 0.097470 au	2.652 eV	21392.3 cm <sup>-1</sup>
	136a → 148a :	0.135941 (c= 0.36870224)	
	139a → 142a :	0.187954 (c= 0.43353687)	
	139a → 149a :	0.094185 (c= -0.30689613)	
	140a → 142a :	0.361292 (c= -0.60107583)	
	140a → 149a :	0.058245 (c= 0.24133996)	
STATE 11:	E= 0.109444 au	2.978 eV	24020.3 cm <sup>-1</sup>
	137a → 141a :	0.390513 (c= -0.62491024)	
	137a → 143a :	0.262719 (c= -0.51256110)	
	137a → 144a :	0.149098 (c= -0.38613269)	
STATE 13:	E= 0.115107 au	3.132 eV	25263.1 cm <sup>-1</sup>
	134a → 141a :	0.074470 (c= 0.27289258)	
	137a → 141a :	0.462023 (c= -0.67972267)	
	137a → 143a :	0.087879 (c= 0.29644460)	
	137a → 144a :	0.057417 (c= 0.23961851)	
	138a → 144a :	0.053839 (c= 0.23203264)	
STATE 18:	E= 0.121865 au	3.316 eV	26746.2 cm <sup>-1</sup>
	135a → 141a :	0.087130 (c= -0.29517817)	
	137a → 142a :	0.457120 (c= -0.67610656)	
	137a → 144a :	0.072037 (c= -0.26839783)	
	138a → 144a :	0.096602 (c= 0.31080783)	

\*transitions below 5% were omitted

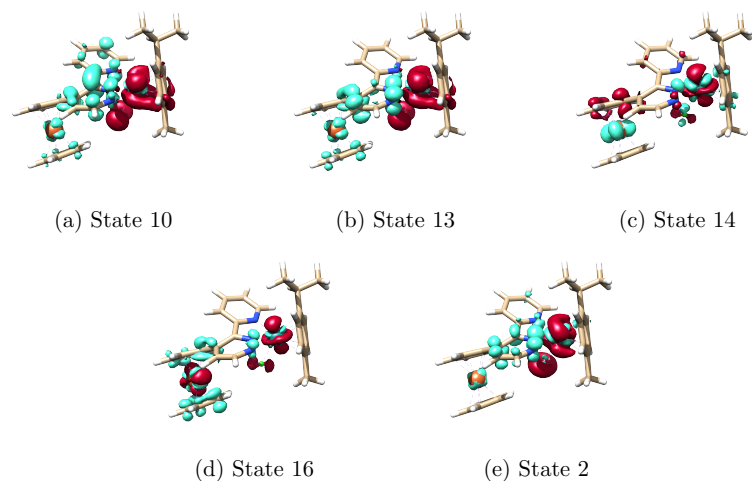


Figure S53: Electron density difference map shown at isosurface = 0.002, of the major transitions found in the UV-Vis NIR spectrum of  $\text{CyRuCl}(\text{DzFcPy})^{2+}$ . Green denotes gain in electron density and red loss of electron density

Table S7: Transitions\* Determined by TD-DFT of closed-shell structure  $\text{CyRuCl}(\text{DzFcPy})^{2+}$

STATE 10:	E= 0.084451 au	2.298 eV	18534.8 $\text{cm}^{-1}$
	140a $\longrightarrow$ 141a :	0.412217 (c= 0.64204122)	
	140a $\longrightarrow$ 142a :	0.158128 (c= 0.39765365)	
	140a $\longrightarrow$ 143a :	0.093170 (c= 0.30523787)	
	139b $\longrightarrow$ 141b :	0.156405 (c= 0.39548020)	
STATE 13:	E= 0.085573 au	2.329 eV	18781.1 $\text{cm}^{-1}$
	139a $\longrightarrow$ 142a :	0.050192 (c= 0.22403477)	
	140a $\longrightarrow$ 141a :	0.494121 (c= -0.70293755)	
	140a $\longrightarrow$ 142a :	0.084016 (c= 0.28985484)	
STATE 14:	E= 0.098015 au	2.667 eV	21511.7 $\text{cm}^{-1}$
	139a $\longrightarrow$ 145a :	0.140980 (c= -0.37547304)	
	139a $\longrightarrow$ 146a :	0.065151 (c= -0.25524614)	
	136b $\longrightarrow$ 140b :	0.309373 (c= -0.55621316)	
	138b $\longrightarrow$ 145b :	0.120835 (c= 0.34761341)	
	138b $\longrightarrow$ 146b :	0.061537 (c= -0.24806665)	
STATE 16:	E= 0.099001 au	2.694 eV	21728.2 $\text{cm}^{-1}$
	129a $\longrightarrow$ 141a :	0.208609 (c= -0.45673763)	
	130a $\longrightarrow$ 141a :	0.052798 (c= -0.22977909)	
	139a $\longrightarrow$ 141a :	0.240669 (c= 0.49058057)	
STATE 22:	E= 0.105030 au	2.858 eV	23051.4 $\text{cm}^{-1}$
	139a $\longrightarrow$ 142a :	0.084950 (c= -0.29146216)	
	140a $\longrightarrow$ 145a :	0.075513 (c= -0.27479664)	
	140a $\longrightarrow$ 146a :	0.063743 (c= -0.25247461)	
	138b $\longrightarrow$ 141b :	0.113889 (c= -0.33747378)	
	139b $\longrightarrow$ 142b :	0.204578 (c= 0.45230320)	
	139b $\longrightarrow$ 145b :	0.109751 (c= -0.33128696)	

\*transitions below 5% were omitted

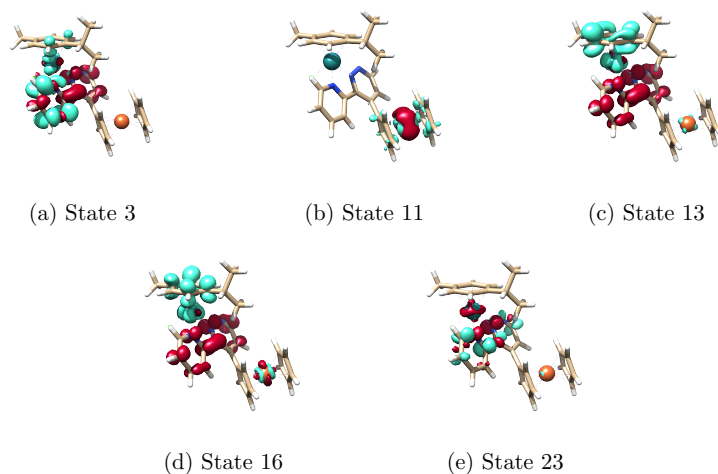


Figure S54: Electron density difference map shown at isosurface = 0.002, of the major transitions found in the UV-Vis NIR spectrum of  $\text{CyRuCl}(\text{DzFcPy})^0$ . Green denotes gain in electron density and red loss of electron density

Table S8: Transitions\* Determined by TD-DFT of closed-shell structure  $\text{CyRuCl}(\text{DzFcPy})^0$

STATE 3:	E= 0.052285 au	1.423 eV	11475.2 $\text{cm}^{-1}$
	141a $\rightarrow$ 144a :	0.941464 (c= -0.97029062)	
STATE 11:	E= 0.080402 au	2.188 eV	17646.3 $\text{cm}^{-1}$
	139a $\rightarrow$ 147a :	0.086314 (c= -0.29379221)	
	140a $\rightarrow$ 146a :	0.154885 (c= 0.39355483)	
	139b $\rightarrow$ 145b :	0.055636 (c= -0.23587185)	
	139b $\rightarrow$ 147b :	0.109803 (c= -0.33136463)	
	140b $\rightarrow$ 146b :	0.180821 (c= -0.42523009)	
STATE 13:	E= 0.077168 au	2.100 eV	16936.3 $\text{cm}^{-1}$
	141a $\rightarrow$ 145a :	0.055184 (c= -0.23491342)	
	141a $\rightarrow$ 146a :	0.075832 (c= 0.27537577)	
	141a $\rightarrow$ 147a :	0.266763 (c= -0.51649092)	
	141a $\rightarrow$ 148a :	0.319992 (c= -0.56567850)	
	141a $\rightarrow$ 149a :	0.175257 (c= 0.41863748)	
STATE 16:	E= 0.084341 au	2.295 eV	18510.6 $\text{cm}^{-1}$
	141a $\rightarrow$ 146a :	0.052380 (c= 0.22886581)	
	141a $\rightarrow$ 148a :	0.142156 (c= -0.37703622)	
	141a $\rightarrow$ 149a :	0.536671 (c= -0.73257806)	
STATE 23:	E= 0.104982 au	2.857 eV	23040.8 $\text{cm}^{-1}$
	141a $\rightarrow$ 150a :	0.721402 (c= -0.84935375)	
	138b $\rightarrow$ 141b :	0.065279 (c= 0.25549762)	

\*transitions below 5% were omitted



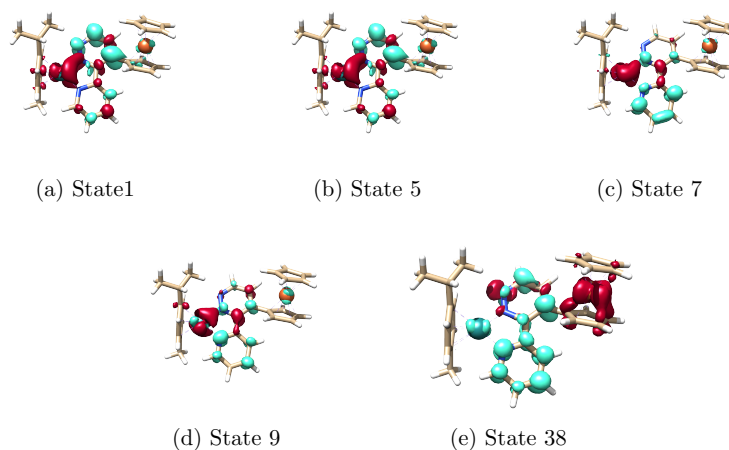


Figure S55: Electron density difference map shown at isosurface = 0.002, of the major transitions found in the UV-Vis NIR spectrum of  $\text{CyRu}(\text{DzFcPy})^0$ . Green denotes gain in electron density and red loss of electron density

Table S9: Transitions\* Determined by TD-DFT of closed-shell structure  $\text{CyRu}(\text{DzFcPy})^0$

STATE 1:	E= 0.067453 au	1.835 eV	14804.3 $\text{cm}^{-1}$
	132a $\longrightarrow$ 133a :	0.863049 (c= -0.92900416)	
	132a $\longrightarrow$ 135a :	0.067854 (c= -0.26048873)	
STATE 5:	E= 0.090808 au	2.471 eV	19930.1 $\text{cm}^{-1}$
	131a $\longrightarrow$ 133a :	0.339747 (c= 0.58287802)	
	131a $\longrightarrow$ 134a :	0.275971 (c= -0.52532971)	
	131a $\longrightarrow$ 135a :	0.059859 (c= -0.24466111)	
	132a $\longrightarrow$ 134a :	0.069222 (c= 0.26310063)	
STATE 7:	E= 0.093122 au	2.534 eV	20437.9 $\text{cm}^{-1}$
	130a $\longrightarrow$ 133a :	0.135094 (c= 0.36755142)	
	132a $\longrightarrow$ 134a :	0.464355 (c= 0.68143568)	
	132a $\longrightarrow$ 135a :	0.218363 (c= -0.46729355)	
STATE 9:	E= 0.108264 au	2.946 eV	23761.2 $\text{cm}^{-1}$
	130a $\longrightarrow$ 133a :	0.113010 (c= 0.33617004)	
	132a $\longrightarrow$ 134a :	0.076504 (c= 0.27659376)	
	132a $\longrightarrow$ 135a :	0.512113 (c= 0.71562084)	
STATE 38:	E= 0.150633 au	4.099 eV	33060.1 $\text{cm}^{-1}$
	122a $\longrightarrow$ 133a :	0.086951 (c= 0.29487419)	
	125a $\longrightarrow$ 133a :	0.328604 (c= 0.57323974)	
	128a $\longrightarrow$ 135a :	0.259129 (c= -0.50904690)	
	129a $\longrightarrow$ 135a :	0.078776 (c= -0.28067089)	

\*transitions below 5% were omitted

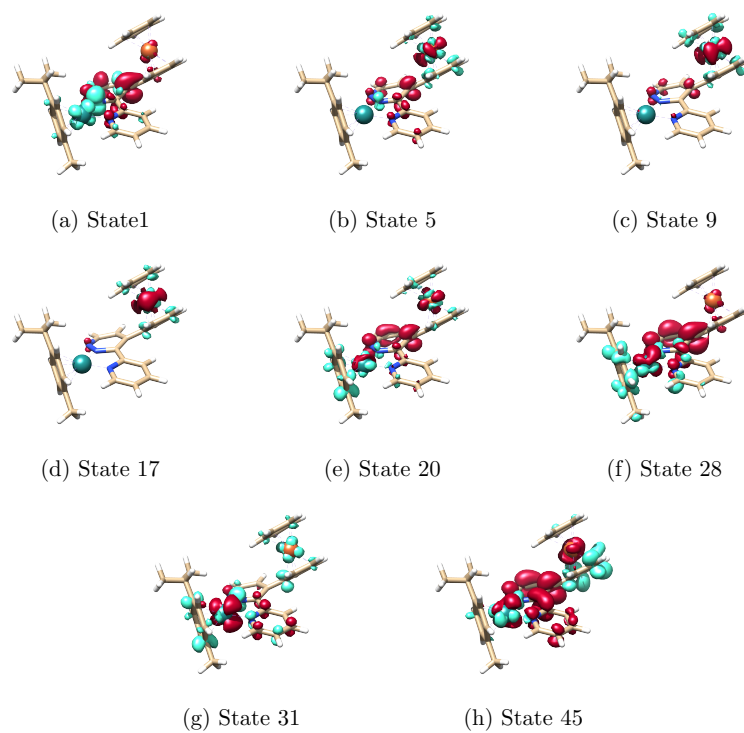


Figure S56: Electron density difference map shown at isosurface = 0.002, of the major transitions found in the UV-Vis NIR spectrum of  $\text{CyRu}(\text{DzFcPy})^{-1}$ . Green denotes gain in electron density and red loss of electron density

Table S10: Transitions\* Determined by TD-DFT of closed-shell structure  $\text{CyRu}(\text{DzFcPy})^{-1}$ 

STATE 1:	E= 0.030002 au	0.816 eV	6584.7 $\text{cm}^{-1}$
	133a $\longrightarrow$ 134a :	0.878944 (c= 0.93752006)	
STATE 3:	E= 0.047542 au	1.294 eV	10434.2 $\text{cm}^{-1}$
	132a $\longrightarrow$ 134a :	0.259137 (c= 0.50905470)	
	133a $\longrightarrow$ 135a :	0.174283 (c= 0.41747275)	
	133a $\longrightarrow$ 136a :	0.052487 (c= 0.22909993)	
	133a $\longrightarrow$ 137a :	0.054309 (c= -0.23304228)	
	132b $\longrightarrow$ 133b :	0.212387 (c= -0.46085517)	
STATE 5:	E= 0.053009 au	1.442 eV	11634.1 $\text{cm}^{-1}$
	129a $\longrightarrow$ 136a :	0.079241 (c= 0.28149846)	
	133a $\longrightarrow$ 136a :	0.502845 (c= -0.70911569)	
	132b $\longrightarrow$ 133b :	0.051161 (c= -0.22618706)	
STATE 9:	E= 0.067691 au	1.842 eV	14856.4 $\text{cm}^{-1}$
	133a $\longrightarrow$ 136a :	0.189840 (c= -0.43570658)	
	133a $\longrightarrow$ 137a :	0.078523 (c= -0.28021907)	
	131b $\longrightarrow$ 134b :	0.067984 (c= -0.26073723)	
	131b $\longrightarrow$ 138b :	0.110521 (c= -0.33244754)	
	131b $\longrightarrow$ 139b :	0.124336 (c= -0.35261360)	
STATE 17:	E= 0.083112 au	2.262 eV	18241.0 $\text{cm}^{-1}$
	128a $\longrightarrow$ 136a :	0.070082 (c= 0.26473049)	
	128a $\longrightarrow$ 137a :	0.052873 (c= 0.22994161)	
	129a $\longrightarrow$ 134a :	0.055973 (c= -0.23658603)	
	129a $\longrightarrow$ 136a :	0.239938 (c= 0.48983433)	
	133a $\longrightarrow$ 139a :	0.062303 (c= -0.24960616)	
	129b $\longrightarrow$ 136b :	0.063732 (c= -0.25245274)	
STATE 20:	E= 0.091026 au	2.477 eV	19977.8 $\text{cm}^{-1}$
	125a $\longrightarrow$ 136a :	0.106511 (c= 0.32636023)	
	133a $\longrightarrow$ 140a :	0.458396 (c= 0.67704959)	
STATE 28:	E= 0.099469 au	2.707 eV	21830.8 $\text{cm}^{-1}$
	130a $\longrightarrow$ 134a :	0.056511 (c= 0.23772039)	
	133a $\longrightarrow$ 141a :	0.167284 (c= 0.40900327)	
	133a $\longrightarrow$ 142a :	0.300740 (c= -0.54839738)	
	133a $\longrightarrow$ 144a :	0.132872 (c= 0.36451587)	
STATE 31:	E= 0.105407 au	2.868 eV	23134.2 $\text{cm}^{-1}$
	132a $\longrightarrow$ 134a :	0.109800 (c= -0.33136038)	
	132a $\longrightarrow$ 136a :	0.141376 (c= 0.37599961)	
	131b $\longrightarrow$ 133b :	0.052722 (c= -0.22961228)	
	132b $\longrightarrow$ 135b :	0.063532 (c= 0.25205471)	
	132b $\longrightarrow$ 138b :	0.138192 (c= -0.37174229)	
STATE 45:	E= 0.121938 au	3.318 eV	26762.3 $\text{cm}^{-1}$
	132a $\longrightarrow$ 143a :	0.051646 (c= 0.22725724)	
	132a $\longrightarrow$ 144a :	0.062419 (c= 0.24983849)	
	133a $\longrightarrow$ 147a :	0.420326 (c= 0.64832544)	
	133a $\longrightarrow$ 148a :	0.054621 (c= -0.23371136)	

\*transitions below 5% were omitted

## 8 XYZ Coordinates from DFT calculations

Table S11: XYZ file generated for B3LYP CyRuClTzPy<sup>+</sup>

```

43
Coordinates from ORCA-job B3LYP_CyRuClTzPy+
Ru 10.21601526809457 13.69063154191002 11.32070457313824
N 11.43805880995938 14.67217971059158 9.93578346501821
H 10.76103106449831 15.34863590361079 12.33266881922820
C 11.67767485528829 14.26490195600753 8.68602135937623
H 11.22642727596028 13.33221476288980 8.38682736161672
N 10.39378474218586 15.61520443678156 13.56635083069376
N 12.06003351475731 17.32242762968368 12.26806363149347
C 11.94401985931006 15.85887971927722 10.33807278505171
C 12.45527811485638 15.00538637575938 7.80891414727631
H 12.63030121468283 14.62865807692039 6.81082573043948
C 11.58243090548308 16.22187793300278 11.69925001230011
C 12.9899654725748 16.21653541557379 8.22629658180394
H 13.59210180626024 16.81447073908787 7.55626785504919
N 11.71040403867364 17.59288125066929 13.50313633544697
C 12.72596813556258 16.65527602408826 9.51464718904557
H 13.10093155950973 17.59537562119482 9.89242889178735
C 10.88461544383544 16.72814770559357 14.10191417175577
H 10.58675757638892 16.95353160223063 15.11698052579263
Cl 8.47746657767136 14.97242774132043 10.33150439973091
C 11.01785017752882 12.30006261093471 12.88995699882744
C 9.61532202023319 12.47904246930440 13.09944024488758
H 9.26958149729674 12.89792713537178 14.03381306077519
C 8.70171301095546 12.23633711534134 12.07379179353945
H 7.65928089023624 12.47708588112364 12.22565615665922
C 10.48989906513426 11.56162616779993 10.59330759775018
H 10.85602394993816 11.24297074419048 9.62858505892506
C 9.11894592359528 11.73647411786349 10.79207437088515
C 11.43714235131972 11.85937924586739 11.61895060359817
H 12.49309153002734 11.75536098777419 11.40888753160392
C 8.07733382189504 11.43826024656897 9.74285237933712
H 7.26493336186100 12.14957729508226 9.90820231921539
C 11.98853724207502 12.61819699738996 13.98155791264652
H 12.98401244777155 12.61896459322307 13.58692501014656
H 12.05814844198922 11.77149948945904 14.66876428096711
H 11.65468904628827 13.47920315755671 14.56055000592416
C 7.54041104586686 10.01481050357056 9.97713269384019
H 8.30983398968373 9.27185986516575 9.75625321751738
H 6.69151408171719 9.82784989130251 9.31961612588365
H 7.20742896386479 9.86617837996034 11.00593461093020
C 8.56285893009574 11.61135908919758 8.30651526609080
H 8.89051860601918 12.6351766152288 8.12381762196864
H 7.74559043543521 11.39316636837094 7.61940568015272
H 9.37265905797482 10.92086283986280 8.06120879188204

```

Table S12: XYZ file generated for B3LYP CyRuClTzPy<sup>0</sup>

43  
Coordinates from ORCA-job B3LYP\_CyRuClTzPy\_0

Ru	10.15986337947185	13.66569716249051	11.26577060261644
N	11.42490412196446	14.68387184707989	9.92787090557014
N	10.67016248647381	15.35823691526803	12.29868384214042
C	11.68390917481674	14.29574635770379	8.67280149019806
H	11.19921474347428	13.38932821130546	8.34358298786035
N	10.28259453061658	15.59382627936142	13.59567180808814
N	12.12663894240030	17.22947674491213	12.32659026778557
C	11.96074730457083	15.83485734710330	10.38282976520268
C	12.51231550315078	15.01921960544075	7.83593979960554
H	12.70006311909470	14.66236101781273	6.83277766429233
C	11.57653479655172	16.19346546202285	11.74927343289248
C	13.08545078206874	16.19729388385051	8.30751461865125
H	13.73205313098503	16.78688262451313	7.67123627689697
N	11.73968511743505	17.50893308955887	13.61830020006472
C	12.80653863510131	16.61274602402817	9.59511327537416
H	13.19704151923347	17.52280666147016	10.02114597193962
C	10.85114043890297	16.66170929953963	14.13822245977614
H	10.54893760623554	16.87293443491845	15.15938307057355
Cl	8.41609340719797	14.93360802004965	10.20166209479773
C	11.04082881281076	12.37112433256870	12.82812674519660
C	9.63752595095481	12.52675421015295	13.06743746876974
H	9.31316709006882	13.00424814587819	13.98093142362280
C	8.70172679205374	12.22576500517425	12.07397938739163
H	7.66026470076719	12.46009633931145	12.24182679352616
C	10.47214033251995	11.56112558148932	10.56005588927892
H	10.82335560354887	11.24286587720232	9.58951081579452
C	9.10153079782246	11.71698403365725	10.79036936411199
C	11.43504889174623	11.90121033066464	11.56001657141033
H	12.48846592562304	11.83401757853892	11.32128706834239
C	8.04146567185623	11.39155005047979	9.76649669060942
H	7.22575917530591	12.09667196158290	9.94248134375588
C	12.03159092098332	12.7590858870291	13.87961486346115
H	13.01289781234731	12.96255117372423	13.44656832680044
H	12.13250762969127	11.95675893330101	14.61520124640674
H	11.6968094668336	13.6554409762427	14.40030184512073
C	7.52314068098440	9.96487972781554	10.00965198893821
H	8.30018890106226	9.23040567905255	9.78351311263584
H	6.66678820915286	9.75929942529265	9.36555675316504
H	7.21006498979413	9.81796276545540	11.04532786551040
C	8.49385481022941	11.57048444953766	8.31991458404598
H	8.80399801191497	12.59991433709872	8.13873889557202
H	7.66709491008235	11.33923089436574	7.64683110331094
H	9.31241149224846	10.89459519793388	8.06174931890397

Table S13: XYZ file generated for B3LYP CyRuClTzPy<sup>-1</sup>

43  
Coordinates from ORCA-job B3LYP\_CyRuClTzPy\_neg

Ru	10.73519344478238	13.49117317866002	11.62125492488728
Cl	8.279208	15.601083	9.113781
N	11.52824162988066	14.54351625881073	10.01937859305694
N	10.90481132293013	15.24141058984949	12.38809661157795
C	11.84008004150079	14.04713581531388	8.80476081516409
H	11.73769808273140	12.97978164801076	8.68628216775198
N	10.64205563303250	15.59193450695514	13.69723537244688
N	11.49588274982261	17.52586815681565	11.95098775199060
C	11.66821944189412	15.87999051869411	10.22029154539972
C	12.26018036602354	14.84370062274112	7.76541815049396
H	12.48785865209535	14.39183964466645	6.80977216757087
C	11.35117788323014	16.29015196763799	11.56608520435506
C	12.37834686869138	16.22491805438827	7.96353537480150
H	12.69293623413182	16.87283258144522	7.15666413182534
N	11.22361387259146	17.86936923590088	13.22404982641669
C	12.09014064434963	16.74113151813711	9.20846965854886
H	12.17285907100511	17.79628977341352	9.42474498157841
C	10.82111165771924	16.84962356990123	14.00941546261202
H	10.61538363860269	17.11191608274317	15.04271461043767
C	11.11576996767998	11.91871160442844	13.13146463878747
C	9.78140436749786	12.38144298053726	13.25489646645767
H	9.46109951893858	12.82963637573426	14.18464147786798
C	8.90566214630322	12.38211052154782	12.14216181950679
H	7.91415728996542	12.80222869561821	12.24758044751791
C	10.63432573160079	11.39067690941304	10.7742878990493
H	11.00604551704940	11.05775677578233	9.81632449870534
C	9.30446618198753	11.85907972884392	10.88452962501112
C	11.53081083013306	11.41935411693355	11.86652819784294
H	12.55062936869738	11.08730172657565	11.73001556914537
C	8.29223200130503	11.76527636484263	9.76305116429784
H	7.56146511391448	12.55805012218817	9.93957324800195
C	12.04740769941762	11.95203537270874	14.30571222919359
H	13.08314220791836	11.83972090455681	13.98433499668807
H	11.81418574627578	11.13702529792100	14.99659784184392
H	11.94645316508105	12.89066018918082	14.85249803399405
C	7.57341979356886	10.40821847675397	9.85114515172852
H	8.26121043147134	9.59616910646240	9.59901038825453
H	6.73935507924571	10.37471369372586	9.14679432414293
C	7.18065529858319	10.22488376411023	10.85354300689206
C	8.86251639810886	11.98227456695936	8.36393122753952
H	9.22184972938331	13.00506742737372	8.25768623441615
H	8.07671436741256	11.81451159015371	7.62376546967444
H	9.67063301619858	11.28255382890318	8.13882787265323

Table S14: XYZ file generated for B3LYP CyRuTzPy<sup>0</sup>

42  
Coordinates from ORCA-job RuTzPy\_0

Ru	10.67576187263200	13.53847277137372	11.57361296153947
N	11.51370121046135	14.56298980829212	9.98098956070760
N	10.88563281236136	15.29084754213538	12.33116643548233
C	11.84387659963156	14.04703088258411	8.77483034740827
H	11.69941861540848	12.98454117612982	8.65799896537675
N	10.61397387332337	15.64931056329401	13.63449383353192
N	11.59282946883846	17.54705066729053	11.9177566132847
C	11.72592506756592	15.89433042030526	10.18699040199452
C	12.32961405820748	14.81954720926226	7.74703778154490
H	12.56765436573861	14.35336181003017	6.80101868702082
C	11.40193988831112	16.31702627616929	11.52454097899765
C	12.50414649399668	16.19631043262518	7.94367604964250
H	12.87084887867682	16.82497655982627	7.14396121865389
N	11.31077890479171	17.89711748385701	13.17936656621911
C	12.21118968749823	16.73066231118553	9.18015352715081
H	12.34521012249477	17.78063716317136	9.39667350469444
C	10.84583258551387	16.89491389531108	13.95719651278779
H	10.63245252283035	17.16424142947083	14.98641744251545
C	11.03809172021076	11.97910885130517	13.12088105301750
C	9.70444804401692	12.44630191386248	13.22061180022352
H	9.37119440513640	12.90274467617872	14.14163741213095
C	8.83948306945033	12.42350053122972	12.10147742151192
H	7.84037927395630	12.82800542582329	12.19510978143169
C	10.58737836744211	11.41895121178877	10.76582141862204
H	10.96891979132461	11.06482441380255	9.81919784230962
C	9.25437161549043	11.87889598759768	10.8572589998102
C	11.47019998625609	11.46795693706475	11.86820505420578
H	12.49226111850196	11.13681933435441	11.74876723491824
C	8.25325885584123	11.74217919976009	9.72946241348962
H	7.47466092658565	12.48853981971097	9.91010722801800
C	11.95344308216153	12.02806258598873	14.30645507115709
H	12.98768702281768	11.85727286967846	14.0084717774489
H	11.67314373972840	11.25633919065618	15.02819128092852
H	11.88309351051502	12.99334403697810	14.80997738278795
C	7.60077210925707	10.35153095858508	9.80210519715733
H	8.32988845683736	9.57621191558142	9.55265763253476
H	6.77624143374138	10.28144255483381	9.08986469191225
H	7.20902421349397	10.14495080279011	10.79990011023997
C	8.8243898622196	11.98775310356538	8.3339863632863
H	9.20214765099509	13.00547660880822	8.23137852520107
H	8.04310180213678	11.83355278363028	7.58744221510806
H	9.63447331192519	11.29375514277834	8.10150768271940

Table S15: XYZ file generated for B3LYP CyRuTzPy<sup>-1</sup>

42  
Coordinates from ORCA-job B3LYP\_CyRuTzPy\_neg

Ru	10.70467217439217	13.50049490962374	11.54923654351107
N	11.49084496128486	14.54821207256988	10.00627715213686
N	10.89536419150719	15.29315994445401	12.33909622266024
C	11.84254579355410	14.07310321868590	8.77969342162735
H	11.714281048665293	13.00947505880656	8.63968634107866
N	10.58278728944505	15.57950627059772	13.65728747301888
N	11.55798426983876	17.59559670615586	11.97752641685700
C	11.70011186976511	15.90684437319977	10.24612109182534
C	12.32099033207359	14.86289322064632	7.76960703964495
H	12.57105696869020	14.41244504134524	6.81827100701689
C	11.38350966350868	16.31564223392094	11.56359759550067
C	12.47928815331251	16.25571173835655	7.98946923741445
H	12.83839651206533	16.90244869873975	7.19993619214783
N	11.23616370892618	17.86480877306262	13.29220608543469
C	12.17963628940682	16.75603442004966	9.23073957534214
H	12.29999400578395	17.80473182172660	9.46623276346699
C	10.79099200534884	16.84977681881323	14.01195961250194
H	10.54956527460328	17.07894115517828	15.04774845552361
C	11.11892457187942	11.94749070693693	13.10566556620933
C	9.79484836607838	12.40674253786902	13.24185521559544
H	9.48480972201312	12.87448220498202	14.16885403910198
C	8.87866833871337	12.37796184635480	12.15634376537084
H	7.87513357727284	12.76100877851754	12.28914650615443
C	10.60028187956299	11.39323614292299	10.76105766601882
H	10.95257902948975	11.04177771758082	9.80182229976580
C	9.26732157662159	11.85366602241777	10.89344620634594
C	11.51679025114316	11.44048663257342	11.84001706229385
H	12.53319764922464	11.10048972746556	11.69269091565960
C	8.23836217699407	11.71447798242246	9.79048110447764
H	7.46208839732080	12.45879519463529	9.99202710904382
C	12.06235774032876	11.98717808290499	14.27173119261538
H	13.09249512588669	11.84464100369270	13.94308269515415
H	11.82290379075152	11.19686618116496	14.98954096979473
H	11.98917430448553	12.94262354161182	14.79362922850672
C	7.58720954171502	10.32366420861031	9.86483364978238
H	8.31351067343292	9.54987306561301	9.60147262515427
H	6.75100809851330	10.25267459600516	9.16548645626347
H	7.21216540201930	10.11243432782092	10.86830908252572
C	8.77741650662134	11.97111888014847	8.38362491427574
H	9.17365788027838	12.98258127053653	8.28943034333347
H	7.97662125546747	11.83972860734169	7.65277051521369
H	9.57159833394176	11.26830812927676	8.12406777141718



Table S16: XYZ file generated for B3LYP CyRuCl(DzFcPy)<sup>+</sup>

64  
Coordinates from ORCA-job RuClFc+

Ru	3.79939203374333	-3.77922628239478	4.24642213799252
Fe	8.64499264529961	1.38656778763472	2.40243440667048
Cl	5.46953194281093	-5.51817003990230	3.95053284895279
N	5.27198092967602	-3.01711398055078	5.49907353067546
N	4.97127173344271	-2.66421947061573	2.97871864352031
C	6.31314566585243	-2.39747064985319	4.88677059194930
N	4.61511364302217	-2.59986417761410	1.71362731468600
C	8.04292052850437	-0.47268611309030	3.08310638285612
C	6.07748112501452	-2.06473168195290	3.47465168898522
C	7.63768394185678	-2.63474391697371	6.87536065549622
H	8.57785509534816	-2.51503177311345	7.39573554362680
C	2.12876938634845	-3.90844320459517	5.72599038511611
H	2.21858544984465	-3.83761718820717	6.80168100160290
C	10.21491767683616	0.30366720927881	3.21071712059580
H	11.25479749273165	0.47858785212639	2.98721031529137
C	1.93126382388816	-2.84356263201145	3.56197352991597
H	1.88041762265290	-1.96231789204396	2.94027074328987
C	9.46223549160191	0.92609033663358	4.24668938357171
H	9.83320008983879	1.66882729676913	4.94422504243882
C	5.39454695164264	-3.40086261690544	6.77533497379805
H	4.53250472641570	-3.90425797451682	7.20413263843365
C	6.54447771152243	-3.21036524666792	7.50461673992599
H	6.59028308134599	-3.54427151011327	8.53115402225112
C	6.88286026391592	-1.25504262613689	2.63631310701824
C	9.34453727719593	-0.55130065274659	2.48428743738150
H	9.60764738774367	-1.17141383155335	1.64278102323142
C	1.95713240654945	-2.71173699749538	4.96656488803328
C	1.76228545826785	-1.3995056205108	5.68446959704685
H	2.37697124465093	-1.43943303796529	6.58789061302496
C	2.24842823203783	-5.15600229237643	5.11325161437068
H	2.44046611289286	-6.0355551378792	5.71290425824260
C	7.51962111462472	-2.22518933778436	5.55669010170859
H	8.36571939027127	-1.80070378970011	5.04694516878597
C	7.26492517806719	2.13653911858243	1.05343241708593
H	6.35775410706410	1.63409543841612	0.75951869710288
C	2.18378809705853	-5.27997094883115	3.68742400289079
C	8.53876990404394	2.00482247252976	0.42842246413445
H	8.77114875956050	1.38391015576048	-0.42187148136755
C	6.52919951027185	-1.24550530486357	1.29580516850327
H	7.1092899045519	-0.67365456671458	0.58780539854666
C	0.29041268005159	-1.29684609904396	6.11974332447731
H	-0.36264656061394	-1.24874716496798	5.24549240437838
H	0.13740770502456	-0.39404807514849	6.71303011073014
H	-0.00881715399426	-2.15537744278920	6.72295966547071
C	8.12236648035883	0.45995865258983	4.16559793963114
H	7.30468237729698	0.75820223698541	4.80074996121974
C	2.32831911385954	-6.62482084431768	3.05534597850451
H	2.58878360303753	-6.54498430447834	2.00131967641108
H	1.37692321899896	-7.15653371435570	3.14443274781136
H	3.09113249143872	-7.21061456191500	3.56454070945177
C	5.39799105566431	-1.92913921558832	0.88088752472230
H	5.07667662844666	-1.92151370428755	-0.15206780910637
C	2.01480066144474	-4.11559853277225	2.92802645091846
H	2.02773860150963	-4.16941116569284	1.84977506870310
C	9.46132208157930	2.8197381193571	1.14466939302727
H	10.51383840261208	2.92028988739580	0.93293673467336
C	2.17442931539493	-0.17439836043529	4.87325185645198
H	3.21152987170317	-0.24109936088287	4.53795676081267
H	2.06718529588233	0.71890117702810	5.4898982619726
H	1.53927198245736	-0.04345397576465	3.99512019417296
C	7.4016803247524	3.02561641317252	2.15643708311885
H	6.62224069684921	3.30611610997089	2.84610121227110
C	8.76079209305963	3.4470169779373	2.21319005351166
H	9.19280968181952	4.09793093338413	2.95591281615534

Table S17: XYZ file generated for B3LYP CyRuCl(DzFcPy)<sup>2+</sup>

```

64
Coordinates from ORCA-job RuClFc2+
Ru 3.94785778986791 -2.86843472124446 3.88845679034124
Fe 8.98944306313899 0.39193964335348 2.21151120548347
Cl 6.17319008058360 -3.18408138469143 2.92967424823021
N 5.00884329374762 -2.07429828224523 5.49149952990669
N 4.25252276411503 -0.91138455247822 3.30089751061929
C 5.55468292928504 -0.85728054618996 5.25725773090659
N 3.70988625252416 -0.42967655679774 2.20770221325439
C 7.46775241848036 0.89931188170376 3.55990220431478
C 5.30541499639138 -0.33115568543675 3.91453257783814
C 6.37143738000433 -0.74091863160802 7.50383675923700
H 6.87693677391856 -0.20757571909402 8.2968988574212
C 3.03463550368551 -4.64936063340052 4.87168402860637
H 3.41635618829021 -5.16996809540599 5.73949974246140
C 9.66258702259170 0.60045597443392 4.21224537249773
H 10.57199562962045 0.14911919752609 4.57403127526202
C 1.74485223895027 -2.83815592948992 3.89269410487972
H 1.13496035478278 -1.95294165839949 3.98101921785484
C 9.53472160372902 1.90578062649774 3.6742189517110
H 10.33492320360026 2.61674190476483 3.54754472971134
C 5.20039915958490 -2.65532073691107 6.68139404725687
H 4.79789624583477 -3.64741507956994 6.80741217107620
C 5.88514480613841 -2.02601691167642 7.70709718256370
H 6.01415217422806 -2.53476794062516 8.65096370190903
C 6.06474342719850 0.62586565731446 3.22305167234830
C 8.39538928868773 -0.03436442145424 4.13744136378920
H 8.17637797659266 -1.04441141555898 4.43800809012087
C 2.16117136949268 -3.52769185227038 5.04890148159841
C 1.70226332972732 -3.14561659258867 6.43290670253105
H 2.54266870734184 -3.31585674607586 7.11064841556387
C 3.4821038381387 -5.02171000201262 3.60252698178338
H 4.21993401517738 -5.80563875216048 3.50983256072352
C 6.20633450877203 -0.15223260232754 6.25977198969511
H 6.57286002600673 0.84495314358282 6.07004916283584
C 8.15108931128976 -0.61551242166840 0.57427697888905
H 7.09860554036913 -0.8332069485621 0.49134717427869
C 3.0338589925863 -4.33151843060377 2.42285954099257
C 9.11677599504394 -1.43034723341296 1.23251346378632
H 8.91964243183627 -2.36486546360501 1.73129782977577
C 5.46739914435584 1.17305222341703 2.09724310667754
H 5.96519929209619 1.9301579857599 1.50900720017073
C 0.5785884406885 -4.10732623523646 6.84928929566435
H -0.28802511225196 -3.9893919867000 6.19567884017082
H 0.26914367765344 -3.89690632129860 7.87389268972419
H 0.91219285863678 -5.14513492300540 6.79675329438621
C 8.19707575648206 2.09136022802840 3.26047916109827
H 7.79909489614842 2.97271832719490 2.78406781542087
C 3.53803309500801 -4.70771240844935 1.06569028065672
H 3.14321089887480 -4.03287539453309 0.30853614056719
H 3.22627112806410 -5.72613853265831 0.82343362523802
H 4.6275456410919 -4.66752805016117 1.03878764134815
C 4.25314887246382 0.65563199587310 1.66691634753994
H 3.73715164428701 1.05553353035792 0.80548552910060
C 2.15880551040228 -3.25578479849140 2.59743801410743
H 1.86639225835586 -2.66728438367451 1.74047839865097
C 10.37671145068106 -0.77061212465551 1.13631258218490
H 11.30510593484009 -1.11508572369269 1.56213637154907
C 1.26920975000993 -1.68663110315383 6.55918748860566
H 2.06134206001301 -1.00497922581588 6.24409562673285
H 1.02013405995488 -1.46680543989634 7.59791122001908
H 0.38066702394539 -1.47908131509972 5.96033937059596
C 8.81461200166301 0.53879235349019 0.07687210869338
H 8.34951597814111 1.36777277662534 -0.43156410448373
C 10.18485560263000 0.44009822548981 0.41961043599839
H 10.93968264571193 1.18420029702278 0.22271198574408

```

Table S18: XYZ file generated for B3LYP CyRuCl(DzFcPy)<sup>0</sup>

```
64
Coordinates from ORCA-job RuClFc
Ru 3.78751446487586 -3.93531444558825 4.20520844879185
Fe 8.38098877593804 1.47252162223358 2.62567729803935
Cl 5.21178240490377 -5.82217377655140 3.46550860911880
N 5.42319316707012 -3.43679705475323 5.36010299153185
N 4.92185409011862 -2.80877917270495 2.92486527086201
C 6.41625522202481 -2.69891268885158 4.73757242792469
N 4.48985829527262 -2.59475645925449 1.69291247981892
C 7.95151497461937 -0.51572057855071 3.06220208819035
C 6.09600164295749 -2.24801551595386 3.42931964325746
C 7.82608330830619 -3.01457270115192 6.68110923859858
H 8.77631550636285 -2.88292322928251 7.1820944906333
C 2.3398975433963 -3.57242175016344 5.81153658767975
H 2.59536867922652 -3.27138805911191 6.81906342291342
C 10.06540524675710 0.41932023761785 3.19061278017624
H 11.07136791095332 0.70806847148982 2.93155571286641
C 1.94840818426734 -3.00688922288666 3.49559114071683
H 1.91579659543087 -2.28386142173395 2.69298549668693
C 9.3386963322012 0.84110269932776 4.34083636329698
H 9.69821051969367 1.50612857976705 5.10924510222127
C 5.61249925682416 -3.90499129879733 6.60344172619712
H 4.79768047191670 -4.47909691583884 7.0203569990975
C 6.77357386391379 -3.70702237162008 7.31413450529981
H 6.87444823111663 -4.11285273671223 8.31017464531834
C 6.80506541602721 -1.31505882660101 2.60926241203467
C 9.21192739204202 -0.41012698232618 2.41212116642240
H 9.46256111612511 -0.88903731761416 1.47950183214864
C 2.16471839551661 -2.56391631685921 4.82849913942430
C 2.14262979845313 -1.10059380058694 5.20438625888089
H 2.40863363984030 -1.04137929421748 6.26319093017950
C 2.25193479605636 -4.94750163753036 5.50609966093810
H 2.42326473043253 -5.68701808958170 6.27475585957789
C 7.65048776812353 -2.52921690591343 5.41218985383630
H 8.46294949795013 -2.03352689187766 4.91091012971529
C 6.87088992825945 2.26072827344842 1.45083053551445
H 5.99632960504525 1.71218267031356 1.14176893518550
C 2.01675101778436 -5.36127065309827 4.17270625858927
C 8.11305132975956 2.32054460380327 0.75552483953308
H 8.34753437818955 1.82825376236988 -0.17471054217132
C 6.36630327401336 -1.16003412580623 1.31850478154109
H 6.86196779107572 -0.46927974543575 0.65398840041908
C 0.70844473789563 -0.57558721388903 5.04114540956782
H 0.41255077052703 -0.59270065413677 3.98916460204783
H 0.63371645095374 0.45218957814721 5.40168562160897
H -0.00120708141527 -1.18802942250934 5.60015011761937
C 8.03550809478572 0.27645177906911 4.26817286567828
H 7.24204954203852 0.41322360713454 4.98361849834233
C 1.97134254056133 -6.81777841026530 3.84082815734198
H 2.17289156104821 -6.99207943515807 2.78561224093951
H 0.97521914152012 -7.20322886642566 4.07764732218518
H 2.6935366796002 -7.37215806216787 4.43100538769366
C 5.20282734377733 -1.83544131824992 0.89366208528971
H 4.81482502992777 -1.71217415291191 -0.10936369394370
C 1.84907697658082 -4.37636809496965 3.16832382858750
H 1.72278454230565 -4.67491025250783 2.13823686099816
C 9.00799609207894 3.11732528898756 1.52658003913829
H 10.03456865674815 3.33491605002308 1.27838456585967
C 3.14553897511008 -0.24787936924621 4.42792813303502
H 4.16632498354733 -0.57799225170052 4.62027214768991
H 3.05555206029954 0.79549467923219 4.73671023977388
H 2.97130797358888 -0.29789042506419 3.35092264745682
C 6.99958722594883 3.01511867191075 2.65063681130599
H 6.23891450725757 3.14068114918464 3.40394472199566
C 8.3213650596554 3.54272536526807 2.69912701264427
H 8.73951614618270 4.13430882720523 3.49734772688909
```

Table S19: XYZ file generated for B3LYP CyRuCl(DzFcPy)<sup>-1</sup>

```

64
Coordinates from ORCA-job RuClFc-1
Ru 3.72734735604577 -3.23926324344023 4.49111697608522
Fe 8.68348085112444 1.48510072669830 2.64006364347843
Cl 6.58870298910605 -7.54254063704985 4.47269336201541
N 5.6297911187368 -3.42861795584292 5.13705096557272
N 4.71937171307256 -2.23563230353532 3.13594854687809
C 6.60986276636823 -2.75299372911156 4.42815169680272
N 4.10665640630500 -1.78059987619723 2.00960370636075
C 8.09295194877986 -0.5042778582225 2.84445798930105
C 6.08995271844925 -1.98234479049850 3.34678956474437
C 8.33222839702868 -3.80404241453815 5.76163529544239
H 9.37633389109432 -3.98191303458528 5.98404540975829
C 2.10900682605922 -2.89357222606682 6.00108026309369
H 2.12153086925892 -2.2322598512240 6.85781416886587
C 10.28716920084127 0.17776641757179 2.58590063426306
H 11.24328034728460 0.40345040520865 2.14138090444659
C 1.67376640898339 -3.30345340998553 3.65012325903153
H 1.39972201956936 -2.94854648635402 2.66854050325009
C 9.90247599791291 0.43574612949402 3.93277447529584
H 10.51366277630822 0.90211961328205 4.68830497098748
C 6.01802353508590 -4.22526884792750 6.14797496334089
H 5.21986921995327 -4.76966902712289 6.65622971173785
C 7.32334906551771 -4.45899927059616 6.49160848795633
H 7.56179497310018 -5.15114716438637 7.28637917261065
C 6.75290521066105 -1.03699331594766 2.53637893196657
C 9.17256768430739 -0.39377053921336 1.91364040703216
H 9.13796683340774 -0.70223790957226 0.88103840399137
C 1.65023343610168 -2.40933049876692 4.74726799092019
C 1.09181332704893 -1.00640577407749 4.64374305002253
H 1.59498212842208 -0.41104862287070 5.41167137389042
C 2.55274581167948 -4.22896669098713 6.13873667821228
H 2.93881435098411 -4.55679735236748 7.09493713352935
C 7.96893611931201 -2.96259958767075 4.73926218329180
H 8.72543816246895 -2.47844503881327 4.14429229715597
C 7.0276673578498 2.71239132015458 2.41959021732641
H 6.01501008893370 2.38104131475716 2.58381740904571
C 2.56946669413563 -5.13006583071697 5.04786542454146
C 7.74657351974779 2.64149902082403 1.19207728020901
H 7.36499809991439 2.27176148953904 0.25419225871269
C 6.08601411659109 -0.56350951530660 1.42061617084627
H 6.53952300787912 0.16968124918693 0.7734707831395
C -0.40885761682729 -1.0270002251296 4.96892883465392
H -0.94865236944855 -1.62630198681573 4.23174515097782
H -0.81631914293266 -0.01371164803867 4.94403785107760
H -0.59839879107343 -1.45364517527789 5.95591047681306
C 8.54985889377117 0.02694483124456 4.08936274716453
H 7.95824735284278 0.10844688779204 4.98575244436393
C 3.04106849052768 -6.54623452460919 5.2287723848439
H 2.81392932419967 -7.13997406431893 4.34330774844200
H 2.54529417457093 -7.00744834224447 6.08569038291115
H 4.12131007207782 -6.60331434378355 5.38312546409627
C 4.77863048825737 -1.01053754131930 1.19142159813040
H 4.22976468142315 -0.68802023593083 0.31268782805347
C 2.13912076539992 -4.63587924603340 3.78975376017531
H 2.15872269798233 -5.28644740694377 2.92565397448111
C 9.06590589007717 3.12304637617787 1.42524559517898
H 9.85871590558852 3.17492435826114 0.69650991389536
C 1.33048750020474 -0.33209447130350 3.29308908645754
H 2.38250754520591 -0.35182202463520 3.01535100121492
H 0.98986254111215 0.70495579187896 3.33290123230577
H 0.76951815373757 -0.82901028986731 2.49873107592609
C 7.9005182907054 3.24179446032751 3.4100712677308
H 7.65840252971919 3.39250718669781 4.44983259087312
C 9.16111390881162 3.49525346262071 2.79641876994437
H 10.04304745919559 3.86923042229228 3.29080828828551

```

Table S20: XYZ file generated for B3LYP CyRu(DzFcPy)<sup>0</sup>

```

63
Coordinates from ORCA-job RuFc
Ru 3.69816247324618 -3.20291952147162 4.51765603374614
Fe 8.74742963095021 1.46133024566139 2.60337602109609
M 5.59752194534707 -3.36687248532094 5.16107253723112
N 4.67558993718209 -2.16235169294475 3.17287199198424
C 6.57700970900702 -2.70345049254001 4.43511509134555
N 4.04970962169377 -1.68977258786988 2.06238923711957
C 8.07548301457162 -0.49657894490018 2.82652671670786
C 6.04873527473629 -1.92667900559000 3.36446953483999
C 8.30947198054474 -3.77900322476940 5.74137524704410
H 9.35422148817359 -3.97145434557720 5.94649839884196
C 2.04426744383137 -2.93474117191243 6.01471183176158
H 2.02135467031219 -2.28765440150555 6.88115050446584
C 10.29302274485183 0.08532146763734 2.53375627309359
H 11.25203744499453 0.26596810558239 2.07542267741129
C 1.64979995124103 -3.32359125486682 3.65357010551253
H 1.37195467581385 -2.96308175387911 2.67491563810984
C 9.93931365139004 0.36775346978163 3.88405735931787
H 10.58129750708715 0.81078067484606 4.62789713617548
C 5.99314137044871 -4.17457100380707 6.18667440375149
H 5.19458150475098 -4.64792805281938 6.73591625779993
C 7.30087406984317 -4.40155710832305 6.50647979802083
H 7.54232150847549 -5.06448189871949 7.32560997023403
C 6.71576809277996 -0.98875298808165 2.54318672105828
C 9.14545863453595 -0.43983679552551 1.87986062641116
H 9.08174109156737 -0.75172892561756 0.84972185262641
C 1.58027238148400 -2.4482778284405 4.76391942631414
C 0.97544893154255 -1.06288434783765 4.68489294473905
H 1.46012800636421 -0.46859601453323 5.46527529620242
C 2.54478894675391 -4.24921691270240 6.13746267432787
H 2.93801889410732 -4.57364738067173 7.0916612477321
C 7.93874086921550 -2.93846682458317 4.72200860084924
H 8.69167528907197 -2.47127385492557 4.10977437992740
C 7.14208807910236 2.74889659964713 2.35638975451210
H 6.11400217020841 2.45647846309532 2.49679631764937
C 2.63073642205896 -5.12328509586800 5.02730823802782
C 7.88417511500134 2.65870338712280 1.14386624246551
H 7.50941554059851 2.30897465874663 0.1955135344544
C 6.03638586994426 -0.49755681886893 1.44584027693269
H 6.48991756804168 0.23077459037348 0.79275972748956
C -0.52335561827520 -1.13562131810449 5.01266797425625
H -1.05016418262488 -1.72209000835261 4.25595142664683
H -0.95679734329251 -0.13316747134287 5.02610251452587
H -0.69858821009202 -1.60080516577049 5.98458996338602
C 8.57257037707820 0.01988783271195 4.06235363269804
H 7.99810482353673 0.13147771262486 4.96672697904281
C 3.18950885685148 -6.50688567395811 5.19033412044269
H 3.60268748193296 -6.87736952159377 4.25142184753079
H 2.40998716405350 -7.19979143655479 5.52054896586880
H 3.98029162708800 -6.52469622637151 5.94137908336057
C 4.71642591004232 -0.92265703363458 1.23817028149470
H 4.15591309456003 -0.58433147577711 0.37312348688821
C 2.17814303698548 -4.63466432540491 3.77286786243837
H 2.24642499071439 -5.26384171712799 2.89540337910113
C 9.21419455967907 3.09279159183026 1.40899546217031
H 10.02441481869121 3.12040535704148 0.69941062445312
C 1.19416903140465 -0.35185890082657 3.34991684747015
H 2.24584321929941 -0.33741211681287 3.06950678242076
H 0.82838944321929 0.67499470711408 3.41655743701212
H 0.64262905363143 -0.84262807586733 2.54490574302929
C 8.01143511206269 3.24020924833444 3.36894056353822
H 7.75220659159579 3.39303962521081 4.40425356592166
C 9.29282398700511 3.45319800467577 2.78416964021153
H 10.17674896454996 3.79224995438966 3.29961000870055

```

Table S21: XYZ file generated for B3LYP CyRu(DzFcPy)<sup>-1</sup>

```

63
Coordinates from ORCA-job RuFc_neg
Ru 3.79645264698112 -3.11203489348716 4.54866288337279
Fe 8.56285343301304 1.39377595172194 2.69721728195017
H 5.69316103586472 -3.39127981805308 5.16474583510194
H 4.80704112915764 -2.22480685460010 3.10061355277741
C 6.68695615336672 -2.85253142331478 4.33202400191579
N 4.17607935943036 -1.80347274704590 1.99136543731546
C 8.23117303145648 -0.71821701372325 2.58242012278593
C 6.19331088818327 -2.11270268813708 3.24173808273028
C 8.40235687341536 -3.97137001271943 5.64383451274713
H 9.43975414339426 -4.23155968760591 5.81548420426630
C 2.15827384500118 -2.64631749599508 6.03574107541960
H 2.15501925272607 -1.94872169374328 6.86336686239953
C 10.28670402014477 0.35170531673664 2.28733077151667
H 11.15186576290418 0.77550191935177 1.81983247863075
C 1.74430628541103 -3.17027758382824 3.69916384450946
H 1.49728548612761 -2.85125656441703 2.69817280869523
C 10.00631920455834 0.32375260212448 3.68477828559029
H 10.6290343988581 0.72840531741999 4.46714393301139
C 6.08208287074904 -4.14438363891001 6.22244796342711
H 5.27837204507162 -4.51483354949123 6.84294583007946
C 7.38819641137785 -4.45304893602394 6.50873513199159
H 7.61999897744504 -5.06227816057164 7.37158819779121
C 6.94969328104543 -1.32044886734025 2.29551279045561
C 9.18387899966276 -0.25589556075967 1.61211783309867
H 9.10009621515250 -0.37930287697622 0.54432543844032
C 1.72935479293645 -2.21895726952859 4.75016377633227
C 1.18718943898999 -0.81655817948743 4.56719093924864
H 1.72091969144892 -0.17926023667943 5.27990102611644
C 2.59283626449360 -3.97703629439138 6.23853307637049
H 2.97407324892332 -4.26304309699639 7.21055859089719
C 8.04532971265090 -3.18402791286341 4.57998970724854
H 8.79607030350549 -2.81874120914798 3.89714432355417
C 6.71342534432725 2.30017835711781 2.39147797272522
H 5.81346214718384 1.73646398831421 2.20745543739142
C 2.62533825131498 -4.92595050188978 5.18389592717002
C 7.63983682109198 2.73315128137355 1.40285202532380
H 7.53922762345618 2.58326665350963 0.33989305821967
C 6.26904398539556 -0.99461894273849 1.10575954108242
H 6.76264121799646 -0.42866400181069 0.32767565312416
C -0.30378481327414 -0.78459292811219 4.93467731735679
H -0.87447663727217 -1.42966048347105 4.26224414253508
H -0.69857832774437 0.23004884396017 4.83974992765542
H -0.47423694366264 -1.13030066589706 5.95652167211817
C 8.73995813191375 -0.30418307739647 3.86072277003777
H 8.23508602485940 -0.44929182919935 4.79987154254820
C 3.10803420603445 -6.32611103744605 5.43276603071006
H 3.48532761307845 -6.77749558765956 4.51402757272285
H 2.30338113172562 -6.95841738768092 5.82103123570227
H 3.91552724738159 -6.33927813196721 6.16662216310680
C 4.92308683296925 -1.26150702361400 1.00780114614000
H 4.35844033547500 -0.97790045002151 0.12662195647379
C 2.18623164731153 -4.50267299817006 3.90247740888021
H 2.20024150268483 -5.19497995327486 3.07070414723099
C 8.7244016072458 3.37740564864109 2.06288790919559
H 9.59461633513505 3.80672724453527 1.58752204763308
C 1.39861008702677 -0.24028017293242 3.18744096299378
H 2.43594156806766 -0.32832994125282 2.84749594375647
H 1.09735478712392 0.8099826356465 3.14866503764427
H 0.78421400175444 -0.76416608557576 2.43176451724690
C 7.23514542693693 2.66142876693251 3.66411661640740
H 6.78215374099465 2.44168951335098 4.61735389511238
C 8.47632294551427 3.33218353406548 3.46245090149276
H 9.12009657088767 3.72025300072830 4.23534955845538

```

Table S22: XYZ file generated for B3LYP [1(2,5)H<sub>2</sub>Fc-a]<sup>+</sup>

```

66
Coordinates from ORCA-job Ru25H2Fc+
Ru 3.97333456881846 -3.72489490141980 4.04551848810568
Fe 7.62584497866844 1.35426123516377 2.83959030940543
Cl 5.01486853276828 -5.64065297458082 2.99137972430813
N 5.62044792782288 -3.77941332001597 5.31418492532702
N 5.43612435976310 -2.66680281655186 3.01025574221524
C 6.75349546041688 -3.21043322337360 4.82973062185169
N 5.20848027418704 -2.20006768683472 1.76386448161493
C 8.13006337521813 -0.56696152778133 3.45093975688687
C 6.62538955358894 -2.5825326921557 3.52957349741917
C 7.97875080698457 -3.92935842230545 6.76177569928376
H 8.89795856614385 -3.99268748745286 7.32434996874224
C 2.58220804744042 -3.11330136124106 5.63651163368875
H 2.86908767856325 -2.85247324540915 6.64630865008476
C 9.32356521833278 1.32567734932834 4.0223769038768
H 10.06997519145246 2.10376010769475 4.02368390755439
C 2.26376036535496 -2.50830889795045 3.32362606083828
H 2.29677599637183 -1.77818666895499 2.52711917444153
C 8.15496226187025 1.28274636849890 4.83463423564943
H 7.85518362404323 2.01902472946130 5.56299309423548
C 5.65260222152510 -4.41168815734341 6.49185891031376
H 4.72973579361034 -4.85944883392117 6.82717104583303
C 6.80933801875226 -4.50575085485802 7.24623175294591
H 6.78587973675627 -5.02474299739474 8.19316014464018
C 7.79428819954232 -1.91794629485699 2.84301368673906
C 9.30725663194920 0.18719076572372 3.16961827343250
H 10.0445702906503 -0.0573660925502 2.42113724773616
C 2.54429462497262 -2.09773871584403 4.65801976709173
C 2.74238435312566 -0.65421519407588 5.05096933902348
H 3.30412930957354 -0.65707088058138 5.98836937402162
C 2.29417427025225 -4.46807812546924 5.32885685882766
H 2.34701287629296 -5.21974891914252 6.10302490117877
C 7.94606176675035 -3.26959722011247 5.54515061126907
H 8.83528344256891 -2.80398145688084 5.14883879125947
C 5.9747575819263 1.36653149110704 1.60259881224803
H 5.26229241698727 0.56118773873278 1.54829918515189
C 2.00336705634602 -4.85371142323663 4.00900913452741
C 7.16454042795989 1.48890336469558 0.82614087234783
H 7.51016886193001 0.79301650646832 0.08070645345591
C 7.52365421418431 -1.89620808627075 1.36115470491403
C 1.36301890105952 -0.03337046453936 5.32664347829284
H 0.76700443009511 -0.00631614450239 4.41117618695975
H 1.47687860379606 0.98832249623334 5.6295112979436
H 0.81349811787918 -0.60716541640784 6.07436204666195
C 7.41924097762522 0.11754034464547 4.48101527553629
H 6.47970849863073 -0.18609712888473 4.91134858107637
C 1.74504471072823 -6.28739977695772 3.68277155581954
H 1.98794034593060 -6.50927125575484 2.64575550307901
H 0.68450611978837 -6.49702068221902 3.8505357277722
H 2.32539446297607 -6.94323569975652 4.32882648732843
C 6.28309521280437 -2.00492718871672 0.89955356686676
H 6.00613703590509 -1.94486854131117 -0.14252610479573
C 2.00569861030088 -3.849894211839474 2.99638364457466
H 1.83499119795710 -4.12907868548429 1.96622678722156
C 7.84186687469295 2.66790582494588 1.24450096182367
H 8.78962469606315 3.02019461130487 0.87014164742142
C 3.52482034033576 0.16622779565075 4.02952206922861
H 4.48794587382399 -0.28524961119589 3.80239135638770
H 3.70826271600065 1.16412769536088 4.42787324043731
H 2.97509926240277 0.28015290537068 3.093386869482532
C 5.91923222900034 2.47416135413224 2.49581765128970
H 5.15171752337998 2.65583002052508 3.23552172012575
C 7.07472738364805 3.2756994462601 2.27690167110779
H 7.34427643065017 4.16584270681423 2.82278804575147
H 8.66802212909070 -2.55295264080680 3.01992365709086
H 8.35254200852422 -1.77325093913122 0.68085703103356
H 4.33800975813296 -2.52611781137864 1.37697202124815

```

Table S23: XYZ file generated for B3LYP [1(2,5)H<sub>2</sub>Fc-b]<sup>+</sup>

66			
Ru	4.04188290730275	-3.58493812729488	4.17821128726881
Fe	8.9398370308904	0.91275429561152	2.09942823345872
Cl	6.06650492775786	-4.39693534761921	3.14493611474810
N	5.26498865910750	-2.76214343575086	5.64125178183604
N	4.62921136139123	-1.75182000005163	3.36911654973211
C	5.73267037127516	-1.51395870106904	5.38748289036363
N	4.27567959312340	-1.39829518447453	2.12562743221457
C	7.55105993964677	-0.02068092106360	3.31601331611150
C	5.41398668767178	-0.98655311062667	4.07485775806794
C	6.78601168323707	-1.44590358127173	7.54080532727006
H	7.36632407723026	-0.92371698959724	8.28893708373915
C	2.5330153486781	-4.12840149274700	5.67405230219422
H	2.60358640755589	-3.89848483037336	6.72892675072235
C	9.48438678177928	-1.03050374620275	2.56429376287548
H	10.17046495961375	-1.62240620897273	1.98051889561252
C	1.96321732481753	-3.47832793718775	3.42317429721785
H	1.59120746324549	-2.75078754712597	2.71846313090129
C	9.83650038495742	-0.14800853980820	3.62457303253346
H	10.83317115746893	0.05010670058011	3.98500082120699
C	5.58378119528379	-3.36738162484536	6.79080261166137
H	5.21549779498694	-4.37256709371459	6.92669774067933
C	6.34667099241267	-2.74538321776562	7.76339038332794
H	6.58123238411423	-3.27419558094158	8.67578497178925
C	6.08116866820517	0.26873289668571	3.53631198666954
C	8.07893342906307	-0.95161585750263	2.37178006520127
H	7.50691417415052	-1.49090751710625	1.6349869585195
C	1.92809431348517	-3.18537319011916	4.81413572835058
C	1.26012291732439	-1.95818821860224	5.38531630552235
H	1.7638096586720	-1.73789971068908	6.33025103005909
C	3.10787274518458	-5.33242592274195	5.19423121803031
H	3.59061768435486	-6.01162145842205	5.88189443596701
C	6.48863042232932	-0.83125163913205	6.33630030937388
H	6.83970516892447	0.16579699515827	6.12721294795574
C	8.24023283223529	2.73533906158781	1.41300206315924
H	7.36682541366932	3.24050355349029	1.7922370912854
C	3.10415261823491	-5.62170153282205	3.61513730937554
C	8.27091418736109	1.78968410417577	0.34742746024191
H	7.42131104070922	1.44111514630435	-0.21692988091562
C	5.34427344276299	0.70638236266559	2.29812948936536
C	-0.20353928976612	-2.30861414471643	5.69871685671954
H	-0.73661952721078	-2.58393669975592	4.78519156853120
H	-0.70722761181804	-1.45107954929242	6.14809452062440
H	-0.26856284236132	-3.14637086357116	6.39457513311991
C	8.64544397697709	0.47436557073410	4.08868957096797
H	8.58060623072705	1.21492988820240	4.87015408597207
C	3.72915668465041	-6.88014079032439	3.31235521571870
H	4.05964532495186	-6.7792652831552	2.28073189045284
H	2.98253973345045	-7.6778776648181	3.36510279308473
H	4.57716986448385	-7.16781026008439	3.93029650768004
C	4.53150918648457	-0.12367972961815	1.64786996720403
H	4.01413563711340	0.12140815171355	0.73231110532937
C	2.53522400183417	-4.66894277532313	2.92454314935713
H	2.57567842646764	-4.83905362919876	1.85869601752874
C	9.61629659772991	1.34975409143074	0.19090060456683
H	9.96335542992260	0.60930292807871	-0.51163670294705
C	1.36266358774233	-0.71942631491592	4.49700185340454
H	2.40028713001782	-0.47120138470820	4.27070941251537
H	0.91510277867218	0.13255273280689	5.01028261269214
H	0.82823036505322	-0.85226801446855	3.5543788022869
C	9.56564371343352	2.87965900345925	1.91326235221003
H	9.8675646428325	3.50168342596357	2.74063245268113
C	10.41548445978252	2.01917325805970	1.16107600898731
H	11.47013558976526	1.86856470597051	1.32766152346653
H	6.00813134771615	1.05567418151545	4.29186916961594
H	5.50824488275727	1.70493975115063	1.92518579688339
H	3.60611424134048	-2.00180408892805	1.68275808820677



Table S24: XYZ file generated for B3LYP [1(4,5)H<sub>2</sub>Fc-a]<sup>+</sup>

66

Coordinates from ORCA-job Ru45H2Fc+

Ru	3.98389564492985	-3.68732763024371	4.08575873256446
Fe	7.68720651416954	1.40330665497657	2.84487925201326
Cl	5.08236166178968	-5.56663681941394	3.02585886125982
N	5.65129309434172	-3.70552178576812	5.33658049845603
N	5.37123042647436	-2.55811106080208	3.07321967766890
C	6.77871680435913	-3.17077564622999	4.80246673269663
N	4.98809066530202	-1.90785576376156	1.89413518847636
C	8.14942655827897	-0.56321336153573	3.33466269332605
C	6.58743937330106	-2.51975288626989	3.5179658347679
C	8.07020859706877	-3.90892423900125	6.6774083654555
H	9.01431509317561	-3.99754268263318	7.19657458312408
C	2.54495934529922	-3.12020476199483	5.65996351186025
H	2.80302724923384	-2.82705461014513	6.66867496628184
C	9.50606204704667	1.23816099905179	3.82054023500182
H	10.2885821711958	1.97714974386674	3.75702719298749
C	2.22876732277151	-2.56708235829351	3.33157157092596
H	2.26385340649557	-1.85481263924536	2.52042906265238
C	8.44067529885523	1.22770391729514	4.76263856434014
H	8.27390022206832	1.95358929569201	5.54180308880413
C	5.71977575651981	-4.32609937356226	6.51653861826702
H	4.80246543276851	-4.74885824160281	6.89694600463989
C	6.90853300476951	-4.43941786123618	7.22130571018900
H	6.91294253238373	-4.94407017081063	8.17632813669809
C	7.71786198893434	-1.89108378508414	2.75441008026220
C	9.32670920192946	0.14045319454749	2.93735741112473
H	9.96113489083107	-0.11574711958307	2.10347475678202
C	2.45747996442627	-2.12388545982002	4.66569617236547
C	2.52600126465240	-0.65991434333561	5.02880069496158
H	2.80729923739921	-0.60661783785019	6.08345514486119
C	2.31897825176336	-4.49206754046567	5.37318904148970
H	2.39352062744925	-5.22730121906344	6.16128434605143
C	8.00262630917964	-3.26551375681744	5.45222560024339
H	8.89778186609406	-2.84298128632816	5.00136107160617
C	5.93998796002583	1.59584555592384	1.74556063163646
H	5.16905723447595	0.84859045303304	1.67432527683977
C	2.05610818927687	-4.90872937269638	4.05993017120057
C	7.07108590489764	1.72921949136377	0.88966420060058
H	7.31602416548053	1.09884430614605	0.05030822827470
C	7.35971777356744	-1.88831671594744	1.26317488824170
C	1.11477476859690	-0.07098267610879	4.87554373458932
H	0.80452052685126	-0.08610044035797	3.62788211171341
H	1.09918507191731	0.96333594773790	5.22321722300780
H	0.38452649893640	-0.63911591897850	5.45363045979931
C	7.60303704742722	0.11840859192449	4.46357697800796
H	6.70493104229239	-0.1514939682757	4.9935880477382
C	1.85604646479806	-6.35633504215380	3.75492322160568
H	2.11830760105986	-6.58507292262738	2.72410712577539
H	0.80267824117230	-6.60441472733407	3.91493097215880
H	2.45413261403327	-6.97969750751014	4.41697742083848
C	5.91141378568483	-1.61264805147678	1.06431899277429
H	5.57599825377975	-1.12394003729399	0.15520076513444
C	2.03562852635701	-3.92371575393310	3.02656617131878
H	1.90789367608825	-4.22922755505471	1.99877288034224
C	7.84013840934102	2.83471006972444	1.34998006275078
H	8.77334186426583	3.17497718141667	0.93088997351290
C	3.55415297320656	0.13676514496140	4.23172982230366
H	4.58883510389371	-0.24644925488232	4.39931199821310
H	3.53222905165797	1.18060100548895	4.54786277814337
H	3.35390207289311	0.10206177889650	3.16022142251211
C	6.01204932347605	2.61750012708444	2.73217501953437
H	5.31527969664085	2.76460796718232	3.54089125722259
C	7.1868151268056	3.38341906647733	2.48897397537608
H	7.54259413512491	4.20953350087951	3.08354486338500
H	7.95528347488984	-1.15704013267857	0.72196416765219
H	8.56870860349702	-2.56591503428527	2.87092059805040
H	7.58145155663565	-2.86585464063530	0.82094340525009

Table S25: XYZ file generated for B3LYP [1(4,5)H<sub>2</sub>Fc-b]<sup>+</sup>

66			
Ru	4.25775499567350	-3.78183496295393	4.59434426985205
Fe	9.87633044390865	-1.22383450025912	1.58076135138602
Cl	6.28300837916916	-5.09906018896217	4.76203192981136
N	5.26135737770189	-2.54602610662571	5.92268998088278
N	5.34651729001437	-2.54027561418257	3.37615254896589
C	6.13467459686357	-1.66708005040296	5.36596523821303
N	5.27450422965300	-2.74858642935182	1.99101550195139
C	8.39845395830087	-1.34018086647110	3.03204157886643
C	6.13454919444577	-1.66168370764308	3.91181277429823
C	6.91241925896873	-1.00775320930832	7.53271608735588
H	7.5609578172190	-0.41433883018645	8.16190462788141
C	2.40231203670914	-4.01723747570195	5.80835052892081
H	2.28052608663037	-3.75172323621747	6.85009699225012
C	10.15131132437443	-2.82831899950130	2.85685106799983
H	10.73137229772533	-3.70091393121834	2.60336052509343
C	2.42877231569155	-3.38600252724393	3.47477798342711
H	2.34284004372660	-2.64340610175177	2.69462649085992
C	10.64811315837797	-1.63769143857848	3.45808347093479
H	11.67017897170518	-1.44528601377705	3.74192632095869
C	5.21409854065091	-2.66971901066604	7.25149375248814
H	4.52425037720813	-3.39940671889441	7.64642125720177
C	6.02123759559140	-1.91534328222581	8.08871549692704
H	5.94814762281818	-2.05546306213682	9.15769245081826
C	7.00614709546761	-0.75541772855287	3.08073096637037
C	8.76704652941006	-2.64896631460788	2.59386047853665
H	8.11253426507936	-3.37401609764478	2.1393255525971
C	2.17609206962318	-3.02043625913629	4.81578946910203
C	1.64883166780843	-1.66036701202189	5.20235451168254
H	1.76623354587830	-1.57320521437506	6.28591164410441
C	2.8522217778701	-5.30033306307397	5.47814493360032
H	3.07339259130439	-6.01110465870264	6.26080323353308
C	6.96737508952333	-0.88049648841776	6.15237154329168
H	7.65872335338229	-0.19469224452541	5.68803361146593
C	9.53745694222782	0.24582401485073	0.14162719433848
H	8.83085413073450	1.05548876275017	0.22798276660756
C	3.06194023779326	-5.66835025745619	4.11188574313071
C	9.27779039909291	-1.04674173844779	-0.39904770117245
H	8.33763936801086	-1.39703117029834	-0.79421740621509
C	6.30477137003325	-0.54090569580526	1.73373788064335
C	0.14768552796384	-1.61836846224153	4.87641775182501
H	-0.01657638411316	-1.71749997139951	3.80085705237055
H	-0.28180925205469	-0.67043237418668	5.20502771262727
H	-0.38741209929367	-2.42758547628231	5.37563283668598
C	9.56914985188104	-0.72142672463374	3.57673842683778
H	9.62345297638408	0.27886414325284	3.96744230374992
C	3.55190740350505	-7.04229601446334	3.78712923006048
H	3.9226441373809	-7.10456410962533	2.78547778165546
H	2.72497058787229	-7.74754079211093	3.90673488272446
H	4.34643809144341	-7.33640299643063	4.47056362608248
C	5.70430058101973	-1.80851453364580	1.24044023695847
H	5.60819556351165	-1.98818569911128	0.17437547833803
C	2.83496816631449	-4.70351233102445	3.11994466480759
H	3.04878677074274	-4.93236322428770	2.08684398724009
C	10.47811037923150	-1.80692172210487	-0.31094908366346
H	10.60167173955438	-2.83404485633283	-0.61457964857077
C	2.39694947830499	-0.4926997834007	4.55785607196723
H	3.44761813915388	-0.49073400407217	4.8511706016394
H	1.95435827865715	0.44810080064423	4.88858057610590
H	2.34025533986433	-0.52146837373499	3.46785336652859
C	10.89386282701703	0.27994081073856	0.57011793359306
H	11.38593227546317	1.11037371614833	1.05016485784160
C	11.47573494895039	-0.98848218781901	0.28805922603040
H	12.48236574872369	-1.29354140723670	0.52484413273309
H	5.49659469176461	0.19180039524614	1.84605763482957
H	7.07076073272000	0.20916783375782	3.58145900873384
H	6.99835427539599	-0.13829502097717	1.00119424401807



## Supporting Infos of Manuscript Paper 4.

### Supporting Information

Immobilization by iEDDA [4+2] cycloaddition of a 3-(pyrid-2-yl)-s-tetrazine-tricarbonylrhenium(I)-chloride derivative onto a norbonen-trimethoxysilane functionalized SBA-15.

Marc Schnierle<sup>‡[1]</sup>, Laura Neumüller<sup>‡[1]</sup>, Felix Ziegler<sup>[3]</sup>, Kim-I. Mehnert<sup>[1]</sup>, Osman Bunjaku<sup>[2]</sup>, Mario Winkler<sup>[4]</sup>, Indro Biswas<sup>[5]</sup>, Johanna Bruckner<sup>[4]</sup>, Joris van Slageren<sup>[4]</sup>, Michael Buchmeiser<sup>[3]</sup>, Deven P. Estes<sup>\*[2]</sup>, Mark R. Ringenberg<sup>\*[1]</sup>

[1] Institut für Anorganische Chemie, Universität Stuttgart, Pfaffenwaldring 55, 70569 Stuttgart, Germany.

[2] Institut für Technische Chemie, Universität Stuttgart, Pfaffenwaldring 55, 70569 Stuttgart, Germany.

[3] Institut für Polymer Chemie, Universität Stuttgart, Pfaffenwaldring 55, 70569 Stuttgart, Germany.

[4] Institut für Physikalische Chemie, Universität Stuttgart, Pfaffenwaldring 55, 70569 Stuttgart, Germany.

[5] Institut für Technische Thermodynamik, Deutsches Zentrum für Luft- und Raumfahrt Stuttgart, Pfaffenwaldring 38-40, 70569 Stuttgart, Germany.

### Experimental

$^1\text{H}$   $^{13}\text{C}$   $^{19}\text{F}$  COSY spectra were taken on a Bruker AC 250, 500 or 700 MHz spectrometer.  $^1\text{H}$  NMR spectra were referenced versus residual solvent peak. UV/Vis absorption spectra were recorded on J&M TIDAS spectrophotometer. Cyclic voltammetry was carried out in 0.1 M  $\text{Bu}_4\text{NPF}_6/\text{CH}_2\text{Cl}_2$  solutions using a three-electrode configuration (glassy carbon working, Pt wire counter, and Ag quasi-reference) and were performed using a Metrohm Autolab potentiostat. The ferrocene/ferrocenium ( $[\text{FcCp}2]^{0/+}$ ) couple served as internal reference to all potentials reported herein. X-ray diffraction data were collected using a Bruker Kappa Apex2duo diffractometer. The structures were solved using charge flipping and refined by full-matrix least-squares techniques on F2 using the OLEX2 program<sup>[1]</sup>. The absorption corrections were done by multiscan technique. All non-hydrogen atoms were refined anisotropically. Hydrogen atoms were included in the refinement process as per the riding model.

### References:

- [1] O. V. Dolomanov, L. J. Bourhis, R. J. Gildea, J. A. K. Howard, and H. Puschmann, "Olex2: a complete structure solution, refinement and analysis program," *J. Appl. Cryst.*, vol. 42, pp. 339–341, 2009.

Table 1: Crystallography of [L]-H und [C]-H.

	[L]-H	[C]-H
Identification code	stams16	ac520
Empirical formula	C <sub>8</sub> H <sub>7</sub> N <sub>5</sub>	C <sub>11</sub> H <sub>7</sub> ClN <sub>5</sub> O <sub>3</sub> Re
Formula weight	173.19	478.87
Temperature/K	293(2)	140.01
Crystal system	Monoclinic	monoclinic
Space group	P2 <sub>1</sub> /c	P2 <sub>1</sub> /n
a/Å	10.1065(19)	9.0780(3)
b/Å	7.0822(8)	12.1585(4)
c/Å	12.018(2)	12.5914(5)
α/°	90	90
β/°	112.704(13)	96.764(2)
γ/°	90	90
Volume/Å <sup>3</sup>	793.6(2)	1380.10(8)
Z	4	4
ρ <sub>calc</sub> /cm <sup>3</sup>	1.450	2.305
μ/mm <sup>-1</sup>	0.098	9.015
F(000)	360.0	896.0
Crystal size/mm <sup>3</sup>	? × ? × ?	0.439 × 0.314 × 0.044
Radiation	MoKα (λ = 0.71073)	MoKα (λ = 0.71073)
2θ range for data collection/°	4.368 to 65.678	4.672 to 61.266
Index ranges	-14 ≤ h ≤ 15, -10 ≤ k ≤ 10, -18 ≤ l ≤ 18	-12 ≤ h ≤ 12, -17 ≤ k ≤ 17, -16 ≤ l ≤ 17
Reflections collected	14162	28459
Independent reflections	2795 [R <sub>int</sub> = 0.0716, R <sub>sigma</sub> = 0.0656]	4213 [R <sub>int</sub> = 0.0365, R <sub>sigma</sub> = 0.0261]
Data/restraints/parameters	2795/0/119	4213/0/191
Goodness-of-fit on F <sup>2</sup>	1.026	1.064
Final R indexes [I >= 2σ (I)]	R <sub>1</sub> = 0.0605, wR <sub>2</sub> = 0.1590	R <sub>1</sub> = 0.0192, wR <sub>2</sub> = 0.0355
Final R indexes [all data]	R <sub>1</sub> = 0.1131, wR <sub>2</sub> = 0.1834	R <sub>1</sub> = 0.0298, wR <sub>2</sub> = 0.0394
Largest diff. peak/hole / e Å <sup>-3</sup>	0.47/-0.28	1.97/-0.98

Table 2: Crystallography of [L]-Me und [C]-Me.

	[L]-Me	[C]-Me
Identification code	ac521	ac541
Empirical formula	C <sub>9</sub> H <sub>9</sub> N <sub>5</sub>	C <sub>12</sub> H <sub>9</sub> ClN <sub>5</sub> O <sub>3</sub> Re
Formula weight	187.21	493.40
Temperature/K	140.0	140.02
Crystal system	monoclinic	monoclinic
Space group	P2 <sub>1</sub> /c	Cc
a/Å	12.50(2)	25.3225(9)
b/Å	11.38(2)	7.8713(3)
c/Å	12.89(3)	15.3320(5)
α/°	90	90
β/°	104.05(12)	108.219(3)
γ/°	90	90
Volume/Å <sup>3</sup>	1778(7)	2902.79(18)
Z	8	8
ρ <sub>calc</sub> /g/cm <sup>3</sup>	1.398	2.258
μ/mm <sup>-1</sup>	0.093	8.576
F(000)	784.0	1860.0
Crystal size/mm <sup>3</sup>	0.266 × 0.249 × 0.194	0.486 × 0.076 × 0.04
Radiation	MoKα (λ = 0.71073)	MoKα (λ = 0.71073)
2θ range for data collection/°	3.36 to 54.25	3.386 to 61.202
Index ranges	-15 ≤ h ≤ 15, -13 ≤ k ≤ 11, -16 ≤ l ≤ 15	-36 ≤ h ≤ 36, -11 ≤ k ≤ 11, -21 ≤ l ≤ 21
Reflections collected	15330	30038
Independent reflections	3690 [R <sub>int</sub> = 0.0600, R <sub>sigma</sub> = 0.0575]	8546 [R <sub>int</sub> = 0.0433, R <sub>sigma</sub> = 0.0588]
Data/restraints/parameters	3690/0/257	8546/2/401
Goodness-of-fit on F <sup>2</sup>	1.042	0.947
Final R indexes [I ≥ 2σ (I)]	R <sub>1</sub> = 0.0586, wR <sub>2</sub> = 0.1532	R <sub>1</sub> = 0.0279, wR <sub>2</sub> = 0.0412
Final R indexes [all data]	R <sub>1</sub> = 0.1069, wR <sub>2</sub> = 0.1791	R <sub>1</sub> = 0.0485, wR <sub>2</sub> = 0.0458
Largest diff. peak/hole / e Å <sup>-3</sup>	0.30/-0.30	0.91/-1.06

Table 3: Crystallography of [L]-OMe und [C]-OMe.

	[L]-OMe	[C]-OMe
Identification code	ac552	ac540
Empirical formula	C <sub>9</sub> H <sub>9</sub> N <sub>5</sub> O	C <sub>12</sub> H <sub>9</sub> ClN <sub>5</sub> O <sub>4</sub> Re
Formula weight	203.21	508.89
Temperature/K	145.0	140.02
Crystal system	Monoclinic	Triclinic
Space group	P2 <sub>1</sub> /n	P-1
a/Å	11.2309(9)	7.0062(2)
b/Å	3.9391(4)	9.8973(3)
c/Å	20.9816(13)	11.1614(3)
α/°	90	93.8700(10)
β/°	96.765(5)	91.238(2)
γ/°	90	107.1270(10)
Volume/Å <sup>3</sup>	921.76(13)	737.25(4)
Z	4	2
ρ <sub>calc</sub> /cm <sup>3</sup>	1.464	2.292
μ/mm <sup>-1</sup>	0.861	8.450
F(000)	424.0	480.0
Crystal size/mm <sup>3</sup>	0.3 × 0.123 × 0.03	0.364 × 0.278 × 0.076
Radiation	CuKα (λ = 1.54178)	MoKα (λ = 0.71073)
2θ range for data collection/°	8.488 to 132.968	3.66 to 61.378
Index ranges	-13 ≤ h ≤ 13, -4 ≤ k ≤ 4, -24 ≤ l ≤ 23	-10 ≤ h ≤ 10, -14 ≤ k ≤ 14, - 16 ≤ l ≤ 16
Reflections collected	5167	16420
Independent reflections	1507 [R <sub>int</sub> = 0.0405, R <sub>sigma</sub> = 0.0396]	4548 [R <sub>int</sub> = 0.0325, R <sub>sigma</sub> = 0.0297]
Data/restraints/parameters	1507/0/172	4548/0/210
Goodness-of-fit on F <sup>2</sup>	1.030	1.053
Final R indexes [I ≥ 2σ (I)]	R <sub>1</sub> = 0.0388, wR <sub>2</sub> = 0.0983	R <sub>1</sub> = 0.0188, wR <sub>2</sub> = 0.0431
Final R indexes [all data]	R <sub>1</sub> = 0.0533, wR <sub>2</sub> = 0.1075	R <sub>1</sub> = 0.0228, wR <sub>2</sub> = 0.0449
largest diff. peak/hole / e Å <sup>-3</sup>	0.16/-0.20	1.30/-1.06



Table 4 Crystallography of [L]-CF<sub>3</sub> and [C]-CF<sub>3</sub>.

	[L]-CF <sub>3</sub>	[C]-CF <sub>3</sub>
Identification code	ac543	ac538
Empirical formula	C <sub>9</sub> H <sub>6</sub> N <sub>5</sub> F <sub>3</sub>	C <sub>12</sub> H <sub>6</sub> N <sub>5</sub> O <sub>3</sub> F <sub>3</sub> ClRe
Formula weight	241.19	546.868
Temperature/K	139.99	140.0
Crystal system	monoclinic	triclinic
Space group	P2 <sub>1</sub> /c	P-1
a/Å	6.338(3)	8.4366(4)
b/Å	6.653(3)	8.9172(4)
c/Å	23.514(14)	10.5795(5)
α/°	90	79.023(2)
β/°	91.74(3)	83.571(2)
γ/°	90	84.924(3)
Volume/Å <sup>3</sup>	991.0(9)	774.59(6)
Z	4	2
ρ <sub>calc</sub> /cm <sup>3</sup>	1.617	2.345
μ/mm <sup>-1</sup>	0.145	8.074
F(000)	488.0	511.4
Crystal size/mm <sup>3</sup>	0.407 × 0.218 × 0.06	0.32 × 0.111 × 0.04
Radiation	Mo Kα (λ = 0.71073)	Mo Kα (λ = 0.71073)
2θ range for data collection/°	3.466 to 53.426	3.94 to 56.7
Index ranges	-7 ≤ h ≤ 7, -8 ≤ k ≤ 8, -29 ≤ l ≤ 29	-11 ≤ h ≤ 11, -11 ≤ k ≤ 11, -14 ≤ l ≤ 13
Reflections collected	13288	15109
Independent reflections	2070 [R <sub>int</sub> = 0.0686, R <sub>sigma</sub> = 0.0512]	3836 [R <sub>int</sub> = 0.0440, R <sub>sigma</sub> = 0.0497]
Data/restraints/parameters	2070/0/156	3836/0/227
Goodness-of-fit on F <sup>2</sup>	1.113	1.045
Final R indexes [I ≥ 2σ (I)]	R <sub>1</sub> = 0.2416, wR <sub>2</sub> = 0.5771	R <sub>1</sub> = 0.0296, wR <sub>2</sub> = 0.0590
Final R indexes [all data]	R <sub>1</sub> = 0.2615, wR <sub>2</sub> = 0.5840	R <sub>1</sub> = 0.0396, wR <sub>2</sub> = 0.0632
Largest diff. peak/hole / e Å <sup>-3</sup>	1.32/-1.25	2.14/-1.20

Table 5: Crystallography: linker-[C]-CF<sub>3</sub>.

	[C]-CF <sub>3</sub>
Identification code	ac551b
Empirical formula	C <sub>22</sub> H <sub>24</sub> ClF <sub>3</sub> N <sub>3</sub> O <sub>6</sub> ReSi
Formula weight	733.18
Temperature/K	145.0
Crystal system	Triclinic
Space group	P-1
a/Å	7.6088(10)
b/Å	11.4798(16)
c/Å	15.971(2)
α/°	71.677(10)
β/°	87.952(10)
γ/°	89.575(10)
Volume/Å <sup>3</sup>	1323.5(3)
Z	2
ρ <sub>calc</sub> /g/cm <sup>3</sup>	1.840
μ/mm <sup>-1</sup>	10.917
F(000)	716.0
Crystal size/mm <sup>3</sup>	0.078 × 0.066 × 0.024
Radiation	CuKα (λ = 1.54178)
2θ range for data collection/°	5.832 to 132.65
Index ranges	-8 ≤ h ≤ 8, -13 ≤ k ≤ 13, -18 ≤ l ≤ 18
Reflections collected	12704
Independent reflections	4322 [R <sub>int</sub> = 0.0920, R <sub>sigma</sub> = 0.0969]
Data/restraints/parameters	4322/0/350
Goodness-of-fit on F <sup>2</sup>	1.002
Final R indexes [I >= 2σ (I)]	R <sub>1</sub> = 0.0498, wR <sub>2</sub> = 0.1136
Final R indexes [all data]	R <sub>1</sub> = 0.0860, wR <sub>2</sub> = 0.1384
Largest diff. peak/hole / e Å <sup>-3</sup>	1.52/-1.14

Kinetics:

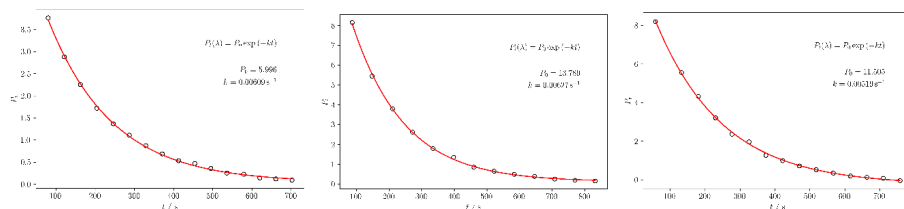


Figure 1: Kinetics of [L]-H + NBE (1:50) at 20 °C determined from <sup>1</sup>H NMR of the reaction in CD<sub>2</sub>Cl<sub>2</sub>.

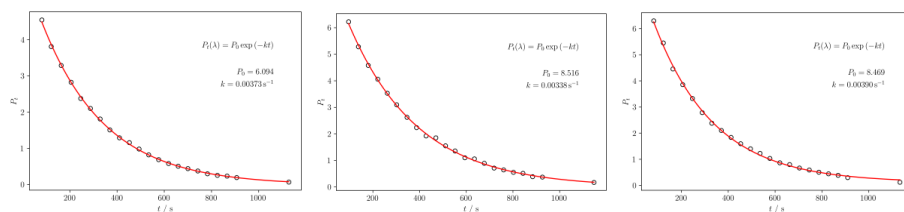


Figure 2: Kinetics of [L]-Me+ NBE (1:50) at 20 °C determined from <sup>1</sup>H NMR of the reaction in CD<sub>2</sub>Cl<sub>2</sub>.

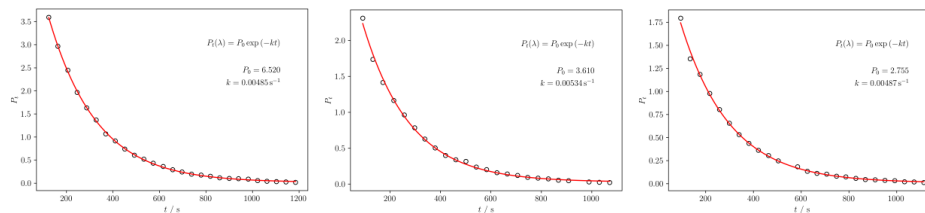


Figure 3: Kinetics of [L]-OMe+ NBE (1:50) at 20 °C determined from <sup>1</sup>H NMR of the reaction in CD<sub>2</sub>Cl<sub>2</sub>.

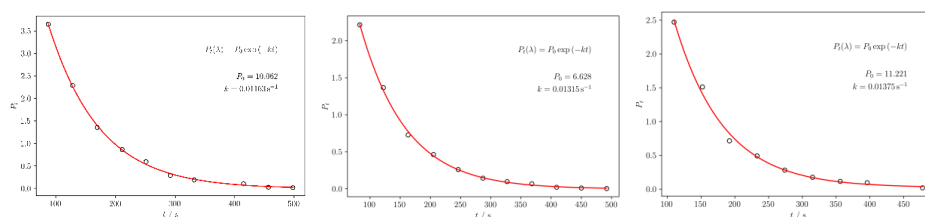


Figure 4: Kinetics of [L]-CF<sub>3</sub>+ NBE (1:50) at 20 °C determined from <sup>1</sup>H NMR of the reaction in CD<sub>2</sub>Cl<sub>2</sub>.

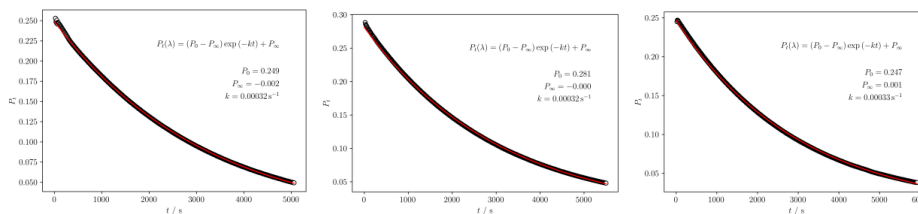


Figure 5: Kinetics of [C]-H + NBE (1:50) at 20 °C determined from UV/Vis of the reaction in C<sub>2</sub>H<sub>4</sub>Cl<sub>2</sub>.

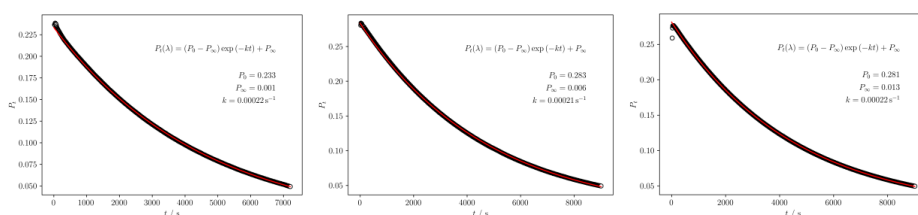


Figure 6: Kinetics of [C]-Me + NBE (1:50) at 20 °C determined from UV/Vis of the reaction in C<sub>2</sub>H<sub>4</sub>Cl<sub>2</sub>.

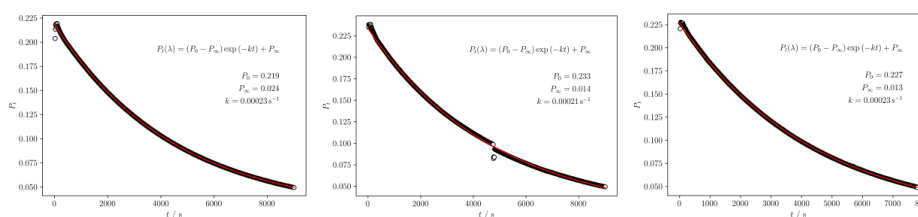


Figure 7: Kinetics of [C]-OMe + NBE (1:50) at 20 °C determined from UV/Vis of the reaction in C<sub>2</sub>H<sub>4</sub>Cl<sub>2</sub>.

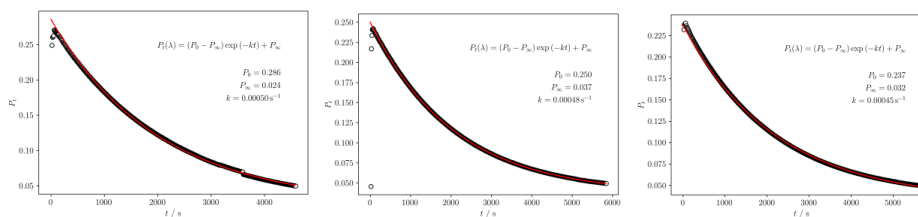


Figure 8: Kinetics of [C]-CF<sub>3</sub> + NBE (1:50) at 20 °C determined from UV/Vis of the reaction in C<sub>2</sub>H<sub>4</sub>Cl<sub>2</sub>.

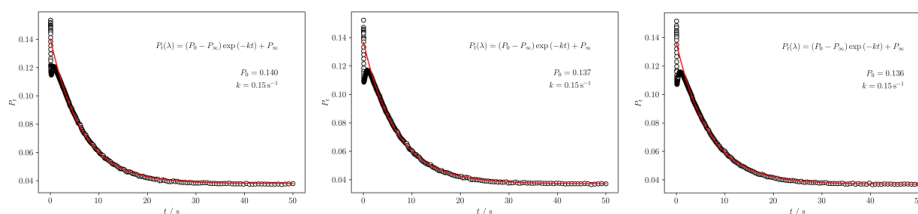


Figure 9: Kinetics of [L]-H + TCO (1:50) at 5.3°C determined from UV/Vis of the reaction in C<sub>2</sub>H<sub>4</sub>Cl<sub>2</sub>.

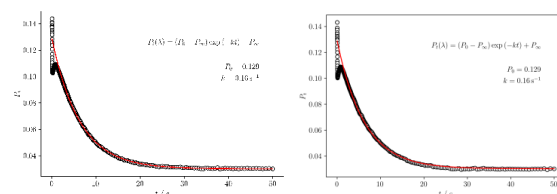


Figure 10: Kinetics of [L]-H + TCO (1:50) at 8.9°C determined from UV/Vis of the reaction in C<sub>2</sub>H<sub>4</sub>Cl<sub>2</sub>.

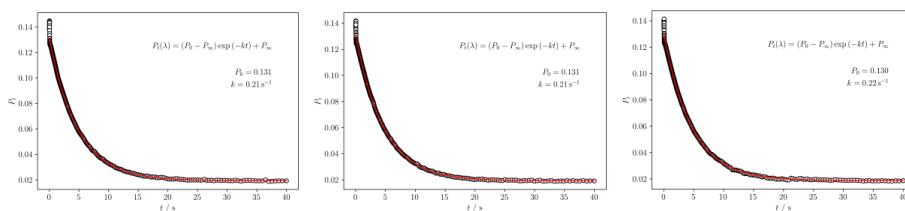


Figure 11: Kinetics of [L]-H + TCO (1:50) at 20.8°C determined from UV/Vis of the reaction in C<sub>2</sub>H<sub>4</sub>Cl<sub>2</sub>.

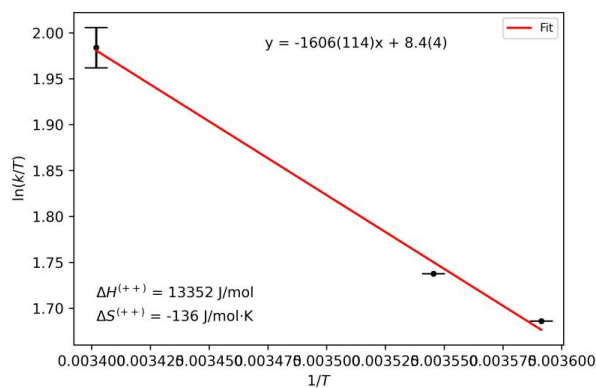


Figure 12: Eyring Plot of [L]-H + TCO.

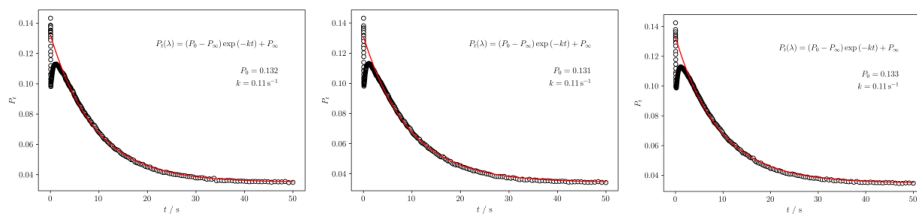


Figure 13: Kinetics of [L]-Me + TCO (1:50) at 5.7°C determined from UV/Vis of the reaction in C<sub>2</sub>H<sub>4</sub>Cl<sub>2</sub>.

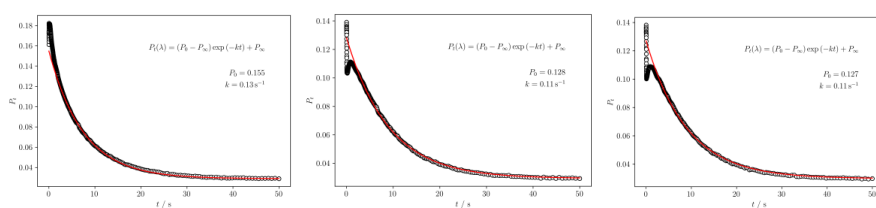


Figure 14: Kinetics of [L]-Me + TCO (1:50) at 9.2°C determined from UV/Vis of the reaction in C<sub>2</sub>H<sub>4</sub>Cl<sub>2</sub>.

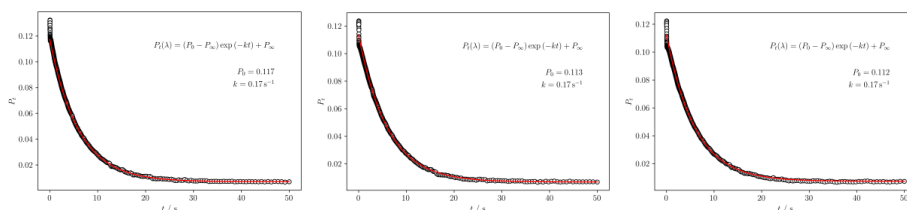


Figure 15: Kinetics of [L]-Me + TCO (1:50) at 20.8°C determined from UV/Vis of the reaction in C<sub>2</sub>H<sub>4</sub>Cl<sub>2</sub>.

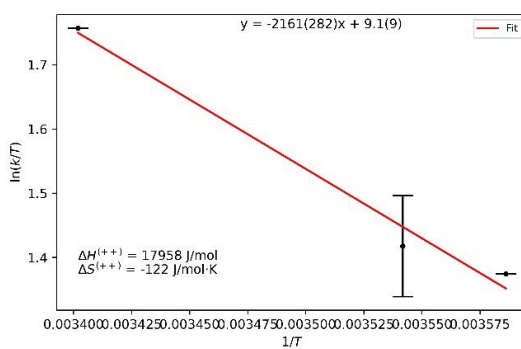


Figure 16: Eyring Plot of [L]-Me + TCO.

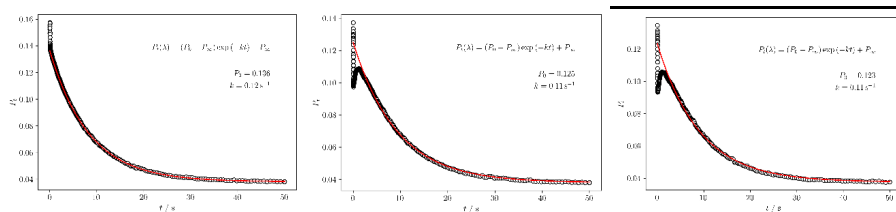


Figure 17: Kinetics of [L]-OME + TCO (1:50) at 3.9°C determined from UV/Vis of the reaction in C<sub>2</sub>H<sub>4</sub>Cl<sub>2</sub>.

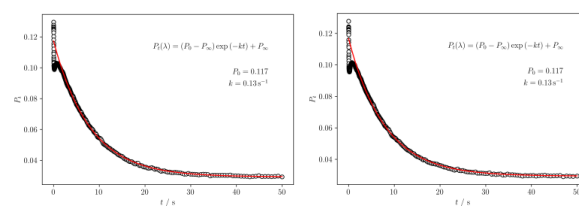


Figure 18: Kinetics of [L]-OME + TCO (1:50) at 9.7°C determined from UV/Vis of the reaction in C<sub>2</sub>H<sub>4</sub>Cl<sub>2</sub>.

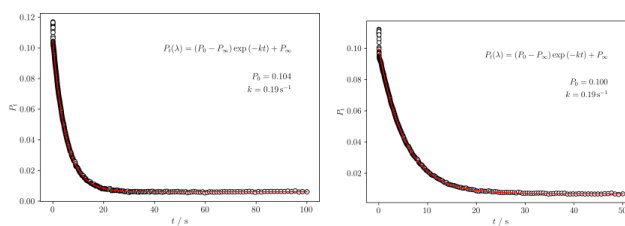


Figure 19: Kinetics of [L]-OME + TCO (1:50) at 20.8°C determined from UV/Vis of the reaction in C<sub>2</sub>H<sub>4</sub>Cl<sub>2</sub>.

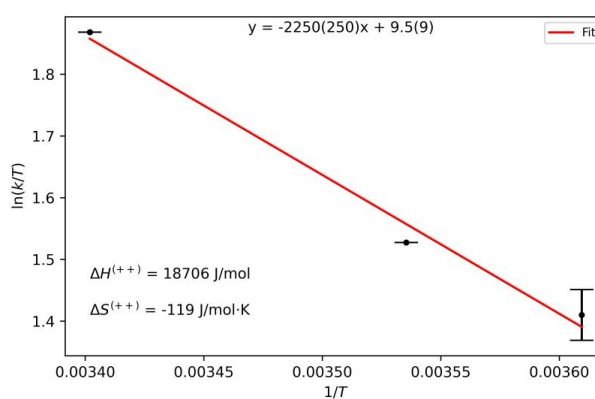


Figure 20: Eyring Plot of [L]-OME + TCO.

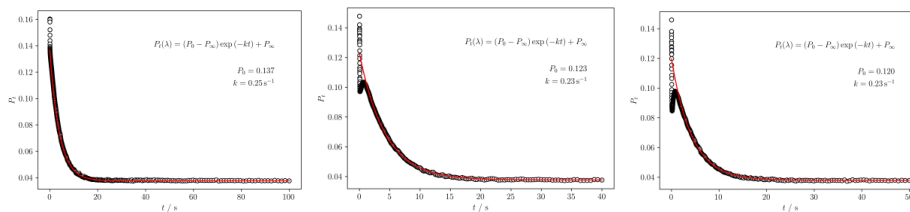


Figure 21: Kinetics of [L]-CF<sub>3</sub> + TCO (1:50) at 3.6°C determined from UV/Vis of the reaction in C<sub>2</sub>H<sub>4</sub>Cl<sub>2</sub>.

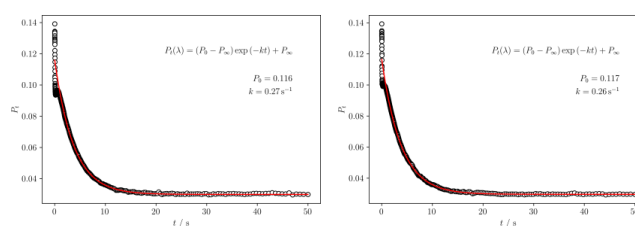


Figure 22: Kinetics of [L]-CF<sub>3</sub> + TCO (1:50) at 9.7°C determined from UV/Vis of the reaction in C<sub>2</sub>H<sub>4</sub>Cl<sub>2</sub>.

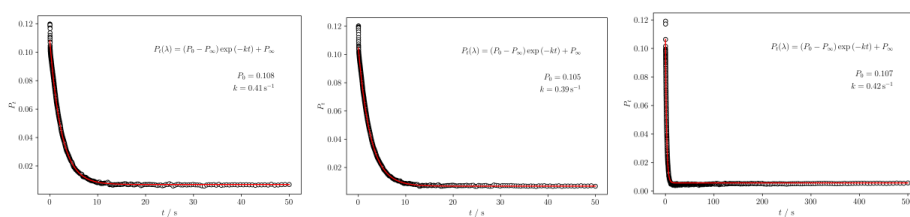


Figure 23: Kinetics of [L]-CF<sub>3</sub> + TCO (1:50) at 20.8°C determined from UV/Vis of the reaction in C<sub>2</sub>H<sub>4</sub>Cl<sub>2</sub>.

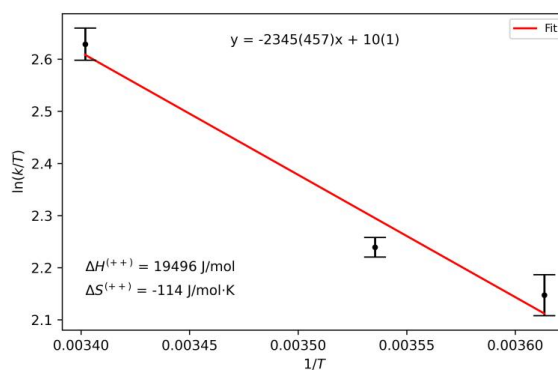


Figure 24: Eyring Plot of [L]-CF<sub>3</sub> + TCO.



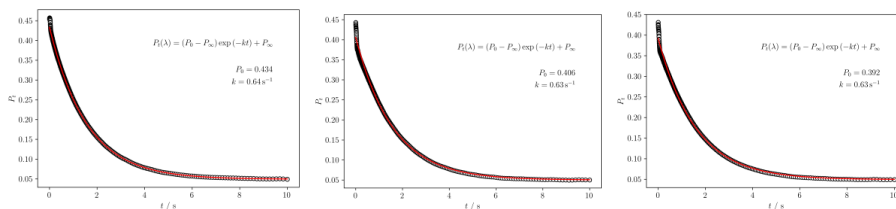


Figure 25: Kinetics of [C]-H + TCO (1:50) at 5.3°C determined from UV/Vis of the reaction in C<sub>2</sub>H<sub>4</sub>Cl<sub>2</sub>.

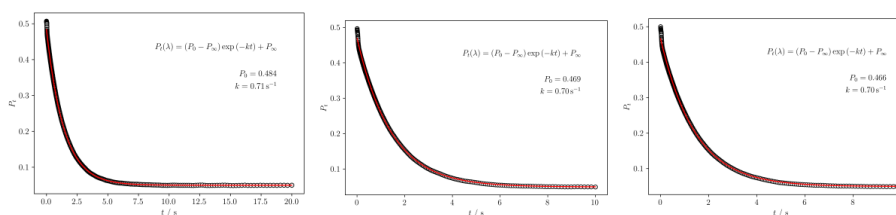


Figure 26: Kinetics of [C]-H + TCO (1:50) at 9.6°C determined from UV/Vis of the reaction in C<sub>2</sub>H<sub>4</sub>Cl<sub>2</sub>.

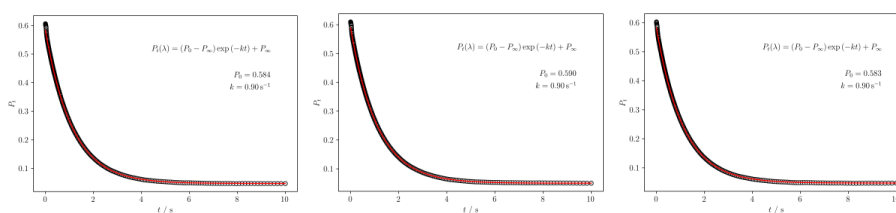


Figure 27: Kinetics of [C]-H + TCO (1:50) at 20.8°C determined from UV/Vis of the reaction in C<sub>2</sub>H<sub>4</sub>Cl<sub>2</sub>.

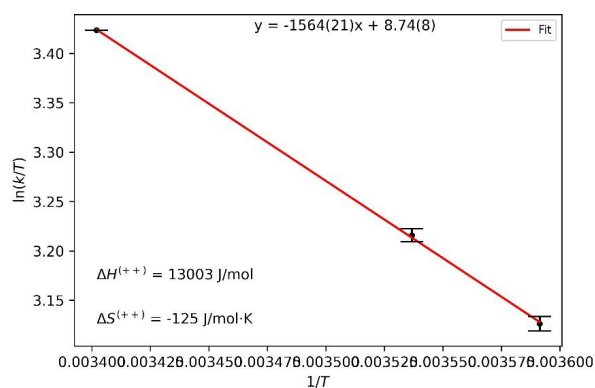


Figure 28: Eyring Plot of [C]-H + TCO.

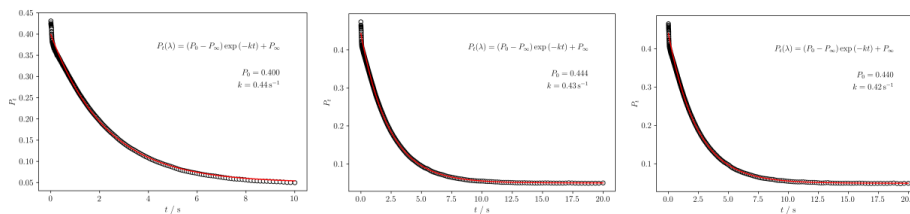


Figure 29: Kinetics of [C]-Me + TCO (1:50) at 4.7°C determined from UV/Vis of the reaction in C<sub>2</sub>H<sub>4</sub>Cl<sub>2</sub>.

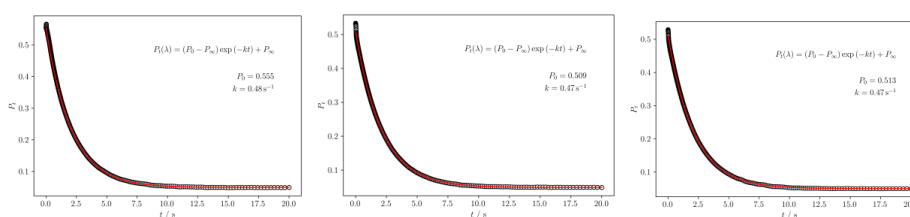


Figure 30: Kinetics of [C]-Me + TCO (1:50) at 9.9°C determined from UV/Vis of the reaction in C<sub>2</sub>H<sub>4</sub>Cl<sub>2</sub>.

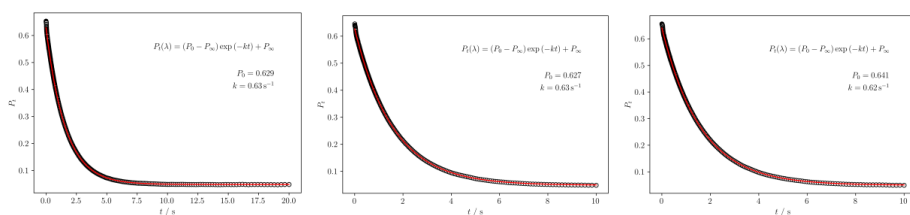


Figure 31: Kinetics of [C]-Me + TCO (1:50) at 20.8°C determined from UV/Vis of the reaction in C<sub>2</sub>H<sub>4</sub>Cl<sub>2</sub>.

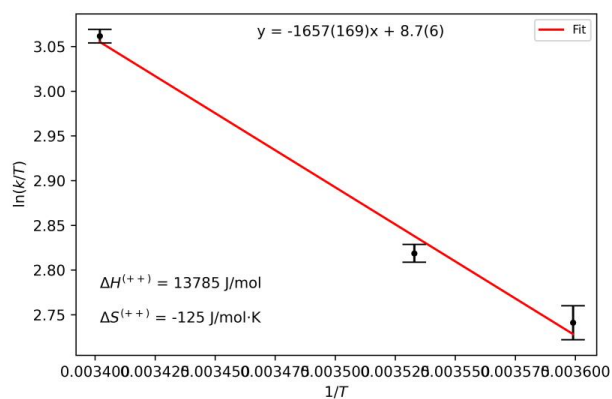


Figure 32: Eyring Plot of [C]-Me + TCO.

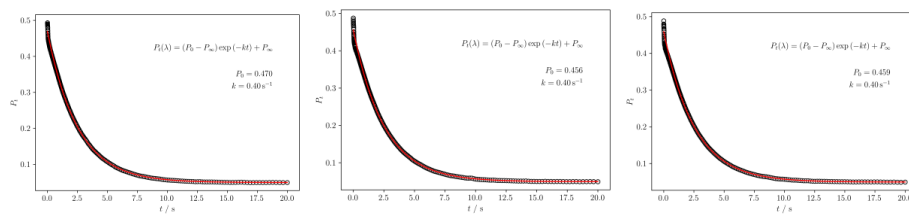


Figure 33: Kinetics of [C]-OME + TCO (1:50) at 4.3°C determined from UV/Vis of the reaction in C<sub>2</sub>H<sub>4</sub>Cl<sub>2</sub>.

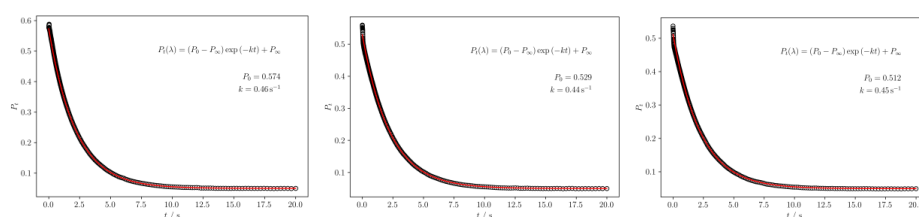


Figure 34: Kinetics of [C]-OME + TCO (1:50) at 8.8°C determined from UV/Vis of the reaction in C<sub>2</sub>H<sub>4</sub>Cl<sub>2</sub>.

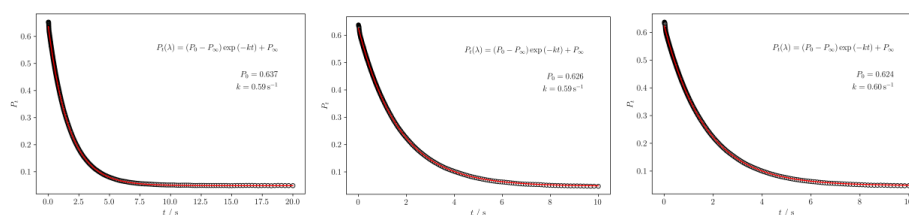


Figure 35: Kinetics of [C]-OME + TCO (1:50) at 20.8°C determined from UV/Vis of the reaction in C<sub>2</sub>H<sub>4</sub>Cl<sub>2</sub>.

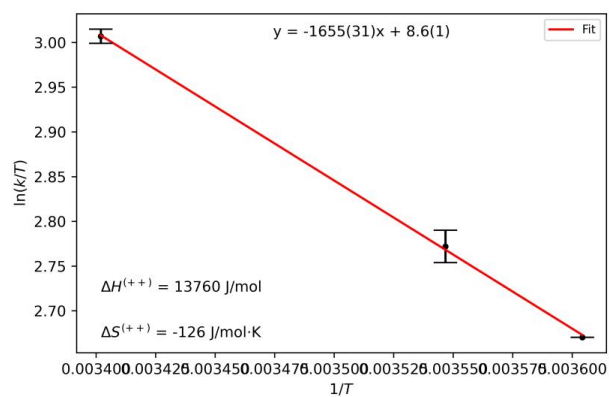


Figure 36: Eyring Plot of [C]-OME + TCO.

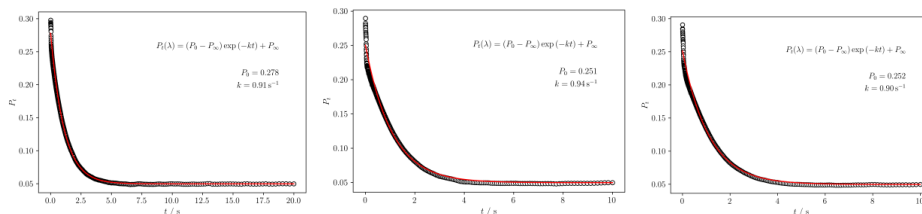


Figure 37: Kinetics of [C]-CF<sub>3</sub> + TCO (1:50) at 3.8°C determined from UV/Vis of the reaction in C<sub>2</sub>H<sub>4</sub>Cl<sub>2</sub>.

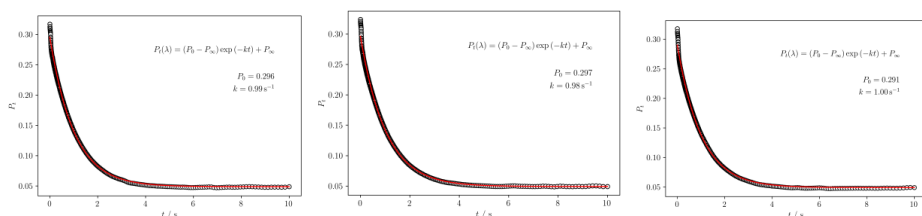


Figure 38: Kinetics of [C]-CF<sub>3</sub> + TCO (1:50) at 20.8°C determined from UV/Vis of the reaction in C<sub>2</sub>H<sub>4</sub>Cl<sub>2</sub>.

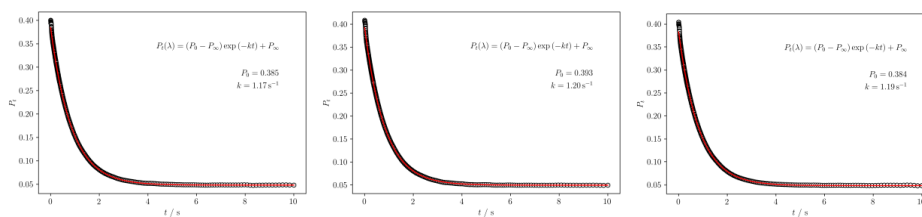


Figure 39: Kinetics of [C]-CF<sub>3</sub> + TCO (1:50) at 20.8°C determined from UV/Vis of the reaction in C<sub>2</sub>H<sub>4</sub>Cl<sub>2</sub>.

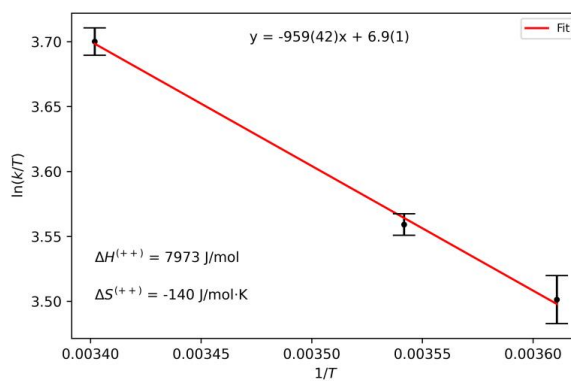
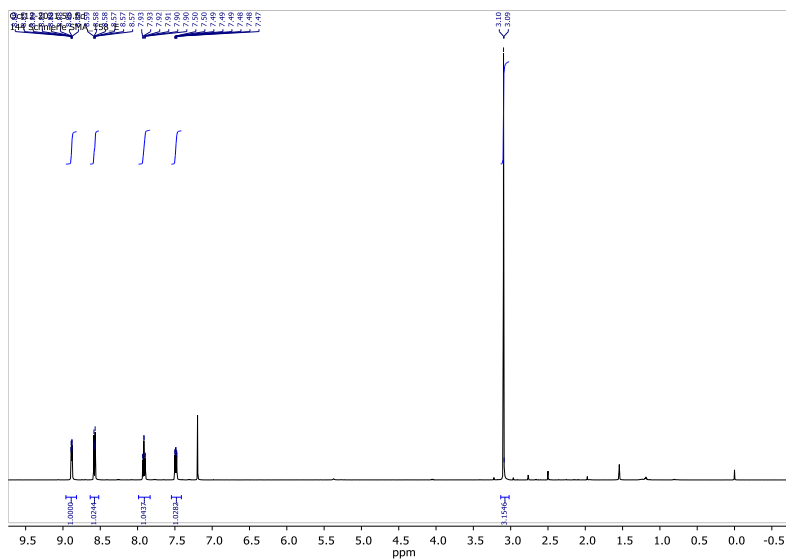
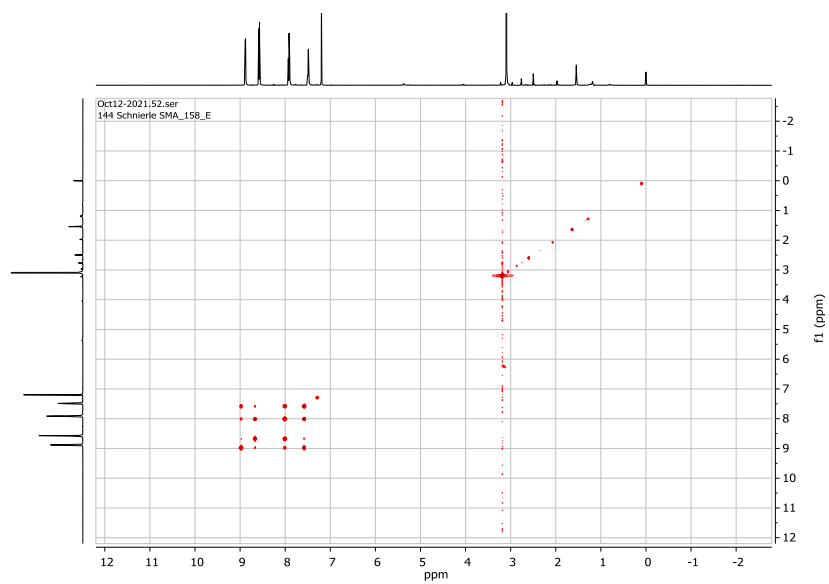
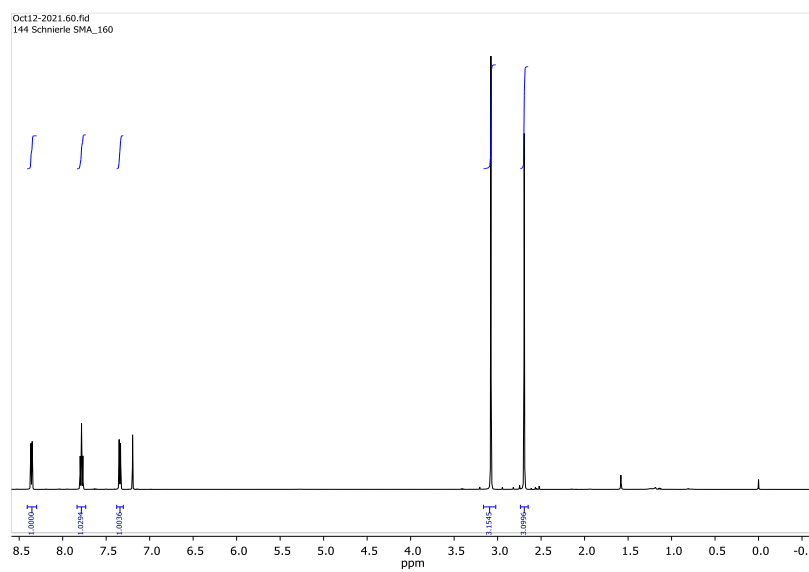


Figure 40: Eyring Plot of [C]-CF<sub>3</sub> + TCO.

NMR Spectroscopy:



Figure 43: COSY NMR of [L]-H in  $\text{CDCl}_3$ .Figure 44:  $^1\text{H}$  NMR of [L]-Me in  $\text{CDCl}_3$ .

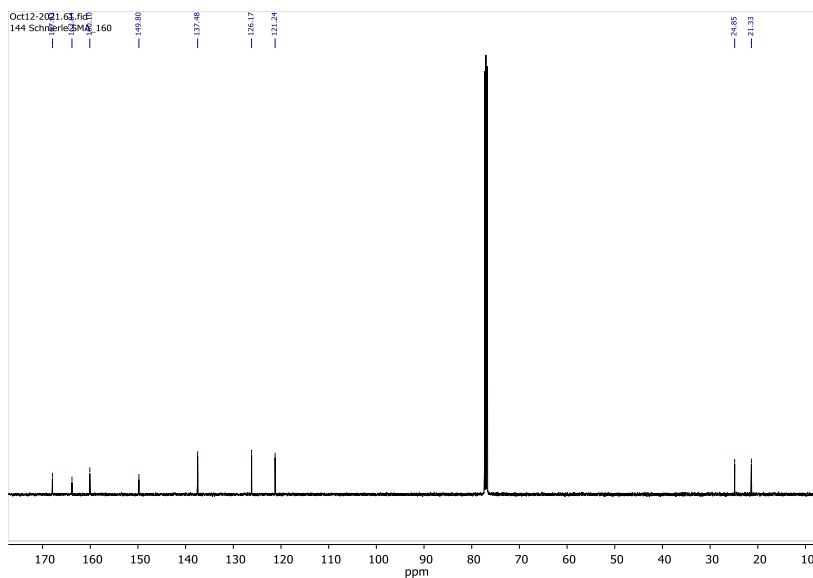


Figure 45:  $^{13}\text{C}$  NMR of [L]-Me in  $\text{CDCl}_3$ .

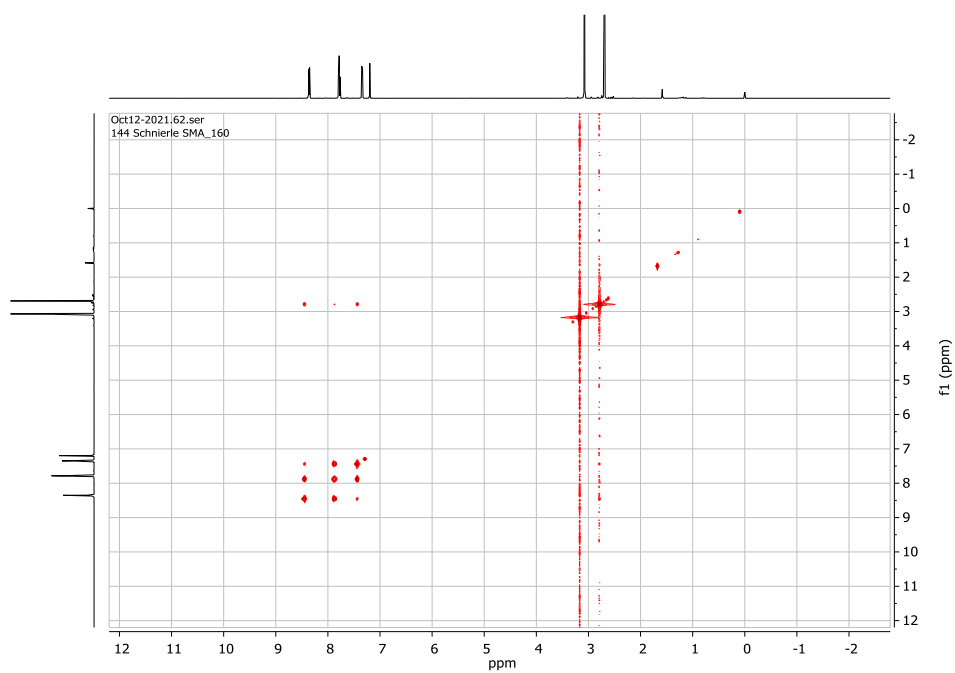
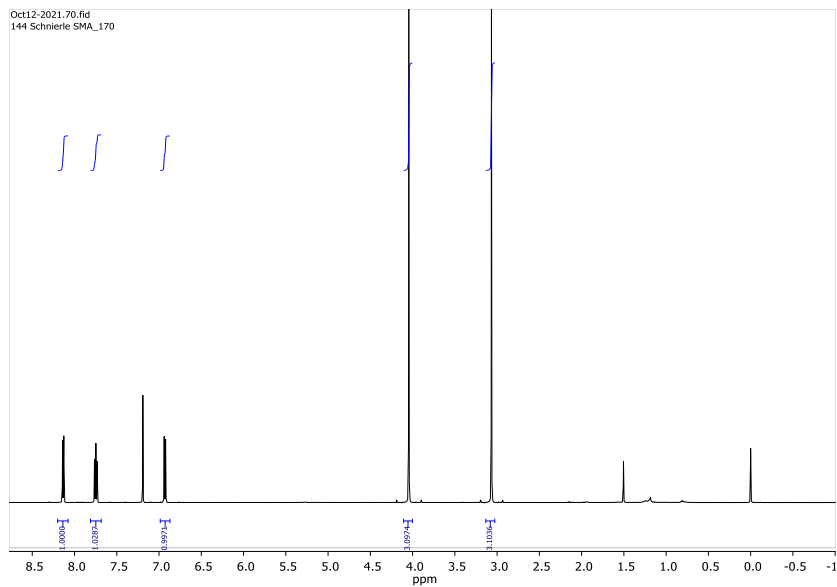
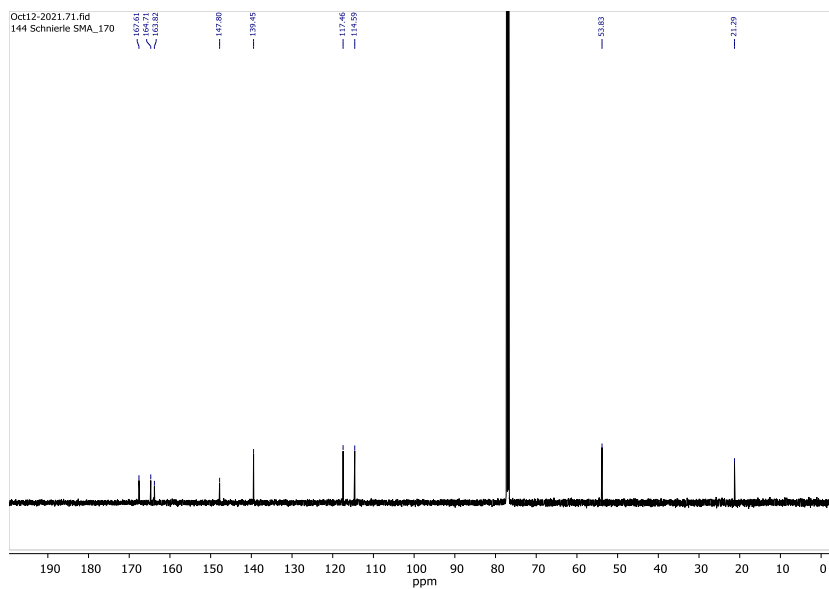
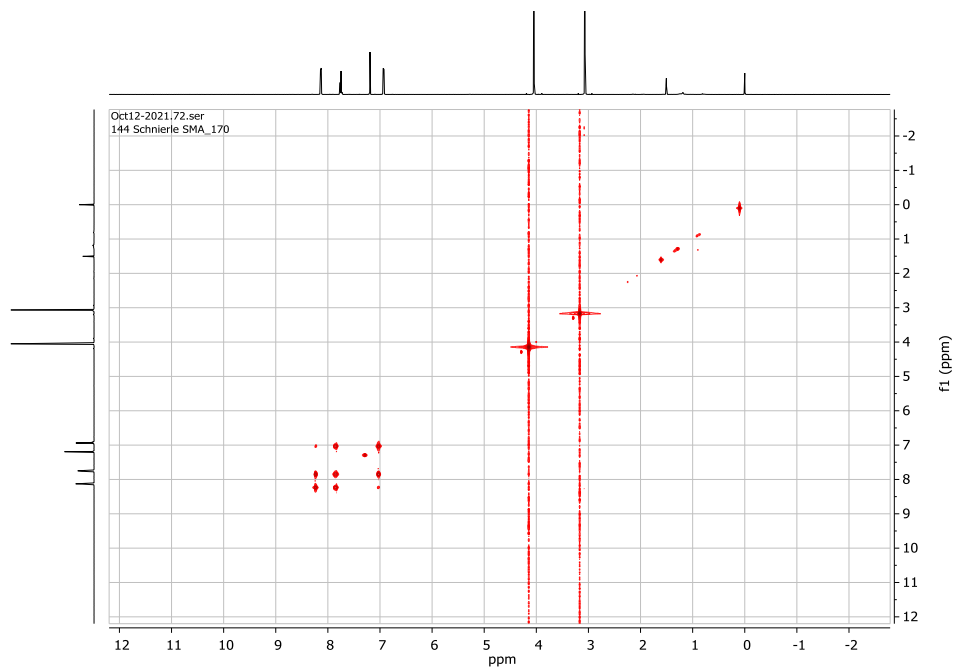
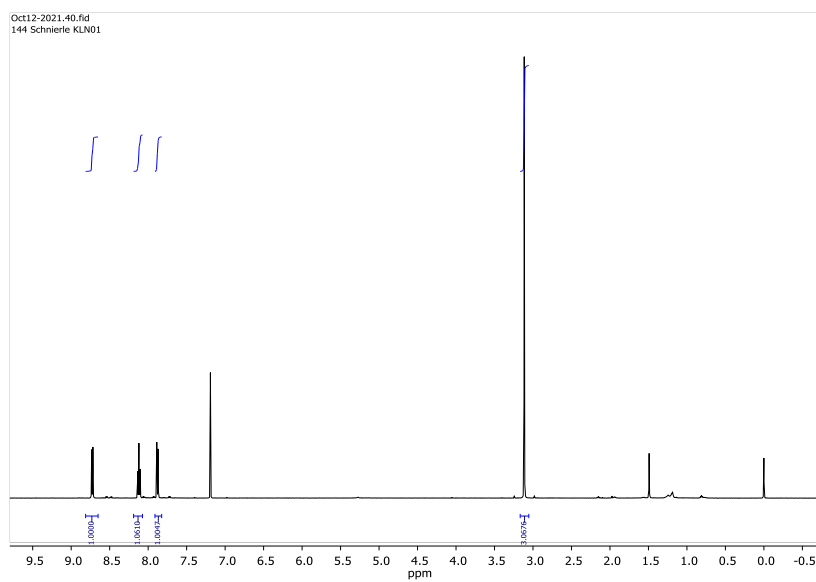
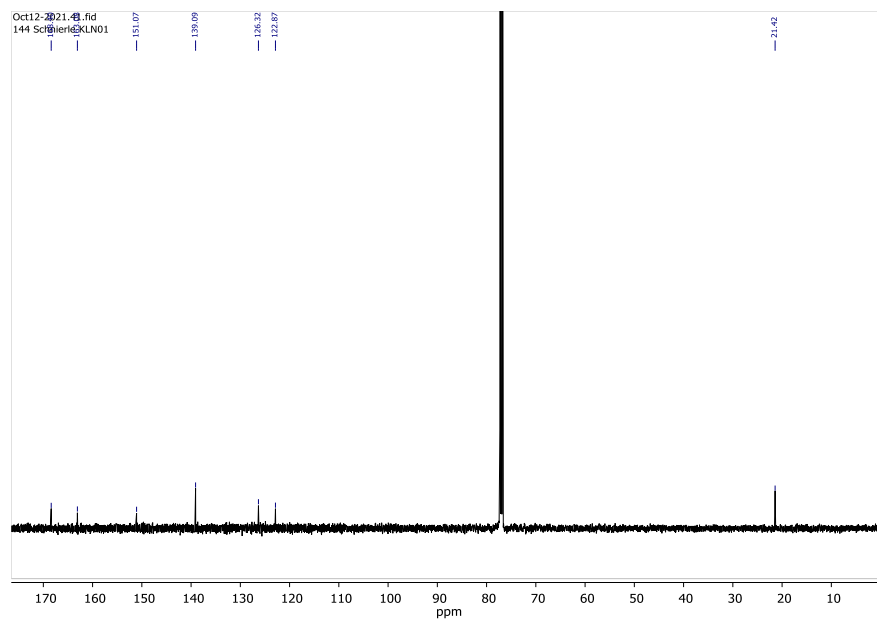
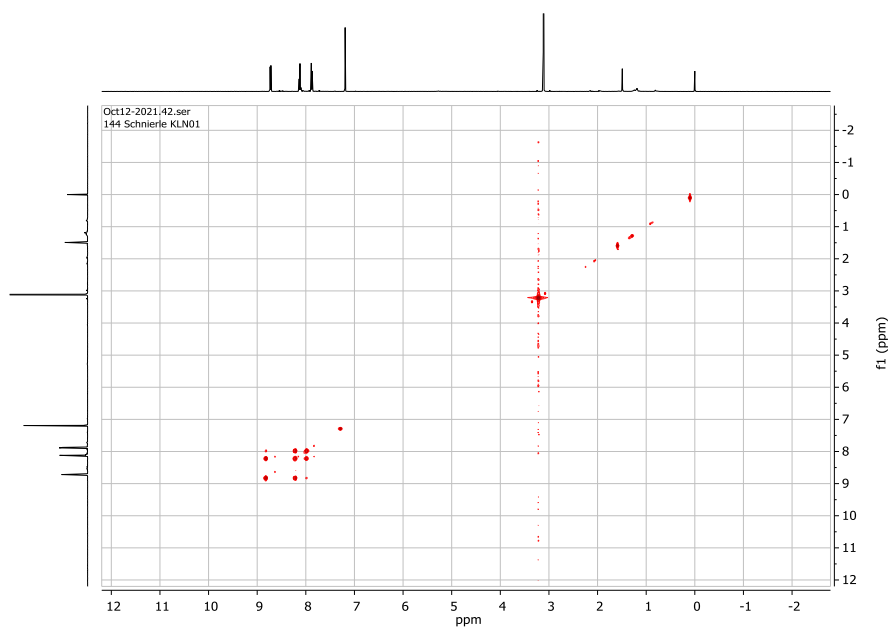


Figure 46: COSY NMR of [L]-Me in  $\text{CDCl}_3$ .

Figure 47:  $^1\text{H}$  NMR of [L]-OMe in  $\text{CDCl}_3$ .Figure 48:  $^{13}\text{C}$  NMR of [L]-OMe in  $\text{CDCl}_3$ .



Figure 49: COSY NMR of [L]-OMe in  $\text{CDCl}_3$ .Figure 50:  $^1\text{H}$  NMR of [L]- $\text{CF}_3$  in  $\text{CDCl}_3$ .

Figure 51:  $^{13}\text{C}$  NMR of [L]-CF<sub>3</sub> in CDCl<sub>3</sub>.Figure 52: COSY NMR of [L]-CF<sub>3</sub> in CDCl<sub>3</sub>.

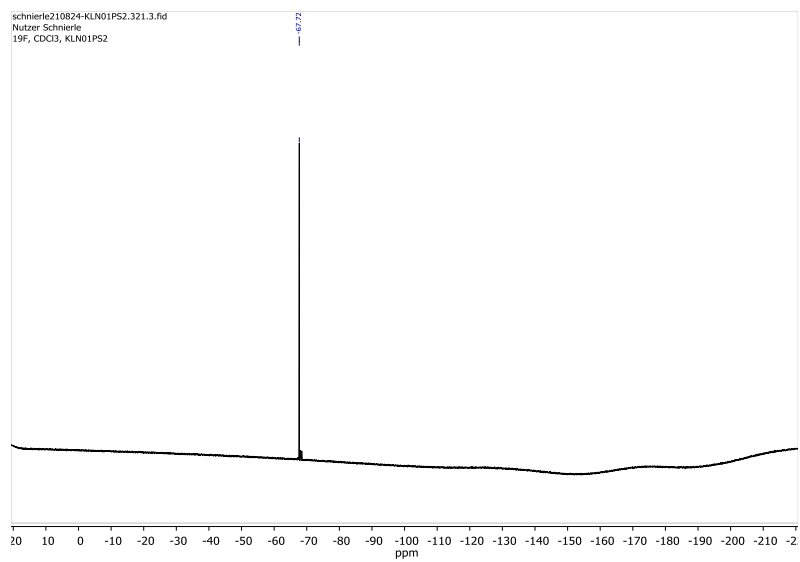


Figure 53:  $^{19}\text{F}$  NMR of [L]- $\text{CF}_3$  in  $\text{CDCl}_3$ .

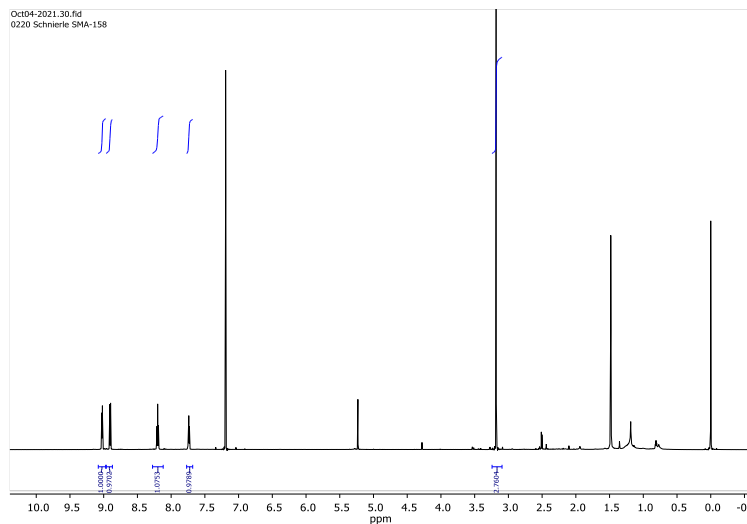


Figure 54:  $^1\text{H}$  NMR of [C]-H in  $\text{CDCl}_3$ .

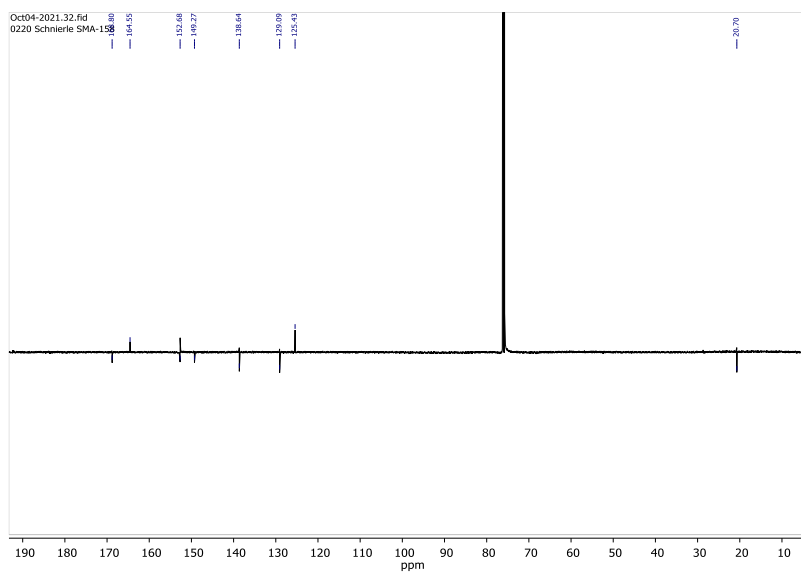
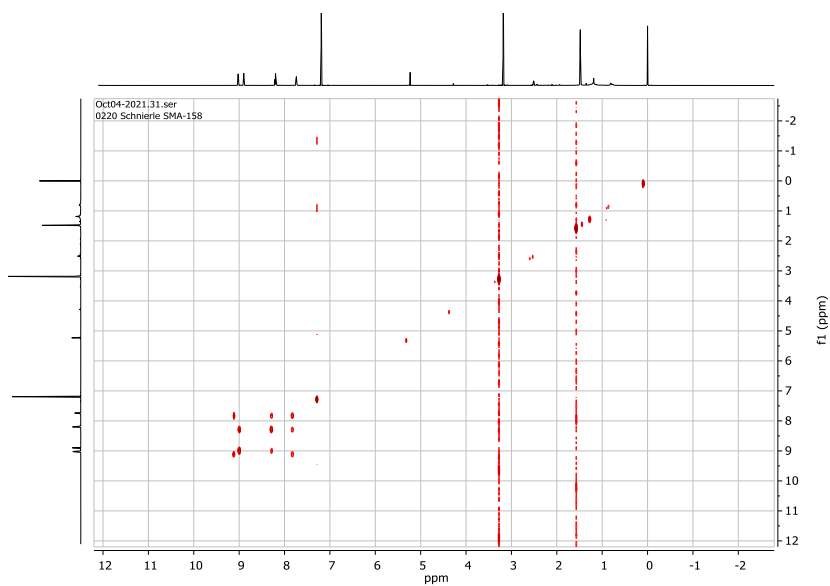
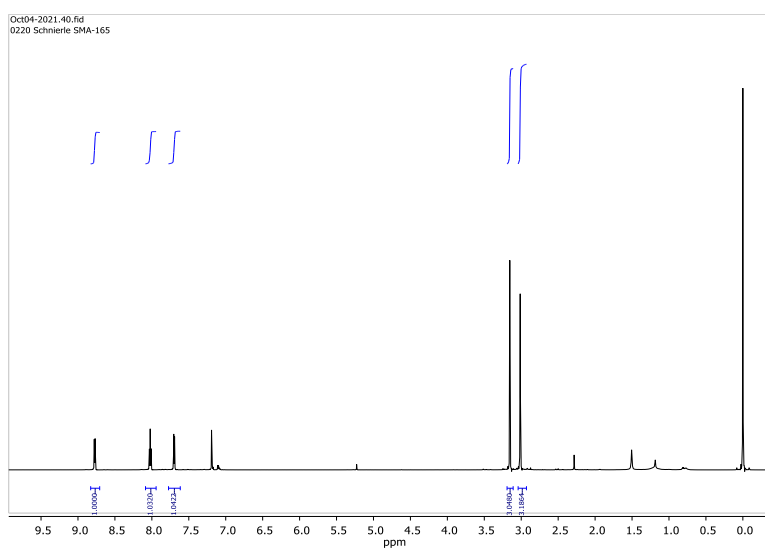


Figure 55:  $^{13}\text{C}$  NMR of [C]-H in  $\text{CDCl}_3$ .

Figure 56: COSY NMR of [C]-H in CDCl<sub>3</sub>.Figure 57: <sup>1</sup>H NMR of [C]-Me in CDCl<sub>3</sub>.

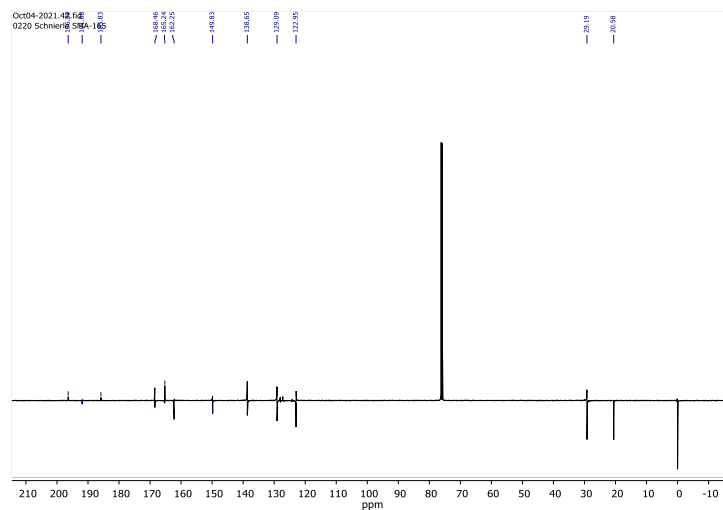


Figure 58:  $^{13}\text{C}$  NMR of [C]-Me in  $\text{CDCl}_3$ .

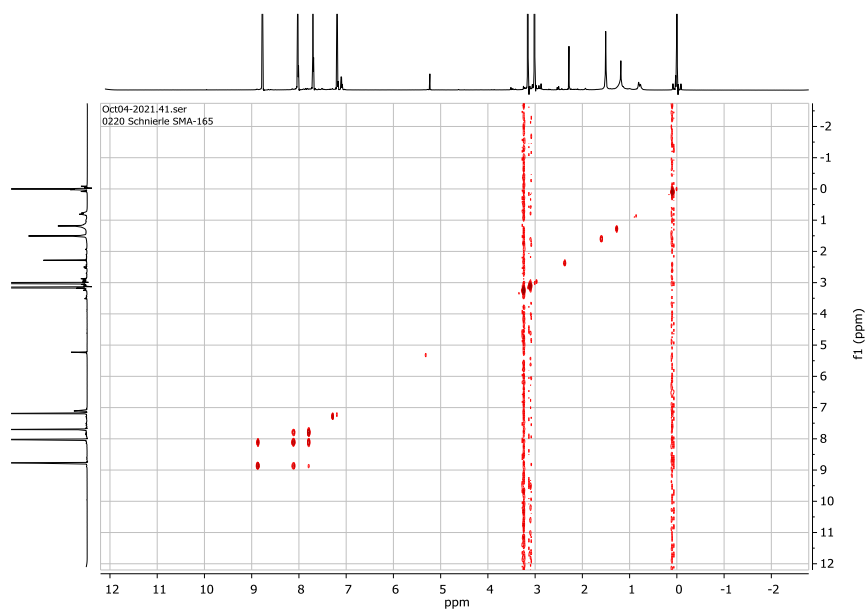
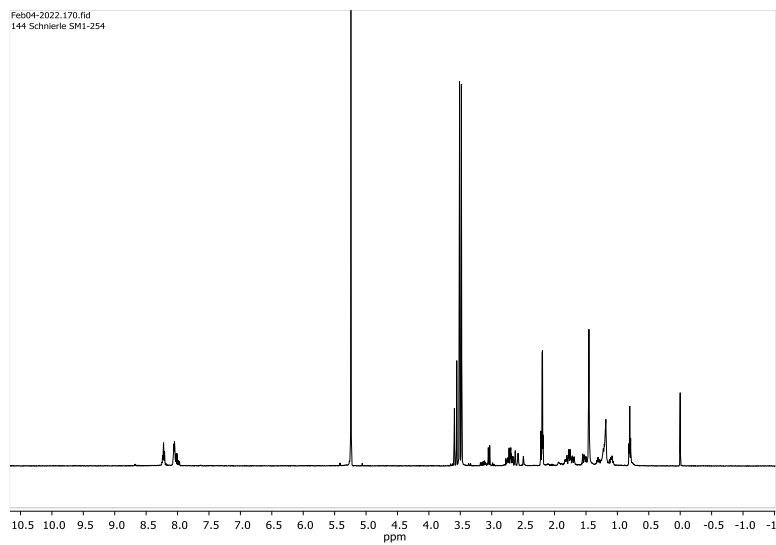
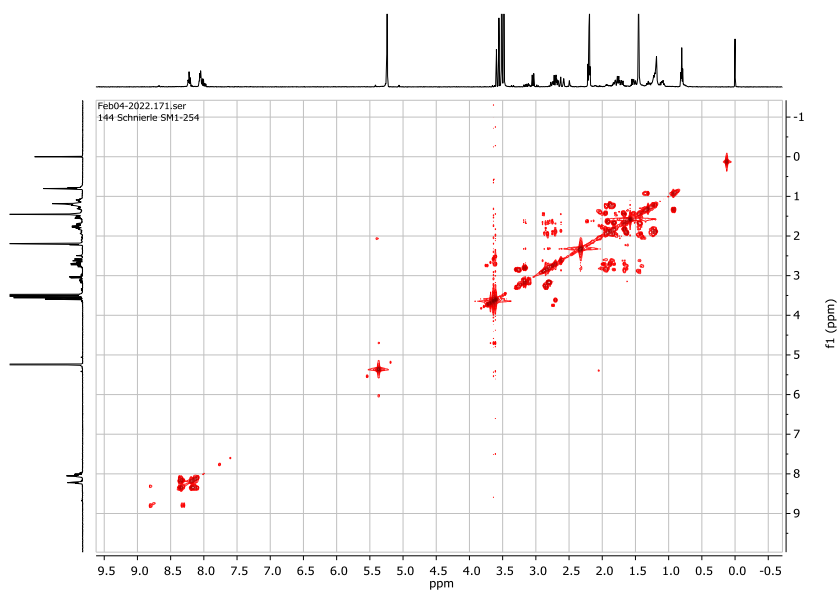


Figure 59: COSY NMR of [C]-Me in  $\text{CDCl}_3$ .

Figure 60:  $^1\text{H}$  NMR of Linker-[C]-CF<sub>3</sub> in CD<sub>2</sub>Cl<sub>2</sub>.Figure 61: COSY NMR of Linker-[C]-CF<sub>3</sub> in CD<sub>2</sub>Cl<sub>2</sub>.

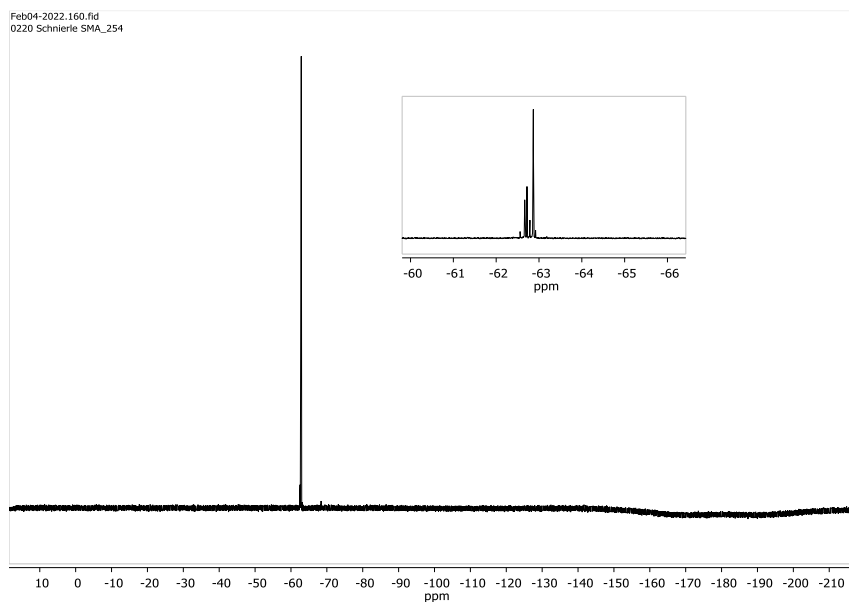


Figure 62:  $^{19}\text{F}$  NMR of Linker-[C]- $\text{CF}_3$  in  $\text{CD}_2\text{Cl}_2$ .



Cyclic Voltammetry:

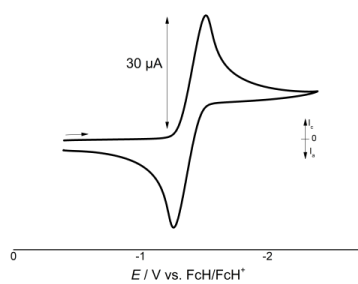


Figure 63: Cyclicvoltammogram of [L]-H in 0.1 M  $n\text{Bu}_4\text{NPF}_6/\text{CH}_2\text{Cl}_2$ .

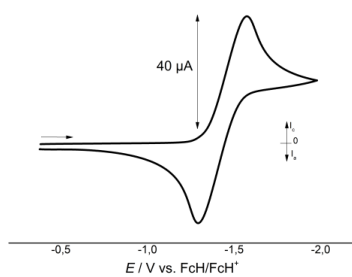


Figure 64: Cyclicvoltammogram of [L]-Me in 0.1 M  $n\text{Bu}_4\text{NPF}_6/\text{CH}_2\text{Cl}_2$ .

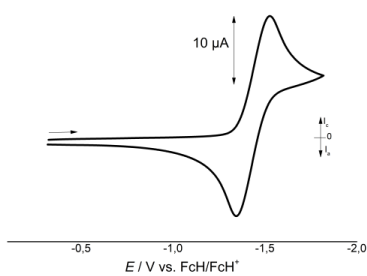


Figure 65: Cyclicvoltammogram of [L]-OMe in 0.1 M  $n\text{Bu}_4\text{NPF}_6/\text{CH}_2\text{Cl}_2$ .

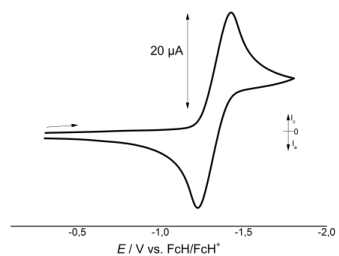


Figure 66: Cyclicvoltammogram of [L]-CF<sub>3</sub> in 0.1 M *n*Bu<sub>4</sub>NPF<sub>6</sub>/ CH<sub>2</sub>Cl<sub>2</sub>.

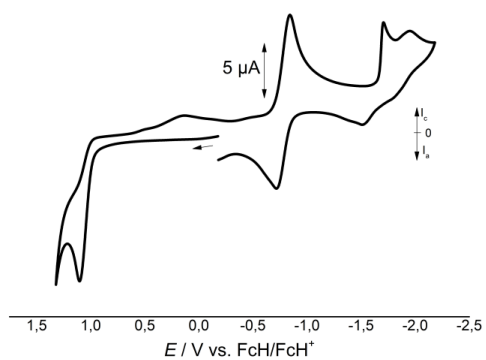


Figure 67: Cyclicvoltammogram of [C]-H in 0.1 M *n*Bu<sub>4</sub>NPF<sub>6</sub>/ CH<sub>2</sub>Cl<sub>2</sub>.

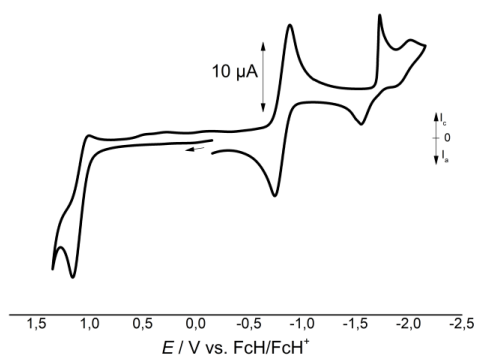
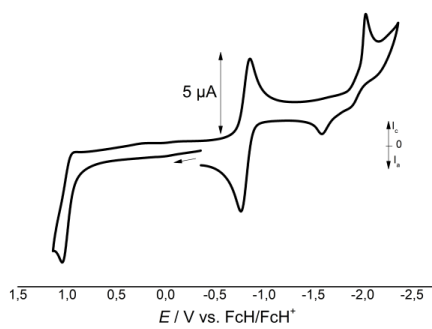
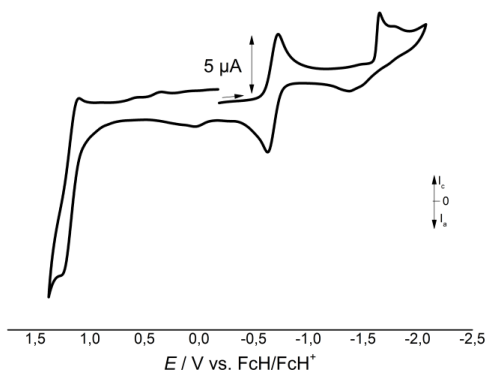
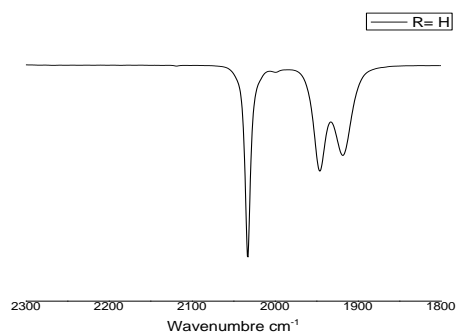
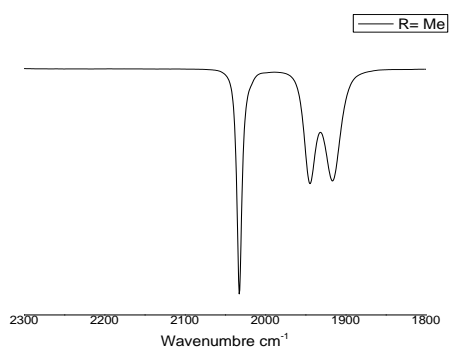
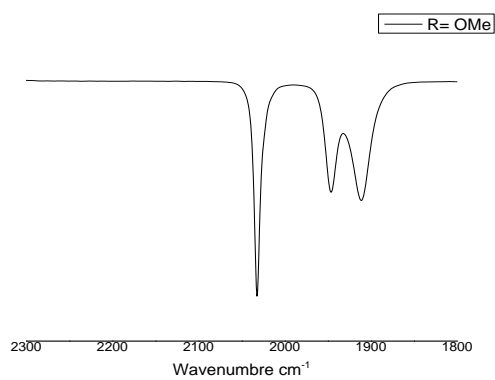


Figure 68: Cyclicvoltammogram of [C]-Me in 0.1 M  $n\text{Bu}_4\text{NPF}_6/\text{CH}_2\text{Cl}_2$ .Figure 69: Cyclicvoltammogram of [C]-OMe in 0.1 M  $n\text{Bu}_4\text{NPF}_6/\text{CH}_2\text{Cl}_2$ .Figure 70: Cyclicvoltammogram of [C]-CF<sub>3</sub> in 0.1 M  $n\text{Bu}_4\text{NPF}_6/\text{CH}_2\text{Cl}_2$ .

## Infrared Spectroscopy

Figure 71: IR of [C]-H in CH<sub>2</sub>Cl<sub>2</sub>.Figure 72: IR of [C]-Me in CH<sub>2</sub>Cl<sub>2</sub>.Figure 73: IR of [C]-OMe in CH<sub>2</sub>Cl<sub>2</sub>.

Absorption Spectroscopy:

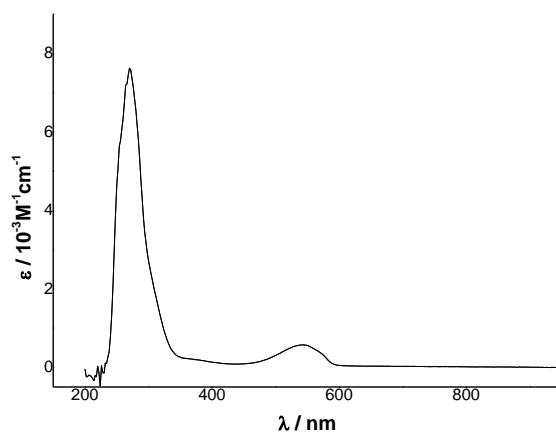


Figure 74: UV/Vis of [L]-H in CH<sub>2</sub>Cl<sub>2</sub>.

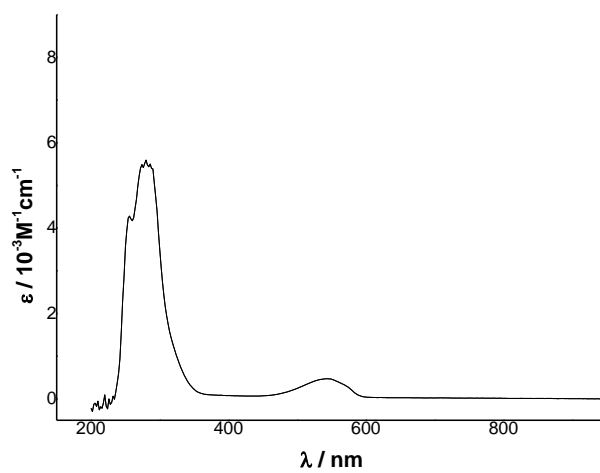
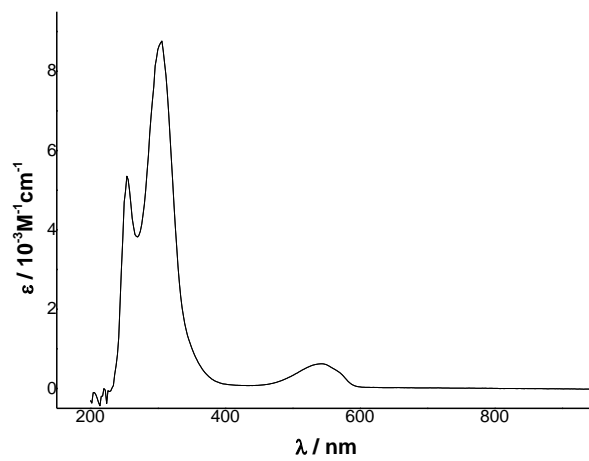
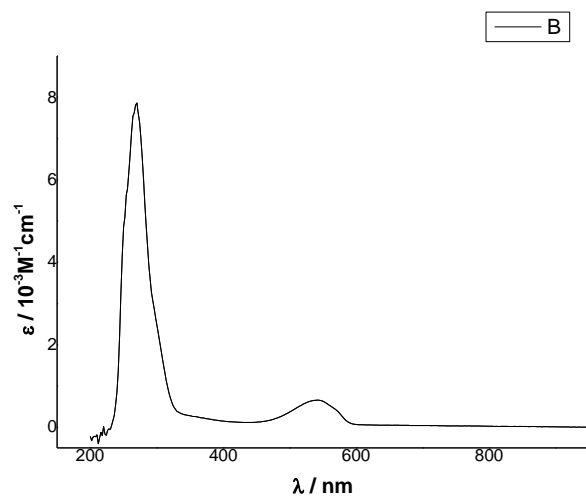
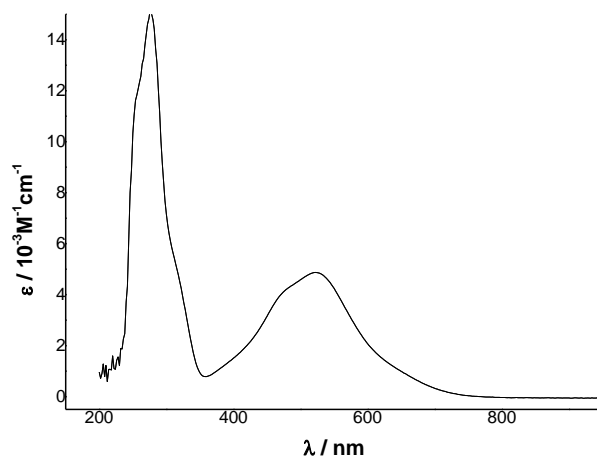
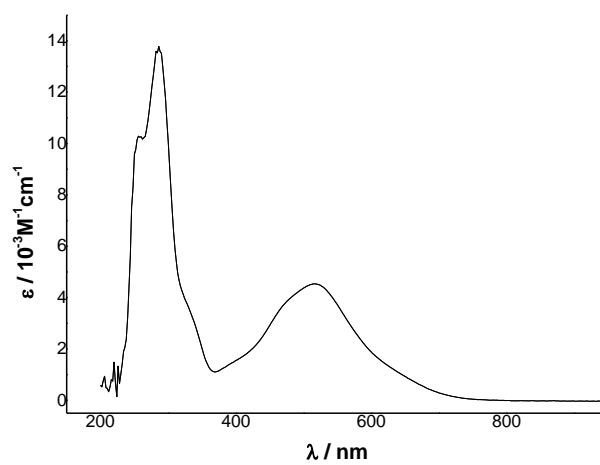


Figure 75: UV/Vis of [L]-Me in CH<sub>2</sub>Cl<sub>2</sub>.

Figure 76: UV/Vis of [L]-OME in CH<sub>2</sub>Cl<sub>2</sub>.Figure 77: UV/Vis of [L]-CF<sub>3</sub> in CH<sub>2</sub>Cl<sub>2</sub>.

Figure 78: UV/Vis of [C]-H in CH<sub>2</sub>Cl<sub>2</sub>.Figure 79: UV/Vis of [C]-Me in CH<sub>2</sub>Cl<sub>2</sub>.

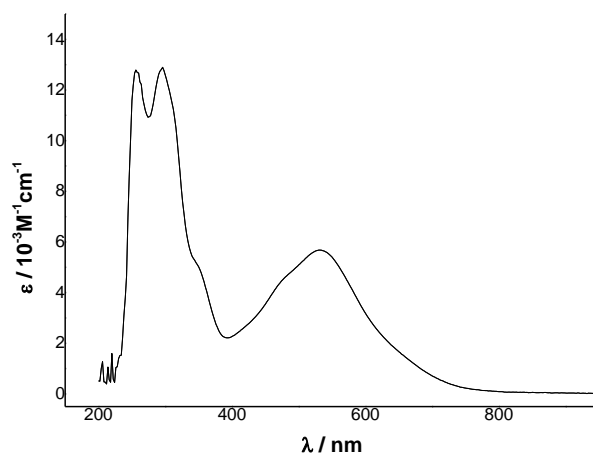


Figure 80: UV/Vis of [C]-OMe in CH<sub>2</sub>Cl<sub>2</sub>.



Solid State UV/Vis:

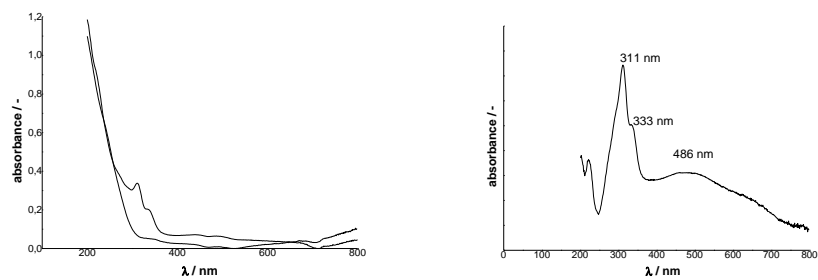


Figure 81: Solid state UV/Vis of [C]-CF<sub>3</sub>.

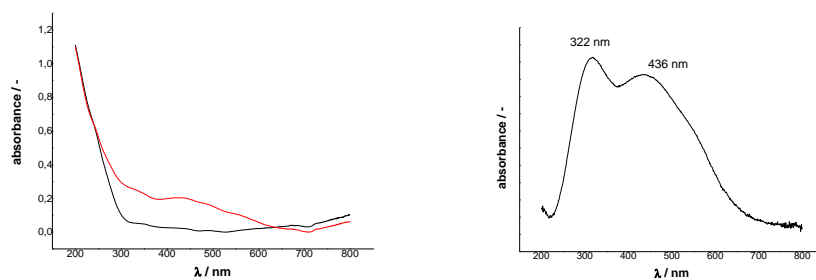


Figure 82: Solid state UV/Vis of linker-[C]-CF<sub>3</sub>.

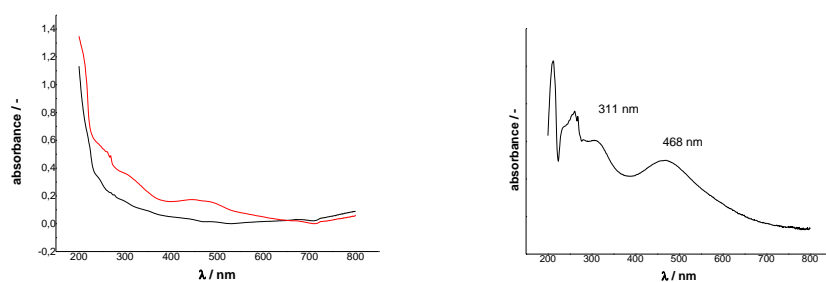


Figure 83: Solid state UV/Vis of SBA-15-[C]-CF<sub>3</sub>.

XPS:

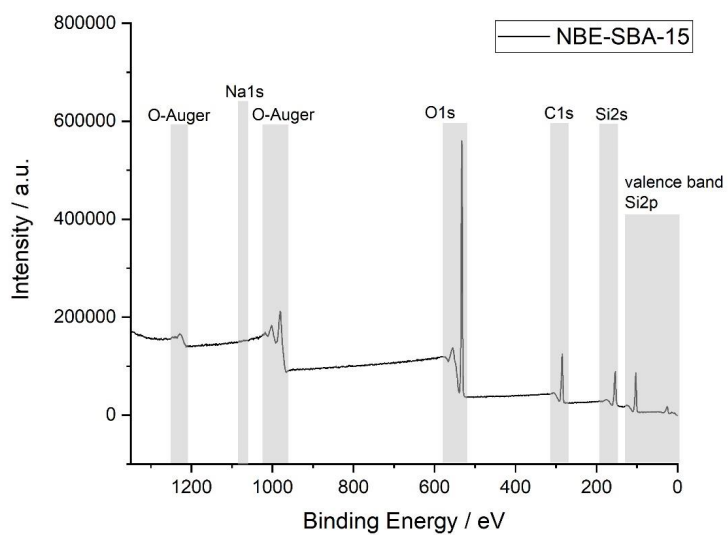


Figure 84: XPS of norbonen-trimethoxysilane functionalized SBA-15.



## Curriculum Vitae

## CURRICULUM VITAE



**MARC  
SCHNIERLE**

#### Personal data

born: 21.02.1992 / Nagold  
marital status: single

address:  
BrückenstraÙ 2  
74219 Möckmühl

mobile:  
01573/4486340  
e-mail:  
marc.schnierle@gmx.de

#### languages:

german   
english



#### Academic career

- since 07/2018 **PhD in inorganic chemistry**  
University of Stuttgart  
Doctoral student speaker of CRC1333  
Focus on synthesis, click chemistry,  
electrochemistry and kinetics
- 10/2016 – 02/2017 **Semester abroad (ERASMUS)**  
Turku, Finland  
Åbo Akademie
- 10/2015 – 06/2018 **Master of Science**  
University of Stuttgart  
focus on polymerchemistry  
Graduation grade: 2.5
- 10/2012 – 09/2015 **Bachelor of Science**  
University of Stuttgart  
Graduation grade: 2.8
- 09/2008 – 06/2011 **ABITUR**  
Technical high school, Nagold  
Graduation grade: 2.1
- 09/2002 – 07/2008 High school Otto-Hahn-Gymnasium, Nagold
- 09/1998 – 07/2002 Elementary school Malmenschule, Rohrdorf



#### Professional career

- 07/2011 – 09/2012 **Voluntary military service**  
Bundeswehr Fernmeldekompanie Calw
- 07/2018 – 09/2022 **University of Stuttgart**  
Scientific research
- since 02/2023 **German Aerospace Center**  
Low Temperature Electrolyzers & Fuel Cells



#### Specific skills

very good general computer skills  
GLP, MS Office, LaTeX, Origin  
driver license B  
International leader training for scouts (Woodbadge)